Supramolecular Coordination Cages based on Bispyridyl-ligands with Redox Properties

Dissertation

zur Erlangung des mathematisch-naturwissenschaftlichen Doktorgrades

"Doctor rerum naturalium"

der Georg-August-Universität Göttingen

im Promotionsprogramm Chemie

der Georg-August University School of Science (GAUSS)

vorgelegt von

Marina Versäumer (geb. Frank)

aus Wischnjowka, Russland

Göttingen, 2016

Betreuungsausschuss

Prof. Dr. Guido H. Clever (Anorganische Chemie, Technische Universität Dortmund, Otto-Hahn-Str. 6, 44227 Dortmund)

Prof. Dr. Franc Meyer (Institut für Anorganische Chemie, Georg-August-Universität Göttingen, Tammannstr. 4 , 37077 Göttingen)

Mitglieder der Prüfungskommission

Referent: Prof. Dr. Guido H. Clever (Anorganische Chemie, Technische Universität Dortmund, Otto-Hahn-Str. 6, 44227 Dortmund)

Korreferent: Prof. Dr. Franc Meyer (Institut für Anorganische Chemie, Georg-August-Universität Göttingen, Tammannstr. 4 , 37077 Göttingen)

Weitere Mitglieder der Prüfungskommission

Dr. Michael John (Institut für Organische und Biomolekulare Chemie, Georg-August-Universität Göttingen, Tammannstr. 2, 37077 Göttingen)

Prof. Dr. Ricardo Mata (Institut für Physikalische Chemie, Georg-August-Universität Göttingen, Tammannstr. 6, 37077 Göttingen)

Prof. Dr. Dirk Schwarzer (Institut für Physikalische Chemie, Georg-August-Universität Göttingen, Tammannstr. 6 , 37077 Göttingen).

Prof. Dr. Thomas Waitz (Institut für Anorganische Chemie, Georg-August-Universität Göttingen, Tammannstr. 4 , 37077 Göttingen)

Tag der mündlichen Prüfung: 27.06.2016

Declaration

I hereby declare that my doctoral thesis entitled “Supramolecular Coordination Cages based on Bispyridyl-ligands with Redox properties” was written independently and with no other sources and aids then quoted. I have indicated the parts which were performed by project collaborators.

ACKNOWLEDGEMENTS

I would like to thank my supervisor Prof. Guido Clever for giving me the opportunity to do my PhD in his research group, for his guidance and motivation in pushing the research to success and for his encouragement in tough times. I am also very grateful to him for his trust and his helpful advices in research and writing scientific publications. I am very thankful to Prof. Guido Clever for giving me the opportunity to spend a very exciting and successful research time in Japan in the group of Prof. Shunichi Fukuzumi.

I would like to thank the Evonik foundation, in particular Dr. Matthias Rochnia, Susanne Peitzmann, Erika Sticht, Prof. Dr. Wolfgang Leuchtenberger and Silvia Pospischil for giving me a scholarship and for the great and enjoyable time at the scholarship meetings (Zurich, Brussels, Antwerpen, Dortmund) and at the Evonik Perspective meetings.

I would like to thank my secondary supervisor Prof. Franc Meyer and also Dr. Michael John, Prof. Ricardo Mata, Prof. Dirk Schwarzer and Prof. Thomas Waitz for taking part within the examination committee.

A very grateful acknowledgments are given to all the collaborators for their support in experiments and interpretation of the data and for fruitful discussions, in particular Jennifer Ahrens and Prof. Dirk Schwarzer (Max Planck Institute for Biophysical Chemistry); Dr. Jakob Hey and Lennard Krause (research group of Prof. Dietmar Stalke, University of Göttingen); Dr. Michael John, Ralf Schöne and Wolfgang Zolke (NMR department, University of Göttingen); Prof. Shunichi Fukuzumi and Dr. Tomoyoshi Suenobu (University of Osaka); Sebastian Funke and Dr. Hainer Wackerbarth (Laser-Laboratorium Göttingen); Dr. Holm Frauendorf and Györgyi Sommer-Udvarnoki (Mass department, University of Göttingen) and Matthias Hesse (Chemical and Material Storage).

I would like to thank all the research students for their contributions in synthesis and in performance of experiments, namely Jonas Ammermann, Ilker Balcioglu, Isabell Bejenke, Lorenz Deres, Chuan Dong, Michael Hendrich, Jana Lücken, Sonja Schmidt and Willi Smolan.

I would like to thank all the members of the Clever Lab group for the enjoyable daily atmosphere and their encouraging advices in turbulent times. Especially, David, Muxin, Sabrina, Susanne, Marcel, Fernanda, Rongmei, Mark, Witold, Rujin and all the other members of the Clever Lab are gratefully acknowledged for their help at any time. I would like to thank Thorben for the chaotic but pleasant atmosphere in the lab.

Last but not least I would like to thank my family for their support and understanding for the frequent lack of time. My biggest thanks goes to my husband Kai, who was always on my side and supported me in good and bad times.

In loving memory of Beam

and in joyful anticipation of a new member of the pack…

LIST OF PUBLICATIONS

FIRST AUTHOR PUBLICATIONS (THIS THESIS IS BASED ON A COMPENDIUM OF THE FOLLOWING PUBLICATIONS)

- '*Assembly and stepwise oxidation of interpenetrated coordination cages based on phenothiazine*', M. Frank, J. Hey, I. Balcioglu, Y.-S. Chen, D. Stalke, T. Suenobu, S. Fukuzumi, H. Frauendorf, G. H. Clever, *Angew. Chem. Int. Ed.* **2013**, *52*, 10102–10106; *Angew. Chem.* **2013**, *125*, 10288–10293. (CHAPTER III)
- '*Relative anion binding affinity in a series of interpenetrated coordination cages*', M. Frank, J. M. Dieterich, S. Freye, R. A. Mata, G. H. Clever, *Dalton Trans*. **2013**, *42*, 15906–15910. (CHAPTER IV)
- '*Narcissistic self-sorting vs. statistic ligand shuffling within a series of phenothiazine-based coordination cages*', M. Frank, L. Krause, R. Herbst-Irmer, D. Stalke, G. H. Clever, *Dalton Trans*. **2014**, *43*, 4587–4592. (CHAPTER III AND V)
- '*SERS spectroscopic evidence for the integrity of surface-deposited self-assembled coordination cages*', M. Frank, S. Funke, H. Wackerbarth, G. H. Clever, *Phys. Chem. Chem. Phys.* **2014**, *40*, 21930–21935. (CHAPTER VII)
- '*Interpenetrated Cage Structures'*, M. Frank, M. D. Johnstone, G. H. Clever, *Chem. Eur. J.* **2016**, *accepted*, DOI: 10.1002/chem.201601752. (CHAPTER III and IV)
- '*Light-induced Charge Separation in Densely Packed Donor- Acceptor Coordination Cages*', M. Frank, J. Ahrens, I. Bejenke, M. Krick, D. Schwarzer, G. H. Clever, *J. Am. Chem. Soc.* **2016**, *138*, 8279-8287. (CHAPTER VI)

CO-AUTHOR PUBLICATIONS

- '*Stable and Metastable Self-Assembled Rings based on trans-chelated Pd II*', F. A. Pereira, T. Fallows, M. Frank, A. Chen, G. H. Clever, *Z. Anorg. Allg. Chem*. **2013**, *639*, 1598–1605.
- '*Rapid Solvent-Free Synthesis of Pyridyl-Functionalised [5]Polynorbornane-Based Ligands for Metal-Organic Rings and Cages*', M. D. Johnstone, M. Frank, G. H. Clever, F. M. Pfeffer, *Eur. J. Org. Chem*. **2013**, *26*, 5848–5853.

LIST OF ABBREVIATIONS

ATR	attenuated total reflection
ANQ	anthraquinone
CE	chemical enhancement
CT	charge transfer
CV	cyclic voltammetry
DOSY	diffusion-ordered spectroscopy
EM	electromagnetic enhancement
ESI	electrospray ionization
EXSY	exchange spectroscopy
IR	infrared
HR-MS	high resolution mass spectrometry
L	ligand
M	metal
M^{n+}	metal cation
mM	millimolar
MOF	metal organic framework
MS	mass spectrometry
m/z	mass-to-charge ratio
NMR	nuclear magnetic resonance
NOESY	nuclear overhauser effect spectroscopy
PET	photoinduced electron transfer
ppm	parts per million
PTZ	phenothiazine
SERS	surface enhanced raman scattering
TMEDA	N,N,N',N'-tetramethylethane-1,2-diamine
TBA	tetrabutylammonium
TFA	trifluoroacetic acid
UV/Vis	ultraviolet/visible

TABLE OF CONTENTS

SUMMARY

This thesis explores the self-assembly, the host-guest chemistry and the redox behavior of novel coordination double-cages based on organic bispyridyl ligands and Pd(II) metal ions. The formation of these double-cages depends on the interplay of many factors, such as solvent, temperature, metal coordination sites, length and shape of ligands, counter anions and guest molecules. These new three-dimensional architectures with nanoscopic size are of special interest for numerous potential applications, in particular for usage as molecular sensors, as nanoreactors or in photoelectronic devices.

In the first part of this thesis, the preparation and characterization of a series of double-cages is presented, which are constructed from eight ligands based on a phenothiazine backbone and four Pd(II) metal ions. The diamagnetic cage compounds adopt a well-defined interpenetrated structure with three pockets capable of binding small anionic guest molecules such as halide anions according to an allosteric binding mechanism. The characterization of the double-cages and the host-guest interactions were studied by means of NMR, UV/Vis, fluorescence, ESI-MS and X-ray techniques. The binding affinities of the guests inside the hosts were determined by competition experiments between different host double-cages and different halide anions. Furthermore, the cages were explored for toleration of different ligands within one double-cage structure. It was found that a mixture of short and long ligands leads to a narcissistic self-sorting, whereas a mixture of ligands with comparable lengths forms double-cages with a statistical distribution of the ligands.

The application of redoxactive phenothiazine backbones as building blocks allowed to study the redox abilities of the double-cages via chemical oxidation and a subsequent oxygenation reaction. Furthermore, a new double-cage based on the electron-deficient anthraquinone backbone was designed with the aim of constructing a donor-acceptor assembly for applications in electroactive systems such as light-powered charge-separation devices. In order to bring the donor and acceptor building blocks in close proximity, new mixed-ligand double-cages with statistically distributed ligands were synthesized. Electron transfer processes within these new donor-acceptor double-cages were studied by cyclic voltammetry, spectroelectrochemistry, steady state UV/Vis and femtosecond transient absorption spectroscopy.

Finally, the double-cages were examined for their stability on surfaces with respect to potential applications of double-cages in thin film electronic devices. As the technique of

choice, Surface Enhanced Raman Scattering (SERS) was applied for the study of surface-deposited double-cages and the results were compared to the measurements in solution phase.

Chapter I

General Introduction

I. GENERAL INTRODUCTION

Supramolecular chemistry is the "chemistry beyond the molecule" as established by the Nobel laureate (1987) Jean-Marie Lehn.[1] Therefore, the supramolecule can be described as an organized complex assembly constructed from at least two chemical components with complementary binding sites and held together by non-covalent intermolecular interactions such as hydrogen bonds, van der Waals forces, π-π and other electrostatic interactions. These intermolecular bonds are relatively weak and reversible in their nature allowing to access highly complex architectures nearly quantitatively in contrast to covalent chemistry, which often suffers from low yields in the course of step by step syntheses with increasing complexity of the system. Even though some of the intermolecular forces are weak, their cooperative interplay within the supramolecule can yield remarkably stable structures. The lability of supramolecular interactions allows the system to correct mistakes that can occur during the self-assembly process. Non-covalent interactions play a crucial role for the construction of highly complex matter in the living world. Nature uses self-assembly based on intermolecular non-covalent interactions to construct highly sophisticated three-dimensional supramolecular architectures. Starting from just a few building blocks, such as nucleic acids, sugars or lipids, covalent polymerization and supramolecular interactions lead to DNA, proteins, enzymes, carbohydrates, lipid membranes and many more, which bear a huge pool of information and functionalities.[2]

Two of the core concepts of supramolecular chemistry are described by the terms self-assembly and self-organization. Self-assembly characterizes a spontaneous process of non-covalent association of at least two molecules into one ordered structure that leads to an equilibrium state, whereas the active self-organization is a time-dependent dissipative non-equilibrium process.[3] Self-organization enabled the evolution of the

---

[1] Jean-Marie Lehn, *Nobel Lecture*, **1987**.

[2] for an overview of supramolecular chemistry, see (a) J.-M. Lehn, *Science* **2002**, *295*, 2400. (b) K. Ariga, T. Kunitake, *Supramolecular chemistry*. *Fundamentals and applications*, Springer, Heidelberg, **2006**. (c) F. Diederich, P. J. Stang, R. R. Tykwinski, *Modern Supramolecular Chemistry - Strategies for Macrocycle Synthesis*, Wiley-VCH, Weinheim, **2008**. (d) J. W. Steed, J. L. Atwood, *Supramolecular chemistry*, Wiley-VCH, Chichester, **2009**.

[3] J.-M. Lehn, *Angew. Chem. Int. Ed.* **2013**, *52*, 2836.

living biological world starting from inanimate matter. Understanding and mimicking these complex self-processes constitute the ultimate challenge for supramolecular chemists. The concept of self-assembly enables a programmed association process to complex architectures from rather simple building blocks bearing chemical moieties for divergent coordination (see Figure I.1).[3,4] The outcome of the self-assembly is normally a thermodynamically stable product, which evolves from all other possible assembly combinations. Thus, an elaborative design strategy via application of complementary molecular entities can afford a selective formation of supramolecular architectures. Nevertheless, unexpected structure formation is observed for some self-assembly mixtures, despite the employment of predictable coordination motifs. This shows that also other factors than the careful selection of building blocks significantly contribute to the outcome of the assembly, namely temperature, solvent, counter anions, pH values, etc.[2b,d]

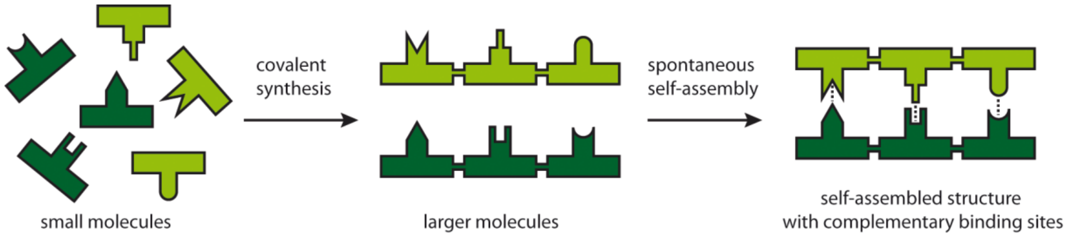

Figure I.1 Schematic illustration of covalent synthesis of building blocks with divergent binding sites and their spontaneous self-assembly into a higher ordered structure.

Coordination driven self-assembly was developed in order to overcome the drawbacks of traditional relatively weak supramolecular attractive forces. Here, a relatively strong bond between an organic ligand and a metal node helps to gain control over the self-assembly. A high degree of directionality is preset by predictable coordination geometries of the metal ions. The stability of the metal-organic coordination bond is ranging between the highly stable covalent bond and comparatively weak supramolecular interactions. Apart from the stability reasons, the diversity of predefined coordination angles and the number of free binding sites of transition metals

---

[4] M. W. Hosseini, *Chem. Commun.* **2005**, 5825.

offers a variety of possibilities for the design of new structures. Even more versatile is the pool of organic linkers which may contain two or more coordination sites with bite angles between 0 and 180°.[5] In order to demonstrate the versatility of the divergent binding concept, some self-assembled architectures based on square-planar coordinating metal ions with ligands bearing two pyridine binding sites will be presented in connection with structures that were reported in the *Clever Lab* (see Figure I.2).[6] The application of *trans*-chelating bispyridyl ligands in combination with bis-monodentate bridging ligands leads to the formation of two- and three-membered ring compounds (see Figure I.2a and I.2b).[7] Exclusive utilization of rigid *trans*-chelating ligands results in the formation of scarcely described *trans*-coordinated complexes (see Figure I.2c).[7,8] Long flexible bispyridyl ligands can yield butterfly shaped complexes (see Figure I.2d)[9] or more sophisticated intertwined structures such as the double-trefoil knot [$M_3\mathbf{L}_6$] (see Figure I.2e).[10] The self-assembly can lead to monomeric coordination cages of the constitution $M_2\mathbf{L}_4$, when four free coordination sites are offered at the metal ions for a single kind of bis-monodentate banana-shaped ligand (see Figure I.2f).[11,12,13,14,15] The formation of interpenetrated dimeric cages is possible if the surrounding conditions regarding the length, rigidity and bite angle of the ligand, solvent, temperature and counter anions are chosen adequately (see Figure I.2g).[16,17,18,19] These dimeric cages are

---

[5] R. Chakrabarty, P. S. Mukherjee, P. J. Stang, *Chem. Rev.* **2011**, *111*, 6810.

[6] for reviews on assemblies with banana-shaped bispyridyl ligands and square-planar coordinating metal ions see (a) M. Han, D. M. Engelhard, G. H. Clever, *Chem. Soc. Rev.* **2014**, *43*, 1848. (b) M. Frank, M. D. Johnstone, G. H. Clever, *Chem. Eur. J.* **2016**, *accepted*, DOI: 10.1002/chem.201601752.

[7] F. A. Pereira, T. Fallows, M. Frank, A. Chen, G. H. Clever, *Z. Anorg. Allg. Chem.* **2013**, *639*, 1598.

[8] (a) Y.-Z. Hu, C. Chamchoumis, J.S. Grebowicz, R.P. Thummel, *Inorg. Chem.* **2002**, *41*, 2296. (b) S. Shotwell, H.L. Ricks, J.G.M. Morton, M. Laskoski, J. Fiscus, M.D. Smith, K.D. Shimizu, H-C. zur Loye, U.H.F. Bunz, *J. Organomet. Chem.* **2003**, *671*, 43. (c) F. A. Pereira, G. H. Clever, *Inorg. Chim. Acta* **2016**, *accepted*, DOI: 10.1016/j.ica.2016.04.024.

[9] M. D. Johnstone, M. Frank, G. H. Clever, F. M. Pfeffer, *Eur. J. Org. Chem.* **2013**, 5848.

[10] D. M. Engelhard, S. Freye, K. Grohe, M. John, G. H. Clever, *Angew. Chem. Int. Ed.* **2012**, *51*, 4747.

[11] T. R. Schulte, M. Krick, C. I. Asche, S. Freye, G. H. Clever, *RSC Adv*. **2014**, *4*, 29724.

[12] M. D. Johnstone, E. K. Schwarze, G. H. Clever, F. M. Pfeffer, *Chem. Eur. J.* **2015**, *21*, 3948.

[13] M. Han, R. Michel, B. He, Y.-S. Chen, D. Stalke, M. John, G. H. Clever, *Angew. Chem. Int. Ed*. **2013**, *52*, 1319.

[14] M. Han, J. Hey, W. Kawamura, D. Stalke, M. Shionoya, G. H. Clever, *Inorg. Chem.* **2012**, *51*, 9574.

[15] S. Löffler, J. Lübben, A. Wuttke, R. A. Mata, M. John, B. Dittrich, G. H. Clever, *Chem. Sci.* **2016**, *7*, 4676.

[16] S. Freye, J. Hey, A. Torras-Galán, D. Stalke, R. Herbst-Irmer, M. John, G. H. Clever, *Angew. Chem. Int. Ed.* **2012**, *51*, 2191.

also named double-cages and exhibit the general molecular formula $M_4\mathbf{L}_8$. Shorter banana-shaped ligands are capable of forming triple catenanes such as {*trans*-$[(MX_2)_2\mathbf{L}_2]\}_3$, when coordinating halide anions are present in excess in the solution (see Figure I.2h).[19] In their open form, light-switchable ligands based on photochromic dithienylethene backbones with a bent angle of 138° can lead to the formation of three- and four-membered rings. In their closed form, the ligands can yield a giant rhombicuboctahedral sphere $[M_{24}\mathbf{L}_{48}]$ (see Figure I.2i).[20] All of the aforementioned examples are built from a Pd(II) source and bispyridyl ligands and show the diversity of accessible architectures by simple variation of some structural parameters or environmental conditions.

---

[17] S. Freye, R. Michel, D. Stalke, M. Pawliczek, H. Frauendorf, G. H. Clever, *J. Am. Chem. Soc.* **2013**, *135*, 8476.

[18] S. Löffler, J. Lübben, L. Krause, D. Stalke, B. Dittrich and G. H. Clever, *J. Am. Chem. Soc.* **2015**, *137*, 1060.

[19] R. Zhu, J. Lübben, B. Dittrich, G. H. Clever, *Angew. Chem. Int. Ed.* **2015**, *54*, 2796.

[20] M. Han, Y. Luo, B. Damaschke, L. Gómez, X. Ribas, A. Jose, P. Peretzki, M. Seibt, G. H. Clever, *Angew. Chem. Int. Ed.* **2016**, *55*, 445.

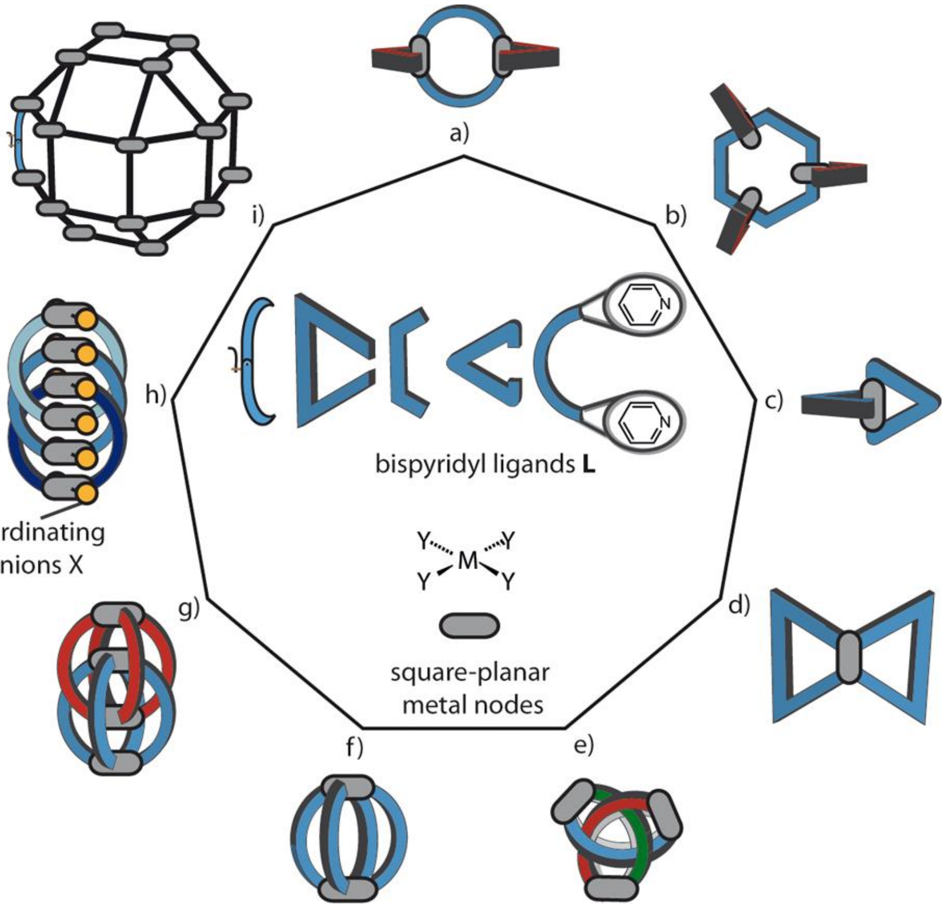

Figure I.2 Self-assembled architectures based on Pd(II) cations and bispyridyl ligands with different lengths, shapes and angles between the binding sites studied in the *Clever Lab*: a) a ring $[M_2\mathbf{L}^X{}_2\mathbf{L}^Y{}_2]$,[7] b) a ring $[M_3\mathbf{L}^X{}_3\mathbf{L}^Y{}_3]$,[7] c) *trans*-chelated complex $[M\mathbf{L}_2]$,[7] d) butterfly-shaped complex $[M\mathbf{L}_2]$,[9] e) double-trefoil knot $[M_3\mathbf{L}_6]$,[10] f) monomeric cage $[M_2\mathbf{L}_4]$,[11,12,13,14,15] g) double-cage $[M_4\mathbf{L}_8]$,[16,17,18,19] h) triple catenane {*trans*-$[(MX_2)_2\mathbf{L}_2]\}_3$,[19] and i) rhombicuboctahedral sphere $[M_{24}\mathbf{L}_{48}]$.[20]

In the last decades a variety of self-assembled coordination structures were reported including capsules, catenanes, rotaxanes, helicates, various knots, molecular grids, cages, metal organic frameworks and many more.[3,5,21] Among them, cages and capsules are of

---

[21] for reviews see (a) S. J. Dalgarno, N. P. Power, J. L. Atwood, *Coord. Chem. Rev.* **2008**, *252*, 825. (b) J. D. Crowley, S. M. Goldup, A.-L. Lee, D. A. Leigh, R. T. McBurney, *Chem. Soc. Rev.* **2009**, *38*, 1530. (c) J. E. Beves, B. A. Blight, C. J. Campbell, D. A. Leigh, R. T. McBurney, *Angew. Chem. Int. Ed.* **2011**, *50*, 9260. (d) R. S. Forgan, J.-P. Sauvage, J. F. Stoddart, *Chem. Rev.* **2011**, *111*, 5434. (e) N. B. Debata, D. Tripathy, D. K. Chand, *Coord. Chem. Rev.* **2012**, *256*, 1831. (f) K. Harris, D. Fujita, M. Fujita, *Chem. Commun.* **2013**, *49*, 6703. (g) P. J. Lusby, *Annu. Rep. Prog. Chem., Sect. A: Inorg. Chem.* **2013**, *109*, 254. (h) M. M. J. Smulders, I. A. Riddell, C. Browne, J. R. Nitschke, *Chem. Soc. Rev.*, **2013**, *42*, 1728. (i) T. R. Cook, P. J. Stang, *Chem. Rev.* **2015**, *115*, 7001.

particular interest due to their ability to host, protect, transport and release guest molecules.[22] A host molecule is defined by a central cavity that is able to include a smaller molecule (see Figure I.3). Noteworthy is that compounds with a three-dimensional spherically-shaped cavity, which are able to enclose the bound guest entirely, form stronger complexes compared to flat shaped macrocycles due to the maximization of possible interactions. In contrast to capsules, which usually have to undergo a deformation or even a partial disassembly in order to encapsulate or release guest molecules, the guest exchange in a cage proceeds through open side windows and thus without significantly changing or even destructing the structure of the cage. The driving force for the encapsulation process is an attractive interaction between the guest and the interior of the host molecule based on electrostatic attraction and/or hydrophobic effect. For this, a rational design of the host molecule is necessary, which considers the cavity to be complementary in size and shape to the guest and takes into account a number of supramolecular host-guest interactions in order to ensure a high stability of the target complex. If a mixture of different suitable guest molecules is offered to the host, the latter should be able to encapsulate the desired guest molecule preferably over the others. This selectivity corresponds to a higher binding constant for the target guest. The binding affinity of the guest should be at least higher than the sum of attractive interactions between the receptor and the solvent molecules, which are released during the encapsulation of the guest. However, some supramolecular hosts are not only able to selectively incorporate the guest molecule, but they can also act as molecular reagent or even catalyst in the chemical transformation of the bound guest.[22]

Some host molecules are designed in a way that they can operate as a supramolecular transport container e. g. a lipophilic supramolecular host can carry a charged guest molecule from one hydrophilic compartment into another via crossing a lipophilic membrane.[1] Another important issue of host-guest characteristics constitutes the reversibility of the assembly, which can be considered as the possibility of the guest to escape. The exchange of the guest with the external environment can proceed via a partial or full dissociation of the host or by diffusion of the guest through the windows of

---

[22] M. Yoshizawa, J. K. Klosterman, M. Fujita, *Angew. Chem. Int. Ed.* **2009**, *48*, 3418.

the host molecule.[23] The guest molecule can also act as a template for the assembly of the supramolecular structure. Charged molecules are usually used as templates due to their directional electrostatic interactions. They help to organize the building blocks in an appropriate manner prior to the final assembly of the structure. In the following, the guest molecule will be written inside the square brackets defining the assembled host, followed by an @ sign standing for the encapsulation. Simple counter anions will be denoted outside the complex formula.

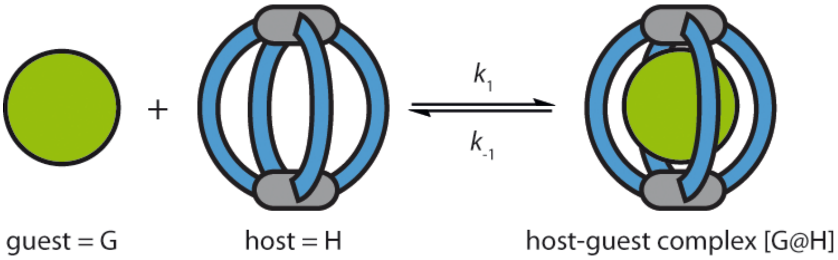

Figure I.3 Guest (G) equilibrium encapsulation inside a coordination cage (H) with a rate constant of k_1 for the complexation and k_{-1} for the decomplexation process yielding a stable host-guest complex [G@H]. Building blocks in grey denote metal cations and in blue the ligands.

The thermodynamic stability of the host-guest complex can be expressed by the association or binding constant (K_a). A high binding constant is correlated to a high equilibrium concentration of the host-guest adduct [G@H] compared to the free components (see Equation I.1). The binding constant can be also expressed via the rate constants of the complexation and decomplexation process. The binding constant can be measured by any experimental technique such as NMR, UV-Vis, fluorescence and calorimetric titrations, whose response signal can be correlated to the concentration of the involved components.[23] Although strong binding may be achieved with rigid host molecules, other higher order processes such as exchange, cooperativity and allostery require a certain degree of host flexibility in order to adapt to the guest.

$$K_\mathrm{a} = \frac{[\mathrm{G@H}]}{[\mathrm{H}] \cdot [\mathrm{G}]} = \frac{k_1}{k_{-1}} \quad (\mathrm{Eq.\ I.1})$$

Some hosts are able to recognize more than one guest molecule. The binding event

---

[23] M. D. Pluth, K. N. Raymond, *Chem. Soc. Rev.* **2007**, *36*, 161.

can proceed in an allosteric fashion with either positive or negative cooperativity (see Figure I.4) or both guest molecules can be bound with the same binding affinity. Positive allosteric binding is a well known phenomenon in biology, for example hemoglobin binds oxygen in a way that binding at any of the four receptor sites increases the oxygen affinity at the other sites. Binding of the first oxygen molecule induces a structural change that preorganizes the binding site for further oxygen molecules.[24] Considering the simplest case of a receptor with two covalently connected binding sites, the binding can be characterized via two association constants. Positive cooperativity at the molecular state results in a higher value for the second association constant compared to the first indicating that the fully bound state is more favorable than the intermediate states. On the other hand a negative cooperativity is found for systems where the binding of the first guest molecule decreases or even inhibits the association affinity for further binding. This is reflected by a significantly smaller second association constant compared to the first.[25]

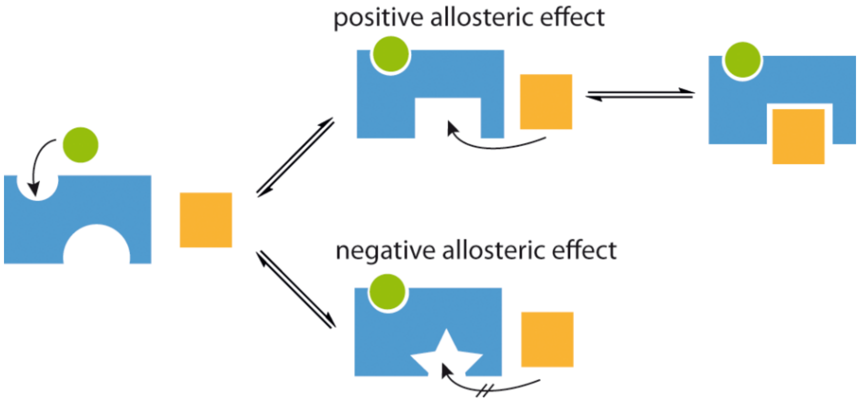

Figure I.4 Schematic illustration of a positive and negative allosteric effect.

An advanced goal in the design of supramolecular self-assembled host molecules is the combination of various functionalities within one system (see Figure I.5). Different properties such as redox-, iono-, photo-, magneto-, thermo- or chemo-activity can be implemented into the host system via the selection of an appropriate organic linker or

---

[24] H. Lodish, A. Berk, S L. Zipursky, P. Matsudaira, D. Baltimore, J. Darnell, *Molecular Cell Biology*, 4th edition, W. H. Freeman, New York **2000**.

[25] C. A. Hunter, H. L. Anderson, *Angew. Chem. Int. Ed.* **2009**, *48*, 7488.

the metal nodes. These properties can be combined with the host-guest properties to give a highly sophisticated supramolecular system which can be applied in supramolecular catalysis or in transport processes of molecules triggered by external stimuli such as redox-potential, light, pH-value. Furthermore, a stimuli-responsive supramolecular system can be used for molecular photonic and electronic devices.

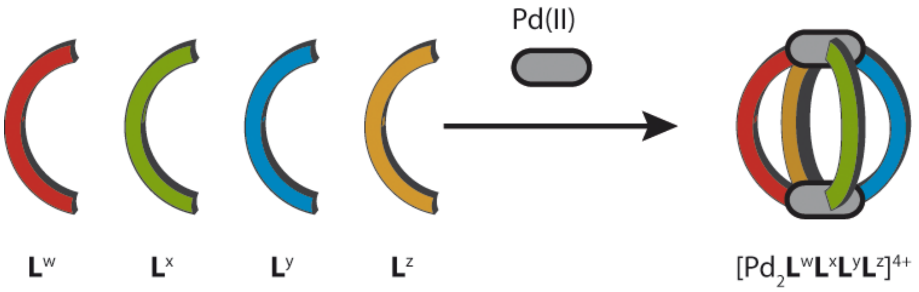

Figure I.5 Schematic illustration of a rational design of a monomeric cage $[\mathrm{Pd}_2\mathbf{L}^{w}\mathbf{L}^{x}\mathbf{L}^{y}\mathbf{L}^{z}]^{4+}$ comprising multi-functionality arising from four ligands with different functional groups.

II. OBJECTIVES

The first reported supramolecular coordination architectures were concentrating on structural facets of supramolecular chemistry creating a pool of novel architectures, such as rings, knots, links, rotaxanes, catenanes, cages.[21] Recent studies show that the focus of this research field tends to move away from pure structural aspects towards implementation of functionalities, which can be carried out either via host-guest chemistry or via incorporation of functional properties into the structure itself.

In this context, this thesis will focus on the preparation of novel coordination cages capable of interpenetrating to give double-cages, investigation of the host-guest chemistry and the introduction of redoxactive properties into these supramolecular systems. The preparation of diamagnetic double-cages based on palladium(II) metal nodes and bispyridyl ligands was demonstrated by the groups of M. Kuroda[26] and G. Clever[16]. Considering the double-cage design, the first goal was to test whether this architecture is suitable to tolerate other backbones than the previously reported dibenzosuberone[16] and benzophenone[26]. Thus, a redoxactive ligand based on a phenothiazine backbone was constructed. Phenothiazine is a well-characterized molecule with a low and reversible oxidation potential. In presence of water or oxygen, it is known to undergo oxygenation reactions at the sulfur atom. These modifications of phenothiazine molecule gave rise to inspiration for preparing of a series of phenothiazine-based double-cages with different degrees of oxygenation. The double-cages were expected to differ in their dimensions and to have internal cavities of different sizes. Additionally, it was envisioned to investigate the post-assembly derivatization of the phenothiazine-based double-cage in terms of oxygenation reactions without degradation of the double-cage structure (**Chapter III**). A further goal was to examine the host-guest properties in dependence of the size of the internal voids (**Chapter IV**).

---

[26] M. Fukuda, R. Sekiya, R. Kuroda, *Angew. Chem. Int. Ed.* **2008**, *47*, 706.

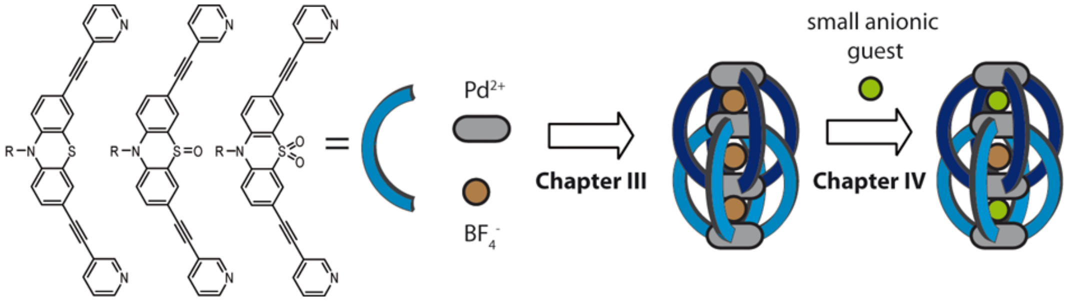

Chapter V will deal with the possibility to incorporate structurally different ligands within one double-cage architecture. The self-assembly of a binary mixture of ligands can give different imaginable outcomes, for example it can lead to: a) a self-sorting into distinct double-cage structures, b) a self-sorting within one structure, for example in a way that one monomeric cage of the double-cage consist of one ligand and the second contains only the other ligand or c) a statistical library of mixed-ligand double-cages.

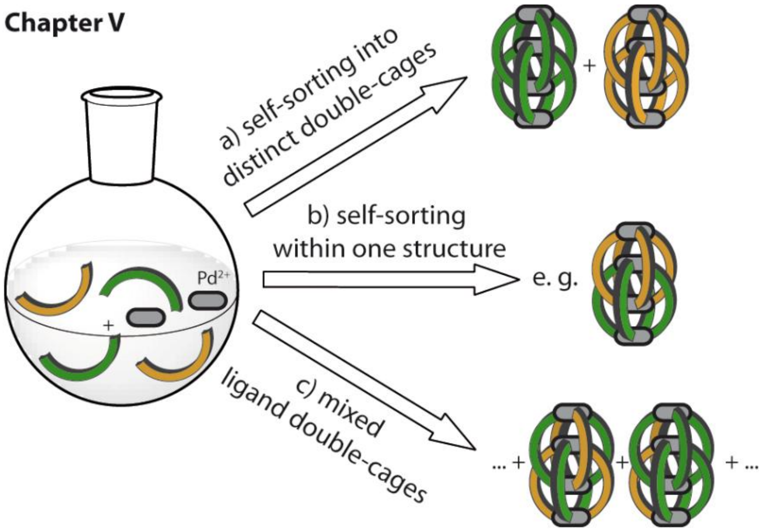

The concept of mixed-ligand double-cages was transferred from application of structurally different ligands to application of ligands comprising different functionalities. For this, a combination of two ligands with different redox abilities based on electron-poor phenothiazine and electron-rich anthraquinone was selected. The goal of the self-assembly in this case was to bring these redoxactive units closer together within one structure. The dense packing was expected to result in electronic communication between the donor and acceptor units in contrast to mixtures of homomeric double-cages, where the redoxactive units are too far away in order to communicate between each other (**Chapter VI**).

Chapter VI

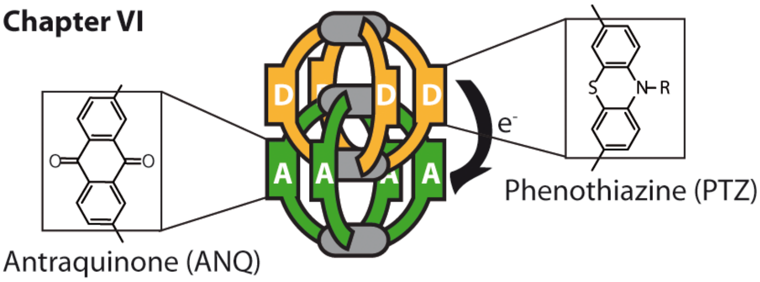

The stability of the double-cages deposited on surfaces was envisioned to be studied regarding possible applications of functional double-cages in thin film photoelectronic devices. As proof of concept, the integrity of the coordination double-cages upon deposition on a gold surface will be studied by Surface Enhanced Raman Scattering (**Chapter VII**).

Chapter VII

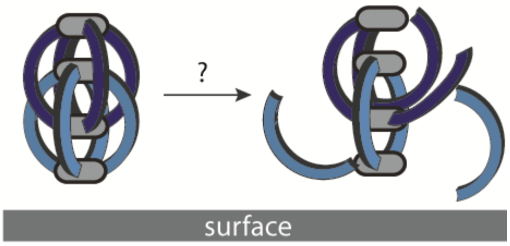

Chapter III

Stepwise Oxidation of Interpenetrated Double-Cages

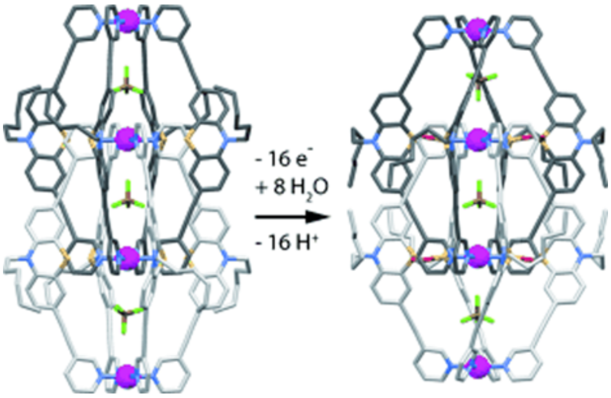

Reproduced with permission from reference [65]. Copyright © 2013 WILEY-VCH Verlag GmbH & Co.

This chapter corresponds to the following publications:

- ‘Assembly and stepwise oxidation of interpenetrated coordination cages based on phenothiazine’, M. Frank, J. Hey, I. Balcioglu, Y.-S. Chen, D. Stalke, T. Suenobu, S. Fukuzumi, H. Frauendorf, G. H. Clever, *Angew. Chem. Int. Ed.* **2013**, *52*, 10102–10106; *Angew. Chem.* **2013**, *125*, 10288–10293.
- ‘Narcissistic self-sorting vs. statistic ligand shuffling within a series of phenothiazine-based coordination cages’, M. Frank, L. Krause, R. Herbst-Irmer, D. Stalke, G. H. Clever, *Dalton Trans*. **2014**, *43*, 4587–4592.
- ‘*Interpenetrated Cage Structures’*, M. Frank, M. D. Johnstone, G. H. Clever, *Chem. Eur. J.* **2016**, *accepted*, DOI: 10.1002/chem.201601752.

III. STEPWISE OXIDATION OF INTERPENETRATED DOUBLE-CAGES

III.1 Introduction

Mechanically interlocked molecules such as catenanes,[21b,27] rotaxanes,[21b,27b,d] molecular shuttles,[21b,28] trefoil[10,29] and pentafoil knots,[30] borromean rings,[31] molecular elevators,[32] solomon rings,[33] olympiadane,[34] interlocked cages (will be described in more detail below) and many more have gained in interest in the last decades due to their complex nature and they moved from being a curiosity towards a highly regarded field in supramolecular chemistry.[21c,d,35] Examples for interpenetrated cage motifs can be found throughout the different fields of chemistry such as interpenetrated organic double-cages, interpenetrated metal organic frameworks (MOFs) or interpenetrated coordination double-cages. While monomeric cages exist in various shapes and sizes,[36] only a small part of them tends to dimerize as will be discussed in the following section.

In general terms, interpenetrated cages belong to the family of catenanes.[37] The monomeric subunits are connected via mechanical rather than covalent bonds. In this manner joined molecules cannot dissociate without breaking chemical bonds. The weakest bonds are usually located between the ligands' donor sites and the metal nodes and are thus predestinated to be cleaved. The kinetic lability of the metal-ligand bond holds the key

---

[27] (a) C. G. Claessens, J. F. Stoddart, *J. Phys. Org. Chem.* **1997**, *10*, 254. (b) R. Jäger, F. Vögtle, *Angew. Chem. Int. Ed.* **1997**, *36*, 930. (c) M. Fujita, *Acc. Chem. Res.* **1999**, *32*, 53. (d) T. J. Hubin, D. H. Busch, *Coord. Chem. Rev.* **2000**, *200-202*, 5. (e) D. A. Leigh, J. K. Y. Wong, F. Dehez, F. Zerbetto, *Nature* **2003**, *424*, 174.

[28] E. R. Kay, D. A. Leigh, *Nature* **2006**, *440*, 286.

[29] (a) J. Guo, P. C. Mayers, G. A. Breault, C. A. Hunter, *Nature chemistry* **2010**, *2*, 218. (b) N. Ponnuswamy, F. B. L. Cougnon, J. M. Clough, G. D. Pantos, J. K. M. Sanders, *Science* **2012**, *338*, 783.

[30] J.-F. Ayme, J. E. Beves, D. A. Leigh, R. T. McBurney, K. Rissanen, D. Schultz, *Nature chemistry* **2012**, *4*, 15.

[31] (a) K. S. Chichak, S. J. Cantrill, A. R. Pease, S.-H. Chiu, G. W. V. Cave, J. L. Atwood, J. F. Stoddart, *Science* **2004**, *304*, 1308. (b) C. D. Meyer, C. S. Joiner, J. F. Stoddart, *Chem. Soc. Rev.* **2007**, *36*, 1705.

[32] J. D. Badjic, V. Balzani, A. Credi, S. Silvi, J. F. Stoddart, *Science* **2004**, *303*, 1845.

[33] (a) C. D. Pentecost, K. S. Chichak, A. J. Peters, G. W. V. Cave, S. J. Cantrill, J. F. Stoddart, *Angew. Chem. Int. Ed.* **2007**, *119*, 222. (b) J. E. Beves, C. J. Campbell, D. A. Leigh, R. G. Pritchard, *Angew. Chem. Int. Ed.* **2013**, *125*, 6592.

[34] D. B. Amabilino, P. R. Ashton, A. S. Reder, N. Spencer, J. F. Stoddart, *Angew. Chem. Int. Ed.* **1994**, *33*, 1286.

[35] (a) F. Aricó, J. D. Badjic, S. J. Cantrill, A. H. Flood, *Top. Curr. Chem.* **2005**, *249*, 203. (b) G. Barin, R. S. Forgan, J. F. Stoddart, *Proc. R. Soc.* **2012**, *468*, 2849.

[36] (a) G. Zhang, M. Mastalerz, *Chem. Soc. Rev.* **2014**, *43*, 1934. (b) L. Chen, Q. Chen, M. Wu, F. Jiang, M. Hong, *Acc. Chem. Res.* **2015**, *48*, 201.

[37] G. Gil-Ramírez, D. A. Leigh, A. J. Stephens, *Angew. Chem. Int. Ed.* **2015**, *54*, 6110.

position in the formation of interpenetrated coordination structures. Nevertheless, the justification of the driving force for the dimerization process is not always as evident. Enthalpic minimization of unfavorable interactions with solvent or maximization of attractive forces between subunits in terms of π-π-stacking or between cationic metals and templating anions[38] can have a significant influence upon the dimerization process. Furthermore, the entropic gain upon release of rather ordered solvent molecules from the inner cavity of the monomeric subunits during the interpenetration can also play a crucial role. Although the factors leading to catenation are not yet fully understood, empirical studies have helped to create a basis for a more predictable design of interpenetrated structures.

III.1.1 Organic interpenetrated cages

Organic interpenetrated double-cages are scarcely reported in literature mainly due to the difficulties in predictability of their formation and due to challenging characterization because of their neutral charges and great dimensions. One prominent example was shown by the group of Mastalerz.[39] They described the synthesis of a cage via a one-pot-48-fold condensation reaction between a benzene(tris-boronic acid) and a triptycene tetraol building blocks with attached alkyl groups and its dimerization upon crystallization process (see Figure III.1). The dimer formation was only found in solid state, whereas in solution the interpenetrated structure disassembled into monomeric cages due to entropic gain in energy. The driving force for this dimer formation can be explained by attractive dispersion interactions expressed via contacts between the alkyl chains of one cage and the aromatic planes of triptycene units of the other monomeric cage. Furthermore, in order to support the aforementioned thesis the authors could show that attachment of shorter alkyl groups to the backbone can hinder the interpenetration presumably due to the lack of attractive forces.

---

[38] (a) M. S. Vickers, P. D. Beer, *Chem. Soc. Rev.* **2007**, *36*, 211. (b) K. M. Mullen, P. D. Beer, *Chem. Soc. Rev.* **2009**, *38*, 1701. (c) G. T. Spence, P. D. Beer, *Acc. Chem. Res.* **2013**, *46*, 571.

[39] G. Zhang, O. Presly, F. White, I. M. Oppel, M. Mastalerz, *Angew. Chem. Int. Ed.* **2014**, *53*, 5126.

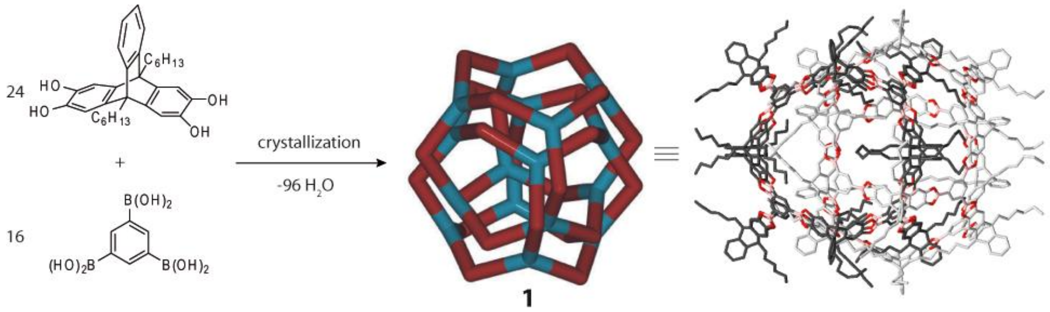

Figure III.1 Reaction scheme of the benzene(tris-boronic acid) and triptycene tetraol building blocks leading upon crystallization to the interlocked boronic ester double-cage **1**, represented as a scheme and X-ray structure (CCDC 980837). Reproduced with permission from reference [39]. Copyright © 2014 WILEY-VCH Verlag GmbH & Co.

A triply interlocked covalent organic cage was synthesized by the group of Cooper via a one-pot cycloamination of a trialdehyde with various diamines in acetonitrile (see Figure III.2).[40] The dimeric cages were obtained when trifluoracetic acid (TFA) was present in solution, whereas in the absence of TFA catalyst the tetrahedral monomeric cages were exclusively formed. TFA most probably acts as a templating molecule for the dimer formation. When the monomeric cages are dissolved in a CH_2Cl_2/*p*-Xylene solution, they tend to dimerize slowly (50 days) due to reversible imine bonds in the tetrahedral monomeric cages. The attractive stabilizing forces for the dimer formation can be mainly attributed to the π-π-stacking of the two aryl rings inside the dimer and aryl-H···imino interactions between the two inner arene rings and the six penetrating bis(imino) strands.

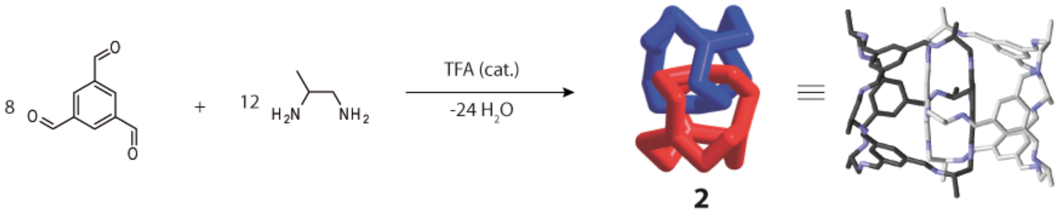

Figure III.2 Reaction scheme of the trialdehyde and diamine building blocks with a catalytic amount of TFA leading to the interpenetrated double-cage **2**, represented as a scheme and X-ray structure (CCDC 765991). Reproduced with permission from reference [40]. Copyright © 2010 Nature Publishing Group.

While the previous examples are based on rather labile covalent bonds, the group of Zhang could demonstrate the synthesis of a permanently interlocked cage (see Figure

---

[40] T. Hasell, X. Wu, J. T. A. Jones, J. Bacsa, A. Steiner, T. Mitra, A. Trewin, D. J. Adams, A. I. Cooper, *Nature chemistry* **2010**, *2*, 750.

III.3).[41] The interpenetrated cages are built upon alkyne metathesis of substituted 1,3,5-tris(phenyl)benzene units with carbazole-containing building blocks in solution. The double-cage is remarkably stable due to ethynylene linkages and is formed as the thermodynamically favored product. In this case *π*-*π*-stacking interactions between aromatic moieties are considered to be the driving force for dimerization process, which help to overcome the entropic penalty arising in the course of dimerization process.

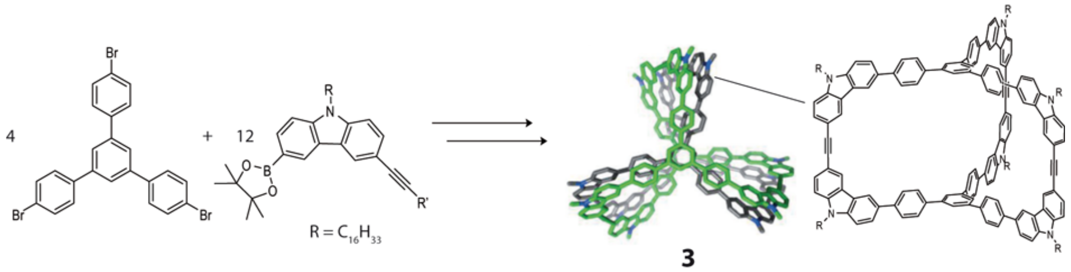

3

Figure III.3 Reaction scheme of selected building blocks: 1,3,5-tris(4-bromophenyl)benzene and a carbazol based building block, leading to the interpenetrated double-cage **3**, represented as a scheme. R' denotes a cleavable residue. Reproduced with permission from reference [41]. Copyright © 2015 WILEY-VCH Verlag GmbH & Co.

Another strategy for the synthesis of permanently interlocked organic cage-like structures was utilized by Beer and co-workers (see Figure III.4).[42] They used a sulfate anion as a templating molecule for the synthesis of a mechanically triply interlocked capsule. Addition of the sulfate anion induces the preorganization of the triurea based ligands in a way that the ligand arms of the two monomeric capsules already interpenetrate each other before the final capping reaction takes place. Attempts to exchange the sulfate anion were unsuccessful showing the strong binding of sulfate inside the inner cavity. Interestingly, reaction of the building blocks in presence of chloride anions instead of sulfate or in absence of any templating molecule resulted in the formation of a monomeric cage.

---

[41] Q. Wang, C. Yu, H. Long, Y. Du, Y. Jin, W. Zhang, *Angew. Chem. Int. Ed.* **2015**, *54*, 7550.

[42] Y. Li, K. M. Mullen, T. D. W. Claridge, P. J. Costa, V. Felix, P. D. Beer, *Chem. Commun.* **2009**, 7134.

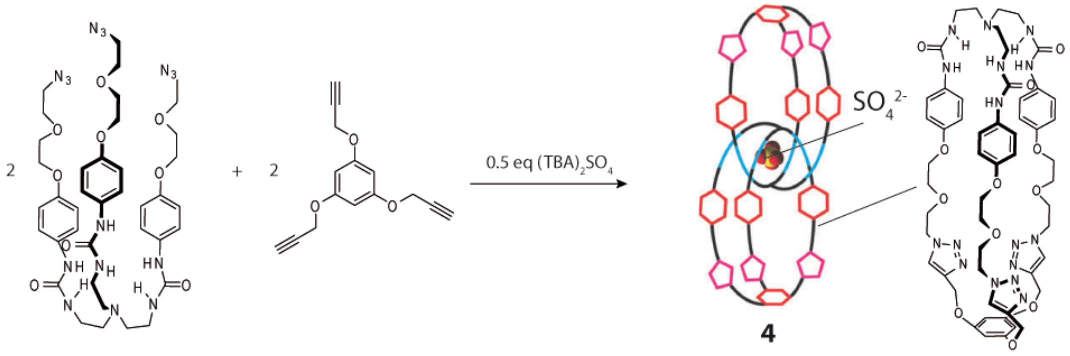

Figure III.4 Reaction scheme of the triazide building block and 1,3,5-tris(prop-2-ynyloxy)benzene with sulfate anion as a templating molecule leading to the interpenetrated double-cage **4**, represented as a scheme. Reproduced with permission from reference [42]. Copyright © 2009 Royal Society of Chemistry.

A very sophisticated synthetic strategy for an organic mechanical interlocked dimer was reported by the group of Böhmer *et al.* (see Figure III.5).[43] They used tetraurea building blocks which can be preorganized via attractive hydrogen bonds prior to the interpenetration process. Finally, the interlocked structure can be obtained after closing the loops via a metathesis reaction. Applying this synthetic strategy, the authors could access homodimeric as well as heterodimeric structures formed from either one or two different tetraurea building blocks. Furthermore, they have studied the rupture and reversible rejoining of the hydrogen bond bridges that hold together the entangled nanocapsules in close proximity to each other by application of AFM-based stretching experiments.[44] A concerted rupture of the 16 hydrogen bridges was postulated based on experimental results and supported by theoretical calculations.

---

[43] L. Wang, M. O. Vysotsky, A. Bogdan, M. Bolte, V. Böhmer, *Science* **2004**, *304*, 1312.

[44] M. Janke, Y. Rudzevich, O. Molokanova, T. Metzroth, I. Mey, G. Diezemann, P. E. Marszalek, J. Gauss, V. Böhmer, A. Janshoff, *Nat. Nanotech.* **2009**, *4*, 225.

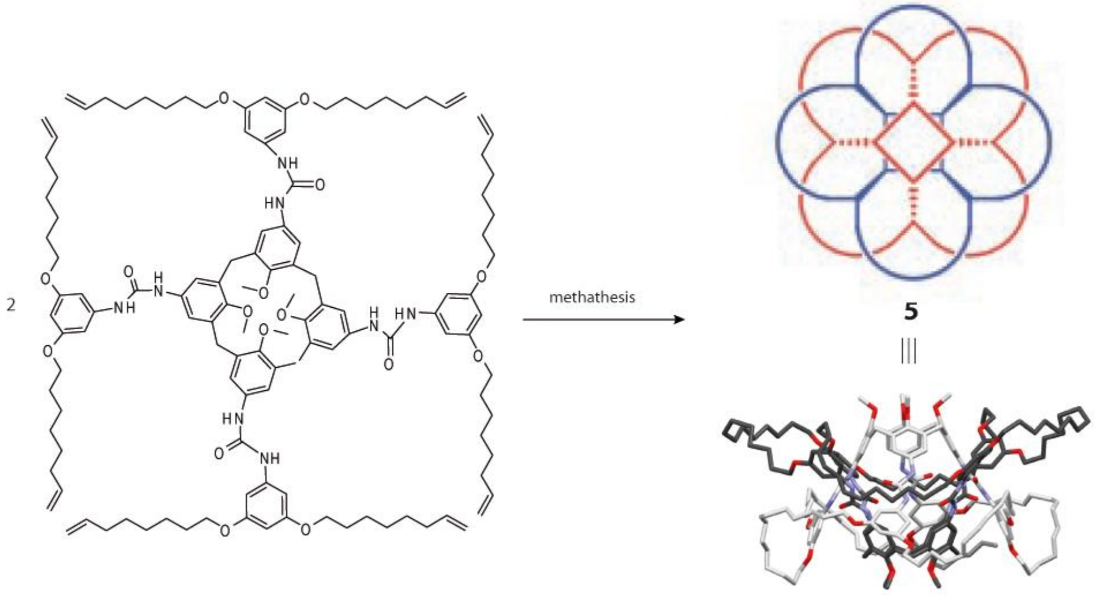

Figure III.5 Reaction scheme of the calixarene building block leading to the interpenetrated double-cage **5**, represented as a scheme and X-ray structure (CCDC 230612). Reproduced with permission from reference [43]. Copyright © 2004 American Association for the Advancement of Science.

III.1.2 Interpenetrated coordination cages

The relatively labile coordination bond between a ligand and a metal node is a suitable tool for a directional design of interpenetrated structures starting from monomeric units. Furthermore, in most cases the coordination chemistry gives rise to almost quantitative yields of the targeted products. The lability of the coordination bond allows the system to correct the assembly mistakes. A lot of different discrete coordination cages[36,45,46,47,48,49] were reported over the last past decades ranging from the Platonic shaped cages (tetrahedron, octahedron, dodecahedron, icosahedron), which are constructed from one single polygon, to more complex Archimedean cages, which consist of two or more polygons and other coordination cages.[5] Although coordination cages are a widely used motif in supramolecular chemistry, interpenetration of such cages is still a rare phenomenon in self-assembly. That leads to the question about the factors that contribute

---

[45] R. Custelcean, *Chem. Soc. Rev.* **2014**, *43*, 1813.

[46] S. Durot, J. Taesch, V. Heitz, *Chem. Rev.* **2014**, *114*, 8542.

[47] A. Schmidt, A. Casini, F. E. Kühn, *Coord. Chem. Rev.* **2014**, *275*, 19.

[48] T. Schröder, S. N. Sahu, J. Mattay, *Top. Curr. Chem.* **2012**, *319*, 99.

[49] A. C. Schulze, I. M. Oppel, *Top. Curr. Chem.* **2012**, *319*, 79.

to dimerization of some cages and why other cages do not form dimers? Selected examples of monomeric cages will be discussed below regarding their suitability for dimerization. One of the simplest designs of a three-dimensional cage structure is the $M_2\mathbf{L}_4$ assembly, in which two square-planar coordinating metal ions are surrounded by four bis-monodentate ligands creating a cavity inside the assembled structure. Figure III.6 shows four examples of banana-shaped bispyridyl ligands coordinated to square-planar Pd(II) cations. One of the first reported $[Pd_2\mathbf{L}_4]$ cages was introduced by Steel and co-workers in 1998.[50] They used 1,4-bis(3-pyridyloxy)-benzene ligand **6** together with $[PdI_2(py)_2]$ in acetonitrile accompanied by silver triflate to produce the monomeric cage $[Pd_2\mathbf{6}_4]$. They did not observe any dimeric products for this cage. The reason for this may be attributed to the relatively short Pd···Pd distance of 8.8 Å within the coordination cage. In an imaginable interpenetrated double-cage structure the four Pd cations would be in a very close distance, so that repelling interactions would force the structure to decompose. The optimal distance for the Pd···Pd arrangement is found, when an anionic molecule of suitable size can fit between the positively charged Pd(II) nodes or when other attractive forces such as π-π-stacking can stabilize the dimeric structure. On the other hand, utilization of much larger ligands such as **7**[14,51] and **8**[12] was also found to result in the formation of monomeric cages $[Pd_2\mathbf{7}_4]$ and $[Pd_2\mathbf{8}_4]$. Although the Pd···Pd distance in these cages is appropriate to form double-cages, these two examples show no dimerization. Here, the bulkiness of the ligands and the lack of groups which can stabilize the dimeric structure via π-π-interactions may be the reasons for the absence of dimerization tendencies. Another banana-shaped ligand of appropriate size for cage dimerization is the light-switchable dithienylethene ligand **9**.[13] This ligand can exist in an open and closed form via a reversible ring cyclization reaction depending on the wavelength of the irradiated light. Due to the flexibility in the open photoisomeric form of the ligand backbone, the monomeric cage can take a bent conformation which would not favor the formation of a dimeric structure.

---

[50] D. A. McMorran, P. J. Steel, *Angew. Chem. Int. Ed.* **1998**, *37*, 3295.

[51] G. H. Clever, S. Tashiro, M. Shionoya, *Angew. Chem. Int. Ed.* **2009**, *48*, 7010.

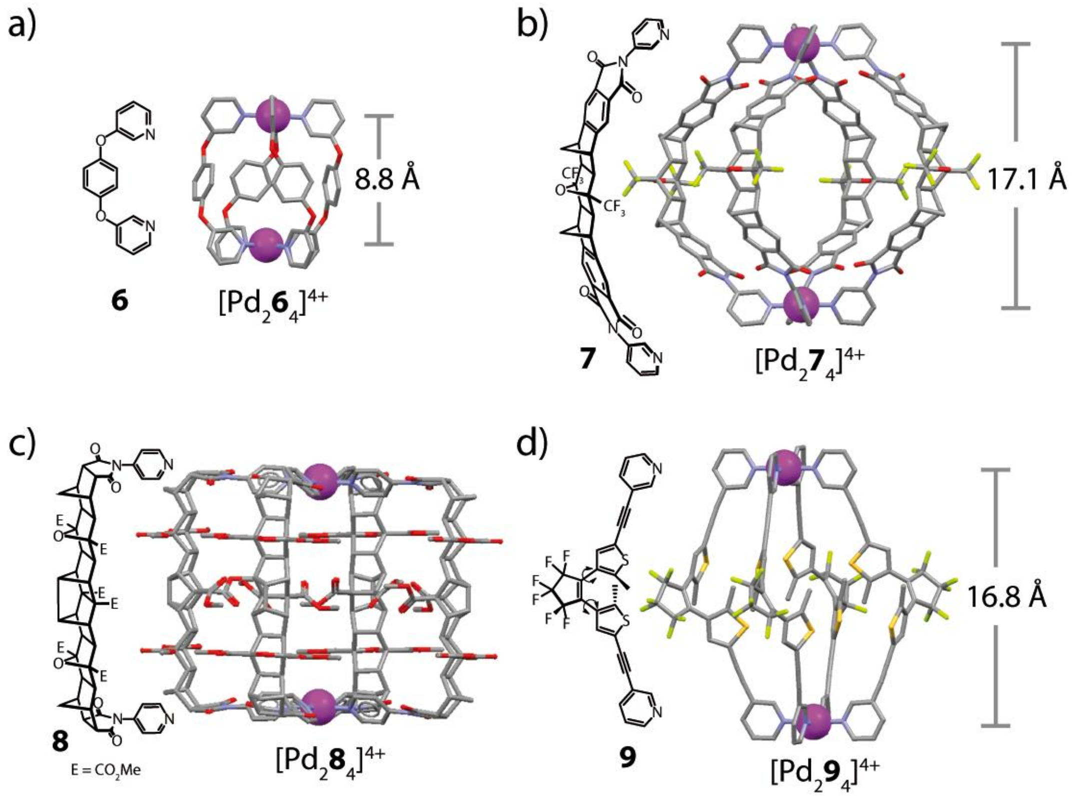

Figure III.6 X-ray structures of monomeric cages (a) $[Pd_2\mathbf{6}_4]^{4+}$ (CCDC 101615),[50] (b) $[Pd_2\mathbf{7}_4]^{4+}$ (CCDC 729445),[14,51] (d) $[Pd_2\mathbf{9}_4]^{4+}$ (CCDC 900746)[13] and a molecular model (PM6, in vacuum)[12] for (c) $[Pd_2\mathbf{8}_4]^{4+}$. Hydrogens, solvent molecules and counter anions are omitted for clarity. C: grey, O:red; N: blue; S: yellow; F:green; Pd: purple. Metal ions are shown in spacefill representation; all other atoms are shown as stick models.

III.1.2.1 Triply interlocked double-cages

The first example of a catenated coordination cage has been published by the group of Makoto Fujita in 1999.[52] The monomeric units are constructed from two different trispyridine ligands **10** and **11** and six square-planar metal cations, either Pd(II) or Pt(II) with *cis*-coordinated ethylenediamine units. Heating the mixture of all building blocks to 100 °C in D_2O afforded first a mixture of kinetic intermediates. After three days the mixture was converted to a single thermodynamically favorable assembly, namely the interpenetrated structure $[M_6(en)_6\mathbf{10}_2\mathbf{11}_2](NO_3)_{12}$ (see Figure III.7). When Pt(II) cations are used, the conversion to the interpenetrated double-cage proceeds much slower, presumably due to the stronger Pt-pyridine bond which is weakened at higher temperatures. The

---

[52] M. Fujita, N. Fujita, K. Ogura, K. Yamaguchi, *Nature* **1999**, *400*, 52.

interpenetrated dimers were characterized via NMR spectroscopic techniques, ESI mass spectrometry and crystallographic analysis. The dimeric structure evolves as the thermodynamically stable product due to energetic favorable π-π-stacking between the aromatic rings of the monomeric subunits. Additionally, the release of solvent molecules and anions from the interior of the monomers leads to entropic favorability of the interlocked structure. The thermodynamic stability of the double-cage was confirmed by mixing experiments. Mixing of the larger monomeric cages built from each distinct ligand, $[Pd_6(en)_6\mathbf{11}_4]^{12+}$ and $[Pd_3(en)_3\mathbf{10}_2]^{6+}$, results in quantitative reorganization of the homomeric cages to give finally the interpenetrated dimeric structure. The reorganization was completed after 24 h at room temperature or even after 10 min after heating to 80 °C.

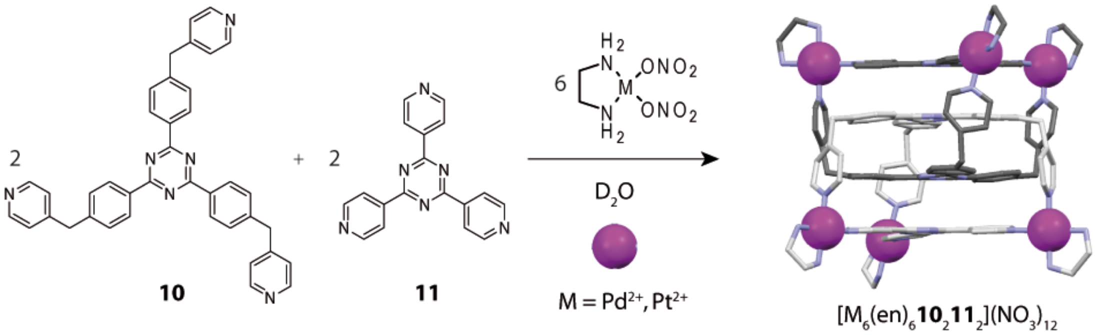

Figure III.7 Reaction scheme of the triazine building blocks **10** and **11** with *cis*-protected PdII) or Pt(II) complexes leading to the interpenetrated double-cage $[M_6(en)_6\mathbf{10}_2\mathbf{11}_2](NO_3)_{12}$, represented as X-ray structure (CCDC 1148701). Reproduced with permission from reference [52]. Copyright © 1999 Nature Publishing Group.

In the next step the authors further developed the design of the double-cage. Mixing the building block **11** with pillars of different sizes (e. g. **12**), triphenylene **13** and $(en)Pd(NO_3)_2$ in D_2O yielded after heating the mixture at 100 °C for 3 h the double-cage structure $[\mathbf{13}_3@Pd_{12}(en)_{12}\mathbf{11}_4\mathbf{12}_6]^{24+}$ (see Figure III.8).[53] Three aromatic guests **13** were found to be stacked between the triazine building blocks. The guest molecules are assumed to serve as templates for the formation of the dimeric structure and to stabilize the dimers via favorable π-π-stacking interactions between the electron deficient triazine ligands and the electron-rich triphenylene molecules. Application of longer pillars for the synthesis results in double or even triple aromatic stacks of triphenylene molecules inside the central pocket of the double-cage.

---

[53] Y. Yamauchi, M. Yoshizawa, M. Fujita, *J. Am. Chem. Soc.* **2008**, *130*, 5832.

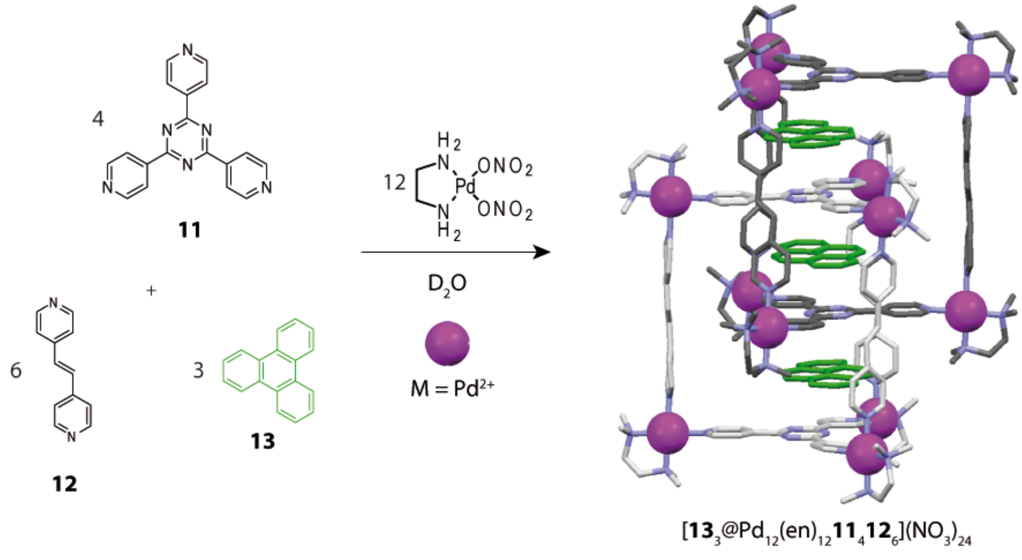

Figure III.8 Reaction scheme of the triazine building blocks **11** with *trans*-1,2-bis84-pyridyl)ethene **12** under templating of triphenylene **13** with *cis*-protected PdI(II) complex leading to the interpenetrated double-cage [$\mathbf{13}_3$@$Pd_{12}(en)_{12}\mathbf{11}_4\mathbf{12}_6](NO_3)_{24}$, represented as X-ray structure (CCDC 646901). Reproduced with permission from reference [53]. Copyright © 2008 American Chemical Society.

Hardie *et al.* have shown an example for interpenetrated double-cages based on only one type of ligand (see Figure III.9).[54] Two bowl-shaped tris-bidentate ligands based on cyclotriveratrylene and three octahedral coordinated metal nodes (M = Zn(II) or Co(II)) build one trigonal bipyramidal monomeric cage in DMSO solution. Two of the six octahedral coordination sites of each metal cation are occupied by one chelating nitrate anion. The monomers dimerize subsequently to the interpenetrated double-cage $[M_6\mathbf{14}_4(NO_3)_6]^{6+}$. Besides the nitrate ligands coordinated to the metal nodes, further nitrates are located in the inner cavity of the double-cage. In contrast to the previous examples, the driving force for dimerization cannot be explained by face-to-face π-π-stacking since the distance between the aromatic rings of 4.77 Å is too long for a significant interaction. The attractive interactions within the double-cage are supposed to be two types of weak hydrogen bonds. One set of hydrogen bonds within a distance of 2.37 Å is located between the CH protons of the bipyridine moiety of one cage and the OMe groups of the inner ligand backbone of the second cage. The second set of hydrogen bonds is found within a distance of 2.46 Å between the OMe group of the bipyridine residues and the non-coordinating oxygens of the

---

[54] A. Westcott, J. Fisher, L. P. Harding, P. Rizkallah, M. J. Hardie, *J. Am. Chem. Soc.* **2008**, *130*, 2950.

chelating nitrates. In a further study, the authors could modify the double-cage structure by combining four bowl-shaped tris(3-pyridylmethyl)cyclotriguaiacylene based ligands with six linear coordinating Ag^+ metal nodes resulting in the targeted entangled cages.[55]

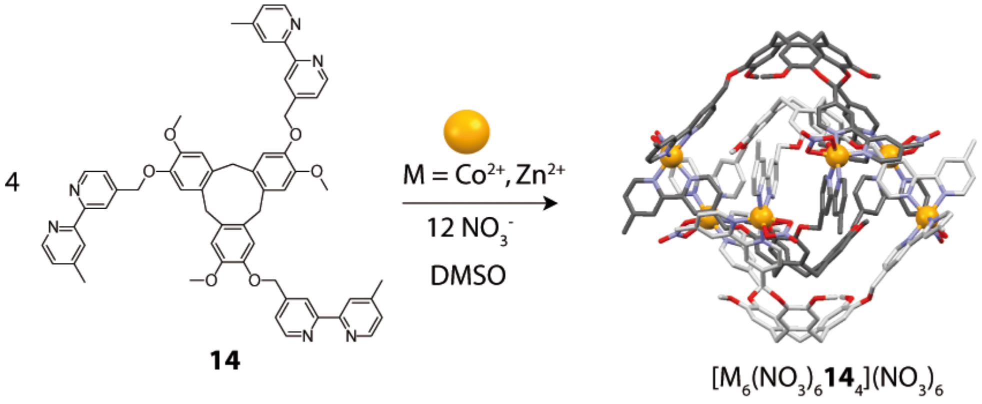

Figure III.9 Reaction scheme of the building block **14** with Co(II) or Zn(II) salt leading to the interpenetrated double-cage $[M_6(NO_3)_6\mathbf{14}_4](NO_3)_6$, represented as X-ray structure (CCDC 691575). Reproduced with permission from reference [54]. Copyright © 2008 American Chemical Society.

Mukherjee and co-workers have shown the synthesis of a double-cage based on 1,3,5-tris((E)-2-(pyridin-3-yl)vinyl)benzene combined with cis-(tmen)$Pd(NO_3)_2$ in D_2O (see Figure III.10).[56] The π-π-stacking between the aromatic phenyl backbones is the main driving force for the dimerization in this case. The X-ray structure showed that the olefin bonds of two adjacent double-cages are in close proximity within a distance of 3.66 Å. When the crystals are exposed to sunlight or are irradiated with UV light, the double-cages undergo a [2+2] cycloaddition reaction. The fused pairs of double-cages can be cleaved in an aqueous solution by heating the sample to 90 °C in order to recover the individual dimeric assemblies. These double-cages are reversible photoactive systems and show potential for applications in materials for photoswitches and optical data storage devices. In a previous work Mukherjee *et al.* studied some influence factors on the dimerization process of cages based on benzene-1,3,5-tricarboxylic acid and bis-monodentate pillars coordinating to Pd(II) nodes. They could show that the bulkiness of the metal-containing building block as well as the size of the pillars and the addition of templating molecules can affect the

---

[55] J. J. Henkelis, T. K. Ronson, L. P. Harding, M. J. Hardie, *Chem. Commun.* **2011**, *47*, 6560.

[56] D. Samanta, P. S. Mukherjee, *J. Am. Chem. Soc.* **2014**, *136*, 17006.

double-cage formation.[57]

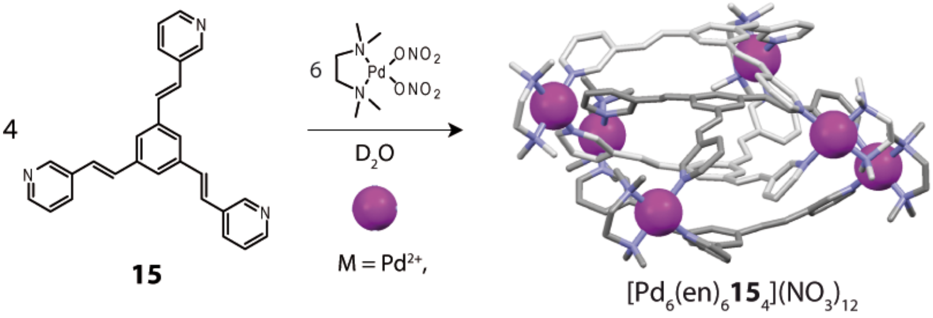

Figure III.10 Reaction scheme of the 1,3,5-tris-((E)-2-pyridin-3-yl)vinyl)benzene building block **15** with Pd(II) salt leading to the interpenetrated double-cage [$Pd_6(en)_6$**15**$_4$]$(NO_3)_{12}$, represented as X-ray structure (CCDC 1427344). Reproduced with permission from reference [56]. Copyright © 2014 American Chemical Society.

Another interesting example of an interpenetrated coordination assembly was reported by Chi and co-workers.[58] They used a tridentate 1,3,5-tris(3-(pyridin-4-yl)-1H-pyrazol-1-yl)benzene ligand **16**, which coordinates to the Ru-containing and π-electron-rich panel **17** to give the dimeric assembly [**16**$_4$**17**$_6$]$^{12+}$ (see Figure III.11). Crystal and NMR spectroscopic analysis showed that significant π-π-interactions between the panels and the trispyridine ligands are responsible for the occurrence of the interlocked structure. Utilization of panels which are lacking suitable aromatic units for the intramolecular attractive forces led to the formation of simple, discrete prisms instead of dimeric assemblies.

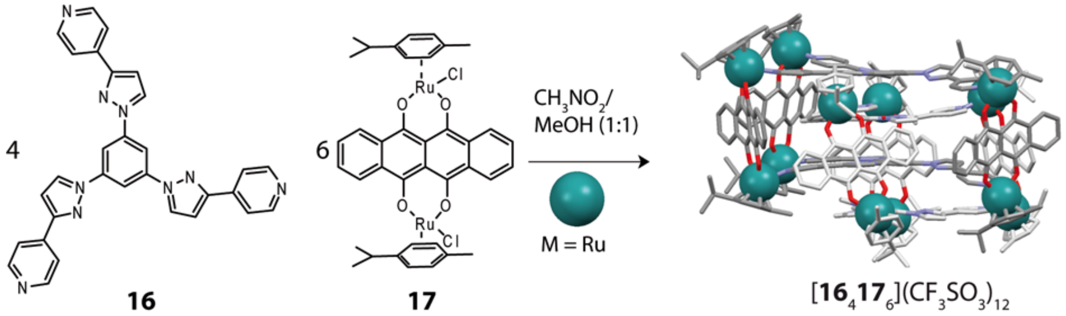

Figure III.11 Reaction scheme of the 1,3,5-tris-(3-(pyridin-4-yl)-1H-pyrazol-1-yl)benzene building block **16** with the Ru-containing building block **17** leading to the partially interpenetrated double-cage [**16**$_4$**17**$_6$]$(CF_3SO_3)_{12}$, represented as X-ray structure (CCDC 991298). Reproduced with permission from reference [58]. Copyright © 2014 Royal Society of Chemistry.

---

[57] A. K. Bar, S. Raghothama, D. Moon, P. S. Mukherjee, *Chem. Eur. J.* **2012**, *18*, 3199.

[58] A. Mishra, A. Dubey, J. W. Min, H. Kim, P. J. Stang, K.-W. Chi, *Chem. Commun.* **2014**, *50*, 7542.

III.1.2.2 Oligomeric and polymeric interlocked cages

Interpenetrated coordination cage structures can also be found in different variations in the field of MOFs (Metal Organic Frameworks) which will not be discussed here.[59] Examples for interpenetrated polymeric cage structures have been reported by the groups of Dehnen[60] and Lu.[61] The first example shows a 2,4,6-tris(4-pyridyl)pyridine ligand **18** coordinated to Zn nodes yielding icosahedral coordination cages with an inner volume of more than 2700 Å, which can be used for uptake of guest molecules (see Figure III.12). The cages are interlocked via two corners allowing for face-to-face π-π interactions of the ligand cores. The entangled cages are arranged in a linear fashion building a chain of interpenetrated assemblies.

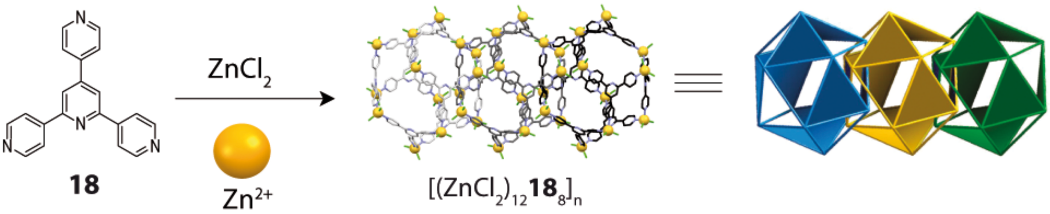

Figure III.12 Reaction scheme of the 2,4,6-tris-(4-pyridyl)-pyridine building block **18** with $ZnCl_2$ leading to the partially interpenetrated double-cage $[(ZnCl_2)_{12}\mathbf{18}_8]_n$, represented as X-ray structure (CCDC 809386). Reproduced with permission from reference [60]. Copyright © 2014 American Chemical Society.

The second example of entangled polycatenated cages was constructed via intercatenation of discrete tetrahedral cages. Each monomeric cage is built from

---

[59] For further reading and examples, see (a) A. J. Blake, N. R. Champness, S. S. M. Chung, W.-S. Li, M. Schröder, *Chem. Commun.* **1997**, 1005. (b) S. R. Batten, R. Robson, *Angew. Chem. Int. Ed.* **1998**, *37*, 1460. (c) J. Fan, H.-F. Zhu, T.-a. Okamura, W.-Y. Sun, W.-X. Tang, N. Ueyama, *Chem. Eur. J.* **2003**, *9*, 4724. (d) H. Kim, M. P. Suh, *Inorg. Chem.* **2005**, *44*, 810. (e) O. M. Yaghi, *Nature Mater.* **2007**, *6*, 92. (f) T. K. Maji, R. Matsuda, S. Kitagawa, *Nature Mater.* **2007**, *6*, 142. (g) L. Ma, W. Lin, *Angew. Chem. Int. Ed.* **2009**, *48*, 3637. (h) S. Bureekaew, H. Sato, R. Matsuda, Y. Kubota, R. Hirose, J. Kim, K. Kato, M. Takata, S. Kitagawa, *Angew. Chem. Int. Ed.* **2010**, *49*, 7660. (i) X. Kuang, X. Wu, R. Yu, J. P. Donahue, J. Huang, C.-Z. Lu, *Nat. Chem.* **2010**, *2*, 461. (j) Y. Takashima, V. M. Martínez, S. Furukawa, M. Kondo, S. Shimomura, H. Uehara, M. Nakahama, K. Sugimoto, S. Kitagawa, *Nat. Commun.* **2011**, *2*, 168. (k) H. Chen, D. Xiao, J. He, Z. Li, G. Zhang, D. Sun, R. Yuan, E. Wang, Q.-L. Luo, *CrystEngComm*, **2011**, *13*, 4988. (l) S. Yang, X. Lin, W. Lewis, M. Suyetin, E. Bichoutskaia, J. E. Parker, C. C. Tang, D. R. Allan, P. J. Rizkallah, P. Hubberstey, N. R. Champness, K. M. Thomas, A. J. Blake, M. Schröder, *Nature Mater.* **2012**, *11*, 710. (m) Q. Yao, J. Su, O. Cheung, Q. Liu, N. Hedin, X. Zou, *J. Mater. Chem.* **2012**, *22*, 10345. (n) S. B. Choi, H. Furukawa, H. J. Nam, D.-Y. Jung, Y. H. Jhon, A. Walton, D. Book, M. O'Keeffe, O. M. Yaghi, J. Kim, *Angew. Chem. Int. Ed.* **2012**, *51*, 8791. (o) H. Lü, Y. Mu, J. Li, D. Wu, H. Hou, Y. Fan, *Inorg. Chim. Acta.* **2012**, *387*, 450. (p) H.-L. Jiang, T. A. Makal, H.-C. Zhou, *Coord. Chem. Rev.* **2013**, *257*, 2232.

[60] J. Heine, J. Schmedt auf der Günne, S. Dehnen, *J. Am. Chem. Soc.* **2011**, *133*, 10018.

[61] L. Jiang, P. Ju, X.-R. Meng, X.-J. Kuang, T.-B. Lu, *Sci. Rep.* **2012**, *2*, 668.

deprotonated ligand **19** which is connected to protected Ni(II) nodes (see Figure III.13).[61] The four ligands are located at four vertexes of the tetrahedral cage, and six Ni(II) cations are sitting at the six edges of the tetrahedral cage. The interpenetration occurs between one tetrahedral cage and an adjacent cage through all of the four vertices, which leads to a 3D extended polycatenated structure $[(\mathrm{NiL})_6\mathbf{19}_4]_n$. Application of chloride as counter anion leads to the formation of one dimensional infinite chains of interpenetrating cages.

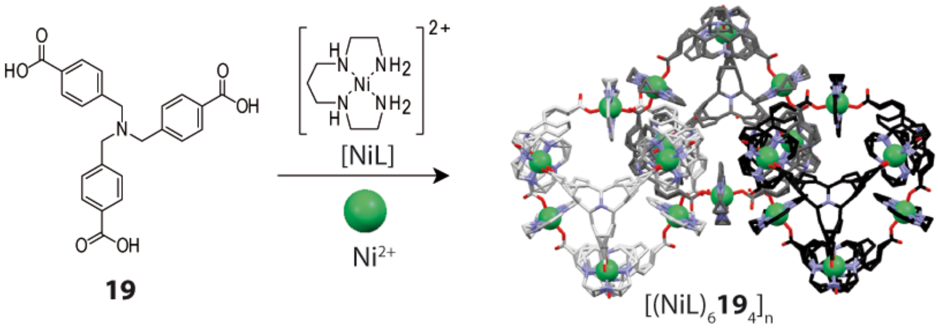

Figure III.13 Reaction scheme of the tri(4-carboxy-benzyl)amine building block **19** with 1,4,8,11-tetraazaundecane protected $\mathrm{Ni(PF_6)_2}$ salt leading to the partially interpenetrated cage oligomers $[(\mathrm{NiL})_6\mathbf{19}_4]_n$, represented as X-ray structure (CCDC 893143). Reproduced with permission from reference [61]. Copyright © 2012 Nature Publishing Group.

III.1.2.3 Double-cages with a Fourfold Symmetry

The first example of a discrete quadruply interpenetrated metal organic double-cage constructed from eight ligands and four metal cations has been reported by the group of Kuroda *et al.* (see Figure III.14 a)).[26] The ligand was designed via coupling of a benzophenone backbone to two 3-pyridylmethoxy arms. Treatment of this ligand with $\mathrm{Pd(NO_3)_2}$ in a 2:1 ration in DMSO solution for one hour at room temperature afforded the quantitative formation of the monomeric cage $[\mathrm{Pd_2}\mathbf{20}_4]^{4+}$. The formation was verified via ESI mass spectrometry and NMR spectroscopic analysis. The pyridyl protons of the ligand (in particular H_a and H_d) exhibit a strong downfield shift upon coordination to the metal cation (see figure III.14 b)). The Pd-Pd distance of 16.14 Å in the monomeric cage could be extracted from the crystal structure. Surprisingly, the monomeric cage was gradually converted into a new species in solution at room temperature. The conversion can be accelerated by increasing the reaction temperature and the product was obtained in quantitative yield after heating to 353 K for 24 h. The ESI analysis identified the new species as the dimeric product of the monomeric cage. The ^{1}H NMR spectrum of the new species showed a doubling of all signals compared to the free ligand indicating that the left and right halves of the ligand within the double-cage experience magnetically different environments. On the basis of NMR spectroscopic analysis a quadruply interpenetrated structure was proposed (see Figure III.14 a)), which was verified by measuring the X-ray structure of the compound. The interpenetrated double-cage shows a C_4 symmetry with the four Pd(II) ions located on one axis. Stabilizing CH-π and π-π-interactions between the neighboring ligands have been found via measuring of interatomic distances. The crystal structure showed that the double-cage possesses three cavities with nearly equal volume of 62 Å^3, which can encapsulate anionic guests. Indeed, the dimer formation is only possible when an appropriate templating anion such as NO_3^- is present (for further description of the anion templating effect see Chapter IV). Analysis of the reaction kinetics showed that the dimerization is a second-order reaction with the collision of two monomeric cages as the rate-determining step. Although the formation of the dimer should be entropically disfavored, the double-cage is the thermodynamically stable product and the monomeric cage is just a kinetic intermediate. The activation energy for the dimerization process was calculated to be +108.9 kJ/mol.

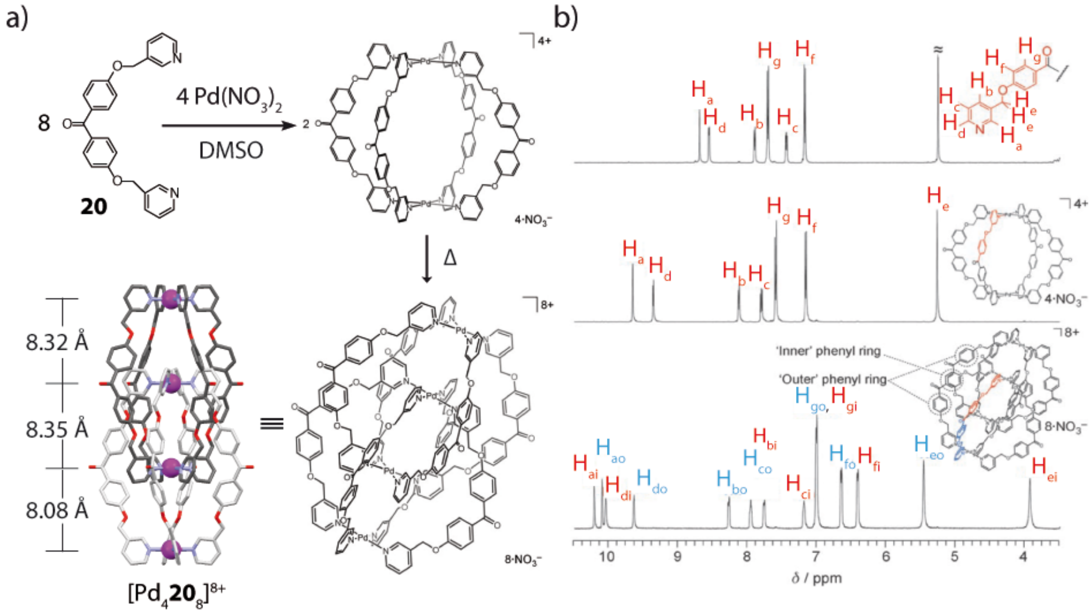

Figure III.14 a) Reaction scheme of the benzophenone building block **20** reacting with $Pd(NO_3)_2$ salt initially to the intermediate monomeric cage $[Pd_2$**20**$_4](NO_3)_4$ and subsequent formation of the quadruply interpenetrated double-cage $[Pd_4$**20**$_8](NO_3)_8$, represented as X-ray structure (CCDC 652007). b) ^1H NMR spectroscopic analysis of ligand **20**, intermediate monomeric cage and double-cage. Reproduced with permission from reference [26]. Copyright © 2008 WILEY-VCH Verlag GmbH & Co.

The second example of a quadruply interpenetrated double-cage was reported by Clever and co-workers in 2012.[16] They also used a rather simple and commercially available backbone for the ligand design, namely a dibenzosuberone building block. In the first attempts a rather short ligand **21** was prepared via introduction of two pyridine arms by a Suzuki cross coupling reaction. Addition of the $[Pd(CH_3CN)_4](BF_4)_2$ salt in a ratio of 2:1 to the acetonitrile solution of the ligand and heating to 70 °C for several hours resulted in the quantitative formation of the small monomeric coordination cage $[Pd_2\mathbf{21}_4](BF_4)_4$ (see Figure III.15 a). Thus, variation of the ligand by introduction of extra ethynyl bridges between the backbone and pyridine arms afforded the new ligand **22**. Applying the same reaction conditions to ligand **22** yielded a larger coordination compound which was identified by NMR spectroscopy and ESI mass spectrometry as the targeted double-cage $[Pd_4\mathbf{22}_8](BF_4)_8$ (see Figure III.15 b)). The formation of the double-cage does not occur directly starting from the ligands and metal nodes. First the monomeric cage is build from the starting material as intermediate structure which subsequently dimerizes to the double-cage. X-ray analysis of single crystals of the dimeric structure revealed a symmetric double-cage with a helical chirality and a Pd_{out}-Pd_{out} distance of 24.44 Å. The distance between Pd_{out} and Pd_{in} was determined to 8.09 Å and between the two internal Pd atoms to 8.25 Å. Hence, the cage features two equal outer cavities and one rather larger central pocket. All of the three pockets were found to contain one disordered BF_4^- ion, further two BF_4^- ions were found to be located near the outer site of the external Pd atoms and residual counter anions were located in solvent channels between the double-cages (the structure with the guest molecules can be described as $[3BF_4@Pd_4\mathbf{22}_8]^{5+}$). Interestingly, ESI mass spectrometric analysis of the double-cage revealed the formation of a $[2Cl{+}BF_4@Pd_4\mathbf{22}_8]^{5+}$ species. Thus, the double-cage was studied for guest exchange properties with halide salts (further details upon anion binding will be discussed in Chapter IV).

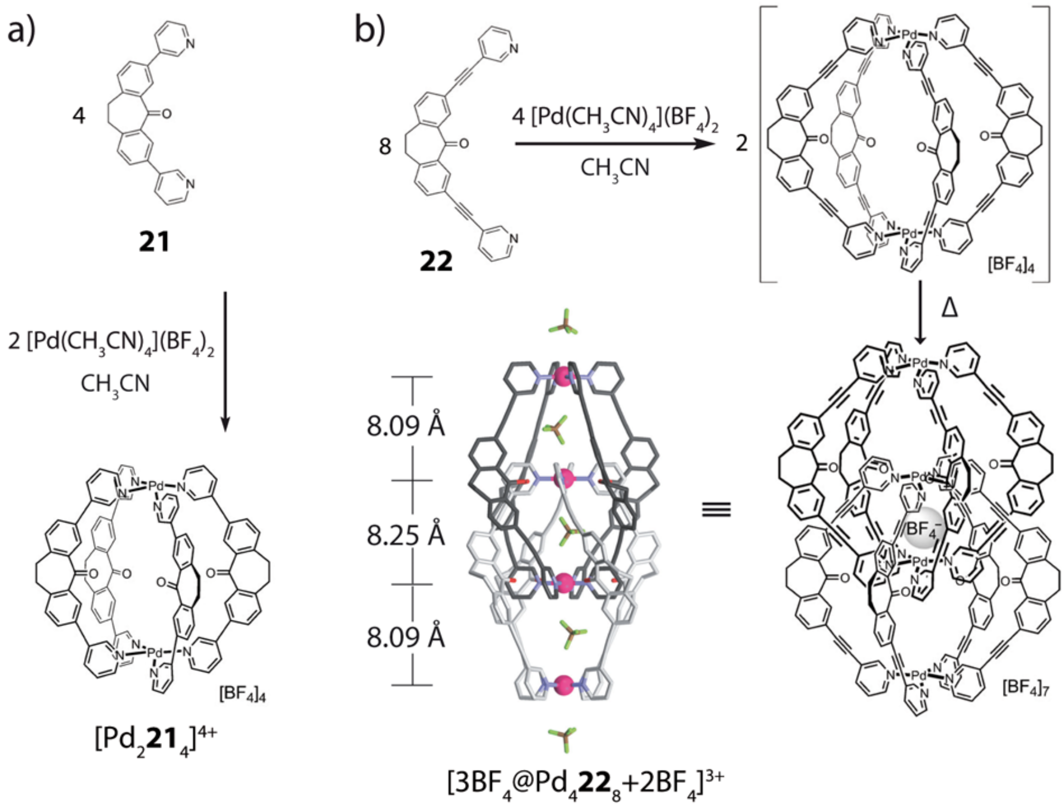

Figure III.15 Reaction of a) the dibenzosuberone based ligand **21** with $[Pd(CH_3CN)_4](BF_4)_2$ salt leading to the monomeric cage $[Pd_2\mathbf{21}_4](BF_4)_4$ and b) the dibenzosuberone based ligand **22** with $[Pd(CH_3CN)_4](BF_4)_2$ salt leading to formation of the intermediate species $[Pd_2\mathbf{22}_4](BF_4)_4$ and subsequent dimerization to the quadruply interpenetrated double-cage $[Pd_4\mathbf{22}_8](BF_4)_8$, represented as X-ray structure (CCDC 844925). Reproduced with permission from reference [16]. Copyright © 2012 WILEY-VCH Verlag GmbH & Co.

In a further study the authors could show that synthetic modification of the ligand structure or the choice of solvent can affect the formation of interpenetrated coordination cages (see Figure III.17).[11] Exchange of the ethynyl bridges of the previously described dibenzosuberone ligand **22** for 1,4-phenylene linkers yields a longer ligand with an *N-N* distance of 17.7 Å compared to ligand **22** with 14.9 Å. Interestingly, reaction of this modified ligand in acetonitrile solution with the $[Pd(CH_3CN)_4](BF_4)_2$ metal source resulted in the formation of the corresponding double-cage structure. But the same reaction in DMSO solution yielded the formation of the monomeric species. The reason for this difference is probably due to the larger size of DMSO molecules compared to acetonitrile, which give less entropic gain upon solvent release in the course of the dimerization process. Desaturation of the dibenzosuberone core gave a further modified ligand. Reaction with the Pd(II) metal source in acetonitrile first led to the formation of a monomeric species, which subsequently was converted to a new species with very low solubility in acetonitrile resulting in a hardly characterizable precipitate. Thus, the same ligand was equipped with two solubilizing methoxy-ethoxy chains and monitoring the same assembly reaction with this ligand revealed that the follow-up product of the monomeric species is indeed the interpenetrated double-cage structure. Reduction of the carbonyl group at the dibenzosuberone backbone afforded a further derivative of the ligand **22**. Interestingly, reaction with Pd(II) source in acetonitrile yielded a monomeric coordination cage as the final product. Theoretical calculation models supported the hypothesis suggesting that the carbonyl oxygens takes part in stabilization of the double-cage via interactions with the inner Pd(pyridine)$_4$ planes and thus their missing does not favor the dimerization process.

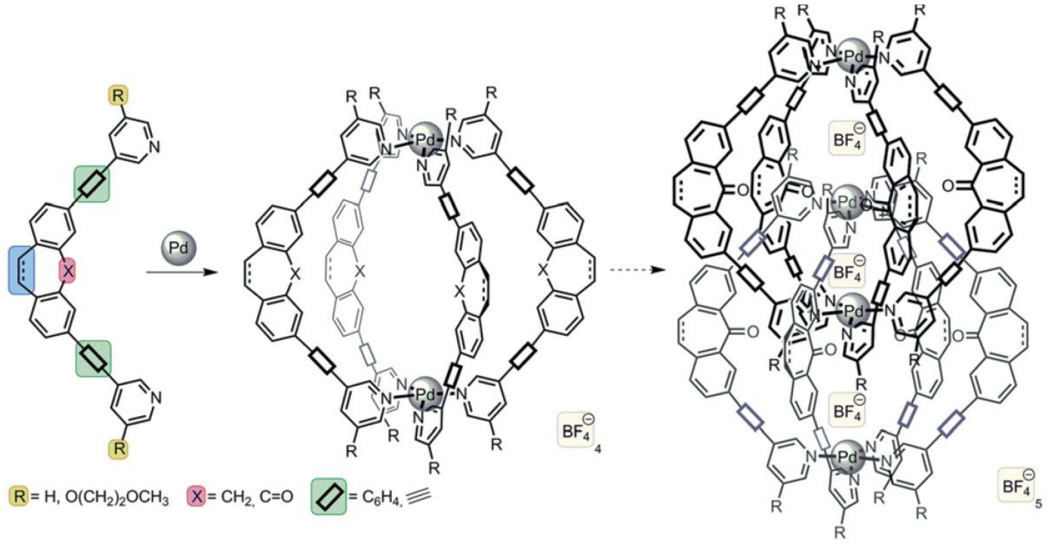

Figure III.16 Ligand derivatives of the dibenzosuberone based cage and schematic representation of the influence of the ligand modification on the outcome of the assembly reaction with a Pd ion source. Reproduced with permission from reference [11].Copyright © 2014 Royal Society of Chemistry.

III.2 Project Target

The focus in this chapter is set on the design and characterization of coordination double-cages built from ligands with redoxactive backbones and Pd(II) metal nodes. The reason for the selection of redoxactive building blocks was the attempt to develop novel materials for applications in molecular electronics and photovoltaics. Hence, a commercially available and well characterized phenothiazine building block was chosen for the backbone skeleton. Phenothiazines are known to undergo reversible one-electron oxidations to radical cations[62] and tend to undergo further oxygenation[63] or disproportionation[64] reactions. After successful design of the double-cage, the latter is intended to be used for examination of redox-abilities of the double-cage in terms of cage-to-cage oxygenation reactions. The influence of the oxygenation degree of the ligands on the inner pockets of the double cage is also intended to be studied.

III.3 Results and Discussion[65,66]

A new ligand $\mathbf{L}^1$ based on a phenothiazine backbone was designed in order to proof the suitability of interpenetrated double-cage design for toleration of other backbones than the previously reported dibenzosuberone[16] or benzophenone[26] building blocks. Phenothiazine and its derivatives are well known compounds since they were extensively studied as pharmaceutical drug substances in particular in the field of psychiatry.[67] Methylene blue, a prominent derivative of phenothiazine, for example was one of the first antimalarial drugs that have been discovered.[68] Most of phenothiazine derivatives have low and reversible first oxidation potentials. Therefore, they have been widely used for photoelectric devices[69] and

---

[62] (a) E. Wagner, S. Filipek, M. K. Kalinowski, *Monatshefte für Chemie* **1988,** *119*, 929. (b) X.-Q. Zhu, Z. Dai, A. Yu, S. Wu, J.-P. Cheng, *J. Phys. Chem. B* **2008**, *112*, 11694.

[63] (a) S. G. Dahl, P. A. Kollman, S. N. Rao, U. C. Singh, *Journal of Computer-Aided Molecular Design* **1992**, *6*, 207. (b) L. Y. Yang, C. Wang, L. Q. Li, S. Janietz, A. Wedel, Y. L. Hua, S. G. Yin, *Journal of Polymer Science: Part A: Polymer Chemistry* **2007**, *45*, 4291. (c) T. Manju, N. Manoj, A. M. Braun, E. Oliveros, *Photochem. Photobiol. Sci.* **2012**, *11*, 1744.

[64] E. E. Bancroft, J. E. Pemberton, H. N. Blount, *J. Phys. Chem.* **1980**, *84*, 2557.

[65] M. Frank, J. Hey, I. Balcioglu, Y.-S. Chen, D. Stalke, T. Suenobu, S. Fukuzumi, H. Frauendorf, G. H. Clever, *Angew. Chem. Int. Ed.* **2013**, *52*, 10102.

[66] M. Frank, L. Krause, R. Herbst-Irmer, D. Stalke, G. H. Clever, *Dalton Trans*. **2014**, *43*, 4587.

[67] M. J. Ohlow, B. Moosmann, *Drug Discov. Today* **2011**, *16*, 119.

[68] P. Guttmann, P. Ehrlich, *Berliner Klinische Wochenschrift* **1891**, *28*, 953.

[69] (a) H. D. Burrows, T. J. Kemp, M. J. Welburn, *J. Chem. Soc. Perkin Trans*. *2* **1973**, 969. (b) J.-P. Collin, S. Guillerez, J.-P. Sauvage, *J. Chem. Soc. Chem. Commun*. **1989**, 776. (c) R. Duesing, G. Tapolsky, T. J. Meyer, *J. Am. Chem. Soc.* **1990**, *112*, 5378. (d) W. E. Jones, Jr., P. Chen, T. J. Meyer, *J. Am. Chem. Soc.* **1992**, *114*, 387. (e) S. Schneider, J. Kurzawa, A. Stockmann, R. Engl, J. Daub, P. Matousek, M. Towrie, *Chem. Phys. Lett.* **2001**, *348*, 277. (f) J. Strauss, J. Daub, *Adv. Mater*. **2002**, *14*, 1652. (g) N. Acar, J. Kurzawa, N. Fritz, A. Stockmann, C. Roman, S. Schneider, T. Clark, *J. Phys. Chem. A* **2003**, *107*, 9530. (h) F. Fungo, S. A. Jenekhe, A. J. Bard, *Chem. Mater.* **2003**, *15*, 1264. (i) D. H. Hwang, S. K. Kim, M. J. Park, J. H. Lee, B. W. Koo, I. N. Kang, S. H. Kim, T. Zyung, *Chem. Mater.* **2004**, *16*, 1298. (j) D. W. Cho, M. Fujitsuka, K. H. Choi, M. J. Park, U. C. Yoon, T. Majima, *J. Phys. Chem. B* **2006**, *110*, 4576. (k) H. Tian, X. Yang, R. Chen, Y. Pan, L. Li, A. Hagfeldt, L. Sun, *Chem. Commun*. **2007**, 3741. (l) Y. Sasaki, Y. Araki, O. Ito, M. M. Alam, *Photochem. Photobiol. Sci*. **2007**, *6*, 560. (m) G. Sang, Y. Zou, Y. Li, *J. Phys. Chem. C* **2008**, *112*, 12058. (n) C. V. Suneesh, K. R. Gopidas, *J. Phys. Chem. C* **2010**, *114*, 18725. (o) C. V. Suneesh, M. V. Vinayak, K. R. Gopidas, *J. Phys. Chem. C* **2010**, *114*, 18735. (p) J. Lee, J. Kwak, K. C. Ko, J. H. Park, J. H. Ko, N. Park, E. Kim, D. H. Ryu, T. K. Ahn, J. Y. Lee, S. U. Son, *Chem. Commun.* **2012**, *48*, 11431. (q) P. Rajakumar, C.

as electron-rich components in charge-transfer donor-acceptor conjunctions.[70]

In the first step of ligand synthesis a hexyl chain was attached to the nitrogen atom of the commercially available 10*H*-phenothiazine building block via *N*-alkylation with *n*-hexylbromide. The aliphatic chain was expected to increase the solubility of the desired cage in organic solvents. Following a literature procedure, the phenothiazine building block was selectively brominated at the position 3 and 7.[71] In the last synthetic step, two pyridine arms were attached via a standard Suzuki cross coupling protocol to give ligand $\mathbf{L}^1$ (see Figure III.17; for synthetic protocols and characterization data see Appendix-Chapter III Section 1). In order to prepare the coordination cage, ligand $\mathbf{L}^1$ was dissolved in acetonitrile and 0.5 equivalents of $[Pd(CH_3CN)_4](BF_4)_2$ were added to the solution. The reaction mixture was heated in a closed vial at 70 °C for 6 h. Subsequent ^1H NMR analysis of the reaction solution showed one set of broad signals (see Figure AP-III.2). The number of aromatic ^1H signals and the downfield shift of the ^1H signals compared to the signals for free ligand indicated the formation of a single new symmetric species. A prolonged heating of the sample at 70 °C did not change the outcome of the reaction verifying that the resulting species is a thermodynamically stable product. ESI mass spectrometric analysis supported the formation of a monomeric cage $[Pd_2\mathbf{L}^1_4]^{4+}$ (see Figure AP-III.3).

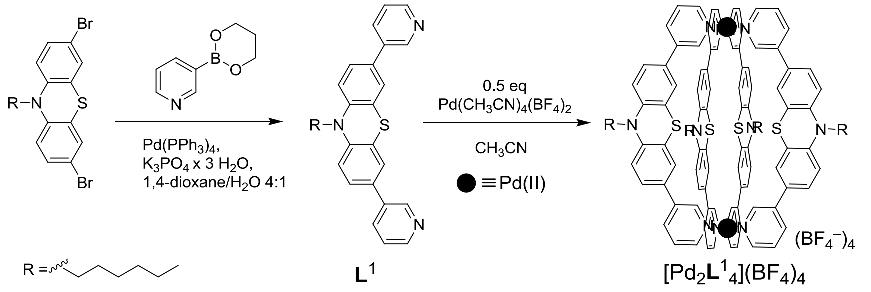

Figure III.17 Synthetic route leading to the ligand $\mathbf{L}^1$ and further reaction of the ligand to the monomeric cage $[Pd_2\mathbf{L}^1_4](BF_4)_4$.

Satheeshkumar, M. Ravivarma, S. Ganesan, P. Maruthamuthu, *J. Mater. Chem. A* **2013**, *1*, 13941. (r) A. Aguirre-Soto, C.-H. Lim, A. T. Hwang, C. B. Musgrave, J. W. Stansbury, *J. Am. Chem. Soc.*, **2014**, *136*, 7418.

[70] (a) P. Berges, J. Kudnig, G. Klar, E. Sanchez-Martinez, R. Diaz-Calleja, *Synth. Met*. **1992**, *46*, 207. (b) A. Knorr, J. Daub, *Angew. Chem. Int. Ed.* **1995**, *34*, 2664. (c) H. Spreitzer, J. Daub, *Chem. Eur. J.* **1996**, *2*, 1150. (d) A. Knorr, J. Daub, *Angew. Chem. Int. Ed.* **1997**, *36*, 2817. (e) S. A. Jenekhe, L. Lu, M. M. Alam, *Macromolecules* **2001**, *34*, 7315. (f) R. Y. Lai, X. Kong, S. A. Jenekhe, A. J. Bard*, J. Am. Chem. Soc.* **2003**, *125*, 12631. (g) X. Kong, A. P. Kulkarni, S. A. Jenekhe, *Macromolecules* **2003**, *36*, 8992. (h) A. Moissette, F. Luchez, C. Brémard, H. Vezin, M. Hureau, *Phys. Chem. Chem. Phys*. **2009**, *11*, 4286.

[71] M. Sailer, A. W. Franz, T. J. J. Müller, *Chem. Eur. J.* **2008**, *14*, 2602.

Since no crystals suitable for crystallographic analysis could be obtained, the structure for the monomeric cage was calculated by geometry optimization on the PM6 semiempirical level of theory with no constraints (charge +4, spin-multiplicity 1) implemented in Gaussian 09[72] (see Figure III.18). The calculated model revealed that the Pd-Pd distance of 12.64 Å is too short to be able to form the electrostatically favorable Pd cation and guest anion stacking as it is the case in the double-cage structure at least under the applied conditions (acetonitrile, BF_4^- anions). Attempts to dimerize the monomeric cage by utilization of other solvents (DMSO, $CHCl_3$) and smaller anions (Br^-, Cl^-, F^-) did not lead to the formation of a double-cage. These results are in accordance with the findings for the dibenzosuberone based system,[16] where a similar short ligand with an *N*-*N*-distance of 11.36 Å[73] also did not give a dimeric cage as the thermodynamic product, but yielded a monomeric cage. Therefore, a longer ligand $\mathbf{L^2}$ containing an ethynyl bridge was designed in order to give the desired double-cage assembly (see Figure III.19).

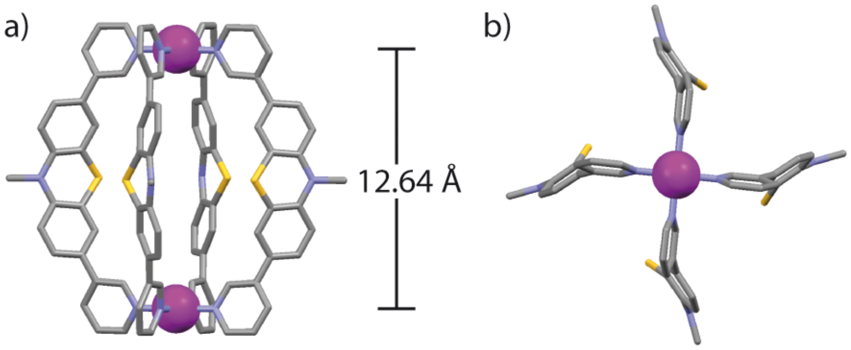

Figure III.18 (a) Side view and (b) top view along the Pd_2 axis of the PM6 model of the monomeric cage $[Pd_2\mathbf{L}^1_4]^{4+}$ (Pd space fill view, color magenta; S, N and C as stick view, color yellow, blue and grey). Anions and solvents were omitted and the hexyl chains were substituted by methyl chains. Reproduced with permission from reference [66].Copyright © 2014 Royal Society of Chemistry.

---

[72] M. J. Frisch, G. W. Trucks, H. B. Schlegel, G. E. Scuseria, M. A. Robb, J. R. Cheeseman, G. Scalmani, V. Barone, B. Mennucci, G. A. Petersson, H. Nakatsuji, M. Caricato, X. Li, H. P. Hratchian, A. F. Izmaylov, J. Bloino, G. Zheng, J. L. Sonnenberg, M. Hada, M. Ehara, K. Toyota, R. Fukuda, J. Hasegawa, M. Ishida, T. Nakajima, Y. Honda, O. Kitao, H. Nakai, T. Vreven, J. A. Montgomery Jr., J. E. Peralta, F. Ogliaro, M. Bearpark, J. J. Heyd, E. Brothers, K. N. Kudin, V. N. Staroverov, R. Kobayashi, J. Normand, K. Raghavachari, A. Rendell, J. C. Burant, S. S. Iyengar, J. Tomasi, M. Cossi, N. Rega, J. M. Millam, M. Klene, J. E. Knox, J. B. Cross, V. Bakken, C. Adamo, J. Jaramillo, R. Gomperts, R. E. Stratmann, O. Yazyev, A. J. Austin, R. Cammi, C. Pomelli, J. W. Ochterski, R. L. Martin, K. Morokuma, V. G. Zakrzewski, G. A. Voth, P. Salvador, J. J. Dannenberg, S. Dapprich, A. D. Daniels, O. Farkas, J. B. Foresman, J. V. Ortiz, J. Cioslowski and D. J. Fox, Gaussian 09, Gaussian, Inc., Wallingford CT, 2009.

[73] B3LYP/6-31G* DFT optimization of ligand.

The synthesis of the envisioned interpenetrated double-cage started from 3,7-dibromo-10-hexyl-phenothiazine. In the next step two 3-ethynylpyridine arms were attached to the building block via a Sonogashira cross coupling reaction, which yielded the ligand **L**^{2}. After purification, ligand **L**^{2} was dissolved in acetonitrile and 0.5 equivalents of $[Pd(CH_3CN)_4](BF_4)_2$ were added to the solution. After heating the reaction mixture at 70 °C for 6 h, a single species was obtained in quantitative yield, which was identified as the double-cage $[3BF_4@Pd_4\mathbf{L}^2_8](BF_4)_5$ assembly (see Figure III.19). Due to complete conversion into the dimeric coordination assembly, no further purification of the double-cage was needed. The ligand and its corresponding double-cage were characterized by 1D and 2D NMR spectroscopic analysis, via high resolution ESI mass spectrometry and X-ray analysis (for synthetic protocols and characterization data see Appendix-Chapter III Section 1).

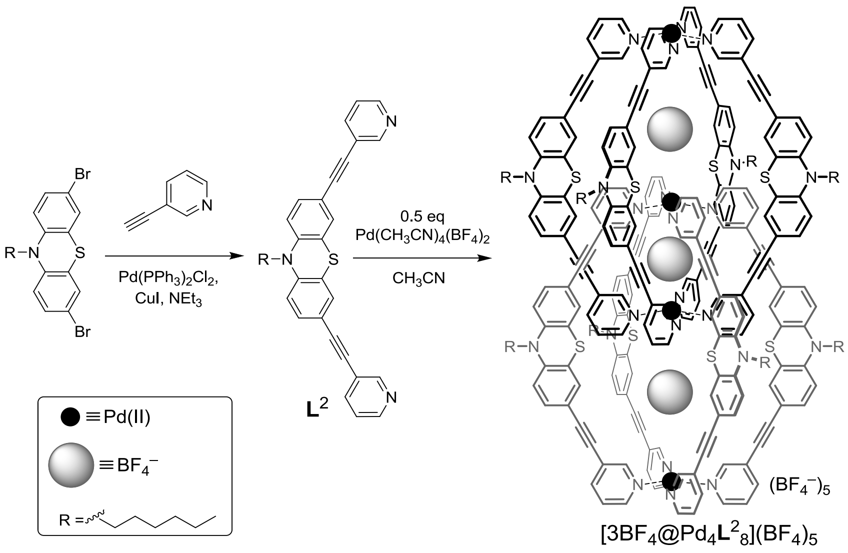

Figure III.19 Synthetic route leading to ligand **L**^{2} and further reaction of the ligand to interpenetrated double-cage $[3BF_4@Pd_4\mathbf{L}^2_8](BF_4)_5$.

The ^1H NMR spectrum of ligand **L**^{2} shows seven equivalent signals in the aromatic region of the chemical shift scale. The two protons adjacent to the pyridine nitrogen (H_g and H_f) show the highest downfield shift (see Figure III.20a). Upon incorporation of the ligand **L**^{2} into the highly symmetric double-cage structure $[3BF_4@Pd_4\mathbf{L}^2_8]^{5+}$, the signals split into two sets of equal intensity indicating different environments of the two halves of the ligand within the double-cage construction. The pyridine protons H_g and H_f show a very strong downfield shift due to coordination to the positively charged Pd(II) cations. The protons in close proximity to neighboring ligands of the second monomeric unit (H_a, $H_{a'}$, $H_{e'}$, $H_{d'}$) as well as the *N*-CH_2 protons of the hexyl chains exhibit an upfield shift. The high resolution ESI mass spectrum of the double-cage solution showed a series of species with varying number of counter anions, which were identified as $[3BF_4@Pd_4\mathbf{L}^2{}_8]^{5+}$+*n*$BF_4^-$ (*n*=0-2) (see Figure III.20b). Also the double-cage species containing two Cl^- anions were detected. The chloride anions may originate from a contamination of either the solution or the mass equipment. The guest binding abilities of the double-cages towards halide anions will be discussed further in Chapter IV.

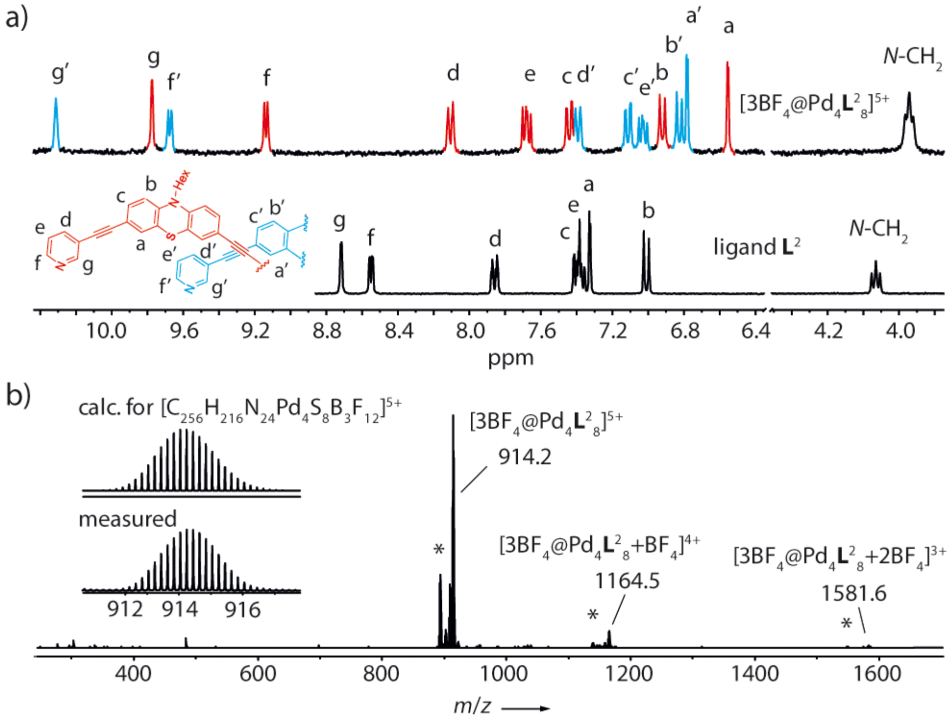

Figure III.20 a) ^{1}H NMR spectrum (298 K, 300 MHz, acetonitrile-d_3) of ligand $\mathbf{L}^2$ and the double-cage $[3BF_4@Pd_4\mathbf{L}^2{}_8](BF_4)_5$; b) ESI mass spectrum of the double-cage $[3BF_4@Pd_4\mathbf{L}^2{}_8+nBF_4]^{(5-n)}$ *n*=0-2 (* denotes Cl^- containing species $[2Cl+BF_4@Pd_4\mathbf{L}^2{}_8+nBF_4]^{(5-n)}$. Reproduced with permission from reference [65]. Copyright © 2013 WILEY-VCH Verlag GmbH & Co.

Single crystals of $[3BF_4@Pd_4\mathbf{L}^2{}_8](BF_4)_5$ suitable for X-ray diffraction were obtained via slow diffusion of diethyl ether into the acetonitrile solution of the double-cage. The assembly crystallized in the tetragonal space group P4/nnc with unit cell dimensions of a = b = 21.122(2) Å and c = 34.263(3) Å. The D_4-symmetric structure of the double-cage is built from four square planar coordinated Pd(II) cations aligned on one axis and eight ligands (see

Figure III.21). The distance between the outer two Pd metals in the double-cage was determined to 28.39 Å. The internal and the next outer Pd(II) cation are separated by 9.77 Å and the distance between two internal Pd cations was measured to 8.85 Å. Formally, the structure is composed of two monomeric cages obeying the formula $[Pd_2\mathbf{L}^2{}_4]^{4+}$. The two monomeric cages quadruply interpenetrate each other and give finally the thermodynamically stable interpenetrated double-cage structure. The structure features three internal cavities, each filled with a BF_4^- anion. Further two BF_4^- anions are located outside at the face of the two outer palladium cations. The remaining three BF_4^- anions are sitting in the channels between the double-cages. The hexyl chains of one monomeric cage are tilted in one direction, whereas the hexyl chains of the second monomeric cage show in the opposite direction thus minimizing the steric hindrance (for further crystallographic data see Appendix-Chapter III Section 2).

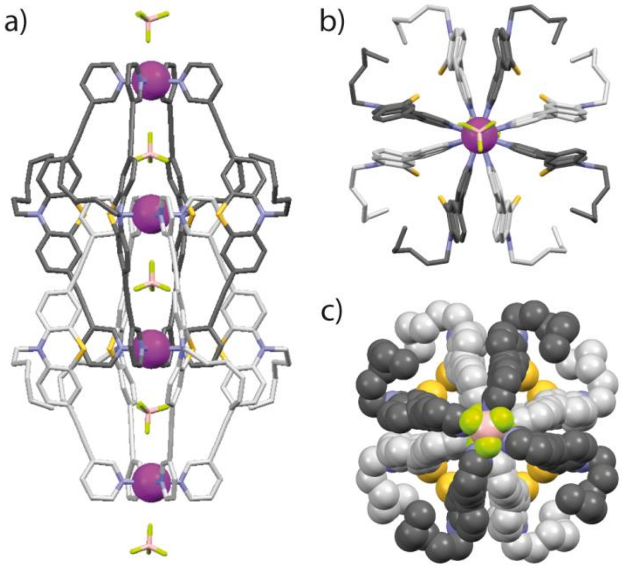

Figure III.21 X-ray single-crystal structure of double-cage $[3BF_4@Pd_4\mathbf{L}^2{}_8](BF_4)_5$ (CCDC 904004) is shown as a) side view, b) view along the Pd_4-axis and as c) space fill view. Only two BF_4^- counter anions are shown, further three counter anions are located between the double-cage channels. Reproduced with permission from reference [65]. Copyright © 2013 WILEY-VCH Verlag GmbH & Co.

In order to examine the redoxchemistry of the new phenothiazine based coordination cage, ligand $\mathbf{L}^2$ was modified to the S-monooxygenated ligand $\mathbf{L}^3$ via application of a mild two electron oxidation with $Cu(NO_3)_2{\cdot}3H_2O$ in CH_2Cl_2 (see Figure III.22).[74] The ^{1}H NMR signals of the phenothiazine backbone of the monooxygenated derivative $\mathbf{L}^3$, in particular the protons next to the sulfoxide group H_a, H_b and H_c, show a significant downfield shift as a consequence of introduction of an electron withdrawing group at the sulfur atom (see Figure III.23a). Like its precursor, ligand $\mathbf{L}^3$ is capable of forming a double-cage. ESI mass spectrometry showed the quantitative formation of a single species obeying the formula $[3BF_4@Pd_4\mathbf{L}^3_8{+}n BF_4]^{(5-n)+}$ with n=0-2 (see Figure III.23b). Although the ^{1}H NMR spectrum of the double-cage assembly showed resonances in the ppm range as expected from previously reported double-cages,[16,26] the spectrum was accompanied by signal broadening between 238 K and 298 K (see Appendix-Chapter III Section 1). Presumably, ligand $\mathbf{L}^3$ exists as a mixture of two ring-flip isomers with the oxygen substituent being either in the pseudo-axial or the pseudo-equatorial position.[75] Gas-phase DFT calculations (B3LYP/6-311++G(d,p) implemented in Gaussian09[72]) of 10-methyl-10*H*-phenothiazine-5-oxide showed that the pseudo-axial isomer is favored only by 2 kJ·mol^{-1} over the pseudo-equatorial derivative with a ring-flip barrier of 22 kJ·mol^{-1}, which allows for a quick equilibration between the two isomers. These ligand isomers give rise to a mixture of several diastereomeric double-cages, which would explain the signal broadening in the ^{1}H NMR spectrum and the presence of only one species in the ESI mass spectrum (for synthetic protocols and characterization data see Appendix – Chapter III Section 1).

---

[74] L. Găină, A. Csámpai, G. Túrós, T. Lovász, V. Zsoldos-Mády, I. A. Silberg, P. Sohár, *Org. Biomol. Chem.* **2006**, *4*, 4375.

[75] (a) Q. Wang, L. Yang, Z. Xu, Y. Sun, *Acta Cryst Section E* **2009**, *65*, o1978. (b) R.-F. Jin, K. Yu, S.-Y. Yang, R.-B. Huang, *Acta Cryst. Section E.***2010**, *66*, o3267.

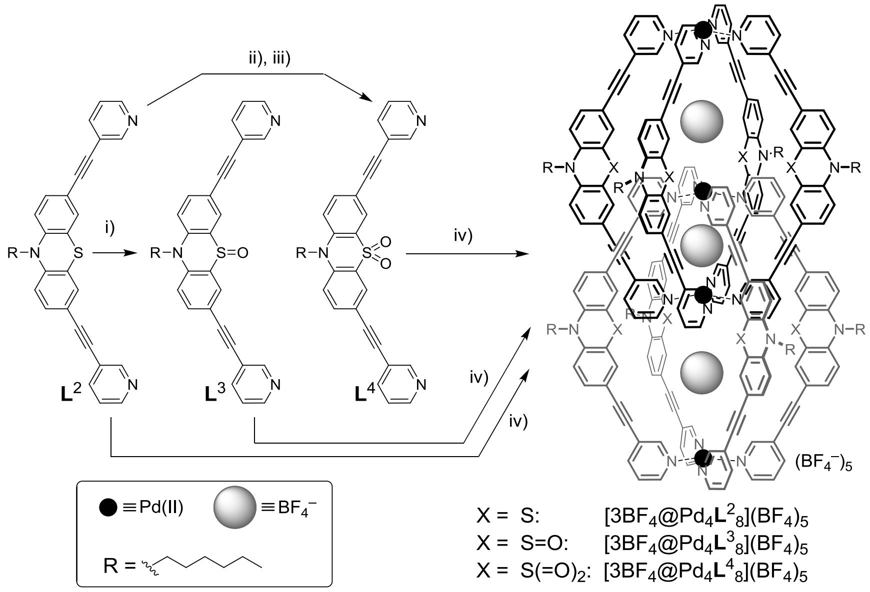

Figure III.22 Synthesis of ligands $\mathbf{L}^3$ and $\mathbf{L}^4$ starting from the precursor ligand $\mathbf{L}^2$. i) $Cu(NO_3)_2 \cdot 3H_2O$, CH_2Cl_2, ultrasonic bath; ii) *m*-CPBA, CH_2Cl_2; iii) Fe powder, HOAc. Self-assembly of the ligands leading to the double-cages $[3BF_4@Pd_4\mathbf{L}^2{}_8](BF_4)_5$, $[3BF_4@Pd_4\mathbf{L}^3{}_8](BF_4)_5$ and $[3BF_4@Pd_4\mathbf{L}^4{}_8](BF_4)_5$. iv) $[Pd(CH_3CN)_4](BF_4)_2$, CH_3CN, 70 °C, 6 h. Reproduced with permission from reference [65]. Copyright © 2013 WILEY-VCH Verlag GmbH & Co.

Oxidation of ligand $\mathbf{L}^2$ with a harsher oxidizing reagent such as *meta*-chloroperbenzoic acid (*m*-CPBA)[76] yielded a derivative with dioxygenated S-atom and *N*-oxygenated pyridine arms. Finally, the sulfone ligand $\mathbf{L}^4$ was obtained after reduction of the oxygenated pyridine residues with iron powder in acetic acid (see Figure III.22). The ^{1}H NMR spectrum of ligand $\mathbf{L}^4$ shows analogue resonances as for the monoxygenated ligand $\mathbf{L}^3$ with two differences: proton H_a next to the sulfone group is further shifted downfield and the N-CH_2 proton signals are slightly shifted upfield (see Figure III.23a). The sulfone ligand $\mathbf{L}^4$ is also able to form interpenetrated double-cage assemblies when 0.5 equivalents of $[Pd(CH_3CN)_4](BF_4)_2$ are added to acetonitrile solution of the ligand and the mixture is heated to 70 °C for 6 h. The conversion to the double-cage $[3BF_4@Pd_4\mathbf{L}^4{}_8](BF_4)_5$ was confirmed by ^{1}H NMR spectroscopic analysis as well as via high resolution ESI mass spectrometry (see Figure III.23 a,b). The ^{1}H NMR spectrum of $[3BF_4@Pd_4\mathbf{L}^4{}_8](BF_4)_5$ shows two sets of sharp signals as in the case of the nonoxygenated derivative $[3BF_4@Pd_4\mathbf{L}^2{}_8](BF_4)_5$, but in contrast to monooxygenated double-cage $[3BF_4@Pd_4\mathbf{L}^3{}_8](BF_4)_5$. This supports the previous hypothesis,

---

[76] T. Ishihara, H. Kakuta, H. Moritani, T. Ugawa, I. Yanagisawa, *Chem. Pharm. Bull.* **2004**, *52*, 1204.

that in the sulfoxide derivative a partial inversion of the lone pair at the tetrahedral S-atom site is responsible for ^{1}H NMR signal broadening, which is lacking in case of the dioxygenated derivative.

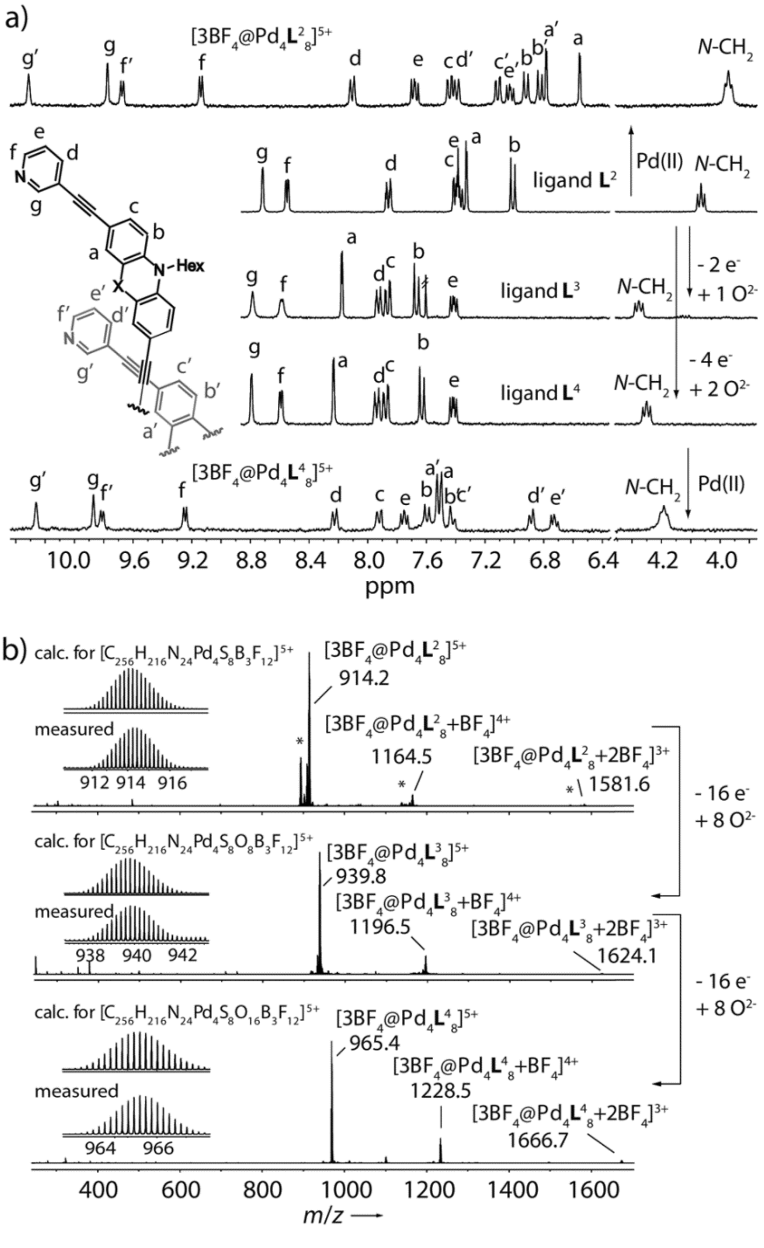

Figure III.23 a) ^{1}H NMR spectra (300 MHz, CD_3CN, 293 K) of ligands $\mathbf{L}^2$, $\mathbf{L}^3$ and $\mathbf{L}^4$ (2.80 mM) and the double-cages $[3BF_4@Pd_4\mathbf{L}^2_8]^{5+}$ and $[3BF_4@Pd_4\,\mathbf{L}^4_8]^{5+}$ (0.35 mM). X: S for $\mathbf{L}^2$, X: S=O for $\mathbf{L}^3$ and X: SO_2 for $\mathbf{L}^4$. b) HR-ESI mass spectra of double-cages $[3BF_4@Pd_4\mathbf{L}^2_8{+}n BF_4]^{(5-n)+}$, $[3BF_4@Pd_4\mathbf{L}^3_8{+}n BF_4]^{(5-n)+}$ and $[3BF_4@Pd_4\mathbf{L}^4_8{+}n BF_4]^{(5-n)+}$ with n = 0-2. (* denotes chloride containing species $[2Cl{+}BF_4@Pd_4\mathbf{L}^2_8{+}n BF_4]^{(5-n)+}$). Reproduced with permission from reference [65]. Copyright © 2013 WILEY-VCH Verlag GmbH & Co.

For a full characterization of the series of ligands and corresponding double-cages, further spectroscopic analyses via UV/Vis absorption and fluorescence spectroscopy were performed. Figure III.24 shows the UV/Vis spectra of the ligands and the corresponding double-cages dissolved in acetonitrile. Ligand $\mathbf{L}^2$ shows a strong absorption with a maximum at 287 nm and a weaker band around 368 nm. The spectra of the oxygenated derivatives $\mathbf{L}^3$ and $\mathbf{L}^4$ are similar and show one prominent absorption band with the maxima found at 359 nm and 362 nm, respectively. The spectrum of the double-cage $[3BF_4@Pd_4\mathbf{L}^2{}_8](BF_4)_5$ shows a similar absorption pattern as the ligand $\mathbf{L}^2$, but whole spectrum is shifted to longer wavelengths with absorption maxima at 294 nm and 407 nm. The spectrum of monooxygenated derivative $[3BF_4@Pd_4\mathbf{L}^3{}_8](BF_4)_5$ shows two intense absorption bands with maxima at 275 nm and 365 nm in contrast to the corresponding ligand $\mathbf{L}^3$, which has only one strong absorption maximum. The spectrum of the dioxygenated double-cage $[3BF_4@Pd_4\mathbf{L}^4{}_8](BF_4)_5$ is very similar to the corresponding ligand $\mathbf{L}^4$ with a slightly blue-shifted absorption maximum at 356 nm. In summary, the spectra of double-cages are clearly distinguishable from those of the corresponding ligands.

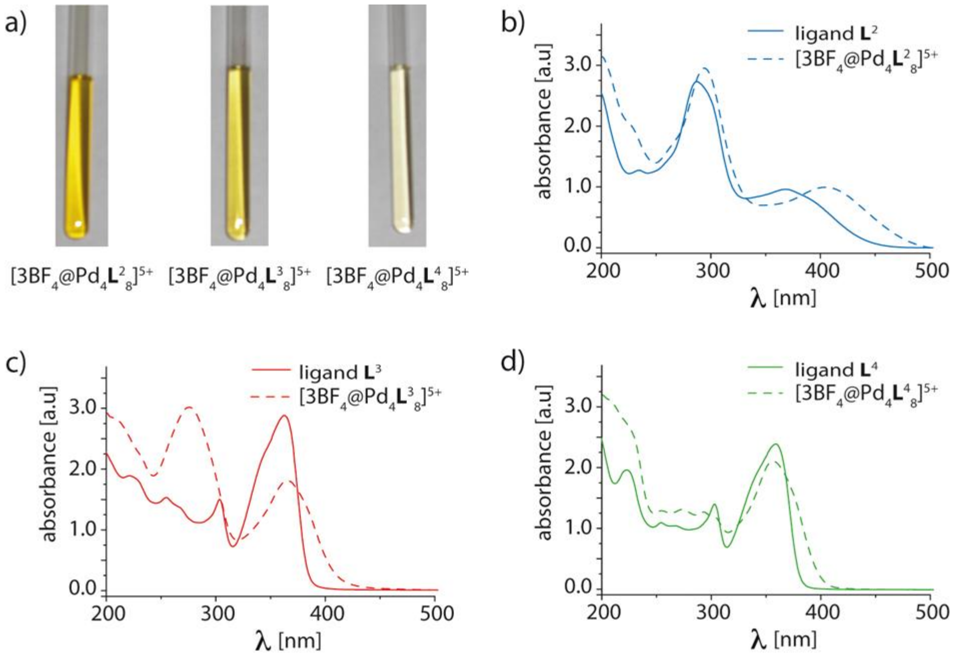

Figure III.24 a) Photographs of solution of the double-cages $[3BF_4@Pd_4\mathbf{L}^{2\text{-}4}{}_8](BF_4)_5$ (c = 0.35 mM in CH_3CN). UV/Vis spectra of b) ligand $\mathbf{L}^2$ and double-cage $[3BF_4@Pd_4\mathbf{L}^2{}_8](BF_4)_5$, c) ligand $\mathbf{L}^3$ and double-cage $[3BF_4@Pd_4\mathbf{L}^3{}_8](BF_4)_5$, d) ligand $\mathbf{L}^4$ and double-cage $[3BF_4@Pd_4\mathbf{L}^4{}_8](BF_4)_5$ dissolved in acetonitrile (ligand concentration: 0.35 mM; double-cage concentration: 0.04 mM). Reproduced with permission from reference [65]. Copyright © 2013 WILEY-VCH Verlag GmbH & Co.

Another characteristic feature of phenothiazine based ligands $\mathbf{L}^2$, $\mathbf{L}^3$ and $\mathbf{L}^4$ is their high luminescence due to the extended π-system as can be seen from the fluorescence spectra in figure III.25. Ligand $\mathbf{L}^2$ shows a yellow-green fluorescence with a maximum at 495 nm, while the oxygenated ligands $\mathbf{L}^3$ and $\mathbf{L}^4$ show a blue-shifted emission with maxima at 428 nm and 399 nm, respectively. All ligand solutions were excited at their absorption maximum. The double-cages do not show any emission, presumably due to effective quenching of the fluorescence by the heavy palladium cations.

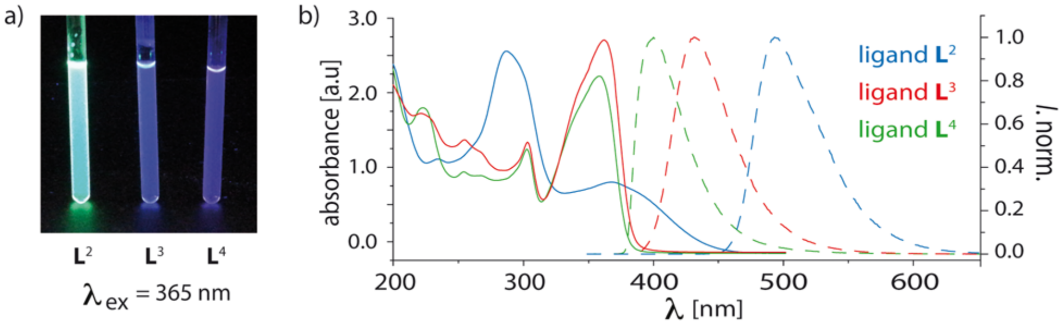

Figure III.25 a) Photographs of solutions of the ligands in acetonitrile after irradiation at 365 nm. b) UV/Vis (solid lines) and fluorescence (dashed lines) spectra of ligands $\mathbf{L}^2$, $\mathbf{L}^3$ and $\mathbf{L}^4$ in acetonitrile. Fluorescence measurements: concentration of ligands 2.80 mM; intensities normalized; excitation at absorbance maximum; 2 nm slit. Reproduced with permission from reference [65]. Copyright © 2013 WILEY-VCH Verlag GmbH & Co.

Furthermore, also the two oxygenated double-cage derivatives $[3BF_4@Pd_4\mathbf{L}^3{}_8](BF_4)_5$ and $[3BF_4@Pd_4\mathbf{L}^4{}_8](BF_4)_5$ were characterized via their crystal structure. Although all three double-cages have a common topology, they differ significantly in their shape expressed by the Pd-Pd distances, ligand bending and size of the voids within the double-cages (see Figure III.26a). The crystal of double-cage $[3BF_4@Pd_4\mathbf{L}^3{}_8](BF_4)_5$ was obtained from the solution of $[3BF_4@Pd_4\mathbf{L}^2{}_8](BF_4)_5$ after two months exposure of crystals to air presumably via a crystal to crystal oxygenation reaction. Thereby, all eight phenothiazine ligand backbones within the double-cage assembly were converted to monooxygenated derivatives. In contrast to the mixture of diastereomers of double-cage $[3BF_4@Pd_4\mathbf{L}^3{}_8](BF_4)_5$ in solution, the solid-state-oxidized double-cage consists of only one ligand isomer and thus the crystal contains only one highly symmetric double-cage isomer. All eight phenothiazine ligands $\mathbf{L}^3$ within the crystalline sample of $[3BF_4@Pd_4\mathbf{L}^3{}_8](BF_4)_5$ have the oxygen substituent in the pseudo-axial position. The oxygen substituents are arranged in clockwise fashion within one monomeric cage and counterclockwise in the other $[Pd_2\mathbf{L}^3{}_4]^{4+}$ subunit. The double-cage

$[3BF_4@Pd_4\mathbf{L}^4_8](BF_4)_5$ has two oxygens per ligand, one in pseudo-axial and the second in pseudo-equatorial position. All three double-cage structures $[3BF_4@Pd_4\mathbf{L}^n_8](BF_4)_5$ with n = 2-4 contain three voids with open windows, which can be filled with anionic guests and solvent molecules. The two terminal pockets are equivalent in shape and size. The middle pocket differs in size from the outer two pockets owing to the smaller Pd_{in}-Pd_{in} distance. The middle void is more shielded by ligand backbones compared to the terminal voids. In all three double-cage derivatives all the pockets are filled with BF_4^- anions. The channels between the double-cages are filled with solvent or remaining counter anions. In case of non- and monooxygenated double-cage derivatives $[3BF_4@Pd_4\mathbf{L}^2_8](BF_4)_5$ and $[3BF_4@Pd_4\mathbf{L}^3_8](BF_4)_5$ all counter anions are BF_4^- molecules, but for the dioxygenated double-cage one equivalent of chloride counter anions (probably stemming from a contamination) per double-cage was found to be located in the space between the linearly aligned double-cages (for crystal packing see Figure AP-III.23 and for further information on crystal data see Appendix-Chapter III Section 2). This finding is controversial to the behavior in solution phase, where chloride anions are preferably included inside the voids of the double-cage structure because the distance between the Pd cations within the double-cage is optimal for electrostatic interactions between the anionic molecules and the metal cations (see Chapter IV). In case of double-cages $[3BF_4@Pd_4\mathbf{L}^4_8](BF_4)_5$, the linear alignment of the double-cages in the crystal structure offers the possibility for optimal spacing between two double-cages with a Pd-Pd distance of 6.54 Å and thus for a tight binding of a chloride anion outside the pockets. Further comparison of X-ray structures showed that with increasing amount of attached oxygen substituents at the sulfur atoms, the latter have to move away from the palladium centre. Thus, the distance between the sulfur atoms of one monomeric cage subunit and the $Pd(pyridine)_4$-planes of the second subunit increases (see Figure III.26b). The oxygens have to intercalate between the gap of the sulfur atom and the space between two adjacent pyridine rings. Another structural characteristic feature of double-cages is the angle between the pyridine arms of the ligands (see Figure III.26c). The bending angle decreases from 155 ° for $[3BF_4@Pd_4\mathbf{L}^2_8](BF_4)_5$ to 150 ° for $[3BF_4@Pd_4\mathbf{L}^3_8](BF_4)_5$ and is slightly increased to 152° for $[3BF_4@Pd_4\mathbf{L}^4_8](BF_4)_5$. This behavior of ligand bending can be explained by different steric demands of the lone pair at the sulfur atom and the amount of oxygen substituents. Furthermore the Pd-Pd distances can be used to compare the dimensions of the cages along the Pd_4 axis. The non oxygenated cage $[3BF_4@Pd_4\mathbf{L}^2_8](BF_4)_5$

has the longest Pd_{out}-Pd_{out} distance with 26.29 Å, followed by 25.27 Å for $[3BF_4@Pd_4\mathbf{L}^3{}_8](BF_4)_5$ and the shortest distance is found for $[3BF_4@Pd_4\mathbf{L}^4{}_8](BF_4)_5$ with 24.95 Å. This shrinking of the double-cages along the Pd_4 axis with increasing crowding at the sulfur atom has a significant influence on the pocket size. The distance of the two inner Pd_{in}-Pd_{in} shows a significant change, going from 8.85 Å for the nonoxygenated double-cage to 8.63 Å for the monooxygenated and 8.47 Å for the dioxygenated derivative. A further significant change is found for the outer pockets of the double-cages, where the Pd_{in}-Pd_{out} distance is shrinking by 7 % from 8.77 Å for $[3BF_4@Pd_4\mathbf{L}^2{}_8](BF_4)_5$ to 8.16 Å $[3BF_4@Pd_4\mathbf{L}^3{}_8](BF_4)_5$ and is again increased by 3 % to 8.40 Å for the dioxygenated derivative $[3BF_4@Pd_4\mathbf{L}^4{}_8](BF_4)_5$ (see Figure III.26c).

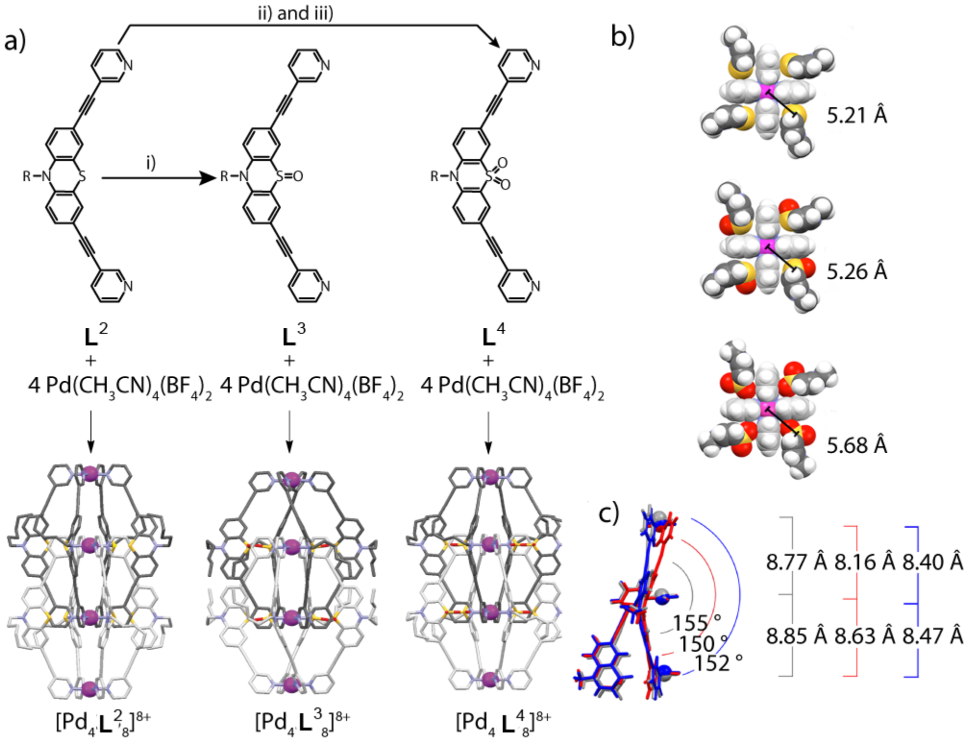

Figure III.26 a) Reaction of ligand $\mathbf{L}^2$ to ligand $\mathbf{L}^3$ via i) $Cu(NO_3)_2{\cdot}3H_2O$ in CH_2Cl_2 and to ligand $\mathbf{L}^4$ via ii) *m*-CPBA in CH_2Cl_2 and iii) Fe in HOAc. Crystal structures of the corresponding double-cages $[3BF_4@Pd_4\mathbf{L}^2{}_8](BF_4)_5$, $[3BF_4@Pd_4\mathbf{L}^3{}_8](BF_4)_5$ and $[3BF_4@Pd_4\mathbf{L}^4{}_8](BF_4)_5$. b) Space-filling view along the Pd_4-axis showing an increase of the distance between this axis and the sulfur atoms at the ligand backbone with increasing oxygenation degree at the sulfur atom. Pd: pink, C: dark grey, H: pale grey; S: yellow, O: red. c) Pd_{out}-Pd_{in}-Pd_{in} distances and the bending angles of the ligands inside the double-cages. Grey line: $[3BF_4@Pd_4\mathbf{L}^2{}_8](BF_4)_5$, red line: $[3BF_4@Pd_4\mathbf{L}^3{}_8](BF_4)_5$ and blue line: $[3BF_4@Pd_4\mathbf{L}^4{}_8](BF_4)_5$. Reproduced with permission from reference [65] and [66]. Copyright © 2013 WILEY-VCH Verlag GmbH & Co and Copyright © 2014 Royal Society of Chemistry.

Next, cage to cage transformations in terms of oxygenation reactions were studied. For the oxygenation reaction of the double-cage $[3BF_4@Pd_4\mathbf{L}^2{}_8]^{5+}$, the same reaction conditions were chosen as for the oxygenation of ligand $\mathbf{L}^2$, namely $Cu(NO_3)_2{\cdot}3H_2O$ in CH_2Cl_2. Due to the broadening of the ^1H NMR signals of double-cage $[3BF_4@Pd_4\mathbf{L}^3{}_8]^{5+}$, the oxidation process was monitored by ESI mass spectrometry (see Appendix - Chapter III Section 3 for experimental conditions and Figure AP-III.25 for the mass spectra after reaction times of 0.5 h, 1.0 h, 1.5 h, 2.0 h and 2.5 h). The analysis of the reaction products showed that the oxidation occurs in a stepwise manner during the reaction time of 2 h. Due to the large excess of nitrate anions, the tetrafluoroborate counter anions were replaced in the course of the reaction. The spectrum measured after 1.5 h oxidation time clearly shows the formation of species with up to eight extra oxygen substituents as indicated by the calculated spectrum (see Figure III.27a). The peak of the eightfold-monooxygenated product $[3NO_3@Pd_4\mathbf{L}^3{}_8+NO_3]^{4+}$ has a much larger intensity than the peaks of the incompletely oxidized products, although a substantial amount of non-oxidized starting material of $[3NO_3@Pd_4\mathbf{L}^2{}_8+NO_3]^{4+}$ is still present in the reaction mixture. Control experiments in acetonitrile showed that none of the oxidation intermediates is disfavored. A statistical distribution of oxygenated double-cages was obtained when the double cages were assembled from a 1 : 1 mixture of the non- and monooxygenated ligands $\mathbf{L}^2$ and $\mathbf{L}^3$ (see Figure AP-III.26a). Furthermore, a very slow ligand exchange between the fully assembled double-cages $[3BF_4@Pd_4\mathbf{L}^2{}_8]^{5+}$ and $[3BF_4@Pd_4\mathbf{L}^3{}_8]^{5+}$ was observed when their mixture was heated for several hours (see Figure AP-III.26b). On the basis of these observations, it can be assumed that the oxidation of cage $[3BF_4@Pd_4\mathbf{L}^2{}_8]^{5+}$ proceeds in a cooperative manner. In this hypothesis, the double-cage species that already carries at least one oxidized sulfur atom is able to undergo further a oxidation reaction much quicker than the parental non-oxidized double-cage $[3X@Pd_4\mathbf{L}^2{}_8]^{5+}$ (X = BF_4^- or NO_3^-). One possible explanation for this reaction behavior can be assumed in steric reasons. The homo-octameric cage $[3X@Pd_4\mathbf{L}^2{}_8]^{5+}$ is not prone to give up its high symmetry by the first oxidation step. Once the oxygenation occurred, the oxygenated ligand distorts the overall symmetry to a certain extend and this facilitates the oxygenation of the other ligands until the highly symmetric product $[3X@Pd_4\mathbf{L}^3{}_8]^{5+}$ is formed. A second explanation may be assigned to the electronic communication between the partially oxidized ligands arranged within the densely packed double-cage structure. Interestingly, the oxidation did not end at the eightfold monooxygenated assembly $[3X@Pd_4\mathbf{L}^3{}_8]^{5+}$, but continued to the dioxygenated assembly $[3X@Pd_4\mathbf{L}^4{}_8]^{5+}$ (see Figure III.27b) showing a two-step oxygenation pattern. The free ligand $\mathbf{L}^2$ was converted only into monooxygenated ligand $\mathbf{L}^3$ under the same reaction conditions and did not further react to the dioxygenated derivative $\mathbf{L}^4$. These observations indicate a non-trivial oxidation mechanism of the cage species that may originate from electronic communication between the densely clustered phenothiazine-based ligands within the double-cage architecture.

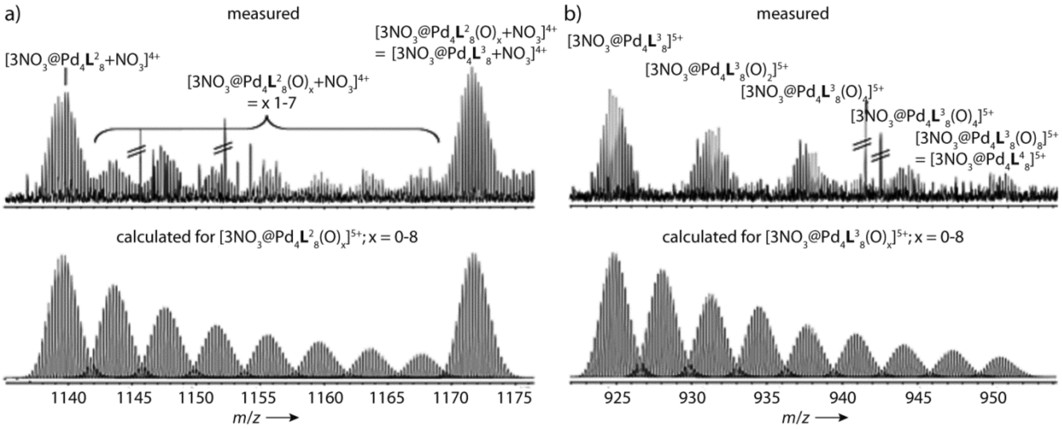

Figure III.27 FTICR-ESI-MS measurement (top) and simulation (bottom) of the oxidation products of cage $[3BF_4@Pd_4\mathbf{L}^2{}_8]^{5+}$ after treatment with $Cu(NO_3)_2\cdot 3H_2O$ in CH_2Cl_2 for a time period of a) 1.5 h and b) 2.5 h.

In a further study comparing the redox behaviors of the double-cage and the corresponding ligand, the double-cage $[3BF_4@Pd_4\mathbf{L}^2{}_8]^{5+}$ as well as the ligand $\mathbf{L}^2$ were titrated with the oxidizing agent $[Fe(III)(bpy)_3](PF_6)_3$[77] (redox potential of $[Fe(bpy)_3](BF_4)_2$ 1.08 V (+3 $\rightleftharpoons$ +2)[78] in CH_3CN vs. SCE) under the nitrogen protection atmosphere (see Figure AP-III.27). After oxidation reaction, the free ligand is expected to form monoradical cations $[\mathbf{L}^2]^{\cdot+}$ and the double-cage is expected to form an oxidized species $[3BF_4@Pd_4\mathbf{L}^2{}_8]^{13\cdot+}$ containing of up to eight radical-cationic ligands. The evolution of the radicals was followed by a characteristic radical absorption band at 680 nm. After creation of the radical cations, the intermediate species were reacted with water to give the oxygenated derivatives. The reaction with water requires a two-electron oxidation of the ligands. The reaction progress

---

[77] (a) J. Bouzaid, M. Schultz, Z. Lao, J. Bartley, T. Bostrom, J. McMurtrie, *Cryst. Growth Des.* **2012**, *12*, 3906. (b) L. Pazderski, T. Pawlak, J. Sitkowski, L. Kozerski, E. Szłyk, *Magn. Reson. Chem*. **2010**, *48*, 450. (c) R. Khattak, I. Imam Naqvi, M. Akhyar Farrukh, *J. Iran. Chem. Soc.* **2008**, *5*, 631.

[78] L. F. Warren, *Inorg. Chem.* **1977**, *16*, 2814.

was followed by the disappearance of the radical band at 680 nm (see Figure III.28 a) for oxidation of ligand $\mathbf{L}^2$ and b) for oxidation of double-cage $[3BF_4@Pd_4\mathbf{L}^2{}_8]^{5+}$). The study revealed that the double-cage $[3BF_4@Pd_4\mathbf{L}^2{}_8]^{5+}$ reacts faster than the corresponding ligand $\mathbf{L}^2$. This difference in reaction kinetics may be dedicated to the possibility of an accelerated intramolecular disproportionation reaction pathway to phenothiazine dications in case of $[3BF_4@Pd_4\mathbf{L}^2{}_8](BF_4)_5$, in which the phenothiazine backbones are packed in close proximity to each other. The dication formation of the free ligand follows a slower intermolecular mechanism due to the lower possibility of collision of two ligand molecules. The evolution of these dication intermediates are known in the synthesis of phenothiazine-5-oxides.[64] In addition, the reaction mixture of the above described oxygenation reaction with $Cu(NO_3)_2{\cdot}3H_2O$ in CH_2Cl_2 after 2.5 h showed an unexpected signal pattern, which does not follow a statistical distribution, but further supports the possibility of an intramolecular disproportionation pathway in case of the double-cage (see Figure AP-III.28 b)). Furthermore, applying $H_2{}^{18}O$ as a reactant showed that the oxygen for the reaction is coming from the water molecules (see Figure AP-III.29).

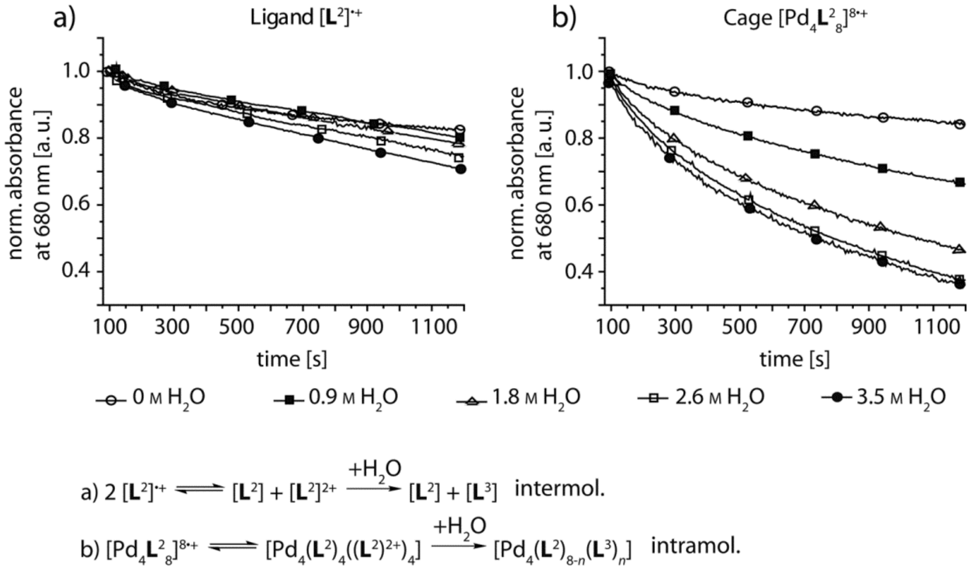

Figure III.28 Titration of a) ligand $\mathbf{L}^2$ (80 μM) and b) double-cage $[Pd_4\mathbf{L}^2{}_8]^{8+}$ with the oxidant $[Fe^{III}(bpy)_3](PF_6)_3$ (addition at *t* = 0 s; solvent CH_3CN; 298 K, N_2 atmosphere). The radical cations can be observed by characteristic absorption band at 680 nm. After oxidation reaction, the reaction mixture was treated with different amounts of water (addition at *t* = 100 s). At the bottom a scheme of proposed reaction mechanisms is shown, that may explain the difference in the observed reaction rates. Reproduced with permission from reference [65]. Copyright © 2013 WILEY-VCH Verlag GmbH & Co.

III.4 Conclusion

This chapter describes the quantitative preparation of three related highly symmetric interpenetrated coordination double-cages constructed from four Pd(II) cations and eight phenothiazine-based ligands. The double-cages differ in their oxygenation state at the sulfur atom resulting in the non-, mono- and dioxygenated double-cage. Besides the preparation via metal-mediated self-assembly from the respective ligands, the direct cage to cage oxygenation transformation in presence of water molecules was demonstrated. Comparison of the reaction of radical cations with water showed that the reaction kinetics of the double-cage follows a faster oxygenation mechanism compared to the free ligand. Presumably, the double-cage can undergo a faster intramolecular disproportionation reaction which is a result of the dense packing of ligands within the double-cage structure. The ligands in the double-cage structure are assumed to communicate with each other and thus accelerate the oxygenation reaction. The free ligands on the other hand react presumably via a slower intermolecular mechanism.

Chapter IV

Host-Guest Chemistry of Interpenetrated Double-Cages

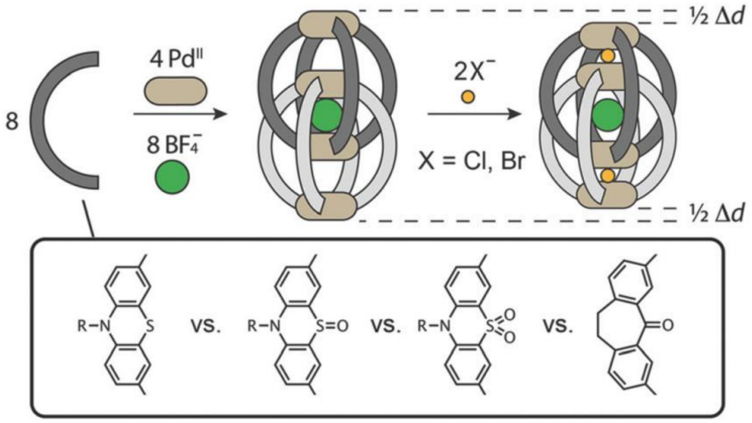

Reproduced with permission from reference [99]. Copyright © 2013 Royal Society of Chemistry

This chapter corresponds to the following publication:

- ‘Relative Anion Binding Affinity in a Series of Interpenetrated Coordination Cages’, M. Frank, J. M. Dieterich, S. Freye, R. A. Mata and G. H. Clever, *Dalton. Trans.* **2013**, *42*, 15906-15910.

IV. HOST-GUEST CHEMISTRY OF INTERPENETRATED DOUBLE-CAGES

IV.1 Introduction

The field of anion recognition with supramolecular host systems has grown very fast. There is a plethora of examples for selective complexation, detection and separation of anionic guest species. Also great advances have been made in anion templated synthesis, directed self-assembly and catalytic applications.[79] Anions play a crucial role in many biological systems. Genetic information is carried by a polyanionic DNA molecule, many of enzyme substrates and co-factors contain groups with a negative charge and some small anions have regulative functions in human body. For example chloride anions are found in extracellular fluid regulating processes[80] that are closely related to diseases such as cystic fibrosis[81] and impairment of muscle functions.[82] Fluoride anions play an important role in bone and teeth growth. Therefore, in some regions of the world they are artificially added to toothpaste or even water supplies. Iodide anions are essential in biosynthesis of hormones by the thyroid gland. Other anions such as nitrate, sulfate or phosphates are responsible for environmental pollution such eutrophication of natural water cycle.[83] Considering the plenty of important applications of these anionic species, an increasing motivation of sensing and binding them inside artificial cage complexes arose in the past decades.

Usually the anions bind via electrostatic interactions between the host and the guest molecule, but there are also examples where hydrogen bonds, anion-dipole- or anion-π-bonds are dominating interactions.[84] The design of receptors for anions is based on careful

---

[79] for reviews on anion binding in supramolecular chemistry see: (a) P. D. Beer, P. A. Gale, *Angew. Chem. Int. Ed.* **2001**, *40*, 486. (b) J. L. Sessler, P. A. Gale, W.-S. Cho, *Anion Receptor Chemistry*, The Royal Society of Chemistry, Cambridge **2006**. (c) A. J. Lowe, B. M. Long, F. M. Pfeffer, *Chem. Commun.* **2013**, *49*, 3376. (d) N. H. Evans, P. D. Beer, *Angew. Chem. Int. Ed.* **2014**, *53*, 11716.

[80] E. Di Stasio, *Biophys. Chem.* **2004**, *112,* 245.

[81] S. M. Rowe, S. Miller, E. J. Sorscher, *N. Engl. J. Med.* **2005**, *352*, 1992.

[82] K. Steinmeyer, C. Lorenz, M. Pusch, M. C. Koch, T. J. Jentsch, *EMBO J.* **1994**, *13*, 737.

[83] W. Kaim, B. Schwederski, Brigitte, A. Klein, *Bioinorganic Chemistry - Inorganic Elements in the Chemistry of Life : An Introduction and Guide*, 2nd Edition, Wiley, Chichester **2013**.

[84] (a) A. J. Goshe, I. M. Steele, C. Ceccarelli, A. L. Rheingold, B. Bosnich, *PNAS* **2002**, *99,* 4823. (b) C. R. Bondy, P. A. Gale, S. J. Loeb, *J. Am. Chem. Soc.* **2004**, *126*, 5030. (c) V. Amendola, M. Boiocchi, B. Colasson, L. Fabbrizzi, M.-

selection of positively charged or neutral electron deficient interaction sites and their spherical orientation within the cavity. Therefore, the highest recognition is found for hosts which are in contact with the guest molecule over a large area. This is usually fulfilled for hosts which are able to wrap around the guest molecule as it is the case for cage-like hosts with intramolecular cavities.[45] Many anions are prone to be protonated at low pH values. Therefore, host molecules should be stable within the pH window of the desired anion. Also other factors can affect the binding strength and selectivity of anions, such as solvent and temperature. Host molecules must be designed in a way to be more effective in binding the targeted anions than the competing surrounding solvent. Neutral hosts, which complex anions via ion-dipole interactions, may have more chances to compete with solvent molecules in aprotic organic media. On the other hand, charged host molecules can bind highly solvated or even hydrated anions also in protic solvents. Dehydration of anions is an energy consuming process, whereas interaction between the anion and the binding site is an energetically favorable process. The stronger the interaction is, the more gain in free energy will result from the binding event. Naturally occurring anion receptors are precisely optimized to work in special environments and show a high degree of selectivity for the targeted anion. In the following, some examples of supramolecular hosts will be presented that are able to bind small anionic guests such as F^-, Cl^-, Br^-, BF_4^-, SO_4^-, NO_3^- anions.

Schmidtchen and co-workers reported an interesting example for a cationic cage-like host.[85] The macrotricyclic quaternary ammonium receptor possesses a cavity with an internal diameter of 4.6 Å and thus can encapsulate various anionic guest molecules in water, in particular halide anions. The first generation of these hosts showed lower binding affinities due to competing counterions for the anion-binding site. This problem was overcome by introduction of additional anionic groups. Indeed the neutral zwitterionic receptor **23** showed stronger binding affinities towards chloride, bromide and iodide ions (Figure IV.1a).[86] More effective receptors for anions are found when a combination of

---

J. Rodriguez Douton, F. Ugozzoli, *Angew. Chem. Int. Ed.* **2006**, *45*, 6920. (d) L. C. Gilday, N. G. White, P. D. Beer, *Dalton Trans.* **2013**, *42*, 15766. (e) H. T. Chifotides, K. R. Dunbar, *Acc. Chem. Res.* **2013**, *46*, 894. (f) L. Adriaenssens, G. Gil-Ramírez, A. Frontera, D. Quiñonero, E. C. Escudero-Adán, P. Ballester, *J. Am. Chem. Soc.* **2014**, *136*, 3208.

[85] (a) F. P. Schmidtchen, *Angew. Chem. Int. Ed.* **1977**, *16*, 720. (b) F. P. Schmidtchen, *Chem. Ber.* **1981**, *114*, 597.

[86] K. Worm, F. P. Schmidtchen, *Angew. Chem. Int. Ed.* **1995**, *34*, 65.

electrostatic interactions together with hydrogen bonds supports the binding process. Figure IV.1b shows one of the first examples for an anion-cage complex namely the macrobicyclic ammonium cage **24** which encapsulates halide anions via usage of both types of bonds.[87] In the past, many other hosts, in particular metal-organic cages, have been developed for anion uptake, sensing, transport and applications in catalysis.[88]

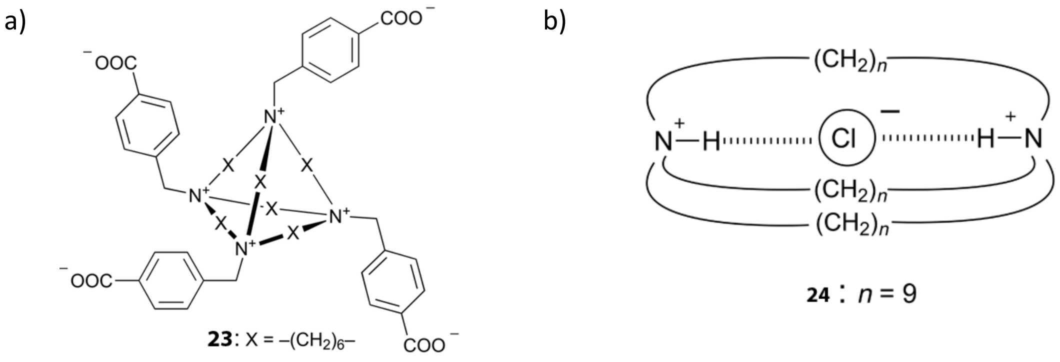

Figure IV.1 a) Zwitterionic host molecule **23** capable of complexing halide anions.[86] b) Complexation of one chloride anion inside the macrobicyclic ammonium cage **24**.[87]

However, anions do not only act as guest molecules or counter anions, but they can also serve as templating anions,[89] which conduct the self-assembly to the targeted structure. Lehn and co-workers could impressively show that the pentametallic circular helicate **25** can be only formed in the presence of chloride anions. The binding of the chloride anion is very strong and thus it cannot be replaced by other anions such as hexafluorophosphate or trifluoroacetate. Utilization of iron(II) salts with other counteranions such as

---

[87] C. H. Park, H. E. Simmons, *J. Am. Chem. Soc.* **1968**, *90*, 2431.

[88] for some selected examples, see (a) G. H. Clever, S. Tashiro, M. Shionoya, *J. Am. Chem. Soc.* **2010**, *132*, 9973. (b) G. H. Clever, M. Shionoya, *Chem. Eur. J.* **2010**, *16*, 11792. (c) G. H. Clever, W. Kawamura, M. Shionoya, *Inorg. Chem.* **2011**, *50*, 4689. (d) R. Sekiya, R. Kuroda, *Chem. Commun*. **2011**, *47*, 12346. (e) J. Zhang, Y. Li, W. Yang, S.-W. Lai, C. Zhou, H. Liu, C.-M. Che, Y. Li, *Chem. Commun.*, **2012**, *48*, 3602. (f) W. J. Ramsay, T. K. Ronson, J. K. Clegg, and J. R. Nitschke, *Angew. Chem. Int. Ed.* **2013**, *52*, 13439. (g) C. García-Simón, M. Garcia-Borràs, L. Gómez, I. Garcia-Bosch, S. Osuna, M. Swart, J. M. Luis, C. Rovira, M. Almeida, I. Imaz, D. Maspoch, M. Costas, X. Ribas, *Chem. Eur. J.* **2013**, *19*, 1445. (h) N. Hafezi, J. M. Holcroft, K. J. Hartlieb, E. J. Dale, N. A. Vermeulen, C. L. Stern, A. A. Sarjeant, J. F. Stoddart, *Angew. Chem. Int Ed.* **2015**, *127*, 466. (i) I. A. Riddell, T. K. Ronson, J. R. Nitschke, *Chem. Sci*. **2015**, 6, 3533. (j) W. Cullen, K. A. Thomas, C. A. Hunter, M. D. Ward, *Chem. Sci*., **2015**, *6* , 4025. (k) P. D. Frischmann, V. Kunz, F. Würthner, *Angew. Chem .Int. Ed* **2015**, *127*, 7393.

[89] (a) M. D. Lankshear, P. D. Beer, *Coord. Chem. Rev.* **2006**, *250,* 3142. (b) N. Gimeno, R. Vilar, *Coord. Chem. Rev.* **2006**, *250*, 3161. (c) Q. Chen, F. Jiang, D. Yuan, L. Chen, G. Lue, M. Hong, *Chem. Commun.* **2013**,*49*, 719.

tetrafluoroborate or sulfate afforded a hexameric helicate **26** (see Figure IV.2).[90]

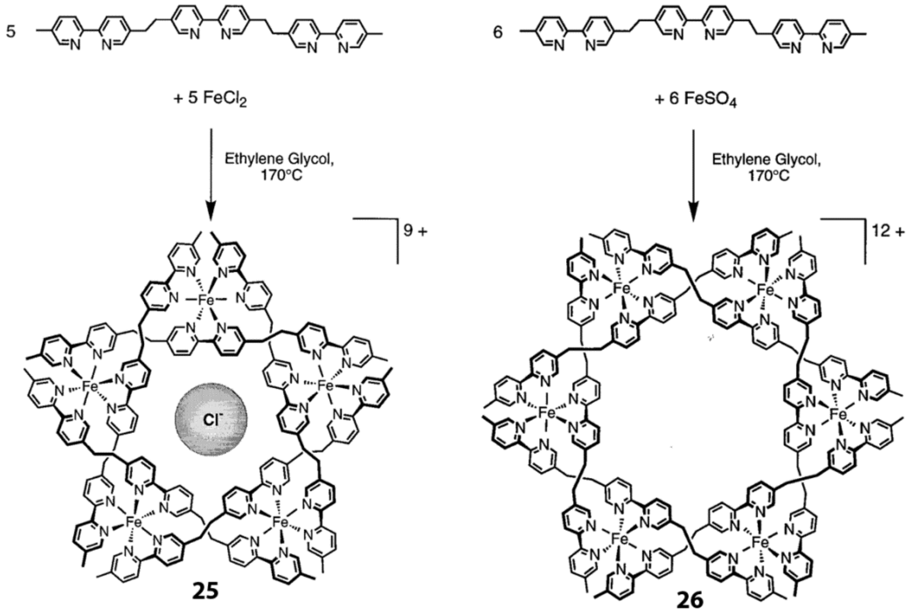

Figure IV.2 Synthesis of helicates **25** and **26**. Helicate **25** is only formed in presence of chloride ions. Reproduced with permission from reference [90b]. Copyright © 1997 American Chemical Society.

Figure IV.3 shows examples of anion-templated coordination cages. Cage **27** is assembled from the reaction of six $NiCl_2$ with eight amidinothiourea units in methanol (see Figure IV.3a). The amidinothiourea is coordinating via both nitrogens and sulfur donor atoms to the metal ions. The chloride is located inside the cage and it stabilizes the overall structure by eight $NH\cdots Cl$ hydrogen bonds. Instead of chloride, also bromide anions can be used for templation reaction. Syntheses with other nickel salts such as acetate, nitrate or perchlorate lead only to simple monomeric complexes. Addition of chloride anions to the solution of simple monomers initiate a spontaneous reorganization resulting in the formation of cage **27**.[91] Ward and co-workers reported about the formation of a BF_4^- templated tetrahedral cage **28** assembled from six di(pyrazolylpyridine) ligands and four Co(II) ions (see Figure IV.3b).[92] Interestingly, the fluorine atoms of the BF_4^- anion are oriented towards the center

---

[90] (a) B. Hasenknopf, J.-M. Lehn, B. O. Kneisel, G. Baum, D. Fenske, *Angew. Chem. Int. Ed.* **1996**, *35*, 1838. (b) B. Hasenknopf, J.-M. Lehn, N. Boumediene, A. Dupont-Gervais, A. Van Dorsselaer, B. Kneisel, D. Fenske, *J. Am. Chem. Soc.* **1997**, *119*, 10956.

[91] R. Vilar, D. M. P. Mingos, A. J. P. White, D. J. Williams, *Angew. Chem. Int. Ed*. **1998**, *37*, 1258.

[92] J. S. Flemming, K. L. V. Mann, C.-A. Carraz, E. Psillakis, J. C. Jeffery, J. A. McCleverty, M. D. Ward, *Angew. Chem. Int. Ed.* **1998**, *37*, 1279.

of the triangular faces of the tetrahedron. From electrostatic point of view the direction towards cobalt centers at the corners of the tetrahedron would be the optimal orientation, but the BF_4^- prefers an orientation that best adapts to the inner shape of the pocket. Besides, the structure is stabilized via multiple hydrogen bonds of BF_4^- to the methylene protons of the bridging ligands. Hay and co-workers rationally developed by computer-aided design a similar cage **29** that is templated by a sulfate ion (see Figure IV.3c). The ligands contain urea backbones, which can bind as a bidentate hydrogen donor to the oxygen atoms of the sulfate anion. The latter is strongly bound inside the cavity by electrostatic interaction to four Ni(II) metal ions and by overall 12 hydrogen bonds to urea units with an experimentally determined binding constant of $K \approx 6 \cdot 10^6\ \mathrm{M}^{-1}$.[93]

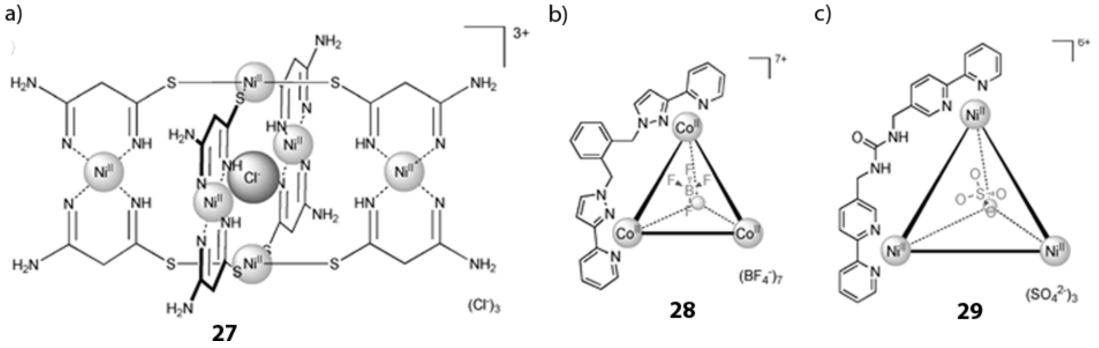

Figure IV.3 a) Halide-templated cage **27**.[91] b) BF_4^- templated tetrahedral cage **28**.[92] c) SO_4^{2-} templated tetrahedral cage **29**.[93] Reproduced with permission from reference [79d]. Copyright © 2014 WILEY-VCH Verlag GmbH & Co.

Particular attraction received the field of control over temporal and spatial rearrangements of metal-organic assemblies triggered by external stimuli such as a chemical species, solvent, pH or light.[94] Guest molecules can also be used as chemical or physical stimuli for reorganization of supramolecular hosts. A structural change occurs when the guest binding templates a new structure and the energetic barrier for the interconversion process between the structures is not too high to be overcome. Nevertheless, examples for guest-induced transformations of metal-organic cages are still

---

[93] R. Custelcean, J. Bosano, P. V. Bonnesen, V. Kertesz, B. P. Hay, *Angew. Chem. Int. Ed*. **2009**, *48*, 4025.

[94] A. J. McConnell, C. S. Wood, P. P. Neelakandan, J. R. Nitschke, *Chem. Rev.* **2015**, *115*, 7729.

rare.[95] For example, Nitschke and co-workers synthesized a tetrahedral cage **30** via the reaction of *p*-toluidine with 6,6’-diformyl-3,3’-bipyridine in presence of $Co(OTf)_2$ (see Figure IV.4). Addition of $LiClO_4$ to the solution of the tetrahedral cage initiated a structural reorganization process which finished in the formation of a barrel-like pentagonal prism **31**. The latter structure is capable of binding a chloride anion within the inner void with a binding affinity of $K > 6\cdot10^5$ M^{-1}.[96]

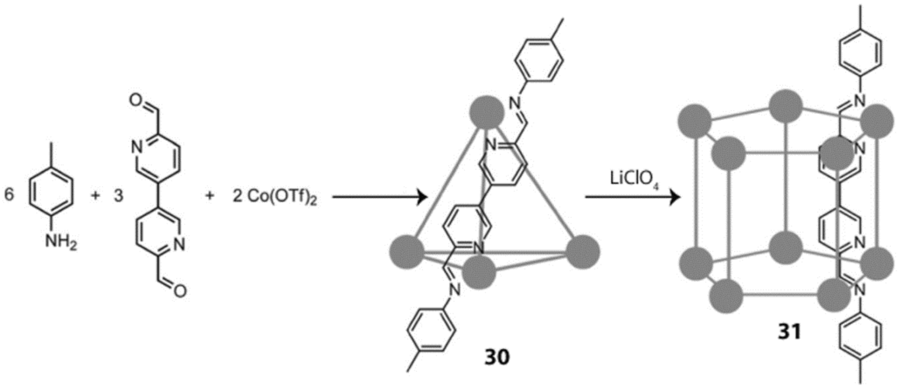

Figure IV.4 Synthesis of the tetrahedral cage **30** and anion responsive reorganization to the pentagonal prism **31**. Filled circles represent the metal nodes.[96] Reproduced with permission from reference [79d]. Copyright © 2014 WILEY-VCH Verlag GmbH & Co.

Kuroda and co-workers could show that the dimerization of the double-cage $[Pd_4\mathbf{20}_8]^{8+}$ (see introduction Chapter III) is driven by anion template and that it is possible to reverse the process back to the monomeric cage by addition an anionic trigger (see Figure IV.5).[26,97] The quadruply interlocked double-cage is built upon a spontaneous dimerization of monomers in presence of NO_3^- anion which serves as templating molecule. Partial dimerization was observed for BF_4^- anion, but no dimers were obtained for PF_6^- or OTf^- anions. This demonstrates that the dimerization is driven by the anion templating effect and the interactions between the ligands are not strong enough to stabilize the interlocked

---

[95] (a) M. Scherer, D. L. Caulder, D. W. Johnson, K. N. Raymond, *Angew. Chem., Int. Ed.* **1999**, *38*, 1587. (b) N. Fujita, K. Biradha, M. Fujita, S. Sakamoto, K. Yamaguchi, *Angew. Chem. Int. Ed*. **2001**, *40*, 1718. (c) J. K. Clegg, J. Cremers, A. J. Hogben, B. Breiner, M. M. J. Smulders, J. D. Thoburn, J. R. Nitschke, *Chem. Sci.* **2013**, *4*, 68. (d) W. Meng, T. K. Ronson, J. K. Clegg, J. R. Nitschke, *Angew. Chem. Int. Ed*. **2013**, *52*, 1017. (e) I. A. Riddell, T. K. Ronson, J. K. Clegg, C. S. Wood, R. A. Bilbeisi, J. R. Nitschke, *J. Am. Chem. Soc*. **2014**, *136*, 9491.

[96] I. A. Riddell, M. M. J. Smulders, J. K. Clegg, Y. R. Hristova, B. Breiner, J. D. Thoburn, J. R. Nitschke, *Nat. Chem.* **2012**, *4*, 751.

[97] R. Sekiya, M. Fukuda, R. Kuroda, *J. Am. Chem. Soc.* **2012**, *134*, 10987.

architecture. Competition experiments between the anions NO_3^-, BF_4^-, PF_6^- and OTf^- showed that the double-cage forms exclusively the $[3NO_3@Pd_4\mathbf{20}_8]^{5+}$ complex, which is the thermodynamically most stable complex and no further anion exchange was observed. Thus, the binding ability of the double-cage $[Pd_4\mathbf{20}_8]^{5+}$ is dependent on the size of the anion and can be classified as strong for NO_3^-, weak for BF_4^- and very weak for PF_6^- and OTf^-. The same binding affinity order was found for the encapsulation within the monomeric cage $[Pd_2\mathbf{20}_4]^{5+}$ with the difference that here two equivalents of anions are bound per cage. Thereby, the second anion is bound upon negative allosteric effect, which is due to electrostatic repulsion between the two anions within the cavity. This indicates the existence of a relationship in the binding affinities between the double-cage and its monomeric counterpart. In both cages the anions are stabilized by electrostatic interaction between the metals and the anion. Also hydrogen bonding between α-pyridyl hydrogen atoms and the anion supports the anion binding. For the monomeric cage one electrostatic contact and four hydrogen bonds were identified, whereas in the double-cage the anion is sandwiched between two $[Pd(py)_4]^{2+}$ planes and thus two Pd-anion and eight hydrogen interactions can be located. A bulky anionic guest such as 2-naphtalenesulfonat (ONs^-) that is not able to fit completely inside the cavities of the double-cage should be able to shift the equilibrium towards the monomeric cage. Indeed, addition of excess of ONs^- anion resulted in displacement of NO_3^- anions inside the cavities and the double-cage was transformed to the monomeric cage. The monomerization process proceeds via an intermediate species namely a double-cage with sulfonate head groups of the ONs^- anions pointing inside the outer pockets. An equilibrium state was reached after 125 h with a product distribution of double-cage $[3NO_3@Pd_4\mathbf{20}_8]^{5+}$, the intermediate species $[2ONs+NO_3@Pd_4\mathbf{20}_8]^{5+}$ and the monomeric cage $[2ONs@Pd_2\mathbf{20}_4]^{2+}$ of 41 %, 42 % and 17 %. In order to separate the dimeric from the monomeric structure, the authors applied OTs^- instead of ONs^- anions, which are known to give a precipitate of monomeric cage $[2OTs@Pd_2\mathbf{20}_4](OTs)_2$ in DMSO solution.[26,88d] Indeed treatment of the double-cage solution with OTs^- yielded 68 % of the monomeric product as precipitate and the residue 32 % of $[3NO_3@Pd_4\mathbf{20}_8]^{5+}$ remained in solution.

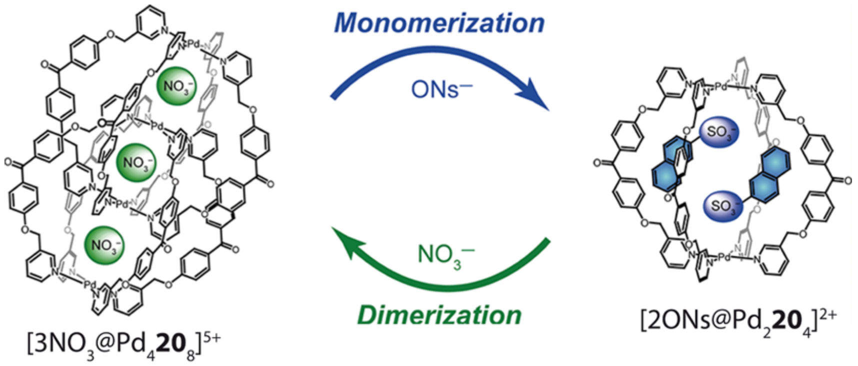

Figure IV.5 Anion-triggered monomerization and dimerization process. Reproduced with permission from reference [97]. Copyright © 2012 American Chemical Society.

The dibenzosuberone-based double-cage $[3BF_4@Pd_4\mathbf{22}_8]^{5+}$ can also undergo structural rearrangement upon anion binding (see Figure IV.6).[16,98] The double-cage $[3BF_4@Pd_4\mathbf{22}_8]^{5+}$ posses three cavities which are initially occupied by one BF_4^- anion introduced via utilization of the metal source $[Pd(CH_3CN)_4(BF_4)_2]$ for the synthesis. Further anions are found in the X-ray structure at each side of the Pd_4 axis and as disordered molecules in the solvents-filled channels between the double-cages. ^{19}F spectroscopic analysis of the double-cage sample at room temperature showed two signals in a ratio of 1:7. One signal detected at δ = -143.6 ppm was assigned to one BF_4^- sitting in the central pocket and the second signal at δ = -151.4 ppm corresponds to remaining BF_4^-. The absence of a separate signal for the two BF_4^- anions in the outer pockets as well as EXSY and low temperature ^{19}F NMR experiments indicated that these anions are loosely bound within the pockets at room temperature and thus, they can easily exchange with the non-encapsulated BF_4^- anions. Exchange of encapsulated BF_4^- with the BF_4^- found in surrounding media is not only dependent on the choice of the temperature, but also of the solvent. The exchange is slowed down in less polar acetone due to more effective stabilization of the charged BF_4^- molecules within the charged cavity. On the other hand, the strongly polar acetonitrile supports a fast exchange of the BF_4^- anions (see Figure IV.6 a)). The lability in the binding of the BF_4^- anions in the two outer pockets allows to exchange them for stronger binding anions such as halide anions.[98] Addition of one equivalent of NBu_4Cl to the double-cage solution yielded a new species, which was found to coexist with the original double-cage $[3BF_4@Pd_4\mathbf{22}_8]^{5+}$ in a ratio

---

[98] S. Freye, D. M. Engelhard, M. John, G. H. Clever, *Chem. Eur. J.* **2013**, *19*, 2114–2121.

of 1:1. Addition of further one equivalent of halide anion resulted in complete conversion to the new highly symmetric species as indicated by ^{1}H NMR spectroscopic analysis. The protons pointing inside the two outer cavities were highly downfield-shifted after encapsulation of the small chloride anions. This new species was identified as $[2Cl+BF_4@Pd_4\mathbf{22}_8]^{5+}$ with each of the outer pockets filled with one chloride anion. No intermediate species containing only one chloride was found in the solution, which indicated a positive allosteric binding mechanism. The binding of the first chloride in one of the outer pockets leads to a reorganization of the double-cage structure along the Pd_4 axis, thereby preorganizing the second outer pocket for binding of the second chloride with enhanced affinity. The binding affinity for chloride anions is so high that it is possible even to dissolve the highly insoluble AgCl in acetonitrile within a time period of 30 min (see Figure IV.6 b)). The binding constant for chloride anions could be estimated by backtitration experiments with $AgBF_4$ to a value of $1{\cdot}10^{20}$ M^{-2}.[98] Furthermore it was shown that this double-cage is capable of binding other halide anions in the same allosteric manner. The binding affinities have been estimated to decrease in the order of chloride > bromide > fluoride. In contrast to chloride, the bound bromide was released by addition of only two equivalents of silver salt, which again supported the exceptional strong binding of chloride. Iodide anions induced a decomposition of the double-cage, presumably due to the preferred binding to the metal nodes. Also addition of more than two equivalents of halide anions leads to partial or complete decomposition of the double-cage and release of free ligand, presumably due to coordination of anions to Pd(II) centers. Addition of PF_6^- anions showed no effect because they are too large to fit into the pockets and do not show a binding affinity to metal nodes. The substitution of BF_4^- for smaller halide anions results in a compression of the double-cages along the Pd_4-axis (see Figure IV.6 c)). This shrinking of the double-cage upon chloride binding was confirmed by diffusion-ordered spectroscopy (DOSY) as well as molecular modeling calculations.[98]

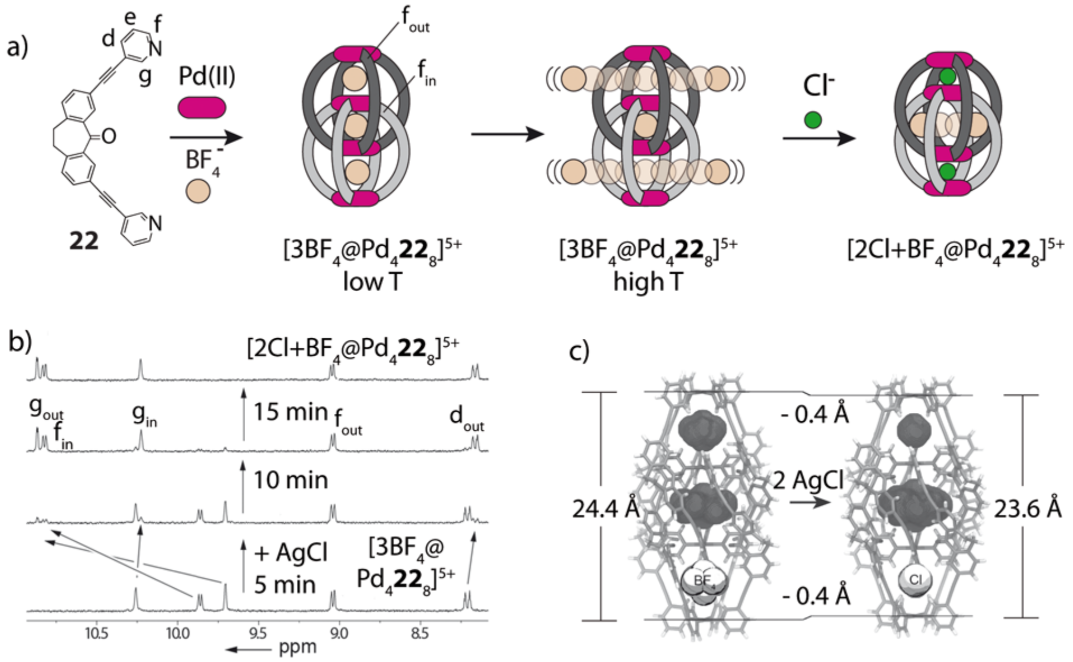

Figure IV.6 a) Reaction scheme of the dibenzosuberone-based ligand **22** with $[Pd(CH_3CN)_4](BF_4)_2$ salt leading to the quadruply interpenetrated double-cage $[3BF_4@Pd_4\mathbf{22}_8]^{5+}$. The BF_4^- anions in the two outer pockets can be replaced by the stronger binding chloride to give $[2Cl+BF_4@Pd_4\mathbf{22}_8]^{5+}$. b) ^1H NMR spectra of the addition of AgCl to the solution of the double-cage $[3BF_4@Pd_4\mathbf{22}_8]^{5+}$ in MeCN-*d*$_3$ (300 MHz, 298 K). c) Comparison of models for $[3BF_4@Pd_4\mathbf{22}_8]^{5+}$ and $[2Cl+BF_4@Pd_4\mathbf{22}_8]^{5+}$. Reproduced with permission from reference [98]. Copyright © 2013 WILEY-VCH Verlag GmbH & Co.

In order to gain control over the dimerization process, a derivative of the dibenzosuberone-based ligand containing a bulky aryl substituent at the backbone was developed (see ligand **32** in Figure IV.7).[17] The assembly of the ligand with $[Pd(CH_3CN)_4](BF_4)_2$ in acetonitrile yielded a monomeric coordination cage $[Pd_2\mathbf{32}_4]^{4+}$. First, no tendencies to dimerize were observed for this monomeric species. This is in contrast to the observations for the dibenzosuberone-based monomeric cage $[Pd_2\mathbf{22}_4]^{4+}$, which is just a kinetic intermediate and tends to quantitatively dimerize at room temperature under the same reaction conditions (see Figure IV.7 reaction scheme at the top). The absence of dimerization tendencies for $[Pd_2\mathbf{32}_4]^{4+}$ can be explained by the steric demand of the attached bulky substituents which would make the two outer voids too crowded for encapsulation of a BF_4^- anion. Interestingly, addition of chloride anions to monomeric cage $[Pd_2\mathbf{32}_4]^{4+}$ and heating the mixture triggered a gradual transformation into a double-cage. Surprisingly, this double-cage was found to contain one chloride molecule inside the central pocket as could be confirmed by a pronounced downfield shift of protons pointing inside the central cavity and two BF_4^- anions inside the outer pockets. The crystal structure of $[2BF_4+Cl@Pd_4\mathbf{32}_8]^{4+}$ revealed a decrease of the distance between the inner Pd centers upon substitution of the BF_4^- by a Cl^- from 8.25 Å to 6.26 Å. On the other hand, the Pd-Pd distance of the two outer pockets increases from 8.09 to 8.79 Å (see Figure IV.7 lower reaction scheme). This increase in the volume of the outer pockets allows for the BF_4^- anions to be encapsulated despite the bulky substituents of the ligands. Even larger anions such as perchlorate, hexafluorophosphate or perrhenate were shown to be encapsulated inside the outer pockets. The encapsulation of larger guests was found to proceed in positive cooperative manner as well, but with much lower affinity as compared to chloride.[17]

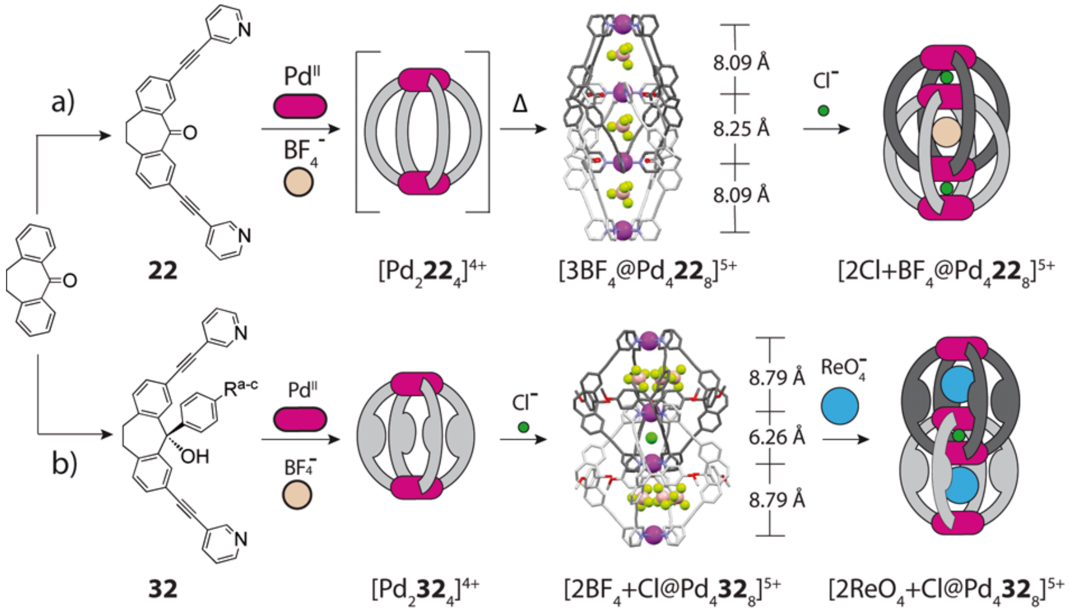

Figure IV.7 a) Reaction scheme of the dibenzosuberone-based ligand **22** with $[Pd(CH_3CN)_4](BF_4)_2$ salt leading initially to the monomeric cage $[Pd_2\mathbf{22}_4]^{4+}$ and further conversion to the quadruply interpenetrated double-cage $[3BF_4@Pd_4\mathbf{22}_8]^{5+}$ (CCDC 844925) upon heating. Formation of $[2Cl+BF_4@Pd_4\mathbf{22}_8]^{5+}$ after addition of chloride. b) Reaction scheme of the dibenzosuberone-based ligand **32** with $[Pd(CH_3CN)_4](BF_4)_2$ salt to the monomeric cage $[Pd_2\mathbf{32}_4]^{4+}$. Conversion to the quadruply interpenetrated double-cage $[2BF_4+Cl@Pd_4\mathbf{32}_8]^{5+}$ (CCDC 954621) upon addition of chloride and uptake of ReO_4^- guest molecules. Reproduced with permission from reference [17]. Copyright © 2013 American Chemical Society.

A further example for a halide-triggered compression of a double-cage structure was reported by Clever and co-workers in 2015.[18] In contrast to the aforementioned example, where the encapsulation of the central template controls the uptake of guests in the outer pockets, here the binding of two halides inside the outer pockets allows for subsequent binding of neutral guests inside the central pocket (see Figure IV.8). The double-cage $[3BF_4@Pd_4\mathbf{33}_8]^{5+}$ was designed using a banana-shaped ligand **33** with an acridone backbone accommodating two ethynylpyridine arms and the $[Pd(CH_3CN)_4](BF_4)_2$ salt. Addition of a halide salt (X^- either Cl^- or Br^-) yielded the double-cage $[2X+BF_4@Pd_4\mathbf{33}_8]^{5+}$ with one halide anion in each of the outer pockets. ^{19}F spectroscopic analysis of $[3BF_4@Pd_4\mathbf{33}_8]^{5+}$ showed three signals: one for free BF_4^- (δ = -151.70 ppm), one for encapsulated BF_4^- inside the inner pocket (δ = -143.32 ppm) and one signal for the two BF_4^- in the outer pockets (δ = -144.85 ppm). The bromide containing species $[2Br+BF_4@Pd_4\mathbf{33}_8]^{5+}$ showed two ^{19}F NMR signals, one for the free BF_4^- and one for the tightly bound BF_4^- in the central pocket (δ = -152.23 ppm). A totally different situation was found for the chloride containing species, which showed only one ^{19}F NMR signal corresponding to the free BF_4^- in solution, which indicated a loose binding of the central BF_4^- in this case. Indeed the crystal structure of the chloride containing species showed that the central BF_4^- anion was replaced by one benzene guest, whereas crystallization of the BF_4^--templated species did not show any exchange of anions under the same crystallization conditions. As a consequence of halide accommodation, the Pd-Pd distance of the outer pockets is reduced from an average of 8.25 Å to 6.61 Å, whereas the distance for central pocket is increased from 8.44 Å to 10.48 Å and thus the central pocket is preorganized for uptake of the relatively large neutral benzene molecule. The binding of neutral guest is probably favored by dispersion interactions as well as the solvophobic effect. The uptake of neutral guest is also possible in solution phase when an excess amount of neutral molecule is offered to the halide-activated double-cage. Cyclohexane, toluene and norbornadiene were found to go inside the central cavity. The kinetics and thermodynamics for uptake of neutral guests depend on their size and dispersion interactions within the central cavity. The uptake of cyclohexane is kinetically hindered in comparison to a benzene molecule, but thermodynamically favored due higher dispersion forces. Also a difference in uptake of neutral guests between the chloride- and bromide-activated double-cages was observed. The chloride-activated double-cage offers a bigger central cavity and thus the incorporation of neutral molecules is kinetically as well as thermodynamically favored. Titration of the bromide-activated double-cage $[2Br+BF_4@Pd_4\mathbf{33}_8]^{5+}$ with Ag^+ salt results in recovering of the BF_4^--templated double-cage, whereas no extraction of chloride was achieved starting from the chloride-activated double-cage indicating a strong binding of chloride. Treating the bromide-activated cage with a solution of neutral guest results in a very tight binding of bromides, which were not any more accessible for immediate extraction with Ag^+.

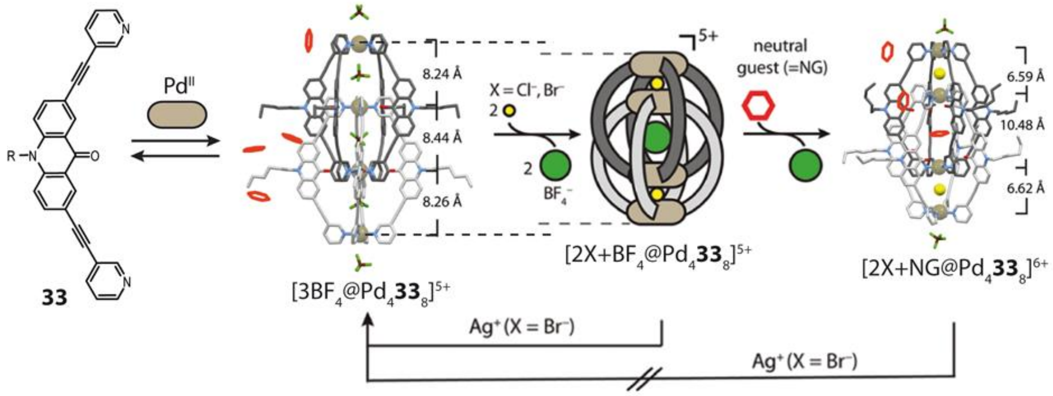

Figure IV.8 Synthesis of double-cage $[3BF_4@Pd_4\mathbf{33}_8]^{5+}$ (CCDC 1035264) starting from the acridone-based ligand **33**. Exchange of the BF_4^- guests in the outer two pockets for halide anions results in the formation of $[2X+BF_4@Pd_4\mathbf{33}_8]^{5+}$ species. Subsequent uptake of neutral guest molecule (NG) into the inner cavity yields the double-cages $[2X+NG@Pd_4\mathbf{33}_8]^{6+}$ (X-ray structure shown for chloride-activated double-cage $[2Cl+Benzene@Pd_4\mathbf{33}_8]^{6+}$; CCDC 1035009). Reproduced with permission from reference [18]. Copyright © 2015 American Chemical Society.

A further example for a stepwise halide-triggered reorganization of double-cages is shown in Figure IV.9a.[19] According to previous results on double-cage structures, a slightly shorter bispyridyl ligand **34** based on a carbazole backbone was calculated to give a monomeric cage $[Pd_2\mathbf{34}_4]^{4+}$ in presence of BF_4^-. The relatively large BF_4^- anions would not fit inside the smaller cavities of the imaginable double-cage $[3BF_4@Pd_4\mathbf{34}_8]^{5+}$ constructed from the carbazole ligand. Indeed, reaction of a 2:1 mixture with $[Pd(CH_3CN)_4](BF_4)_2$ salt yielded a monomeric cage with a relatively short Pd-Pd distance of 14.31 Å (see Figure IV.9b). No dimerization tendencies under applied reaction conditions have been observed so far. Addition of 1.5 equivalents of halide anions to the solution of monomeric cage and heating the solution for several hours gave rise to the formation of an interpenetrated double-cage containing three halide anions inside the pockets. A DFT calculated model (ωB97XD/def2-SVP) of the double-cage $[3X@Pd_4\mathbf{34}_8]^{5+}$ confirmed the experimental results showing much shorter distances for Pd_{outer}-Pd_{outer} of 6.58 Å and Pd_{inner}-Pd_{inner} 7.02 Å compared to the previous examples[15,16] (see Figure IV.9c). Nevertheless, the assembly into the double-cage was found to be incomplete. The double-cage $[3X@Pd_4\mathbf{34}_8]^{5+}$ exists in equilibrium with the monomeric cage $[Pd_2\mathbf{34}_4]^{4+}$ and the free ligand **34** in a ration of 5:3:10 for bromide and 5:5:2 for chloride. Crystallographic analysis of the equilibrium mixture yielded a further product of anion-triggered rearrangement namely the triply catenated compound {*trans*-$[(PdBr_2)_2\mathbf{34}_2]\}_3$. The halide coordinated Pd(II) nodes in this triply catenated link do not possess any net charge. The absence of any counter anions for the triply catenated structure leads to a much closer distance between the Pd atoms with an average of 4.36 Å (see Figure IV.9d) compared to Pd_{out}-Pd_{out} = 6.73 Å found for the chloride-templated double-cage $[3Cl+BF_4@Pd_4\mathbf{22}_8]^{5+}$.[17] The six Pd atoms within this link are aligned on one axis with bromide ligands arranged in a helical fashion around the metal nodes. This arrangement is favoured by the stabilizing π-π-interactions of the carbazole ligand backbone.[19]

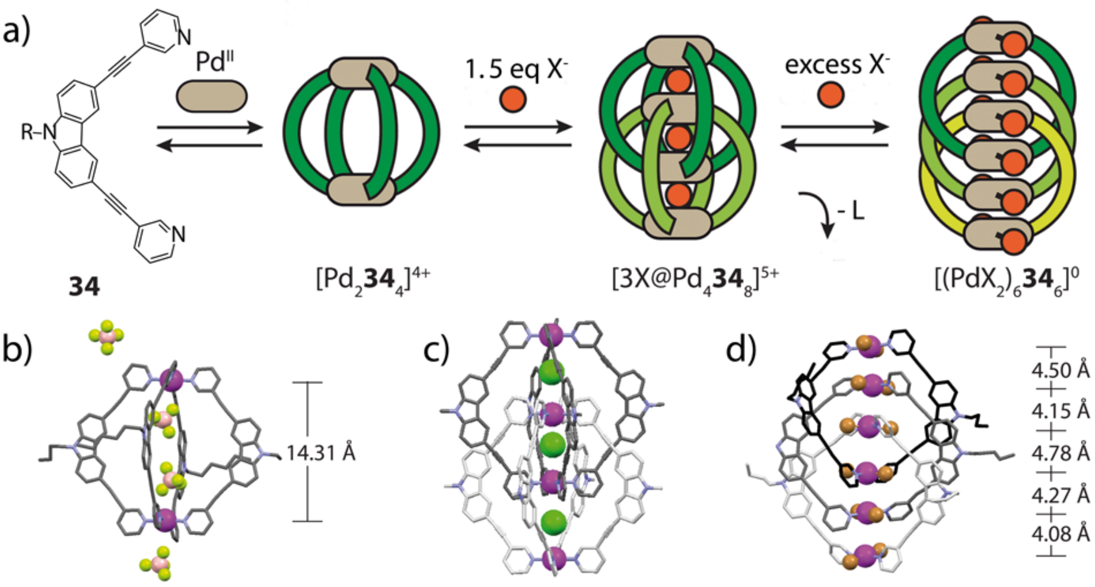

Figure IV.9 a) Synthesis of the monomeric cage $[Pd_2\mathbf{34}_4]^{4+}$ starting from a carbazole-based ligand **34** and Pd(II) ions, followed by the formation of the double-cage $[3X@Pd_4\mathbf{34}_8]^{5+}$ induced by addition of 1.5 equivalents of halide anion and finally conversion into the neutral triple-catenane $[(PdX_2)_6\mathbf{34}_6]^0$ after addition of excess of halide anions. X-ray structures of b) monomeric cage $[Pd_2\mathbf{34}_4]^{4+}$ (CCDC 1011498) and d) triple-catenane $[(PdX_2)_6\mathbf{34}_6]^0$ (1011499). c) DFT calculated structure for the double-cage $[3X@Pd_4\mathbf{34}_8]^{5+}$. Reproduced with permission from reference [19]. Copyright © 2015 WILEY-VCH Verlag GmbH & Co.

IV.2 Project Target

This section will focus on anion binding abilities towards halide anions (Cl^{-} and Br^{-}) of the three in Chapter III introduced phenothiazine-based double-cages. The binding affinities to a particular halide anion will be compared via competition experiments between different double-cages. Also the previously reported dibenzosuberone-based double-cage,[16] which was found to encapsulate halide anions with a very high binding constant, will be used for competition studies. Additionally, competition studies between halide anions for binding within a particular double-cage will be performed. Furthermore, the effect of halide binding on structural rearrangement of the double-cages along the Pd_4-axis will be discussed with the aid of results from ^{1}H NMR titrations, NOESY experiments and model calculations.

IV.3 Results and Discussion[99]

Like the previously reported dibenzosuberone double-cage[16] $[3BF_4@Pd_4\mathbf{L}^5{}_8](BF_4)_5$ (ligand **22** will be denoted as $\mathbf{L}^5$ within this Chapter), all three phenothiazine based double-cages $[3BF_4@Pd_4\mathbf{L}^{2\text{-}4}{}_8](BF_4)_5$ possess small inner voids, which are capable of binding small anionic molecules. Initially all of the three pockets are filled with one BF_4^{-} anion. The two BF_4^{-} anions in the outer two pockets are loosely bound and thus can be replaced by stronger binding halide anions such as Cl^{-} or Br^{-} resulting in the formation of the host-guest complexes $[2X+BF_4@Pd_4\mathbf{L}^n{}_8]^{5+}$ with X = Cl^{-} or Br^{-} and n = 2-5 (see Figure IV.10). The BF_4^{-} anion sitting inside the central pocket is tightly bound and thus cannot be exchanged under selected conditions (acetonitrile, room temperature). As could be previously shown for the $[3BF_4@Pd_4\mathbf{L}^5{}_8](BF_4)_5$ double-cage,[16] the halide binding is accompanied with a shrinkage of the double-cages along the Pd_4-axis due to the smaller size of the chloride anion.

---

[99] M. Frank, J. M. Dieterich, S. Freye, R. A. Mata and G. H. Clever, *Dalton. Trans.* **2013**, *42*, 15906.

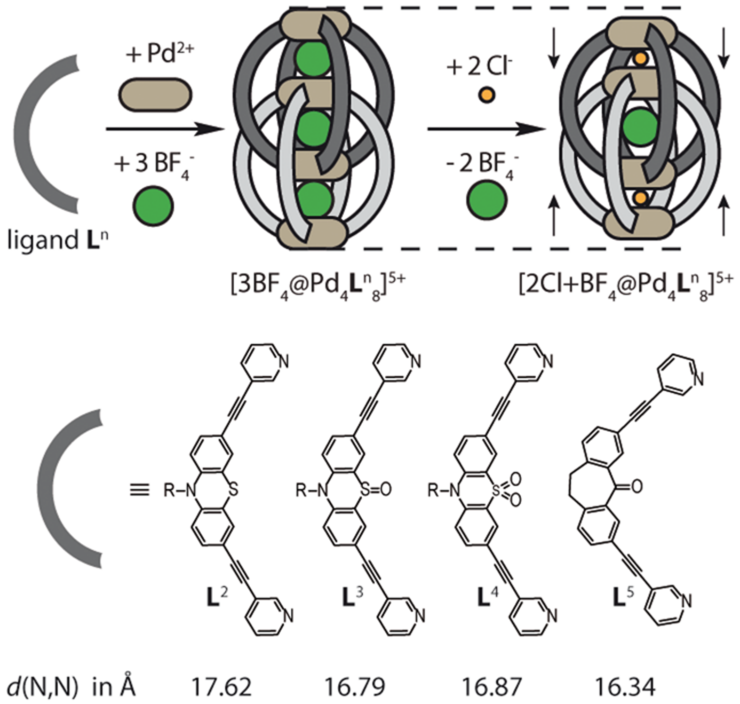

Figure IV.10 Synthesis of double-cages $[3BF_4@Pd_4\mathbf{L}^n{}_8]^{5+}$ with n = 2-5 starting from the corresponding ligand $\mathbf{L}^n$. Exchange of the BF_4^- anions in the outer pockets for halide anions induces a decrease of the Pd-Pd distance along the Pd_4-axis. The compression is dependent on the size of the host as well as of the guest. Structures of ligands $\mathbf{L}^2$-$\mathbf{L}^5$ and the characteristic *N-N* distances in Å (extracted from the X-ray structures of the BF_4^-) templated double-cages are shown below. Reproduced with permission from reference [99]. Copyright © 2013 Royal Society of Chemistry.

Figure IV.11 shows an example for a titration with chloride using NBu_4Cl as halide source. After addition of one equivalent of the halide salt to the double-cage $[3BF_4@Pd_4\mathbf{L}^2{}_8]^{5+}$ solution, the half of the original double-cage was converted to the new species, which was identified as $[2Cl+BF_4@Pd_4\mathbf{L}^2{}_8]^{5+}$ by ESI mass spectrometry (see Appendix IV Section 2a). The signals pointing inside the outer cavities exhibit a very strong downfield shielding ($\Delta\delta$ [ppm] = 1.14 for H_g, 1.44 for $H_{f'}$ and 0.73 for $H_{a'}$) due to the closer proximity to the negatively charged anions. On the other hand, the proton H_a show a very strong upfield shift of 1.54 ppm due to the closer proximity of the aromatic rings of neighboring ligands. As could be observed for the dibenzosuberone-based double-cage,[16] also in this case the ratio after adding one equivalent of chloride is 1:1 for both double-cage species $[3BF_4@Pd_4\mathbf{L}^2{}_8]^{5+}$ and $[2Cl+BF_4@Pd_4\mathbf{L}^2{}_8]^{5+}$. Addition of the second equivalent chloride results in a full conversion of the starting material $[3BF_4@Pd_4\mathbf{L}^2{}_8]^{5+}$ to the chloride-containing double-cage $[2Cl+BF_4@Pd_4\mathbf{L}^2{}_8]^{5+}$. Further addition of chloride affords a gradual downfield shifting of the proton H_f, which is oriented outwards into the bulk solution. This shifting can be explained by the coordination of the extra chloride to the outer site of the external Pd atoms, which results in a gradual degradation of the double-cage structure and consequently the release of free ligands. After addition of eight equivalents of chloride per double-cage the signals of the assembly almost disappeared and signals of free ligand are dominating the spectrum.

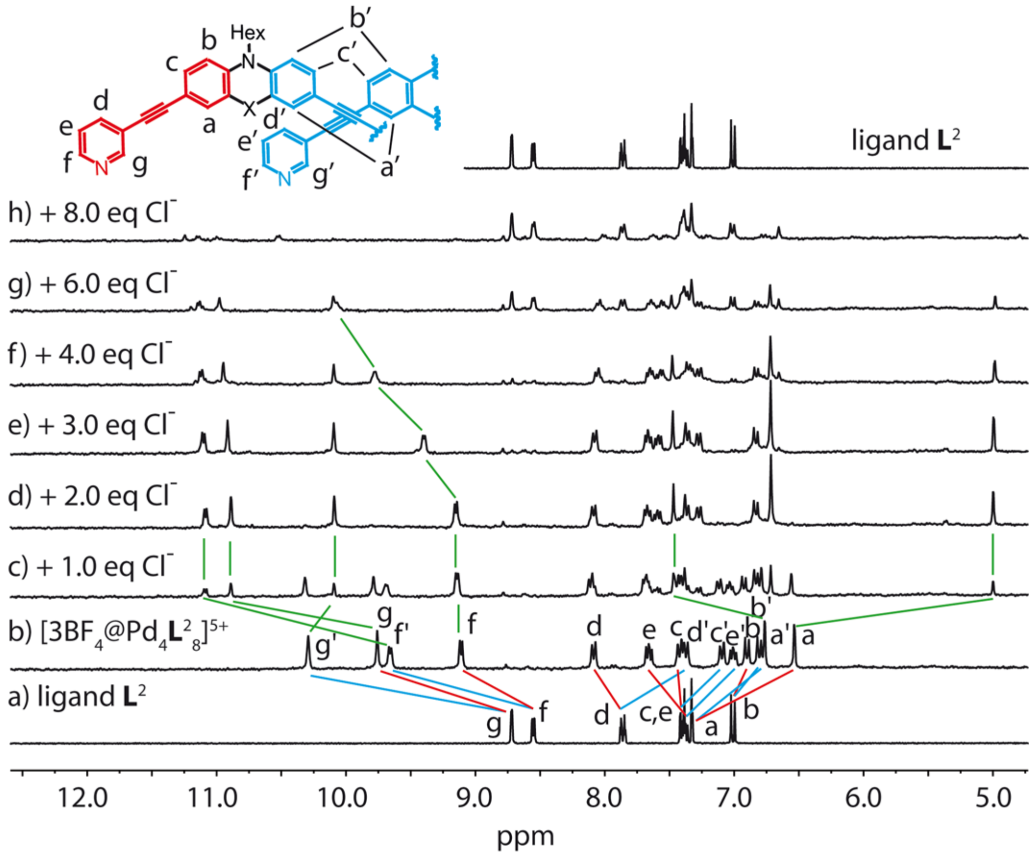

Figure IV.11 a) ^{1}H NMR of free ligand $\mathbf{L}^2$; b) ^{1}H NMR of double-cage $[3BF_4@Pd_4\mathbf{L}^2_8](BF_4)_5$. Red and blue lines indicate two sets of signals belonging to the ligand part pointing inside either the outer or the inner cavity; c)-h) ^{1}H NMR titration (300 MHz, 298 K) of the double-cage solution $[3BF_4@Pd_4\mathbf{L}^2_8](BF_4)_5$ (0.5 mL, 0.35 mM in CD_3CN) with a solution of NBu_4Cl (17.5 mM in CD_3CN). Green lines highlight the most significant shifts in the NMR spectrum occurring upon addition of the halide anion. Reproduced with permission from reference [99]. Copyright © 2013 Royal Society of Chemistry.

Addition of bromide as NBu_4Br salt in acetonitrile showed the same shifting trends of the ^{1}H NMR signals as in the case of chloride (for titration of $[3BF_4@Pd_4\mathbf{L}^2_8]^{5+}$ with bromide see Appendix IV Section 2a and for titration of $[3BF_4@Pd_4\mathbf{L}^4_8]^{5+}$ with chloride and bromide see Appendix IV Section 2b). The titrations with halide anions could not be performed for the double-cage $[3BF_4@Pd_4\mathbf{L}^3_8]^{5+}$ due to the strong ^{1}H NMR signal broadening described in

Chapter III. Figure IV.12a summarizes the results of halide titrations of double-cages $[3BF_4@Pd_4\mathbf{L}^n{}_8]^{5+}$ with n = 2,4,5. In general, the ^{1}H NMR shifts of the signals for bromide-containing double-cages are less pronounced than for chloride-containing double-cages. In particular for the double-cage $[3X@Pd_4\mathbf{L}^2{}_8]^{5+}$, the difference between chloride and bromide guests is more significant. This difference can be best described by the shifting of the H_a and $H_{a'}$ protons, which are located at the core backbone and thus are sensitive to the spatial movement of the two monomeric cages against each other (see Figure IV.12b). Upon anion-induces compression of the double-cage, proton H_a gets closer to the pyridine ring plane of the neighboring ligand resulting in a stronger shielding effect and therefore an upfield shift of the ^{1}H NMR signal. Proton $H_{a'}$ on the other hand is moving away from the pyridine ring plane upon halide binding and gets closer to the ethynyl bridge, which results in a downfield shift of this proton signal. The stronger shiftings of the ^{1}H NMR signals for the chloride-containing double-cage are probably due to the smaller size of the chloride anions resulting in a stronger compression of the double-cage. Thus, the observed ^{1}H NMR shifts $\Delta\delta = \delta([3BF_4@Pd_4\mathbf{L}^2{}_8]^{5+}) - \delta([2X{+}BF_4@Pd_4\mathbf{L}^2{}_8]^{5+})$ are a function of the double-cage contractions Δd. The shifts should be dependent on the initial size of the ligand and the size of the halide anion.

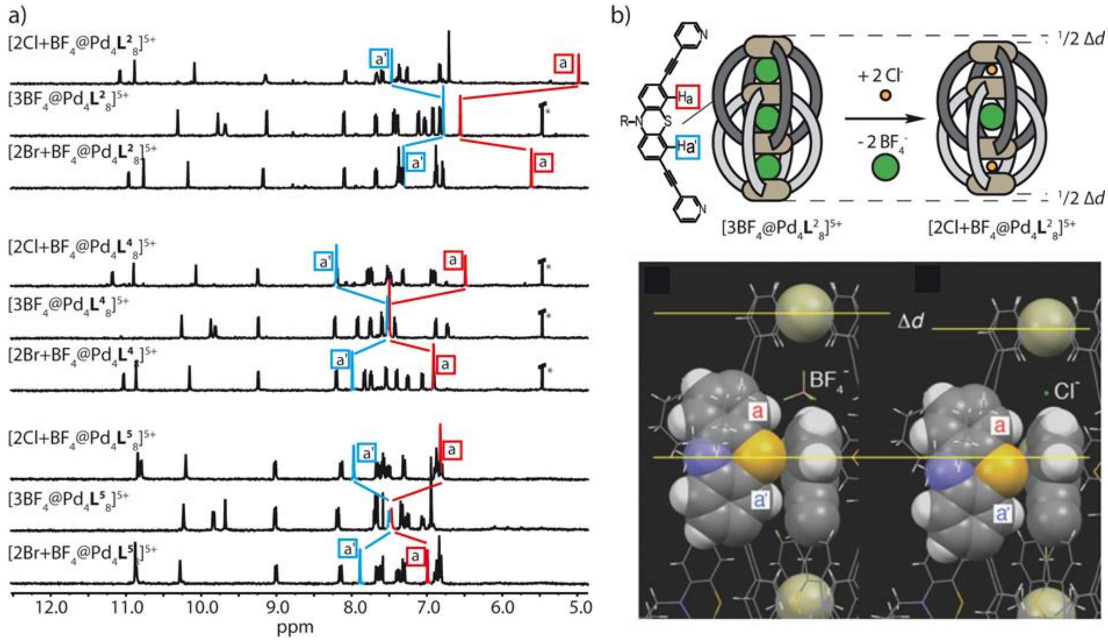

Figure IV.12 a) ^{1}H NMR (300 MHz, 298 K, CD_3CN) of the BF_4^--templated double-cages $[3BF_4@Pd_4\mathbf{L}^n{}_8]^{5+}$ n = 2,4,5 and their halide (X = Cl^- or Br^-) containing analogues $[2X+BF_4@Pd_4\mathbf{L}^n{}_8]^{5+}$. A characteristic parameter for halide uptake is the shifting of protons H_a (red) and $H_{a'}$ (blue). b) Anion induced compression of the double-cages along the Pd_4-axis given by the Δ*d* value (exemplified for the double-cage $[3X@Pd_4\mathbf{L}^2{}_8]^{5+}$). Space-filling view of the outer pocket filled with either a BF_4^- (left) or a Cl^- anion (right), which indicates the relative movement along the Pd_4-axis. The relative distances are based on the X-ray structure for $[3BF_4@Pd_4\mathbf{L}^2{}_8]^{5+}$ and the results from NOESY measurement for $[2Cl+BF_4@Pd_4\mathbf{L}^2{}_8]^{5+}$. Reproduced with permission from reference [99]. Copyright © 2013 Royal Society of Chemistry.

For further considerations on the relationship between the NMR shifts Δ*δ* upon binding of halide anions and the resulting cage compression Δ*d*, a calculation of theoretical Δ*δ* values was performed (for computational details see Appendix IV Section 3). For this, fragment models of double-cages with different Δ*d* values were constructed starting from the X-ray structures $[3BF_4@Pd_4\mathbf{L}^n{}_8]^{5+}$ and the corresponding ^{1}H NMR signals were computed. The calculation results should be treated carefully, because some important factors such as solvent effect and exact anion positions were neglected for the calculation process. Interactions with the solvent inside the cage interior may have an influence on the interactions between the Pd nodes and the anionic guest molecule. The anions were placed exactly in the middle between two $Pd(py)_4$ planes, which is not necessarily the case in the real system. The anion can also be sitting closer to one $Pd(py)_4$ plane than to the other in order to extract the maximum of favorable interactions. Figure IV.13 a) –c) summarizes the computed Δ*δ* values as a function of Δ*d* for the double-cages $[3BF_4@Pd_4\mathbf{L}^n{}_8]^{5+}$ with n = 2,4,5.

Straight horizontal lines indicate the experimental Δ*δ* values obtained from ^{1}H NMR measurements (see Table AP-IV.1). Theoretical Δ*d* values for the double-cage compression upon halide binding could be derived from the intersection of the experimental Δ*δ* values and the calculated Δ*δ* values (see Table IV.1).

Table IV.1 Δ*d* values derived from the intersection of the experimental Δ*δ* and the calculated Δ*δ* for protons H_a and $H_{a'}$.

	$[BF_4@Pd_4\mathbf{L}^2_8]$	$[BF_4@Pd_4\mathbf{L}^4_8]$	$[BF_4@Pd_4\mathbf{L}^5_8]$
	Δ*d* in Å	Δ*d* in Å	Δ*d* in Å
Cl	1.0-1.2	1.1-1.2	> 0.6
Br	0.7-0.8	0.6-0.8	0.5-0.7

Unfortunately the lack of crystal structures for the halide containing double-cages hampers the verification of these results. Therefore, additional calculations of the Δ*d* values for the compression along the Pd_4-axis were performed.[100] For this, the double-cage structure was approximated by a push-and-pull model with three $Pd(py)_4$-anion-$Pd(py)_4$ potentials mechanically joined by rigid linkers with the corresponding length of the ligand $\mathbf{L}^n$ with n =2-5 (for further computational details, see Appendix Chapter IV Section 4). The Δ*d* values derived from these calculations are shown in Table IV.2. These Δ*d* values were used for determination of the calculated Δ*δ* values. Figure IV.13d shows the results of the experimental ^{1}H NMR shifts compared to computed shifts for the double-cages $[3X@Pd_4\mathbf{L}^n_8]^{5+}$ n = 2,4,5 upon encapsulation of halide anions. A qualitative agreement between the experimental and computed values can be derived within the error bars. The trend shows a decrease in the ^{1}H NMR shifts Δ*δ* going from the double-cage with longer ligand $\mathbf{L}^4$ to the one with the shorter ligand $\mathbf{L}^5$. Also a lower value for the Δ*δ* for binding of the smaller anion Cl^- compared to the larger anion Br^- was revealed via the theoretical calculations. For the double-cage based on the longest ligand $\mathbf{L}^2$, the aforementioned neglected effects of the solvent and anion position may hamper the computation and thus can lead to misleading results. In this case, the calculated Δ*δ* value does not follow the

---

[100] The calculations were performed and analyzed by Dr. Johannes M. Dieterich and Prof. Dr. Ricardo A. Mata, Department of Physical Chemistry, University of Göttingen.

experimental trend. Furthermore, NOESY measurements[101] were performed for the double-cage $[3BF_4@Pd_4\mathbf{L}^2{}_8]^{5+}$ and its halide-containing derivatives $[2Cl{+}BF_4@Pd_4\mathbf{L}^2{}_8]^{5+}$ and $[2Br{+}BF_4@Pd_4\mathbf{L}^2{}_8]^{5+}$. Characteristic NOESY contacts of double-cage $[3BF_4@Pd_4\mathbf{L}^2{}_8]^{5+}$ were selected and correlated to corresponding distances obtained from the X-ray structure of $[3BF_4@Pd_4\mathbf{L}^2{}_8]^{5+}$. On the basis of this correlation, Δd values could be obtained from integrals of the corresponding NOESY contacts for halide-containing double-cages $[2Cl{+}BF_4@Pd_4\mathbf{L}^2{}_8]^{5+}$ and $[2Br{+}BF_4@Pd_4\mathbf{L}^2{}_8]^{5+}$ (for details on calculations see Appendix IV Section 5). Based on these distances, models of halide containing double-cages could be obtained, which were used to calculate the relative shifts $\Delta\delta$ of the protons H_a and $H_{a'}$. Figure IV.13d shows the results of the shifts obtained from NOESY measurements compared to the $\Delta\delta$ values determined by the above described methods. The $\Delta\delta$ values based on NOESY measurements reproduce qualitatively the experimental values at least within the error bars.

Table IV.2 Δd values obtained from calculations at the DF-MP2/cc-pVTZ level of theory.

	$[BF_4@Pd_4\mathbf{L}^2{}_8]$	$[BF_4@Pd_4\mathbf{L}^4{}_8]$	$[BF_4@Pd_4\mathbf{L}^5{}_8]$
	Δd in Å	Δd in Å	Δd in Å
Cl	0.63	1.43	0.98
Br	0.63	1.08	0.92

---

[101] NOESY measurements were carried out by Dr. Michael John, University of Göttingen.

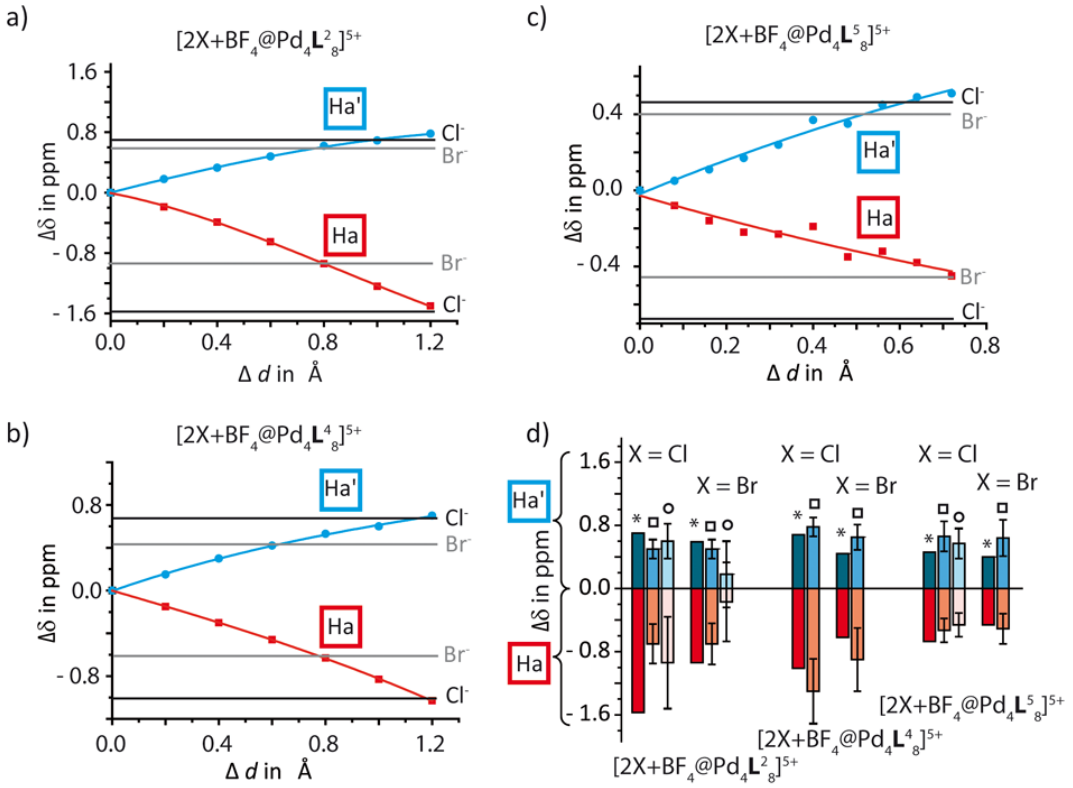

Figure IV.13 Results of the computation of ^{1}H NMR shifts for a) $[2X+BF_4@Pd_4\mathbf{L}^2{}_8]^{5+}$, b) $[2X+BF_4@Pd_4\mathbf{L}^4{}_8]^{5+}$ and c) $[2X+BF_4@Pd_4\mathbf{L}^5{}_8]^{5+}$ with X = Cl^- or Br^- as a function of the double-cage compression Δ*d.* The ^{1}H NMR shifts were referenced to the corresponding non-halide-containing double-cages. The straight horizontal lines assign the experimental differences between the shifts of the $[3BF_4@Pd_4\mathbf{L}^n{}_8]$ double-cage and the $[2X+BF_4@Pd_4\mathbf{L}^n{}_8]$ with X = Cl^- (black line), Br^- (grey line) obtained from ^{1}H NMR spectra. d) Comparison of the Δ*δ* values of protons H_a and $H_{a'}$ extracted from ^{1}H NMR spectra (*), from theoretically computed models (□) and from NOESY measurements (○). Reproduced with permission from reference [99]. Copyright © 2013 Royal Society of Chemistry.

In the next step the affinity of the double-cages $[3BF_4@Pd_4\mathbf{L}^n{}_8]^{5+}$ with n = 2-5 to bind Cl^- or Br^- was studied by applying competition experiments. For this, binary mixtures of double-cages have been prepared in acetonitrile solution and one equivalent of halide (as NBu_4X salt in acetonitrile) was added to the mixture. Subsequently, ^{1}H NMR spectra were recorded of these mixtures revealing either that one double-cage has a higher affinity towards the halide anion or that both cages have nearly equal binding affinities (see Figure IV.14a). One example for competition between $[3BF_4@Pd_4\mathbf{L}^1{}_8]^{5+}$ and $[3BF_4@Pd_4\mathbf{L}^4{}_8]^{5+}$ for uptake of chloride is shown in Figure IV.14b and c (for further competition experiments see Appendix -Chapter IV Section 6). From the results of the competition experiments a trend in binding affinities could be derived following the order:

for Cl$^-$, Br$^-$: $[3BF_4@Pd_4\mathbf{L}^5{}_8]^{5+} \gg [3BF_4@Pd_4\mathbf{L}^4{}_8]^{5+} \approx [3BF_4@Pd_4\mathbf{L}^3{}_8]^{5+} > [3BF_4@Pd_4\mathbf{L}^2{}_8]^{5+}$

This order of binding affinity is associated with the length of the double-cages along the Pd$_4$-axis. The double-cage $[3BF_4@Pd_4\mathbf{L}^5{}_8]^{5+}$ with the shortest ligand shows the highest binding affinity, whereas the double-cage with the longest ligand $[3BF_4@Pd_4\mathbf{L}^2{}_8]^{5+}$ has the lowest binding affinity (for ligand length see the N,N distances in Figure IV.10). The solutions from the competition experiments were left standing over night and repeated ^{1}H NMR measurements revealed no significant changes of product distribution within this time period.

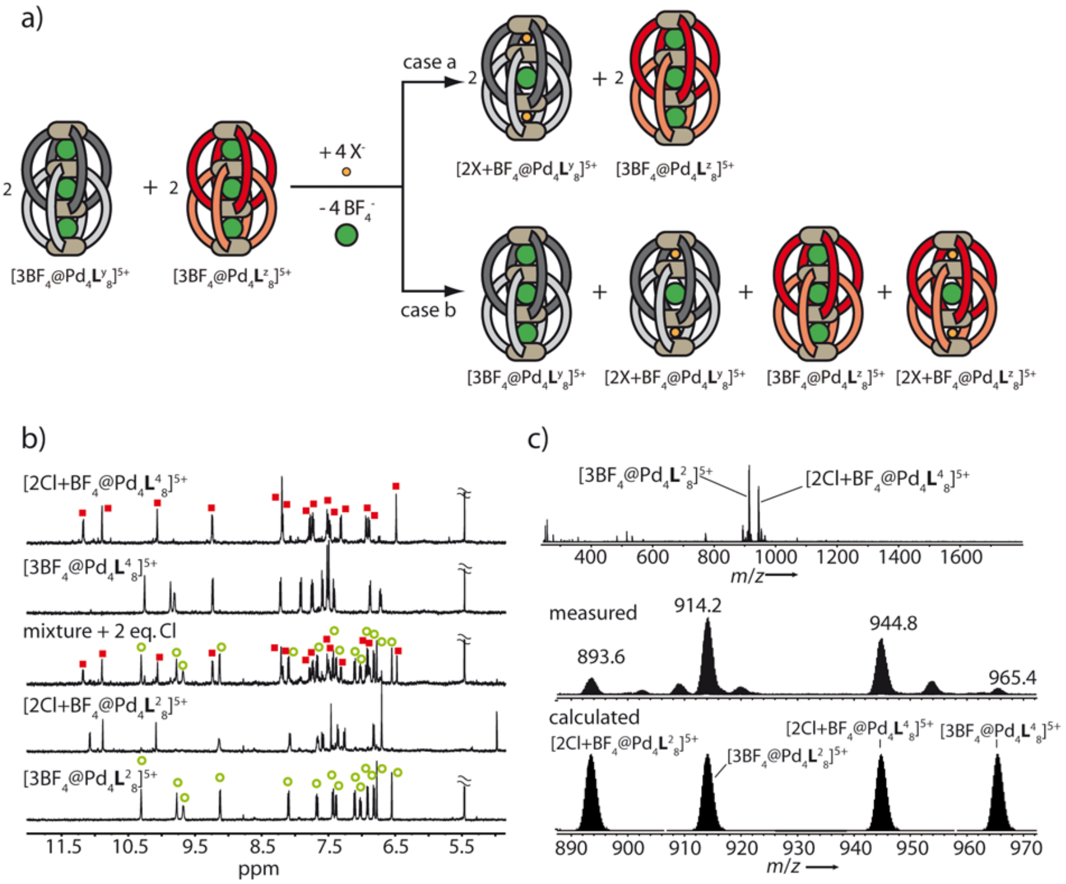

Figure IV.14 a) Experimental setup for the competition experiment for binding of halide anions X = Cl$^-$, Br$^-$. A mixture of double-cages $[3BF_4@Pd_4\mathbf{L}^y{}_8]^{5+}$ and $[3BF_4@Pd_4\mathbf{L}^z{}_8]^{5+}$ was treated with one equivalent of halide and subsequently an ^{1}H NMR spectrum was recorded. Two cases are possible: in case a one double-cage has a stronger affinity to the halide anion than the other resulting in 1:1 mixture of $[3BF_4@Pd_4\mathbf{L}^y{}_8]^{5+}$ and $[3BF_4@Pd_4\mathbf{L}^z{}_8]^{5+}$. In case b both cages have a similar affinity for the halide anion and a 1:1:1:1 mixture $[3BF_4@Pd_4\mathbf{L}^y{}_8]^{5+}$: $[2X+BF_4@Pd_4\mathbf{L}^y{}_8]^{5+}$: $[3BF_4@Pd_4\mathbf{L}^z{}_8]^{5+}$: $[2X+BF_4@Pd_4\mathbf{L}^z{}_8]^{5+}$ is obtained. b) Competition experiment shown exemplary for $[3BF_4@Pd_4\mathbf{L}^2{}_8]^{5+}$ and $[3BF_4@Pd_4\mathbf{L}^4{}_8]^{5+}$ for chloride binding. Green circles and red rectangle assign the species found in the competition experiment (middle spectrum). c) ESI mass spectrum recorded of the solution after the competition experiment and simulated spectra. Reproduced with permission from reference [99]. Copyright © 2013 Royal Society of Chemistry.

The binding affinities towards a particular halide anion were also investigated. For this, to a double-cage solution a solution containing both halide anions in a ratio of 1:1 (Cl^- and Br^- as NBu_4X salt in acetonitrile) was added and an ^{1}H NMR spectrum was recorded (for ^{1}H NMR data see Appendix - Chapter IV Section 7). The measurements revealed that the double-cages constructed from the long ligands $[3BF_4@Pd_4\mathbf{L}^2{}_8]^{5+}$, $[3BF_4@Pd_4\mathbf{L}^3{}_8]^{5+}$ and $[3BF_4@Pd_4\mathbf{L}^4{}_8]^{5+}$ exhibit a roughly equal affinity towards chloride compared to bromide. For the double-cage with the shortest ligand $[3BF_4@Pd_4\mathbf{L}^5{}_8]^{5+}$ a preference towards binding of chloride was previously shown.[16,98] These results are in agreement with the back titration experiments using $AgBF_4$, which give an insoluble precipitate with halide anions and the added BF_4^- replaces the halide anions. For the shortest double-cage $[3BF_4@Pd_4\mathbf{L}^5{}_8]^{5+}$ more than two equivalents of $AgBF_4$ were needed in order to extract both halide anions from the pockets indicating a very strong binding of the halide, whereas only two equivalents of $AgBF_4$ were needed for the residue double-cages containing either chloride or bromide (see Appendix - Chapter IV Section 7).

In order to explain the experimentally observed binding affinities, theoretical calculations of binding affinities were performed (details on calculations see Appendix – Chapter IV Section 4).[102] Figure IV.15 shows the energetical profile for the substitution of BF_4^- anions by a halide anion as a function of the Pd–Pd separation expressed via the characteristic ligand distance *d*(N,N) in the $\{Pd_2\mathbf{L}_4\}$-subunits. For short N-N distances (< 17 Å), the calculation predicts that the chloride binding will be favored over binding of the bromide anion due to energetically lower course of the curve. For longer N-N distances (< ca. 17 Å) no preference neither for chloride nor for bromide anions is expected due to overlap of the two curves. At this distances the interaction between anions and $Pd(py)_4$-planes will be purely electrostatic and both anions will be recognized as point charges. This finding is in accordance to the aforementioned experimental results, which showed that

---

[102] The calculations were performed and analyzed by Dr. Johannes M. Dieterich and Prof. Dr. Ricardo A. Mata, Department of Physical Chemistry, University of Göttingen.

only in case of the double-cage with the shortest ligand $\mathbf{L}^5$ a preference for binding a chloride over bromide is observed. Moreover, the calculation predicts a preferential binding of halide anions inside the pockets of double-cages with shorter ligands. The optimal Pd–Pd separation *d*(N,N) for chloride binding is found around 14.8 Å. For bromide the optimal distance is around 15.4 Å. These calculation results are in qualitative agreement with the experimental observations, where the binding affinity towards a particular halide anion increases with decreasing size of the ligand.

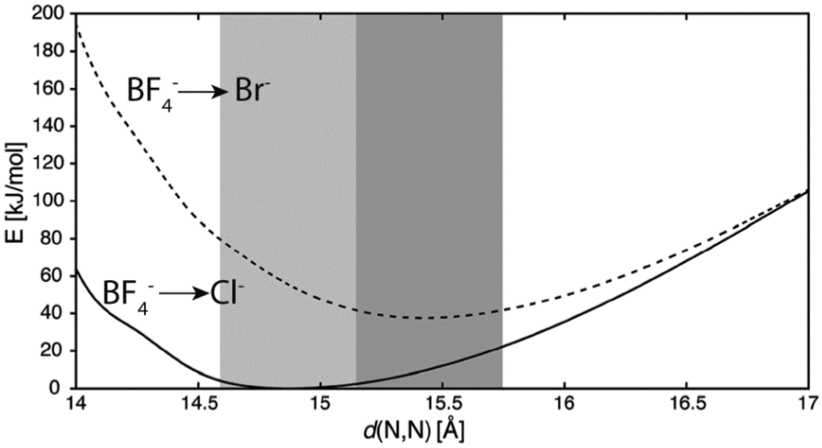

Figure IV.15 Calculated affinity for the exchange of BF_4^- anions for chloride (solid line) or bromide (dashed line) in dependence of the Pd–Pd separation expressed via *d*(N,N) distances in the {$Pd_2\mathbf{L}_4$}-subunits for a series of hypothetical double-cages. The optimal cage size for chloride binding is found at 14.8 Å, whereas for bromide binding a greater cage size with *d*(N,N) 15.4 Å is optimal. Grey areas indicate a region with 1 kcal mol^{-1} deviation from the minimum energy. Reproduced with permission from reference [99]. Copyright © 2013 Royal Society of Chemistry.

IV.4 Conclusion

Herein, the binding ability of three phenothiazine-based double-cages $[3BF_4@Pd_4\mathbf{L}^2{}_8]^{5+}$, $[3BF_4@Pd_4\mathbf{L}^3{}_8]^{5+}$ and $[3BF_4@Pd_4\mathbf{L}^4{}_8]^{5+}$ for halide anions (chloride and bromide) was presented. The halide anions replace the initially contained BF_4^- anions in the outer two pockets of the double-cage. The binding was found to occur in an allosteric fashion with an enhanced affinity for the binding of the second halide. The binding of the halide anions results in characteristic shifts in ^{1}H NMR spectra, which can be correlated to the accompanied compression along the Pd_4-axis. This correlation was studied via experimental data obtained from ^{1}H NMR measurements and was further supported by theoretical calculations. Due to the structural differences of the three related phenothiazine cages (oxygenation state at the sulfur atom), their binding abilities towards halide anions were found to be different. These binding affinities were compared by competition experiments (also in comparison to the previously reported dibenzosuberone double-cage) and were also verified via computational methods. It was observed that the binding affinities of the double-cages towards halide anions decrease with increasing length of the ligands. Furthermore, it was found that the double-cages with relatively long ligands do not show selectivity towards a particular halide anion, whereas the double-cage with the shortest ligand was found to encapsulate the chloride anion preferentially to bromide anion. These experimental results were supported by theoretical calculations.

Chapter V

Ligand Exchange in Double-Cages and Self-Sorting Phenomena

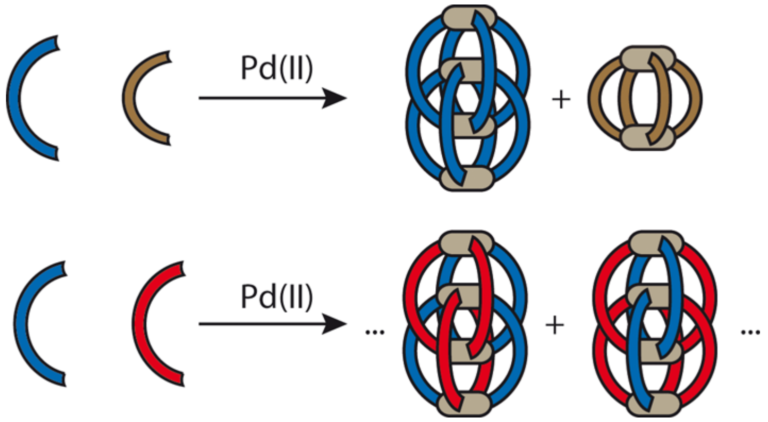

This chapter corresponds to the following publication:

- ‘Narcissistic self-sorting vs. statistic ligand shuffling within a series of phenothiazine-based coordination cages’, M. Frank, L. Krause, R. Herbst-Irmer, D. Stalke, G. H. Clever, *Dalton Trans*. **2014**, *43*, 4587–4592.

V. LIGAND EXCHANGE IN DOUBLE-CAGES AND SELF-SORTING PHENOMENA

V.1 Introduction

Self-sorting describes the ability to distinguish with high efficiency between self- and nonself within complex component mixtures,[103] which is a fundamental property in many natural systems such as self-sorting of base pairs in a DNA helix, formation of genes sequences or self-sorting of carbohydrates, peptides and fatty acids in a cell. In general, the self-sorting process describes the ability to bring a specific order to chaotic states. Artificial self-sorting on molecular level is attending more and more attention, but still it often suffers from low efficiency compared to the naturally occurring counterparts.[104] Self-sorting processes are a common phenomenon in multicomponent environments of supramolecular chemistry.[105] Self-sorting in coordination self-assembly can be induced by various factors such as the type of metal-ligand contact, size of the ligand, denticity, coordination angle, stereochemical information of the reactant molecules, choice of solvent and temperature. The outcome of self-sorting is either a social self-discrimination[106] comprising the selective incorporation of different ligand types in a single coordination assembly or the narcissistic self-recognition[107] comprising selective complex formation with a single ligand type (see

---

[103] P. Mukhopadhyay, A. Wu, L. Isaacs, *J. Org. Chem.* **2004**, *69*, 6157.

[104] M. L. Saha, M. Schmittel, *Org. Biomol. Chem.* **2012**, *10*, 4651.

[105] for reviews on self-sorting see: (a) K. Osowska, O. Š. Miljanić, *Synlett* **2011**, *12*, 1643. (b) M. Safont-Sempere, G. Fernandez, F. Würthner, *Chem. Rev*. **2011**, *111*, 5784. (c) M. L. Saha, S. De, S. Pramanik, M. Schmittel, *Chem. Soc. Rev.* **2013**, *42*, 6860. (d) M. D. Ward, P. R. Raithby, *Chem. Soc. Rev.* **2013**, *42*, 1619. (e) Z. He, W. Jiang, C. A. Schalley, *Chem. Soc. Rev.* **2015**, *44*, 779.

[106] for examples of social self-sorting in coordination chemistry, see (a) Q.-F. Sun, J. Iwasa, D. Ogawa, Y. Ishido, S. Sato, T. Ozeki, Y. Sei, K. Yamaguchi, M. Fujita, *Science* **2010**, *328*, 1144. (b) K. Mahata, M. L. Saha, M. Schmittel, *J. Am. Chem. Soc.,* **2010**, *132*, 15933. (c) M. J. Smulders, A. Jimenez and J. R. Nitschke, *Angew. Chem. Int. Ed.* **2012**, *51*, 6681. (d) M. L. Saha, S. Pramanik, M. Schmittel, *Chem. Commun.* **2012**, *48*, 9459. (e) M. L. Saha, M. Schmittel, *J. Am. Chem. Soc.* **2013**, *135*, 17743. (f) D. Samanta, P. S. Mukherjee, *Chem. Commun.* **2013**, *49*, 4307. (g) T. K. Ronson, D. A. Roberts, S. P. Black, J. R. Nitschke, *J. Am. Chem. Soc.* **2015**, *137*, 14502. (h) A. J. Metherell, M. D. Ward, *Chem. Sci.* **2016**,*7*, 910.

[107] for examples of narcissistic see (a) A. Wu, L. Isaacs, *J. Am. Chem. Soc.* **2003**, *125*, 4831. (b) R. Pinalli, V. Cristini, V. Sottili, S. Geremia, M. Campagnolo, A. Caneschi, E. Dalcanale, *J. Am. Chem. Soc.*, **2004**, *126*, 6516. (c) Y.-R. Zheng, H.-B. Yang, B. H. Northrop, K. Ghosh, P. J. Stang, *Inorg. Chem.* **2008**, *47*, 4706. (d) C. Gütz, R. Hovorka, G. Schnakenburg, A. Lützen, *Chem. - Eur. J.* **2013**, *19*, 10890. (e) A. Jimenez, R. A. Bilbeisi, T. A. Ronson, S. Zarra, C. Woodhead, J. R. Nitschke, *Angew. Chem. Int. Ed.* **2014**, *53*, 4556. (f) G. Meyer-Eppler, F. Topic, G. Schnakenburg, K. Rissanen, A. Lützen, *Eur. J. Inorg. Chem.* **2014**, 2495. (g) C. Gütz, R. Hovorka, N. Struch, J.

Figure V.1). Initially obtained product distributions may not reflect the thermodynamically favored outcome. In some cases, the products are kinetically entrapped and can only convert to thermodynamically favored products when the energy barrier for the interconversion is not too high.[108] The larger the difference between the coordinating ligands, the larger will be the energetic difference between the assembled products and thus the more effective will be the sorting process. In order to program the completive self-sorting, one should consider multiple recognition features that are able to correct errors or reject wrong recognition. When all participants in the library communicate between each other, completive self-sorting only occurs within narrow boundaries and it is strongly influenced by stoichiometry and the presence of other competitors.[104]

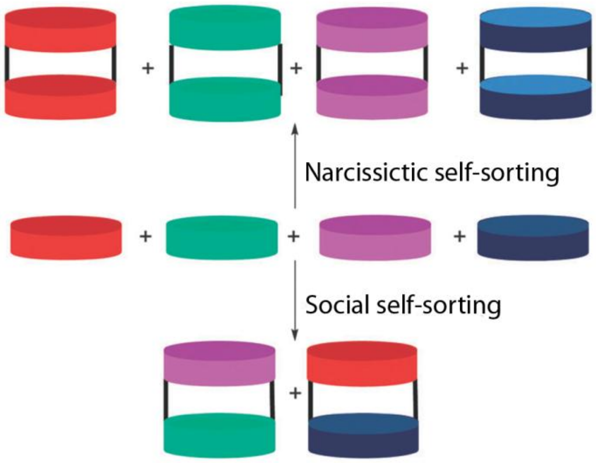

Figure V.1 Two scenarios of self-sorting: either the narcissistic or the social self-sorting. Reproduced with permission from reference [105c]. Copyright © 2013 Royal Society of Chemistry.

Self-sorting systems can be prepared by thermodynamically or kinetically controlled recognition processes. Some sorting phenomena are not thermodynamically favored, but a kinetic control of the reaction can shift the composition of the equilibrium and thus selectively amplify one particular component in a mixture. Thermodynamics and kinetics should be considered in order to gain control over product distribution in coordination

---

Bunzen, G. Meyer-Eppler, Z.-W. Qu, S. Grimme, F. Topić, K. Rissanen, M. Cetina, M. Engeser, A. Lützen. *J. Am. Chem. Soc.* **2014**, *136*, 11830. (h) W. Wang, Y. Zhang, B. Sun, L.-J. Chen, X.-D. Xu, M. Wang, X. Li, Y. Yu, W. Jiang, H.-B. Yang, *Chem. Sci.* **2014**, *5*, 4554. (i) L.-L. Yan, C.-H. Tan, G.-L. Zhang, L.-P. Zhou, J.-C. Bünzli, Q.-F. Sun, *J. Am. Chem. Soc.* **2015**, *137*, 8550. (j) L. R. Holloway, M. C. Young, G. J. O. Beran, R. J. Hooley, *Chem. Sci.* **2015**, *6*, 4801.

[108] J. F. Ayme, J. E. Beves, C. J. Campbell, D. A. Leigh, *Angew. Chem. Int. Ed.* **2014**, *53*, 7823.

chemistry (see Figure V.2 for different interplay of kinetics and thermodynamics). In reactions, which proceed under thermodynamic control, the product distribution is directly related to the relative stabilities of products. Kinetically controlled reactions yield products in a ratio, which reflect the relative rates of product formation and the corresponding relative activation barriers. Some reaction conditions such as high temperature or the presence of equilibration catalysts promote the formation of thermodynamic products since they facilitate the crossing of the system along the energy landscape. On the other hand, low temperatures and highly reactive compounds favor kinetic control. However, in the most cases of reactions, the kinetic and thermodynamic products are the same, which means that the most stable products are also formed as the fastest.[109]

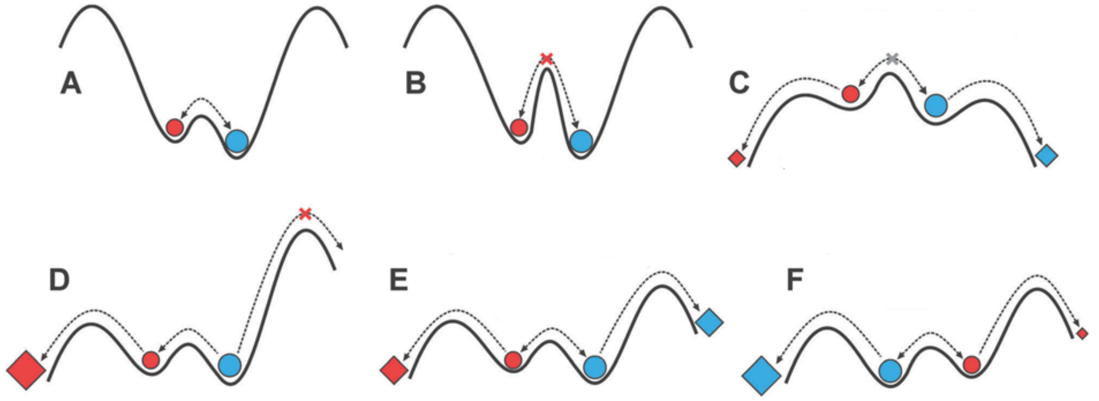

Figure V.2 Circles stand for compounds in equilibrium. Red circle denotes the less stable compound. Rhombuses denote irreversibly formed reaction products. **A** Mixture of equilibrating compounds with hampered further reactions due to very high energy barriers. **B** Mixture of non-equilibrating compounds due to a high activation energy and with hampered further reactions due to very high energy barriers. **C** Non-equilibrating compounds which quickly and irreversibly react to products with a distribution that reflects the initial distribution of educts. **D** The reaction of one compound (blue circle) is kinetically hampered and the equilibrium will be shifted to the second component (red circle) which can irreversibly react to the corresponding product. **E** One component (red circle) reacts faster to the corresponding product, but the other (blue circle) is thermodynamically more favored and can also irreversibly react to its product. In this case the thermodynamics and kinetics work against each other and no selectivity in product formation is observed. **F** One component (blue circle) is more stable and reacts faster to the corresponding product. Although the kinetic barrier of the second components' (red circle) reaction is comparable, the higher thermodynamic stability of the first component (blue circle) will shift the equilibrium selectively to the corresponding irreversible reaction (product is the blue rhombus). In this case the kinetics and the thermodynamics cooperate in the same direction

---

[109] Q. Ji, R. C. Lirag, O. S. Miljanic, *Chem. Soc. Rev.* **2014**, *43*, 1873.

leading to a selective formation of the product. Reproduced with permission from reference [109]. Copyright © 2014 Royal Society of Chemistry.

The selective synthesis of heteromeric coordination cages comprising at least two different ligand types is a desirable goal if one wants to bring building blocks with different functionalities in close proximity to each other within one structure. Nevertheless, a targeted design is complicated due to challenging control of the simultaneous coordination of two kinds of ligand donors to a metal acceptor. Kobayashi and co-workers could show that the selective formation of homo- and heteromeric cages can be controlled by the balance between kinetic and thermodynamic stabilities based on coordination sites of the ligands and the steric demand of the cavities (see Figure V.3a).[110] One of the bowl-shaped ligands **35** possesses cyanophenyl binding sites, whereas the other ligand **36** contains four pyridyl binding arms. The latter ligand shows stronger coordination ability towards metal ions. The rotation of the moieties of both ligands is hindered by the oxygens surrounding the cavitand scaffold. After treatment with a Pd salt, two single species were identified: the stable homomeric cage $[Pd_4\mathbf{36}_2]^{8+}$ and the less stable homomeric cage $[Pd_4\mathbf{35}_2]^{8+}$ (see Figure V.3b). After a while new signals belonging to the heteromeric cage species $[Pd_4(\mathbf{35})(\mathbf{36})]^{8+}$ appeared which increased in time. At room temperature the conversion to the heteromeric species was very slow. The mixture of homomeric cages was stable for 2 days at 23 °C and no significant emergence of heteromeric species was observed (see Figure V.3c curve a). Subsequently, however, the ratio increased slowly from $[Pd_4(\mathbf{35})(\mathbf{36})]^{8+}/[Pd_4\mathbf{36}_2]^{8+} = 0.21$ (24 days), 0.46 (60 days) to 0.97 (134 days). Finally the ratio reached the thermodynamic equilibrium at $[Pd_4(\mathbf{35})(\mathbf{36})]^{8+}/[Pd_4\mathbf{36}_2]^{8+} = 1.0$. The conversion could be accelerated by increasing the temperature to 50 °C (see Figure V.3c curve b). Here the complete conversion was finished after 2 h. The heteromeric cage $[Pd_4(\mathbf{35})(\mathbf{36})]^{8+}$ is also formed by mixing the labile homomeric cage $[Pd_4\mathbf{35}_2]^{8+}$ with the free ligand **36** (see Figure V.3c curve c). In this case the heteromeric cage is initially preferably formed under kinetic control and after one week at room temperature the thermodynamic equilibrium was reached.

---

[110] M. Yamanaka, Y. Yamada, Y. Sei, K. Yamaguchi, K. Kobayashi, *J. Am. Chem. Soc.* **2006**, *128*, 1531.

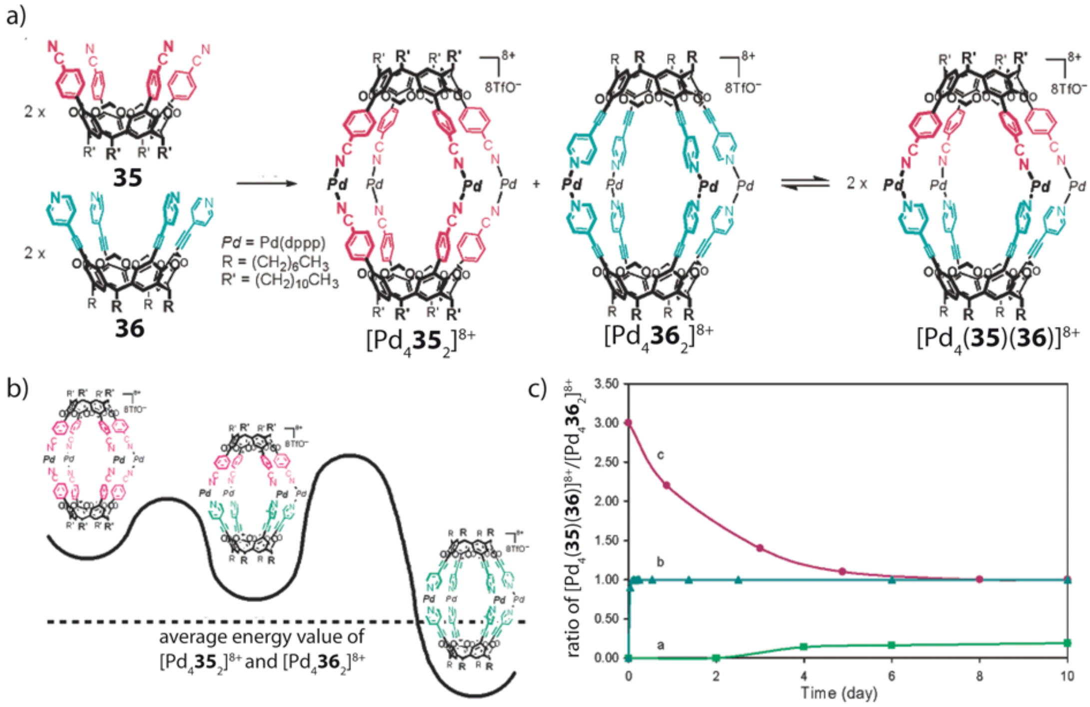

Figure V.3 a) Self-assembly of ligands **35** and **36** to the homomeric cages [Pd$_4$**35**$_2$]$^{8+}$ and [Pd$_4$**36**$_2$]$^{8+}$ and further equilibrium reaction to the heteromeric cage [Pd$_4$(**35**)(**36**)]$^{8+}$. b) Schematic representation of relative energy diagram for cages [Pd$_4$**35**$_2$]$^{8+}$, [Pd$_4$**36**$_2$]$^{8+}$ and [Pd$_4$(**35**)(**36**)]$^{8+}$. c) Ratios of heteromeric cage [Pd$_4$(**35**)(**36**)]$^{8+}$ to homomeric cavitand cage [Pd$_4$**36**$_2$]$^{8+}$ as a function of time (in days), monitored by ^{1}H NMR integration: (a) c(**35**) = c(**36**) = 1 mM and [Pd(II)] = 4 mM in CDCl$_3$ at 23 ° C; (b) c(**35**) = c(**36**) = 1 mM and [Pd(II)] = 4 mM in CDCl$_3$ at 50 ° C; (c) c(**36**) = [Pd$_4$**35**$_2$]$^{8+}$ = 1 mM in CDCl$_3$ at 23 ° C. Reproduced with permission from reference [110]. Copyright © 2006 American Chemical Society.

Less common are examples of self-sorting phenomena in metal-organic catenanes.[111] Catenanes comprising several mechanically interlocked metallacycles are complex compounds and are therefore predestinated to form undesired assemblies. An interesting example of social self-sorting of catenanes was reported by Fujita and co-workers in 2004.[112] They applied two metallacycles [Pd**37**]$^{2+}$ and [Pd**38**]$^{2+}$ for the kinetically controlled quantitative synthesis of the heterocatenane [Pd$_2$(**37**)(**38**)]$^{4+}$ (see Figure V.4a). The homocatenation of the two metallacycles to [Pd$_2$**37**$_2$]$^{4+}$ and [Pd$_2$**38**$_2$]$^{4+}$ occurs on significantly different time scales. Catenation of the metallacycle [Pd**37**]$^{2+}$ to [Pd$_2$**37**$_2$]$^{4+}$ is a very rapid process and occurs on a millisecond timescale. Introduction of sterically demanding groups

---

[111] O. Gidron, M. Jirásek, N. Trapp, M.-O. Ebert, X. Zhang, F. Diederich, *J. Am. Chem. Soc.* **2015**, *137*, 12502.

[112] A. Hori, K.-I. Yamashita, M. Fujita, *Angew. Chem. Int. Ed.* **2004**, *43*, 5016.

into the metallacycle such as a bis(methoxyethoxy) substituent results in a tremendous slowing down of the catenation reaction to time dimensions of several hours and thus the formation of the homocatenane $[Pd_2\mathbf{38}_2]^{4+}$ is kinetically hindered (see Figure V.4b). Therefore, the mixture of the two metallacycles $[Pd\mathbf{37}]^{2+}$ and $[Pd\mathbf{38}]^{2+}$ in water yields exclusively the heterocatenane $[Pd_2(\mathbf{37})(\mathbf{38})]^{4+}$. The heterocatenane and the mixture of homocatenanes are supposed to have almost equal thermodynamic stabilities. However, the formation of the homocatenane $[Pd_2\mathbf{38}_2]^{4+}$ is hampered by the sterically bulky side chains and is therefore kinetically unfavorable. Thus, it was assumed that the narcissistic self-sorted mixture of homocatenanes is only accessible over a long reaction period or at higher temperatures. Indeed, after standing at 25 °C over time new signals indicating the formation of both homocatenanes appeared in the NMR spectrum. The formation of homocatenanes progressively proceeded until an equilibrium state was reached after 8 days with a ratio of 2:1:1 of catenanes $[Pd_2(\mathbf{37})(\mathbf{38})]^{4+}$: $[Pd_2\mathbf{37}_2]^{4+}$: $[Pd_2\mathbf{38}_2]^{4+}$. The same equilibrium mixture was obtained when preassembled homocatenanes $[Pd_2\mathbf{37}_2]^{4+}$ and $[Pd_2\mathbf{38}_2]^{4+}$ were allowed to equilibrate. The equilibration time could be tremendously slowed down from days to several months via decreasing the reaction temperature.

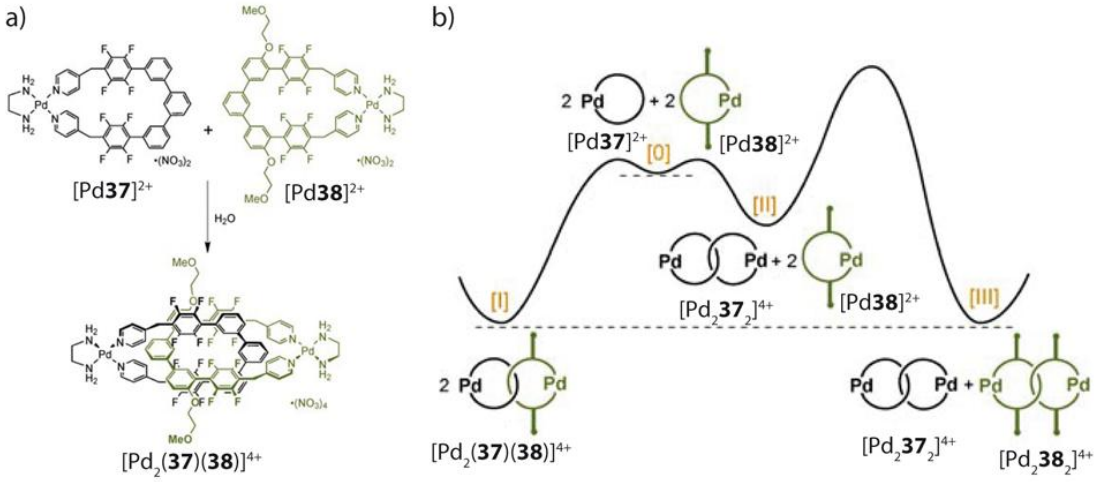

Figure V.4 a) Metallacycles $[Pd\mathbf{37}]^{2+}$ and $[Pd\mathbf{38}]^{2+}$ and their further transformation to the heterocatenane $[Pd_2(\mathbf{37})(\mathbf{38})]^{4+}$. b) Energy diagram for the homo-and hetero-catenanes assembled from metallacycles $[Pd\mathbf{37}]^{2+}$ and $[Pd\mathbf{38}]^{2+}$. Reproduced with permission from reference [112]. Copyright © 2004 WILEY-VCH Verlag GmbH & Co.

Social self-sorting in a multicomponent metal-organic assembly does not necessarily lead to randomly distributed ligands. In some cases, self-assembly give well defined structures with intramolecular self-sorting phenomenon as it could be demonstrated by Fujita and co-workers (see Figure V.5).[113] They applied two similarly shaped ligands **39** and **40** for the assembly of a mixed, yet sorted, $Pd_{12}(\mathbf{39})_{12}(\mathbf{40})_{12}$ cantellated tetrahedron. In a previous study, it could be shown that both ligands give $M_{12}\mathbf{L}_{24}$ cuboctahedral complexes when they are separately mixed with Pd(II) ions.[114] Mixing of both ligands **39** and **40** in one vessel and subsequent assembly with a Pd(II) metal can yield three possible cases of product distribution. In case (1) the self-assembly yields mixed-ligand cages with statistically distributed ligands resulting in 7×10^5 different structures of $Pd_{12}(\mathbf{39})_n(\mathbf{40})_m$ with n+m=24. In case (2) the self-assembly gives one well-defined structure $Pd_{12}(\mathbf{39})_{12}(\mathbf{40})_{12}$, in which every Pd(II) metal coordinates two ligands **39** and two ligands **40** in a *cis* coordination fashion as could be observed for this system. In case (3) the self-assembly leads to a narcissistic self-sorting into distinct homomeric cages $Pd_{12}(\mathbf{39})_{24}$ and $Pd_{12}(\mathbf{40})_{24}$.

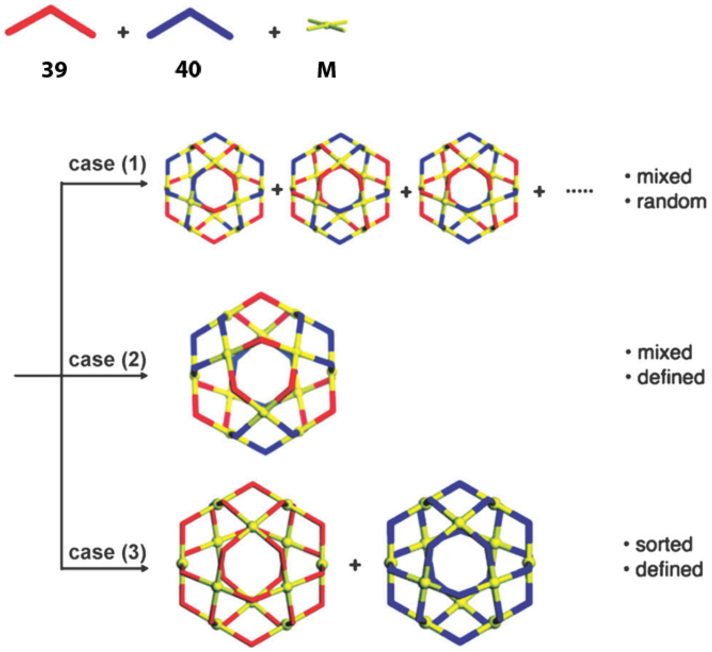

Figure V.5 Possible outcomes for the self-assembly of two similarly shaped ligands **39** and **40** with a metal M = Pd(II). Reproduced with permission from reference [113]. Copyright © 2014 WILEY-VCH Verlag GmbH & Co.

---

[113] Q.-F. Sun, S. Sato, M. Fujita, *Angew. Chem. Int. Ed.* **2014**, *53*, 13510.

[114] (a) M. Tominaga, K. Suzuki, M. Kawano, T. Kusukawa, T. Ozeki, S. Sakamoto, K. Yamaguchi, M. Fujita, *Angew. Chem. Int. Ed.* **2004**, *43*, 5621. (b) Q.-F. Sun, T. Murase, S. Sato, M. Fujita, *Angew. Chem. Int. Ed.***2011**, *50*, 10318. (c) D. Fujita, K. Suzuki, S. Sato, M. Yagi-Utsumi, Y. Yamaguchi, N. Mizuno, T. Kumasaka, M. Takata, M. Noda, S. Uchiyama, K. Kato, M. Fujita, *Nat. Commun*. **2012**, *3*, 1093.

Another example of a self-sorting phenomenon for ligands with identical coordination angle and geometry was reported by Hooley and co-workers (see Figure V.6a).[115] They used ligands **41**-**44** which have the same length, angle and coordinating motif, differing only in a single functional group at the backbone. Applying binary mixtures of these ligands in a lanthanide-mediated self-assembly resulted in a complete narcissistic self-sorting yielding the homomeric cages $\mathbf{41_3}$Ln$_2$, $\mathbf{42_3}$Ln$_2$, $\mathbf{43_3}$Ln$_2$ and $\mathbf{44_3}$Ln$_2$ (see Figure V.6b). No evidence of mixed-ligand cages was observed even after several days. Control experiments with ligands which contain only a single salicylhydrazone coordinating motif showed that variations in donor ability are not enough for narcissistic self-sorting to occur and that the supramolecular nature of the $\mathbf{L}_3$Ln$_2$ assembly is essential for a successful sorting. Model studies of the assemblies showed that a close packing of functional groups within the assembly disfavors the heteromeric structures.

---

[115] A. M. Johnson, C. A. Wiley, M. C. Young, X. Zhang, Y. Lyon, R. R. Julian, R. J. Hooley, *Angew. Chem. Int. Ed.* **2015**, *54*, 5641.

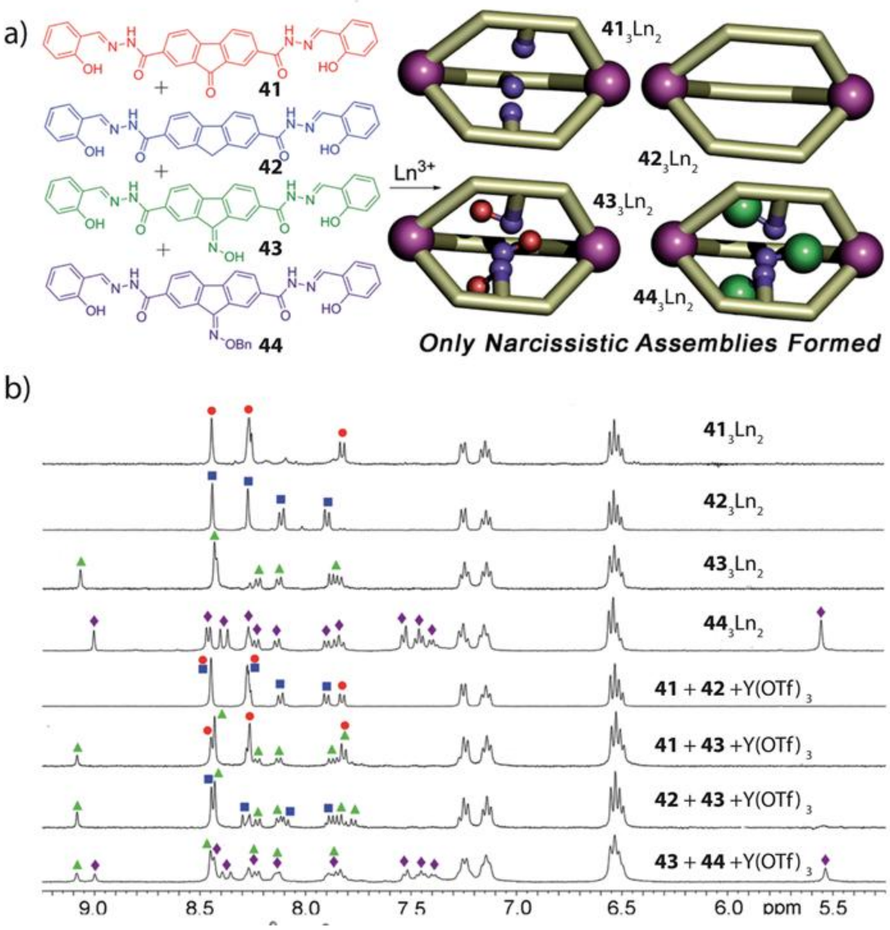

Figure V.6 a) Narcissistic self-sorting between ligands of identical angle and length, differing only in endohedral functionality. b) ^{1}H NMR spectra (400 MHz, 298 K, DMSO-d_6) of self-sorting experiments. Reproduced with permission from reference [115]. Copyright © 2015 WILEY-VCH Verlag GmbH & Co.

V.2 Project Target

The structurally related phenothiazine-based ligands $\mathbf{L}^{1\text{-}4}$ differ either in the length of the pyridine arms or in the oxygenation state at the sulfur atom. Herein, these ligands will be applied for mixing experiments prior to the self-assembly process in order to answer the following questions. Will the double-cage motif tolerate ligands of different length and oxygenation within one assembly or will this system tend to sort the ligand mixture into homomeric assemblies resulting in a narcissistic self-sorting? Furthermore, if social self-sorting occurs, will the product yield randomly distributed mixed-ligand assemblies or will a single defined mixed-ligand structure result from the self-assembly? Social self-sorting is an attractive tool, when the aim of the assembly is to bring ligands with different functionalities in close proximity to each other. For example, the social self-sorting can lead to a large simplification in synthesis of donor-acceptor assemblies (see Chapter VI), where the distance between the donor and acceptor units is crucial for further applications such as photoelectric devices.

V.3 Results and Discussion[66]

For studying the flexibility of the double-cage system to tolerate ligands with different length, the phenothiazine-based ligands **L**$^{1-4}$ were applied for the self-assembly (for ligand structure see Figure V.7). These ligands vary in their length expressed via the distance between the two pyridine arms with the longest ligand **L**^{2} exhibiting an N-N-distance of 17.62 Å and the shortest ligand **L**^{1} with an N-N-distance of 12.64 Å.

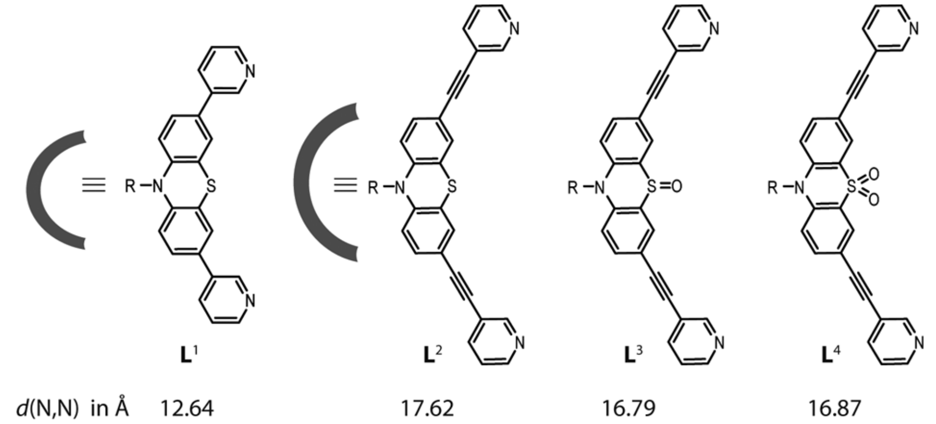

Figure V.7 Structures of the long phenothiazine-based ligands **L**$^{2-4}$ and the short ligand **L**^{1}. The N-N-distances for ligands **L**$^{2-4}$ are obtained from X-ray structures of the corresponding double-cages, for the ligand **L**^{1} the distance is taken from the semiempirical model of the monomeric cage.[65,99]

Mixing two of the long ligands **L**^{x} and **L**^{y} (x,y = 2-4, x ≠ y) in a ratio of 1:1 in acetonitrile (250 µL of a 2.8 mM solution of each ligand) and reaction with 0.5 eq. of $[Pd(CH_3CN)_4](BF_4)_2$ at 70 °C over night yielded a mixture of interpenetrated double-cages comprising a statistical distribution of the two ligands obeying the formula $[3BF_4@Pd_4\mathbf{L}^x_m L^y_{8-m}]^{5+}$ with m = 0-8 (see Figure V.8a case **A**). The ^{1}H NMR signals were broadened due to the presence of several diastereomers in the solution. Even longer heating did not result in narrowing of the signals and thus no evidence for a narcissistic self-sorting was observed (Figure V.8b shows the ^{1}H NMR spectra for mixing of ligand **L**^{2} and **L**^{4}, for other combinations see Appendix – Chapter 5 Section 1). Despite the signal broadening, the shifting of the signals of this mixture indicates the double-cage formation. The statistically distributed mixture was further characterized via ESI mass spectrometric analysis (see Figure V.8c). The mass spectrum fits very well to a binomial distribution of the ligands. Neither a formation of a distinct heteromeric double-cage nor narcissistic self-sorting into homomeric double-cages were observed after prolonged heating of the reaction mixture.

Homomeric double-cages $[3BF_4@Pd_4\mathbf{L}^x{}_8]^{5+}$ and $[3BF_4@Pd_4\mathbf{L}^y{}_8]^{5+}$ (250 µL of a 0.35 mM solution in CD_3CN for each double-cage) were synthesized in a separate reaction vessel via self-assembly of the corresponding ligands with Pd(II) ions. Subsequent mixing of the solutions of preassembled double-cages showed that the homomeric double-cages maintain their original structure without exchanging ligands even after prolonged heating to 70 °C (see Figure V.8a case **B**). The ^{1}H NMR spectrum of the mixture $[3BF_4@Pd_4\mathbf{L}^2{}_8]^{5+}$ + $[3BF_4@Pd_4\mathbf{L}^4{}_8]^{5+}$ shows two sets of signals characteristic for both double-cage structures, which can be clearly assigned to a 1 : 1 mixture of the two double-cages (see Figure V.8b, for other double-cage combinations see Appendix – Chapter 5 Section 1). Also in this case ESI mass spectrometry clearly identifies the expected result of two distinct double-cages (see Figure V.8c).

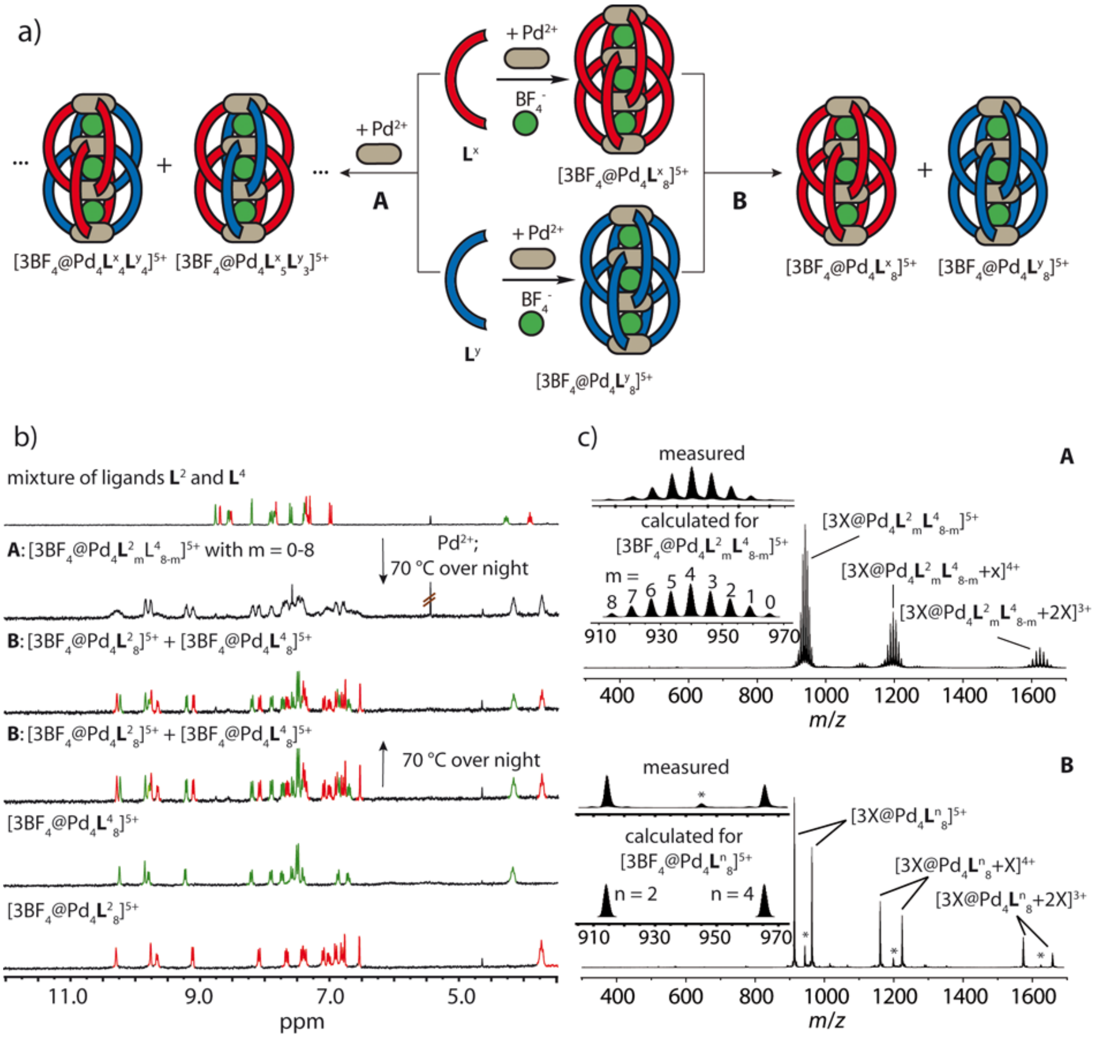

Figure V.8 a) Scheme of experimental results of mixing two different long ligands $\mathbf{L}^{x}$ and $\mathbf{L}^{y}$ (x,y = 2-4, x ≠ y) and reaction with the Pd(II) source, which gives a complex mixture of double-cages with a statistical distribution of the two ligands $[3BF_4@Pd_4\mathbf{L}^{x}{}_{m}\mathbf{L}^{y}{}_{8\text{-}m}]^{5+}$ (case **A**). Binary mixtures of preassembled double-cages $[3BF_4@Pd_4\mathbf{L}^{x}{}_{8}]^{5+}$ and $[3BF_4@Pd_4\mathbf{L}^{y}{}_{8}]^{5+}$ coexist in solution (case **B**). b) ^{1}H NMR spectra (300 MHz, 298 K, CD_3CN) of case **A** and **B** and reference spectra of the ligands $\mathbf{L}^{2}$ and $\mathbf{L}^{4}$ and corresponding double-cages $[3BF_4@Pd_4\mathbf{L}^{2}{}_{8}]^{5+}$ and $[3BF_4@Pd_4\mathbf{L}^{4}{}_{8}]^{5+}$. c) ESI-TOF mass spectra (positive mode, CH_3CN) of results for the experiments **A** and **B**. * double-cages containing other anions as contamination, X = BF_4^-. Reproduced with permission from reference [66]. Copyright © 2014 Royal Society of Chemistry.

These different results for the experimental setup **A** and **B** have led to the question, which of the outcomes represents the thermodynamic and which the kinetic product. For this purpose both mixtures, the mixed-ligand cages $[3BF_4@Pd_4\mathbf{L}^{2}{}_{m}\mathbf{L}^{4}{}_{8\text{-}m}]^{5+}$ as well as the mixture of homomeric double-cages $[3BF_4@Pd_4\mathbf{L}^{2}{}_{8}]^{5+}$ + $[3BF_4@Pd_4\mathbf{L}^{4}{}_{8}]^{5+}$, were heated to 70 °C for a long time period. After time intervals of 22 h, 114 h, 279 h and 615 h a sample was taken from the mixtures and an ESI-TOF spectrum was measured (see Figure V.9, for corresponding NMR spectra see Appendix – Chapter V Section 2). While the spectrum of the mixed-ligand double-cages $[3BF_4@Pd_4\mathbf{L}^2{}_m\mathbf{L}^4{}_{8\text{-}m}]^{5+}$ did not change over time, the spectrum of the mixed homomeric double-cages $[3BF_4@Pd_4\mathbf{L}^2{}_8]^{5+}$ + $[3BF_4@Pd_4\mathbf{L}^4{}_8]^{5+}$ showed the appearance of new signals after prolonged heating. While after 114 h the intensity of the new peaks was still relatively low compared to the initial homomeric double-cage signals, the new signals progressively increased and after 615 h signals of double-cages with exchanged ligands were found in significant quantity. But still after 615 h of heating, the signal pattern was not equal to the statistical distribution of mixed-ligand double-cages indicating that the equilibrium of the ligand exchange was not reached yet. This experiment showed that the mixture of double-cages with a binomial distribution of the ligands is the thermodynamic product exhibiting the global thermodynamic minimum of the system and the mixture of homomeric double-cages is the kinetic product with tremendously slowed exchange of the ligands. Even the addition of catalytic amounts of the competing ligand 2-picoline to the solution $[3BF_4@Pd_4\mathbf{L}^2{}_8]^{5+}$ + $[3BF_4@Pd_4\mathbf{L}^4{}_8]^{5+}$ did not accelerate the ligand exchange significantly at least within a time period of 18 h (see Figures AP-V.9 and AP-V.10).

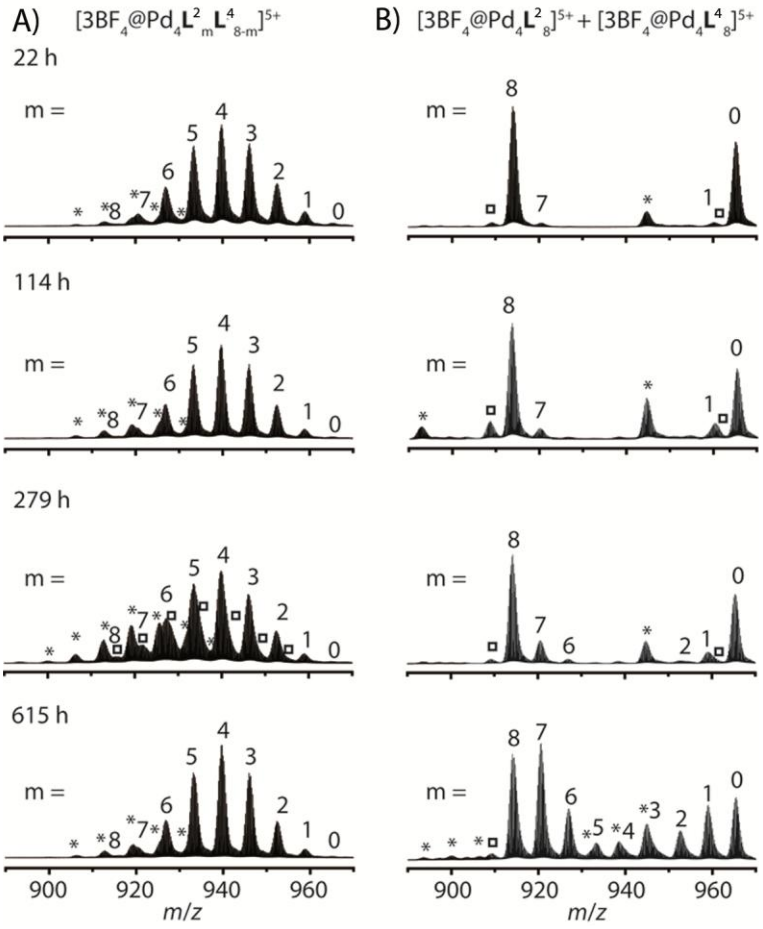

Figure V.9 ESI-TOF mass spectra (positive mode, CH_3CN) of the experiments **A**: mixing of ligands $\mathbf{L}^2$ and $\mathbf{L}^4$ and assembly with $[Pd(CH_3CN)_4](BF_4)_2$ into double-cages with statistical distribution of the ligands $[3BF_4@Pd_4\mathbf{L}^x_m\mathbf{L}^y_{8-m}]^{5+}$ with m = 0-8. Heating the solution at 70 °C over a time period of 615 h resulted in no significant change of the spectrum. **B**: mixing the preassembled homomeric double-cages $[3BF_4@Pd_4\mathbf{L}^2_8]^{5+}$ and $[3BF_4@Pd_4\mathbf{L}^4_8]^{5+}$ and heating at 70 °C indicated a slow ligand exchange over time. Double-cages with anion combination $2Cl^- + BF_4^-$ (*) and double-cages with anion combination $NO_3^- + 2BF_4^-$ (□) were found as minor products. Reproduced with permission from reference [66]. Copyright © 2014 Royal Society of Chemistry.

A completely different situation was found for mixing of one of the long ligands $\mathbf{L}^x$ (x = 2-4) with the short ligand $\mathbf{L}^1$. Here, the assembly of the ligand mixture with Pd(II) ions afforded the narcissistic self-sorting of the ligands into a double-cage $[3BF_4@Pd_4\mathbf{L}^x_8]^{5+}$ and a monomeric cage $[Pd_2\mathbf{L}^1_4]^{4+}$ (see case **A** in Figure V.10a and for ^1H NMR results V.10b). No formation of mixed-ligand cages was observed in this case. Mixing of the preassembled double-cage and the monomeric cage resulted in no change of the reactant composition (see case **B** in Figure V.10). The ESI-TOF measurement confirmed the same outcome of the reaction for both cases **A** and **B** (see Figure V.10c). Also, no change in product composition was observed even after prolonged heating of the both solutions. For other combinations see Appendix – Chapter 5 Section 1.

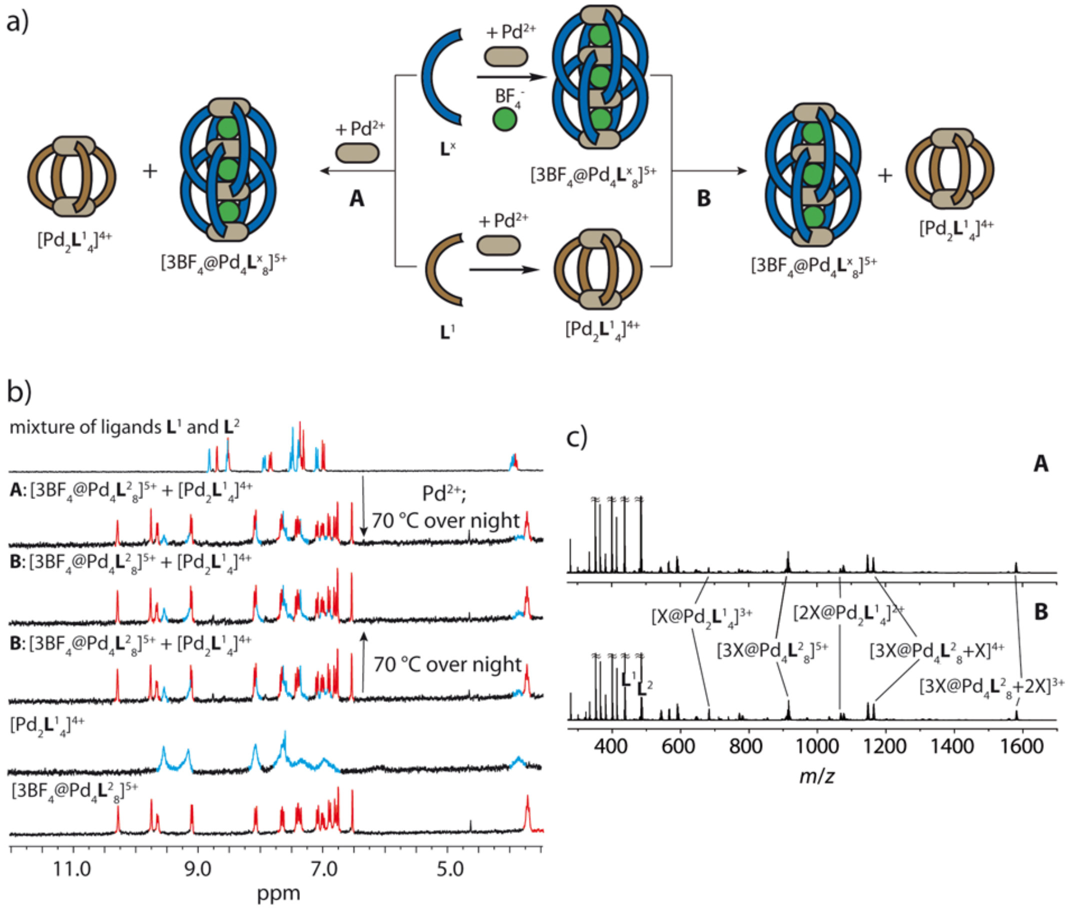

Figure V.10 a) Scheme of experimental results of mixing one long ligand $\mathbf{L}^x$ (x = 2-4) with the short ligand $\mathbf{L}^1$ and reaction with the Pd(II) source, which results in a narcissistic self-sorting into the double-cage $[3BF_4@Pd_4\mathbf{L}^x{}_8]^{5+}$ and the monomeric cage $[Pd_2\mathbf{L}^1{}_4]^{4+}$ (case **A**). Binary mixtures of preassembled double-cage $[3BF_4@Pd_4\mathbf{L}^x{}_8]^{5+}$ and the monomeric cage $[Pd_2\mathbf{L}^1{}_4]^{4+}$ coexist in solution (case **B**). b) ^{1}H NMR spectra (300 MHz, 298 K, CD_3CN) of the experimental setup **A** and **B** and reference spectra of ligands $\mathbf{L}^1$ and $\mathbf{L}^2$, the double-cage $[3BF_4@Pd_4\mathbf{L}^2{}_8]^{5+}$ and the monomeric cage $[Pd_2\mathbf{L}^1{}_4]^{4+}$. c) ESI-TOF mass spectra (positive mode, CH_3CN) of solutions for the experiments **A** and **B**. Both spectra show the nearly the same signal pattern. Reproduced with permission from reference [66]. Copyright © 2014 Royal Society of Chemistry.

V.4 Conclusion

This study showed that the double-cage architecture is able to tolerate ligands within one double-cage structure, which differ in bending angle and steric occupancy around the central atom but have similar length of the N-N distances. Thus, mixing of such ligands and subsequent assembly with Pd(II) ions afforded mixed-ligand double-cages with a statistical distribution of the two ligands. These mixed-ligand double-cages were found to be the thermodynamically favored products. Nevertheless, mixing of preassembled homomeric double-cages did not immediately result in ligand shuffling between the double-cages. A strong kinetic barrier prevents a fast ligand exchange even upon heating or adding of a competitive coordination ligand. Nevertheless, toleration of different ligands within one double-cage structure is limited to a certain length difference between the ligands. It was shown that binary mixtures of one long ligand and one short ligand lead to a narcissistic self-sorting behavior. Here, the ligands favor the formation of the homomeric assemblies. The long ligands $\mathbf{L}^x$ with an N-N distance between 17.62 Å and 16.79 Å form preferably double-cages $[3BF_4@Pd_4\mathbf{L}^x{}_8]^{5+}$ (x = 2-4) and the short ligand $\mathbf{L}^1$ with an N-N distance of 12.64 Å, not capable of forming a double-cage, gives exclusively the monomeric cage $[Pd_2\mathbf{L}^1{}_4]^{4+}$.

Chapter VI

Light-Induced Charge Separation in Donor-Acceptor Mixed-Ligand Double-Cages

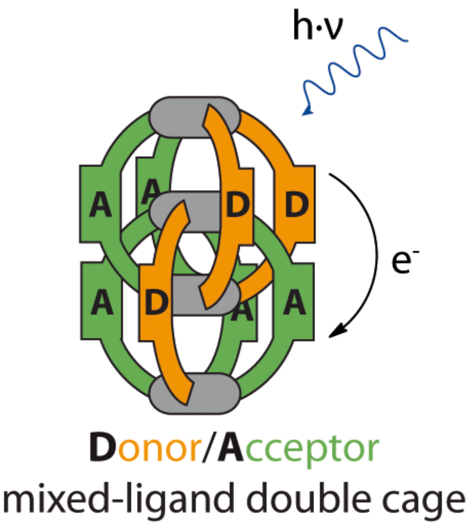

This chapter corresponds to the following publications:

- 'Light-induced Charge Separation in Densely Packed Donor-Acceptor Coordination Cages', M. Frank, J. Ahrens, I. Bejenke, M. Krick, D. Schwarzer, G. H. Clever, *J. Am. Chem. Soc.* **2016**, *138*, 8279.

VI. LIGHT-INDUCED CHARGE SEPARATION IN DONOR-ACCEPTOR MIXED-LIGAND DOUBLE-CAGES

VI.1 Introduction

The incorporation of photoactive and/or electroactive components into supramolecular architectures can modify the ground and excited state properties of the individual components resulting in novel properties. Therefore, supramolecular redoxactive donor-acceptor pairs have gained interest since they posses some beneficial attributes that are needed for advanced and future technologies such as molecular electronics and photovoltaic devices.[116] In particular the latter experienced a rapid growth in the last decade due to a high interest for alternative energy sources compared to the fossil-based fuels.[117] The challenge is thereby to find appropriate donor-acceptor combinations that are able to mimic the natural photophysical and photochemical processes and can convert solar energy efficiently into electric energy.[118] Until the present day, organic photovoltaic devices are suffering of lower quantum efficiency compared to the silicon-based solar cells.[119] In order to overcome this drawback, the organic solar cells need a large area for proper operation, which results in higher installation costs. Besides this, many donor-acceptor systems tend to decompose over the time. On the other hand, the organic solar cells have many advantages such as low cost production regarding the avoidance of high-temperature production procedures and low material input.[120]

Figure VI.1 shows a simplified scheme of an organic solar cell based on donor/acceptor layers.[121] The donor system is usually based on organic carbon substances with a conjugated

---

[116] G. Bottari, O. Trukhina, M. Ince, T. Torres, *Coord. Chem. Rev*. **2012**, *256*, 2453.

[117] T.R. Cook, D. K. Dogutan, S. Y. Reece, Y. Surendranath, T. S. Teets, D. G. Nocera, *Chem. Rev.* **2010**, *110*, 6474.

[118] (a) D. Gust, T. A. Moore, A. L. Moore, *Acc. Chem. Res.* **2001**, *34*, 40. (b) V. Balzani, A. Credi, M. Venturi, *ChemSusChem* **2008**, *1*, 26. (b) P. Ceroni, *The Exploration of Supramolecular Systems and Nanostructures by Photochemical Techniques*, *78*, Springer, **2012**.

[119] A. M. Bagher, *International Journal of Renewable and Sustainable Energy* **2014**, *3*, 53.

[120] (a) A. Hagfeldt, G. Boschloo, L. Sun, L. Kloo, H. Pettersson, *Chem. Rev.* **2010**, *110*, 6595. (b) C. W. Schlenker, M. E. Thompson, *Top. Curr. Chem.* **2012**, *312,* 175. (c) T. M. Clarke, J. R. Durrant, *Chem. Rev.* **2010**, *110*, 6736.

[121] A. Mishra, P. Bäuerle, *Angew. Chem. Int. Ed.***2012**, *51*, 2020.

π-system. Upon irradiation with light, the photoactive donor molecule occupies an excited state, which subsequently leads to a release of an electron. The electron is rapidly transferred to the acceptor molecule. The charge separated state is a meta-stable state due to often fast charge-recombination and other competing processes. If the charge transfer to the electrodes is faster than the back transfer between the donor and acceptor units, then the charge can be collected and guided forward to electrical devices. A high efficiency of the charge transport is achieved for donor-acceptor systems which are arranged in an ordered way. Therefore, an appropriate orientation of the donor/acceptor components with respect to each other should be taken into account, when new materials for photovoltaic applications are developed.[122]

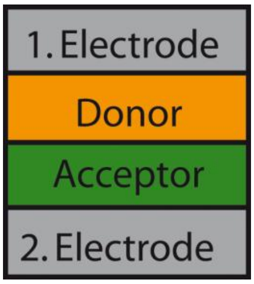

Figure VI.1 Schematic representation of a multi-layer solar cell.

In the past several donor-acceptor systems were designed for applications in photovoltaic devices.[123] Amongst them redox-active organic dye molecules have gained high interest due to various possibilities of synthetic derivatization, which can help to tune the absorption range and the electrochemical potential. For example, phenothiazine-based donor and anthraquinone-based acceptor molecules are widely found in literature.[124]

---

[122] (a) H. Bässler, A. Köhler *Top. Curr. Chem.* **2012**, *312,* 1. (b) P. Ceroni, A. Credi, M. Venturi, *Chem. Soc. Rev.* **2014**, *43*, 4068.

[123] A. Das, S. Ghosh, *Angew. Chem. Int. Ed.* **2014**, *53*, 2038.

[124] for phenothiazine-based donor molecules see (a) P. C. Dwivedi, K. Gurudath Rao, S. N. Bhat, C. N. R. Rao, *Spectrochimica Acta* **1975**, *31A*, 129. (b) R. Lopez, A. M. Leiva, F. Zuloaga, B. Loeb, E. Norambuena, K. M. Omberg, J. R. Schoonover, D. Striplin, M. Devenney, T. J. Meyer, *Inorg. Chem.* **1999**, *38*, 2924. (d) A. W. Franz, F. Rominger, T. J. J. Müller, *J. Org. Chem.* **2008**, *73*, 1795. (e) L. Zhu, D. Magde, J. K. Whitesell, M. A. Fox, *Inorganic Chemistry*, **2009**, *48*, 1811.
for anthraquinone-based acceptor molecules see (a) E. H. van Dijk, D. J. T. Myles, M. H. van der Veen, J. C. Hummelen, *Org. Lett.*, **2006**, *8*, 2334. (b) D. Ajloo, B. Yoonesi, A. Soleymanpour, *Int. J. Electrochem. Sci.*,**2010**, *5*, 459. (c) A. E. Murschell, W. Hay Kan, V. Thangadurai, T. C. Sutherland, *Phys. Chem. Chem. Phys*. **2012**, *14*, 4626. (d) N. Seidel, T. Hahn, S. Liebing, W. Seichter, J. Kortus, E. Weber, *New J.Chem.,* **2013**, 37, 601.

Müller and co-workers could show that arranging of a phenothiazine-based (PTZ) building block **45** in close proximity to an anthraquinone-based (ANQ) unit **46** affords a system which is able to undergo a photoinduced intramolecular electron-transfer.[125] Electrochemical investigations showed that the redox properties of the phenothiazine/anthraquinone-based dyad **47** are very similar to the reference compounds, which contain either the phenothiazine or the anthraquinone backbone. They concluded that the redox units PTZ and ANQ do not affect each other within the PTZ/ANQ dyad in the ground state. The ground-state-decoupled chromophores were analysed by the UV/Vis absorption spectrum (see Figure VI.2a). The spectrum of the PTZ/ANQ dyad could be reconstructed from the sum of the distinct spectra of the PTZ and ANQ building blocks. Excitation of the ANQ chromophore and the subsequent femtosecond transient absorption spectroscopic study revealed an electron transfer from the PTZ to the ANQ unit resulting in an charge separated state of $PTZ^{+\cdot}$ and $ANQ^{-\cdot}$. The successful formation of the charge-separated state was shown via the comparison of the absorption spectrum of the PTZ/ANQ compound to the sum of the radical absorption spectra of the PTZ and ANQ containing reference compounds (see Figure VI.2b). A fast decaying (within 1 ps) singlet charge-separated diradical and a moderately decaying (within 2 ns) triplet charge-separated diradical states could be identified.

---

for combination of phenothiazine and anthraquinone within one donor-acceptor molecule see (a) S. L. Mecklenburg, D. C. McCafferty, J. R. Schoonover, B. M. Peek, B. W. Erickson, T. J. Meyer, *Inorg. Chem.* **1994**, *33*, 2974. (b) D. R. Striplin, S. Y. Reece, D. G. McCafferty, C. G. Wall, D. A. Friesen, B. W. Erickson, T. J. Meyer, *J. Am. Chem. Soc.* **2004**, *126*, 5282. (c) W.-W. Zhang, W.-L. Mao, Y.-X. Hu, Z.-Q. Tian, Z.-L. Wang, Q.-J. Meng, *J. Phys. Chem. A* **2009**, *113*, 9997.

[125] S. Bay, T. Villnow, G. Ryseck, V. Rai-Constapel, P. Gilch, T. J. J. Müller *ChemPlusChem* **2013**, *78*, 137.

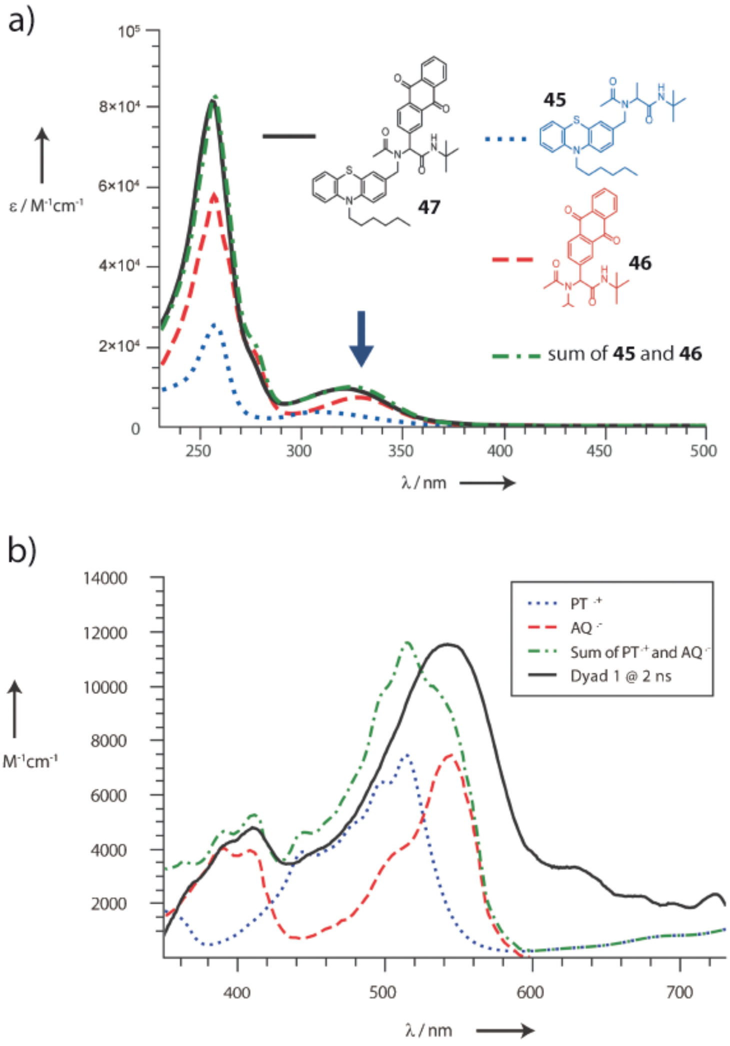

Figure VI.2 a) Ground state absorption spectra of the phenothiazine/anthraquinone compound **47** (black line), the phenothiazine building block **45** (blue dotted line) and the anthraquinone building block **46** (red dashed line). The sum of the spectra of the phenothiazine and the anthraquinone building blocks is shown by the green dash-dotted line. The blue arrow shows the wavelength, which was used for the excitation in transient absorption spectroscopy. b) Corresponding transient absorption spectrum at 2 ns delay time. Reproduced with permission from reference [125]. Copyright © 2013 WILEY-VCH Verlag GmbH & Co.

Introduction of electrochemical properties into supramolecular coordination architectures is not always as easy to realize due to the many contributing factors such as the choice of the metal nodes, which may take part in the electrochemical process, the choice of the solvent, temperature and counter anions. Nevertheless many examples of electroactive self-assembled rings[126] and cages[127] and other supramolecular metal-coordinated compounds[128] were published in the past decades. Some examples of redoxactive coordination cages will be presented below.

Würthner and co-workers reported the self-assembly of a $M_4\mathbf{L}_6$ tetrahedron cage based on octahedral Fe(II) ions and linear perylene bisimide (PBI) dyes with attached 2,2'-bipyridine groups (see Figure VI.3a).[129] The photo- and redoxactivity of the PBI units is maintained upon incorporation of the ligands into the metallosupramolecular host. The supramolecule exhibits a wide-range visible-light absorption. Besides this, the supramolecular host shows seven highly reversible electrochemical oxidation and reduction waves within a range of 3.0 V (see Figure VI.3b). The first oxidation occurs on the Fe^{2+} centers, which are converted to the Fe^{3+} ions. The second oxidation process is assigned to the PBI -> PBI^+ transformation. The first two reduction processes can be ascribed to the successive reduction of the PBI units (PBI -> PBI^- -> PBI^{2-}). The last three reduction waves are characteristic for the reduction of the bipyridine units. The electrochemical behavior of the tetrahedral host was compared to the reference compound $[Fe(bpy)_3]^{2+}$. This study revealed, that the oxidation waves are not significantly affected by the self-assembly into the tetrahedral host, but the reduction processes were found to be more favorable compared to the $[Fe(bpy)_3]^{2+}$ compound. Upon this observation the authors concluded that the close proximity of the highly electron-deficient PBI units within the tetrahedron causes an electronic communication between the ligands and the metal ions in the tetrahedra. In total this tetrahedral host can undergo a cycle of 34 electron redox processes. The cycle between +18 and -16 charged species proceeds without degradation, which is attributed to

---

[126] (a) H. B. Yang, K. Ghosh, Y. Zhao, B. H. Northrop, M. M. Lyndon, D. C. Muddiman, H. S. White, P.J. Stang, *J. Am. Chem. Soc.* **2008**, *130*, 839. (b) M. Frasconi, T. Kikuchi, D. Cao, Y. Wu, W.-G. Liu, S. M. Dyar, G. Barin, A. A. Sarjeant, C. L. Stern, R. Carnieli, C. Wang, M. R. Wasielewski, W. A. Goddart, J. F. Stoddart, *J. Am. Chem. Soc.* **2014**, *136*, 11011. (c) M. Juricek, J. C. Barnes, N. L. Strutt, N. A. Vermeulen, K. C. Ghooray, E. J. Dale, P. R. McGonigal, A. K. Blackburn, A.-J. Avestro, J. F. Stoddart, *Chem. Sci.* **2014**, *5*, 2724.

[127] (a) P. H. Dinolfo, V. Coropceanu, J.-L. Bredas, J. T. Hupp, *J. Am. Chem. Soc.* **2006**, *128*, 12592. (b) J. S. Park, E. Karnas, K. Ohkubo, P. Chen, K. M. Kadish, S. Fukuzumi, C. W. Bielawski, T. W. Hudnall, V. M. Lynch, J. L. Sessler, *Science* **2010**, *329*, 1324. (c) D. Bhattacharya, C.-H. Chang, Y.-H. Cheng, L.-L. Lai, H.-Y. Lu, C.-Y. Lin, K.-L. Lu, *Chem. Eur. J.* **2012**, *18*, 5275. (d) V. Croue, S. Goeb, M. Salle, *Chem. Commun*. **2015**, *51*, 7275.

[128] (a) P. L. Boulas, M. Gomez-Kaifer, L. Echegoyen, *Angew. Chem. Int. Ed*. **1998**, *37*, 216. (b) A. Kaifer, M. Gomez-Kaifer, Supramolecular Chemistry **1999**, Weinheim. (c) C. A. Nijhhuis, B. J. Ravoo, J. Huskens, D. N. Reinhooudt, *Coord. Chem. Rev*. **2007**, *251*, 1761

[129] K. Mahata, P. D. Frischmann, F. Würthner, *J. Am. Chem. Soc.* **2013**, *135*, 15656.

the porous nature of the tetrahedron (internal volume >950 Å^3) allowing the counter anions to flow freely in and out of the host.[129]

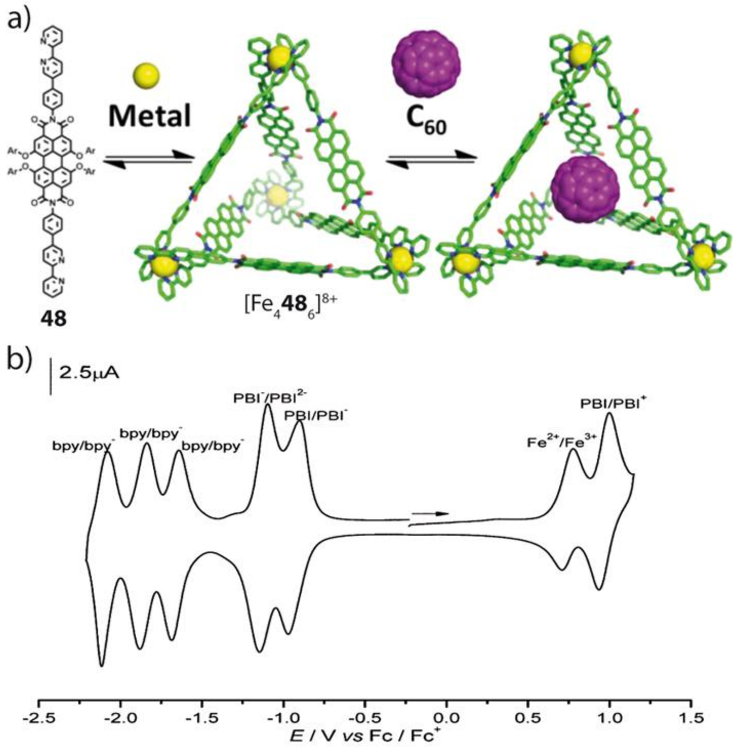

Figure VI.3 a) Self-assembly of the PBI-based ligand **48** with Fe(II) ions into the tetrahedral cage [Fe$_4$**48**$_6$]$^{8+}$. b) Cyclic voltammogram of the tetrahedral cage in CH_3CN in presence of 0.1 M n-Bu_4NPF_6 as supporting electrolyte, scan rate 200 mV·s^{-1}, Ag/AgCl reference electrode. The values are given with regard to Fc/Fc$^+$. Reproduced with permission from reference [129]. Copyright © 2013 American Chemical Society.

Another example of an electroactive supramolecular coordination cage was reported by Stang *et al.*[130] They used ditopic Pt(II) acceptors **49** with bite angles of 120°, which were equipped with ferrrocenyl units, in combination with linear tritopic donor ligands **50** in a ratio of 3:2 (see Figure VI.4a). The resulting cuboctahedral cage contains 12 ferrocene units at the vertexes. In contrast to the previous example, this cage was not equipped with electroactive backbone ligands, but the electroactive groups were attached to the periphery of the cage. The cyclic voltammograms of the multiferrocene cuboctahedral cage showed a single redox wave indicating the lack of interactions among the ferrocene redox centers (see Figure VI.4b). Besides, they observed a large potential difference between the anodic and

---

[130] K. Ghosh, J. M. Hu, H. S. White, P. J. Stang, *J. Am. Chem. Soc.* **2009**, *131*, 6695.

the cathodic peak potentials of 81 ± 8 mV, which is larger than the theoretical value of 59 mV (25 °C). Two explanations for this were considered: either it can be attributed to the ohmic resistance of the solution or to multielectron transfer processes. Steady-state current response measurements with a Pt disc electrode gave a Δ*E* value of 61 mV indicating that the redox centers react independently and are oxidized at the same time. ^{1}H NMR study of the cuboctahedral cage before and after the redox process revealed that the cage was not destroyed upon the redox cycle.

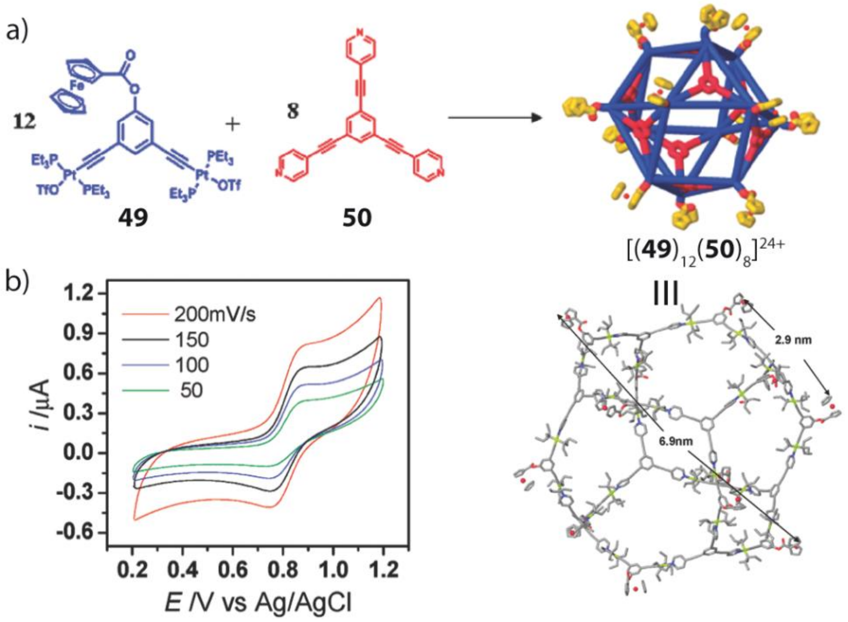

Figure VI.4 a) Self-assembly of building blocks **49** and **50** into the cuboctahedral cage $[(\mathbf{49})_{12}(\mathbf{50})_8]^{24+}$. b) Cyclic voltammogram of the cuboctahedral cage in acetone in presence of 0.1 M n-Bu_4NPF_6 as supporting electrolyte, scan rate 50-200 $mV \cdot s^{-1}$, 1 mm^2 Pt electrode. Reproduced with permission from reference [130]. Copyright © 2009 American Chemical Society.

A similar approach of peripheral functionalization of the self-assembled cage was followed by the group of Crowley and co-workers.[131] They have shown that the self-assembly of tripyridyl ligands **51** containing attached electroactive groups with Pd(II) cations affords the $[Pd_2\mathbf{51}_4]^{4+}$ monomeric cage which can undergo electrochemical reactions (see Figure VI.5a). All electroactive ligands and corresponding cages showed irreversible reductions at ca. -1.7 V and -1.9 V, which are attributed to the 2,6-bis(ethynyl)pyridine

---

[131] J. E. M. Lewis, A. B. S. Elliott, C. J. McAdam, K. C. Gordon, J. D. Crowley, *Chem. Sci*. **2014**, *5*, 1833.

moiety. In case of ligands with a phenyl residue and the corresponding cage no further reductions occured due to the lack of further electroactive groups. Whereas for ligands with a ferrocene residue and the corresponding cage an additional reversible one-electron oxidation process at approximately 0.5 V was observed (see Figure VI.5b). Further functionalized derivatives equipped with moieties such as caffeine and *fac*-[(2-(1-*R*-1H-1,2,3-triazole-4-yl)pyridine)Re(CO)$_3$Cl] and 4-amino-1,8-naphtalimides showed that the oxidation and reduction potentials are not affected by the coordination of the ligands to the Pd(II) centers. Furthermore, no electronic communication was observed between the redox centers within the cage structure.

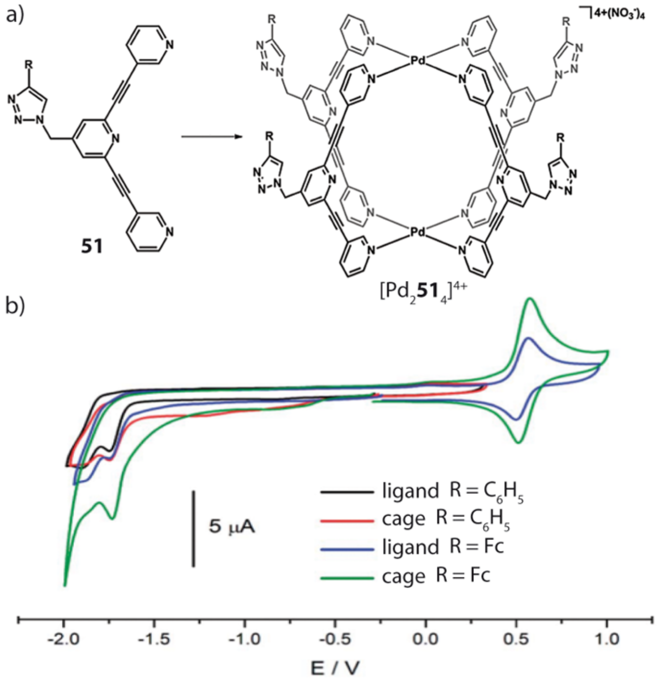

Figure VI.5 a) Self-assembly of ligand **51** with different functional groups R with Pd(II) cations into the $[Pd_2\mathbf{51}_4]^{4+}$ cage. b) Cyclic voltammogram of the ligands and cages in DMF solution in the presence of n-Bu_4NPF_6 as supporting electrolyte with decamethylferrocene $(Fc^*)^{+/0}$ as reference. Reproduced with permission from reference [131]. Copyright © 2014 Royal Society of Chemistry.

An interesting example of a functionalized cage with redoxactive ligand backbones and non redoxactive metals was shown by Salle and co-workers.[132] They used bis-(pyrrolo)tetrathiafulvalene (BPTTF)-based tetratopic ligands **52** which coordinated to

---

[132] S. Bivaud, J.-Y. Balandier, M. Chas, M. Allain, S. Goeb, M. Salle, *J. Am. Chem. Soc.* **2012**, *134*, 11968.

square-planar Pt(II) metal cations yielding the trigonal prismatic cage [Pt_4**52**$_3$]$^{8+}$ (see Figure VI.6a). Cyclic voltammetry of the cage showed two successive oxidation processes. Both redox waves of the cage are shifted by approximately 0.4 V to higher potential compared to the bis(pyrrolo)tetrathiafulvalene (BPTTF). This behavior can be explained by the interaction of the ligands with the metal nodes, which decrease the π-electron-donor abilities of the ligands compared to the BPTTF. The redox processes show poor electrochemical reversibility, which is attributed to the rigidity of the cage structure affecting the kinetics of the electron transfer.

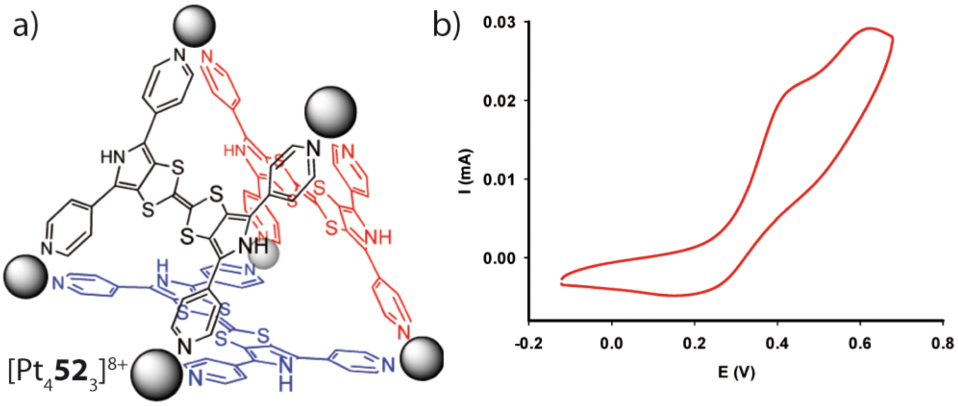

Figure VI.6 a) Self-assembly of the TTF based ligand **52** with Pt(II) metals into the trigonal prismatic cage [Pt_4**52**$_3$]$^{8+}$ b) Cyclic voltammogram of the cage in CH_3CN solution in presence of 0.1 M n-Bu_4NPF_6 as supporting electrolyte, scan rate 50 mV·s^{-1}, the values are given with respect to Fc/Fc^{+}. Reproduced with permission from reference [131]. Copyright © 2012 American Chemical Society.

Only a few examples for three dimensional coordination compounds comprising donor as well as acceptor molecules with photoinduced charge transfer (PET) properties can be found in literature, presumably due to challenging arrangement of the donor and acceptor units within the supramolecular structure. Fujita and co-workers reported about an electron-deficient triazine-based host which is able to act as an electron acceptor.[133,134] A photoinduced electron transfer was observed from the host molecule towards an enclosed adamantane guest molecule which reacts further into oxidized products, 1-adamantyl hydroperoxide and 1-adamantanol (see Figure VI.7a). The proposed PET mechanism was

---

[133] M. Yoshizawa, S. Miyagi, M. Kawano, K. Ishiguro, M. Fujita, *J. Am. Chem. Soc.* **2004**, *126*, 9172.

[134] Y. Furutani, H. Kandori, M. Kawano, K. Nakabayashi, M. Yoshizawa, M. Fujita, *J. Am. Chem. Soc.* **2009**, *131*, 4764.

based on experimental results from in situ IR and UV spectroscopy, electrochemistry and theoretical calculations. First indications for a PET were observed in the photolysis experiment of the host-guest complex which resulted in a blue color of the solution that immediately disappeared upon exposure of the sample to air (see Figure VI.7b). The blue color can be assigned to the radical reduced species of the cage. Control experiments showed that the empty host and the free guest do not react under photolytic conditions. Thus, the close proximity of the bound adamantane and the triazine panels within the host-guest complex is responsible for the occurrence of the PET phenomenon.

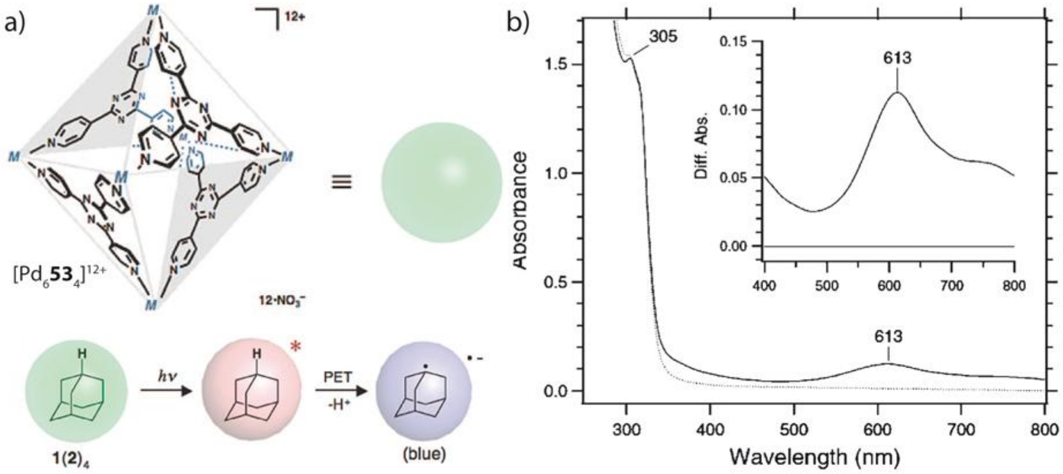

Figure VI.7 a) Proposed PET mechanism for the photoxidation of adamantane within the cavity of the cage $[Pd_4\mathbf{53}_4]^{12+}$. b) UV/Vis absorption spectra before and after UV irradiation of the host-guest complex. Reproduced with permission from reference [134]. Copyright © 2009 American Chemical Society.

Goodson and co-workers reported about two-dimensional metallacycles as well as a three-dimensional metallacage which they applied for the study of charge transfer dynamics and the rate of intersystem crossing in metallacycles of different geometries and dimensions.[135] The metallacycles are based on either anthracene or phenanthrene side walls and Pt metal cations, whereas the metallacage was build from anthracene and trispyridine building blocks coordinated to Pt metal nodes (see Figure VI.8a). Steady-state, femtosecond upconversion and transient absorption spectroscopic techniques were applied, which indicated an intramolecular charge transfer resulting in charge-separated

---

[135] D. C. Flynn, G. Ramakrishna, H.-B. Yang, B. H. Northrop, P. J. Stang, T. Goodson, *J. Am. Chem. Soc.* **2010**, *132*, 1348.

species. Transient absorption experiments showed the appearance of new absorption peaks around 600 and 750 nm after excitation at 390 nm (see Figure VI.8b). The lifetimes of the charge separation and recombination was estimated by a biexponential decay with time-constants of 1.1 and 32.2 ps at 600 nm (see Figure VI.8c). Although the cage structure is more complex than the two-dimensional metallacycles, the dynamics of the electron transfer were found to be very similar in both cases.[135]

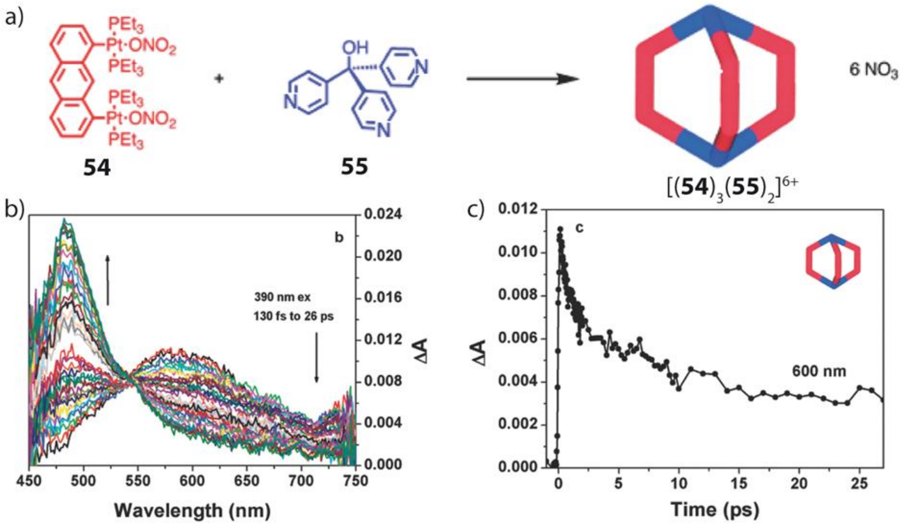

Figure VI.8 a) Self-assembly of the building blocks **54** and **55** to the metallacage $[(\mathbf{54})_3(\mathbf{55})_2]^{6+}$. b) transient absorption spectrum and c) transient absorption kinetics of the metallacage $[(\mathbf{54})_3(\mathbf{55})_2]^{6+}$. Reproduced with permission from reference [135]. Copyright © 2010 American Chemical Society.

VI.2 Project Target

In order to construct novel donor/acceptor double-cages, a new acceptor ligand based on anthraquinone (ANQ), which is capable of forming a double-cage assembly, was designed. Phenothiazine and anthraquinone combinations are attractive redox systems because of their reversible and tunable oxidation/reduction potentials. Intramolecular photoinduced charge transfer (PCT) based on this combination was successfully demonstrated in the past,[125] but not yet for a self-assembled structure. The goal in the first step was to realize a double-cage comprising an electron-rich and an electron poor building block within one structure. In the second step, the mixed donor/acceptor assembly should be studied regarding beneficial properties such as electron or energy transfer, which can result from the interplay of the donor/acceptor units. For this reason, a full spectroscopic and electrochemical characterization of the donor/acceptor double-cages was envisioned including the study via fluorescence and UV/Vis spectroscopic techniques, via cyclic voltammetric and spectroelectrochemical analysis, and finally by femtosecond transient spectroscopy. In order to confirm that the properties are characteristic for the donor/acceptor double-cage and do not arise from individual components, all results for donor/acceptor double-cage should be compared to the properties of the individual homomeric double-cages.

VI.3 Results and Discussion[136]

For this study, a new banana-shaped bismonodentate pyridyl ligand comprising the electron poor anthraquinone backbone was designed. The ligand was shown to assemble successfully into a double-cage. Based on observations reported in Chapter V that (1) double-cages can incorporate more than one kind of ligand as long as they are of comparable length and (2) preformed homomeric double-cages are kinetically hindered from exchanging ligands when mixed in solution, new mixed-ligand double-cages containing both donor as well as acceptor building blocks were synthesized (see Figure VI.9). In this Chapter, the photo- and redox-properties of the following systems will be investigated: (i) pure solutions of either double-cage species, (ii) mixtures of homomeric double-cages and (iii) mixed-ligand double-cages existing as mixtures of all statistical combinations of the two ligands. The phenothiazine based ligand $\mathbf{L}^2$ will be named as **D** and the new anthraquinone based ligands as **A’** ($\mathbf{L}^6$) and **A** ($\mathbf{L}^7$).

---

[136] M. Frank, J. Ahrens, I. Bejenke, M. Krick, D. Schwarzer, G. H. Clever, *J. Am. Chem. Soc.* **2016**, *138*, 8279.

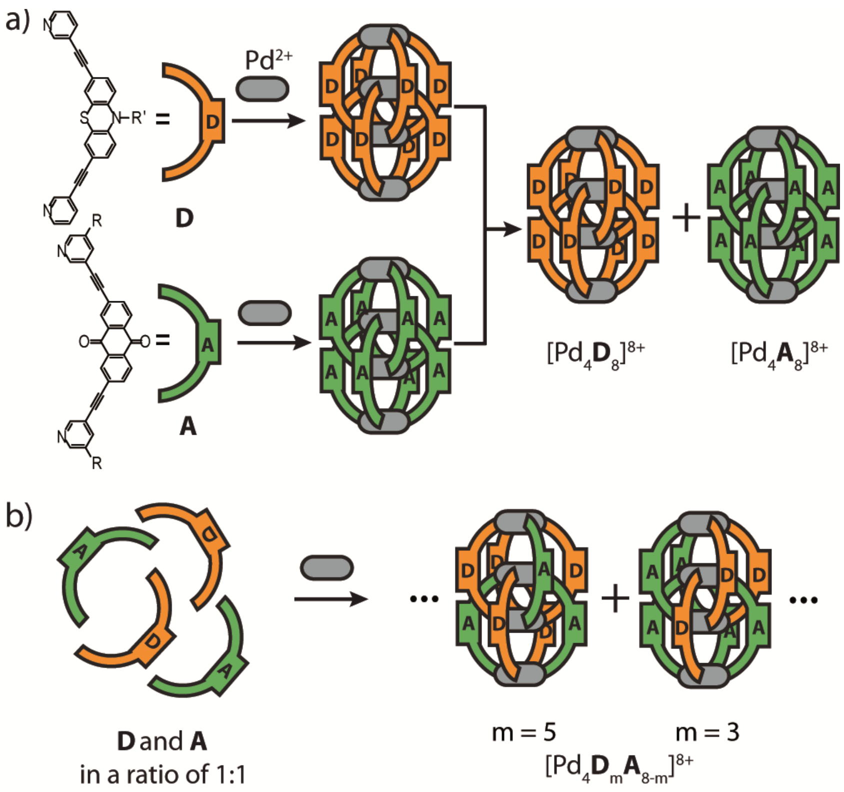

Figure VI.9 a) Mixture of homo-octameric double-cages $[Pd_4\mathbf{D}_8]^{8+}$ and $[Pd_4\mathbf{A}_8]^{8+}$ constructed from ligands **D** and **A**, and $[Pd(CH_3CN)_4](BF_4)_2$ as metal source. b) Mixed-ligand double-cages $[Pd_4\mathbf{D}_m\mathbf{A}_{8\text{-}m}]^{8+}$ (m = 8…0) were constructed from a solution of both ligands **D** and **A** mixed in a ratio of 1:1 and $[Pd(CH_3CN)_4](BF_4)_2$ as metal source. The ligands in $[Pd_4\mathbf{D}_m\mathbf{A}_{8\text{-}m}]$ are statistically distributed. R' = Hexyl chain. R = H for ligand **A'** and R = OEtOEtOMe for ligand **A**. Anions inside the three pockets as well as the counter anions were omitted for clarity. Reproduced with permission from reference [136]. Copyright © 2016 American Chemical Society.

The syntheses of ligand **D** and its corresponding double-cage $[Pd_4\mathbf{D}_8]^{8+}$ were described previously in Chapter 3. The new ligand derivatives **A'** and **A** based on the anthraquinone backbone were prepared in four and seven steps, respectively. The synthesis started with a simultaneous nitration and oxidation of the commercially available anthrone with fuming nitric and acetic acid. A reduction of the nitro groups with sodium sulfide and subsequent Sandmeyer reaction yielded the 2,7-Dibromo-9,10-anthraqinone building block (see Figure VI.10). Finally, the Sonogashira cross-coupling reaction with 3-ethynylpyridine (for **A'**) or 3-ethynyl-5-(2-(2-methoxyethoxy)ethoxy)pyridine (for **A**) gave the final ligands (for synthetic protocols and characterization data see Appendix VI Section 1). Ligand **A’** containing polyethyleneglycol chains was synthesized in order to enhance the solubility in acetonitrile.

The successful synthesis of both ligands **A'** and **A** was verified via ^{1}H NMR spectroscopy (see Figure VI.11 (a) and (c)) and mass spectrometric analysis (see Appendix VI Section 1).

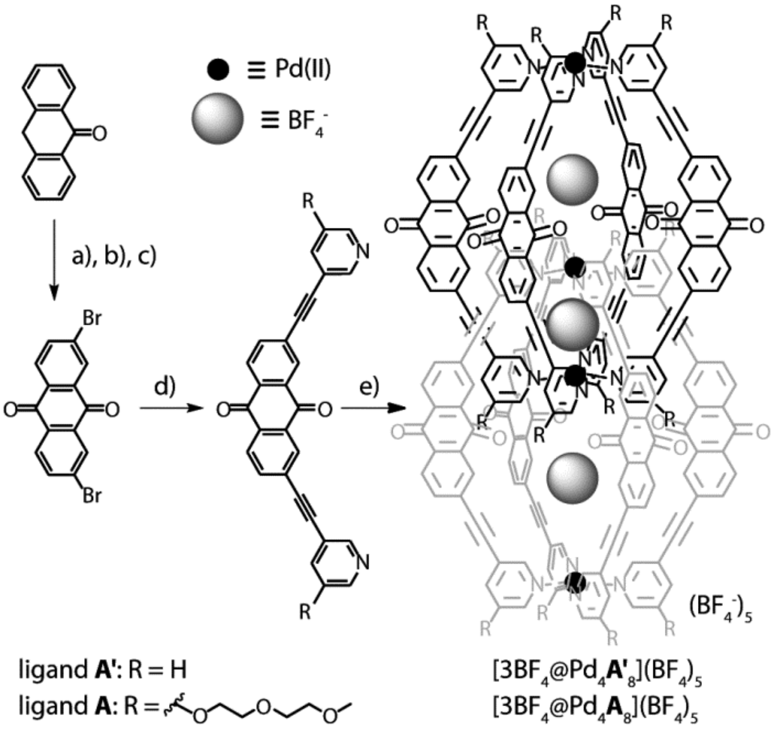

Figure VI.10 Synthetic route to the ligands **A'** and **A**. a) fuming HNO_3, acetic acid; b) Na_2S, NaOH, EtOH/H_2O; c) CuBr, $tBuNO_2$, HCl; d) CuI, $Pd(PPh_3)_2Cl_2$, NEt_3, 3-ethynylpyridine or 3-ethynyl-5-(2-(2-methoxyethoxy)ethoxy)-pyridine; and self-assembly to the double-cages [3BF$_4$@Pd$_4$**A'**$_8$](BF$_4$)$_5$ and [3BF$_4$@Pd$_4$**A**$_8$](BF$_4$)$_5$ e) d3-acetonitrile 70 °C [Pd(CH$_3$CN)$_4$](BF$_4$)$_2$. Reproduced with permission from reference [136]. Copyright © 2016 American Chemical Society.

Unfortunately, both anthraquinone-based ligands **A'** and **A** were found to be insoluble in acetonitrile. Nevertheless, heating the ligand solutions with 0.5 equivalents of [Pd(CH$_3$CN)$_4$](BF$_4$)$_2$ at 70 °C for 12 h in acetonitrile resulted in the quantitative formation of the interpenetrated double-cages as was confirmed by ^{1}H NMR spectroscopy (Figure VI.11 (b) and (d)) and high resolution mass spectrometry (see Appendix VI Section 1). The double cage [3BF$_4$@Pd$_4$**A'**$_8$]$^{5+}$ was still suffering from low solubility in acetonitrile. Therefore, further experiments were mainly performed with the better soluble double-cage [3BF$_4$@Pd$_4$**A**$_8$]$^{5+}$. The ^{1}H NMR spectra of the double-cages showed a splitting of all ^{1}H NMR signals into two sets of equal intensity as it was previously observed for all double-cage species.[16,18,19] The ^{1}H NMR signals of the pyridine arm showed a strong downfield shift, which is characteristic for coordination of the ligands to the electron-deficient Pd(II) cations. The high resolution

ESI mass spectra revealed the presence of penta-, tetra- and tricationic species corresponding to interpenetrated double-cages. Since no crystals suitable for X-ray structure analysis could be obtained, a DFT (ωB97XD/def2-SVP level) model of the double-cage $[3BF_4@Pd_4\mathbf{A}_8]^{5+}$ was developed based on the previously reported crystal structures of double-cages (see Appendix Section 2).[16,18,19] Calculation results indicated a highly symmetric double-cage structure, which has three internal cavities. The Pd-Pd distances for the outer pockets as well as for the inner pocket were found to be in agreement with the distances reported for similar double-cages.[16,18,19]

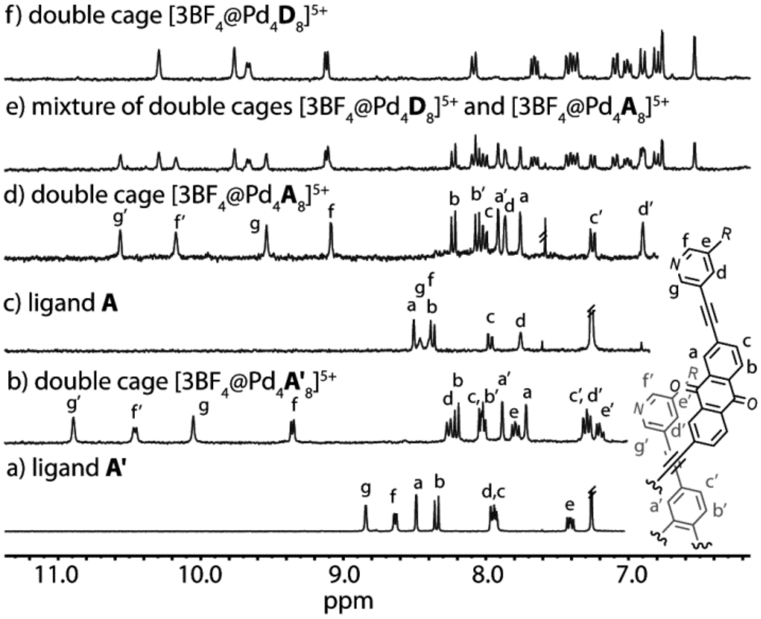

Figure VI.11 ^{1}H NMR spectra (300 MHz, 298 K) of (a) ligand **A'** ($CDCl_3$); (b) double-cage $[3BF_4@Pd_4\mathbf{A'}_8]^{5+}$ (CD_3CN); (c) ligand **A** ($CDCl_3$); (d) double-cage $[3BF_4@Pd_4\mathbf{A}_8]^{5+}$ (CD_3CN); (e) mixture of homo-octameric double-cages $[3BF_4@Pd_4\mathbf{D}_8]^{5+}$ and $[3BF_4@Pd_4\mathbf{A}_8]^{5+}$ in a ratio of 1:1 (CD_3CN); (f) double-cage $[3BF_4@Pd_4\mathbf{D}_8]^{5+}$ (CD_3CN). Reproduced with permission from reference [136]. Copyright © 2016 American Chemical Society.

Next, a mixture of homomeric double-cages $[3BF_4@Pd_4\mathbf{D}_8]^{5+}$ and $[3BF_4@Pd_4\mathbf{A}_8]^{5+}$ was prepared. Therefore the acetonitrile solutions of preassembled double-cages were mixed in one vessel in a ratio of 1:1. Figure V.11e shows the ^{1}H NMR spectrum of the mixture of homomeric double-cages $[3BF_4@Pd_4\mathbf{D}_8]^{5+}$ and $[3BF_4@Pd_4\mathbf{A}_8]^{5+}$. The signals in the ^{1}H NMR spectrum can be assigned to individual cage protons of the each double-cage (compare Figure VI.11e to VI.11d and VI.11f). This shows that both double-cage species can co-exist as a metastable mixture in solution without significantly exchanging ligands with respect to the applied experimental timescale. As was shown in Chapter V, the mixture of two homomeric double-cages is stable for several hours at room temperature. The ESI-HR mass spectrum of the mixed homomeric double-cages $[3BF_4@Pd_4\mathbf{D}_8]^{5+}$ and $[3BF_4@Pd_4\mathbf{A}_8]^{5+}$ showed clear signals for the distinct double-cage species. No signals for species with exchanged ligands were observed within the time period of the measurements, which confirmed the kinetic stability of the homomeric double-cage mixture (see Figure VI.12a). Nevertheless, fresh solutions of the mixed homomeric double-cages were prepared prior to every measurement in order to avoid their disassembly.

The mixed-ligand double-cages $[3BF_4@Pd_4\mathbf{D}_m\mathbf{A}_{8\text{-}m}]^{5+}$ (m = 8…0) were synthesized starting from the mixture of the ligands **D** and **A** in a ratio of 1:1 and subsequent addition of the $[Pd(CH_3CN)_4](BF_4)_2$ salt to the solution of the premixed ligands. The reaction solution was heated to 70 °C for 12 h. The ^1H NMR spectrum of the mixed-ligand double-cages showed very broad signals in the region where characteristic signals of the double-cages appear. The broadening can be attributed to the statistical distribution of both ligands within the double-cages and hence numerous different proton environments (Figure AP-VI.6 and AP-VI.12). ESI high resolution mass spectrum of the mixed-ligand double-cages clearly identified species with a statistical distribution of the ligands obeying the formula $[3BF_4@Pd_4\mathbf{D}_m\mathbf{A}_{8\text{-}m}]^{5+}$ (m = 8…0) (see Figure VI.12b).

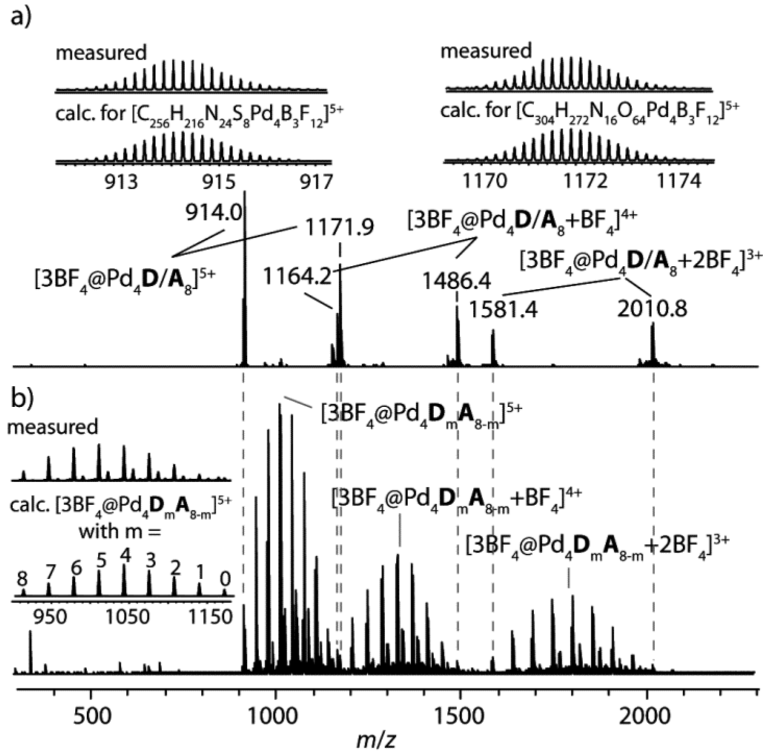

Figure VI.12 ESI mass spectra of a) mixture of homo-octameric double-cages $[3BF_4@Pd_4\mathbf{D}_8]^{5+}$ and $[3BF_4@Pd_4\mathbf{A}_8]^{5+}$ in a ratio of 1:1 and b) mixed-ligand double-cages $[3BF_4@Pd_4\mathbf{D}_m\mathbf{A}_{8-m}]^{5+}$ (m = 8…0) with statistical distribution of ligands. Reproduced with permission from reference [136]. Copyright © 2016 American Chemical Society.

Figure VI.13 shows the ground-state absorption spectra in acetonitrile. All double-cage species show two main absorption maxima. The first intense maximum around 295 nm is probably dominated by intraligand π-π^* transitions. The second less intense absorption maximum is very broad. It is found at 408 nm for the double-cage $[3BF_4@Pd_4\mathbf{D}_8]^{5+}$ and at 365 nm for the double-cage $[3BF_4@Pd_4\mathbf{A}_8]^{5+}$. The spectrum of the mixed homomeric double-cages $[3BF_4@Pd_4\mathbf{D}_8]^{5+}$ and $[3BF_4@Pd_4\mathbf{A}_8]^{5+}$ can be perfectly reconstructed from the sum of the spectra of each single double-cage in a ratio of 1:1 (for calculations of other ratios see Appendix VI Section 3). On the other hand, the steady-state UV/Vis spectrum of mixed-ligand double-cages $[3BF_4@Pd_4\mathbf{D}_m\mathbf{A}_{8-m}]^{5+}$ (m = 8…0) could not be reconstructed from the absorption spectra of the homomeric double-cages. In particular, the region from 350 nm to 500 nm deviates from the sum of the absorption spectra of the homomeric species. This result indicated that the mixed-ligand double cages show a different behavior in solution than the mixture of homomeric double-cages.

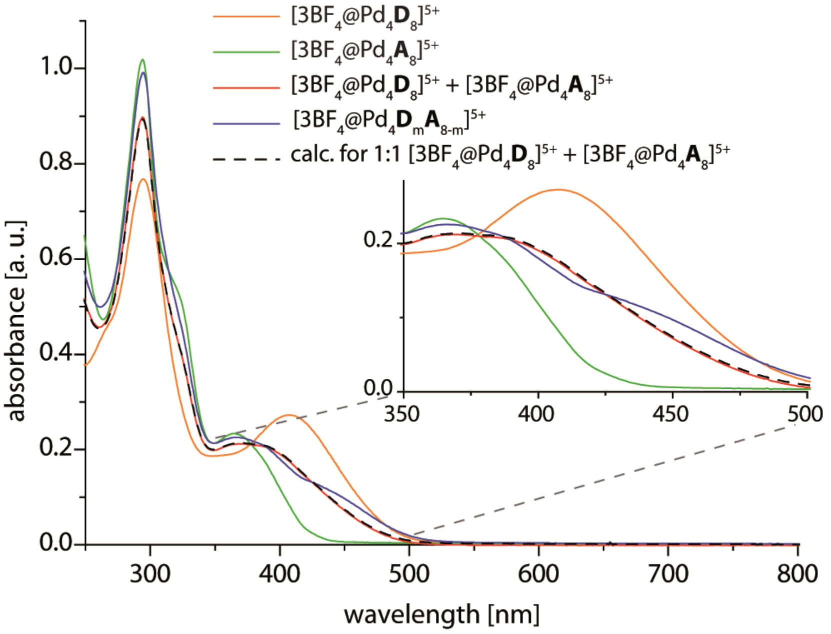

Figure VI.13 UV/Vis spectra of double-cages $[3BF_4@Pd_4\mathbf{D}_8]^{5+}$ (20 µM in CH_3CN, orange line) and $[3BF_4@Pd_4\mathbf{A}_8]^{5+}$ (20 µM in CH_3CN, green line), their mixture (10 µM each in CH_3CN, red line) and mixed-ligand double-cages $[3BF_4@Pd_4\mathbf{D}_m\mathbf{A}_{8-m}]^{5+}$ with m = 8…0 (20 µM in CH_3CN, blue line) with statistical distribution of ligands. The spectrum for the mixture of homo-octameric double-cages $[3BF_4@Pd_4\mathbf{D}_8]^{5+}$ and $[3BF_4@Pd_4\mathbf{A}_8]^{5+}$ (dashed black line) in a ratio of 1:1 can be calculated from the measured single spectra of the double-cages (cuvette path length: 0.1 cm in all cases). Reproduced with permission from reference [136]. Copyright © 2016 American Chemical Society.

In the next step, the redox-abilities of the double-cages were studied. First, it was confirmed that the double-cage composed of donor building blocks $[3BF_4@Pd_4\mathbf{D}_8]^{5+}$ does not decompose upon the redox process since the oxidation of the already cationic double-cage may lead to a Coulomb driven disassembly. Therefore, the stability of the double-cage $[3BF_4@Pd_4\mathbf{D}_8]^{5+}$ was studied after chemical oxidation and reduction reactions, which were monitored by ^{1}H NMR and UV/Vis spectroscopy (see Figure VI.14). All eight donor ligands in the double-cage $[3BF_4@Pd_4\mathbf{D}_8]^{5+}$ were stoichiometrically oxidized in acetonitrile with $[Fe(III)bpy_3](BF_4)_3$ and afterwards reduced with Zn powder (for titrations see Chapter III). Figure VI.14a shows the UV/Vis spectrum of the oxidation/reduction cycles (the spectrum of the formed $[Fe(II)bpy_3]^{2+}$ cation was subtracted; for stepwise oxidation see Appendix – Chapter VI Section 4). After first oxidation, new bands in the visible region appeared in the spectrum. One sharp peak with a maximum at 525 nm and a very broad peak with a maximum around 680 nm were observed. These bands are characteristic for the absorption caused by the radical cation of phenothiazine and are assigned to the species $[3BF_4@Pd_4\mathbf{D}^{(\bullet+)}{}_8]^{13+}$. The color of the solution changed after the oxidation from yellow to dark brown. In order to reduce the radical species back to the double-cage $[3BF_4@Pd_4\mathbf{D}_8]^{5+}$, Zn powder was added to the solution. After reduction, the bands above 500 nm disappeared and the band around 400 nm was recovered. A new band at 387 nm did not vanish upon reduction, probably indicating a partial *S*-oxygenation of the oxidized double-cage (see Chapter III).[65] One oxidation/reduction cycle was performed within a time window of about ten minutes. The spectrum after the oxidation/reduction cycles showed characteristic features of the initial spectrum of the double-cage and not that of the free ligand. This indicated the integrity of the double-cage structure. The second oxidation/reduction cycle showed a similar behavior as the first one. These results suggest that the majority of the double-cages survive the redox cycle.

Further indication for the integrity of the double-cage upon oxidation was demonstrated by ^{1}H NMR spectroscopy (see Figure VI.14b). After oxidation of the double-cage

$[3BF_4@Pd_4\mathbf{D}_8]^{5+}$, all signals disappeared from the spectrum indicating the presence of the paramagnetic double-cage $[3BF_4@Pd_4\mathbf{D}^{(\bullet+)}{}_8]^{13+}$. The characteristic ^{1}H NMR signal pattern of the non-oxidized double-cage was recovered after reduction with Zn powder. The redox cycle can be repeated several times. Upon the ongoing study, the intensities of the double-cage signals decreased with each oxidation/reduction cycle. This indicates a possible decomposition or oxygenation of the double-cage during the oxidation/reduction cycles. The accumulation of oxygenation products after each cycle was observed by ESI mass spectrometry, which shows that a significant ratio of the double-cages survives the relatively harsh oxidation conditions. (see Figure AP-VI.20). No disassembly of the double-cages to smaller fragments or even release of free ligand was observed in the spectra within the duration of the experiments.

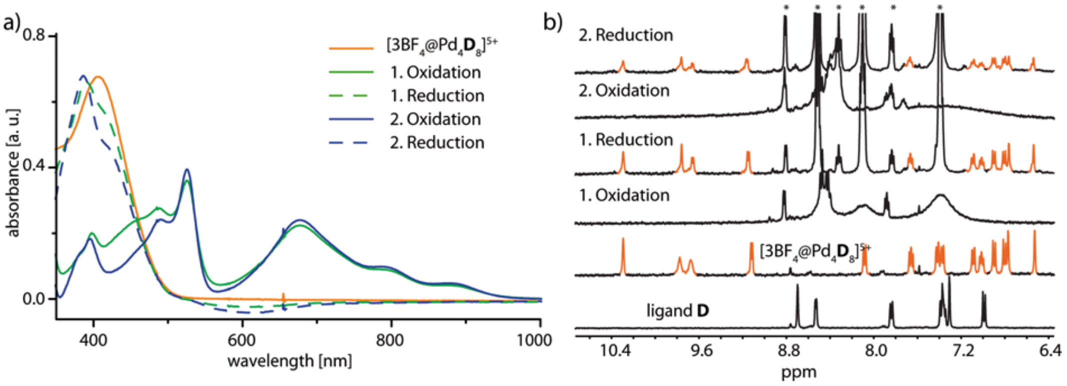

Figure VI.14 Chemical oxidation of the $[3BF_4@Pd_4\mathbf{D}_8]^{5+}$ double-cage in acetonitrile with $[Fe(bpy)_3](BF_4)_3$ and subsequent re-reduction with Zn powder followed by a) UV-Vis spectroscopy (UV/Vis spectrum of $[Fe(II)(bpy)_3](BF_4)_2$ was subtracted) and b) ^{1}H NMR spectroscopy (400 MHz, 298 K, CD_3CN). * denotes signals coming from $[Fe(II)(bpy)_3](BF_4)_2$ and free bpy. Reproduced with permission from reference [136]. Copyright © 2016 American Chemical Society.

Next, cyclic voltammetry measurements were performed on the solutions of the free ligands and the double-cages (see Appendix VI Section 5). One quasi-reversible redox wave was observed in the voltammograms of the donor-based double-cage $[3BF_4@Pd_4\mathbf{D}_8]^{5+}$ as well as of the corresponding free ligand **D** (see Figure VI.15a). A shift to more positive potential compared to the free ligand could be observed in case of the double-cage (+0.13 V in CH_3CN and +0.12 V in CH_2Cl_2). This shift can be assigned to the coordination of the electron-rich ligands to the cationic Pd(II) centers. Further oxidations occur on a higher potential scale and show characteristics of an irreversible oxidation. The irreversibility indicates further reaction pathways such as the previously shown oxygenation with water molecules (see Chapter III). The double-cage $[3BF_4@Pd_4\mathbf{A}_8]^{5+}$ and the ligand **A** were studied in a dichloromethane solution due to precipitate of the double-cage in acetonitrile upon addition of the electrolyte salt. Both substances showed two quasi-reversible redox waves (see Figure VI.15b). Thereby, the first reduction wave of the double-cage $[3BF_4@Pd_4\mathbf{A}_8]^{5+}$ was shifted by 0.10 V and the second by 0.14 V to more negative potential compared to the free ligand **A**. Interestingly, the mixed-ligand double-cages $[3BF_4@Pd_4\mathbf{D}_m\mathbf{A}_{8-m}]^{5+}$ show nearly the same oxidation and reduction potentials as the homomeric double-cages (see Table VI.1). This indicates that the donor and acceptor units do not strongly feel each other in the electronic ground state.

Table VI-1 Cyclic voltammetry parameters. Reproduced with permission from reference [136]. Copyright © 2016 American Chemical Society.

Compound	E_{ox} *[V]*	E_{red1} *[V]*	E_{red2} *[V]*
Ligand **D**	0.39^a		
	0.41^b		
$[3BF_4@Pd_4\mathbf{D}_8]^{5+}$	0.52^a		
	0.53^b		
Ligand **A**		-1.25^b	-1.70^b
$[3BF_4@Pd_4\mathbf{A}_8]^{5+}$		-1.35^b	-1.84^b
$[3BF_4@Pd_4\mathbf{D}_m\mathbf{A}_{8-m}]^{5+}$	0.48^b	-1.30^b	-1.72^b

The measurements were performed [a] in dry CH_3CN or [b] in dry CH_2Cl_2. All values are given with regard to Fc/Fc^+.

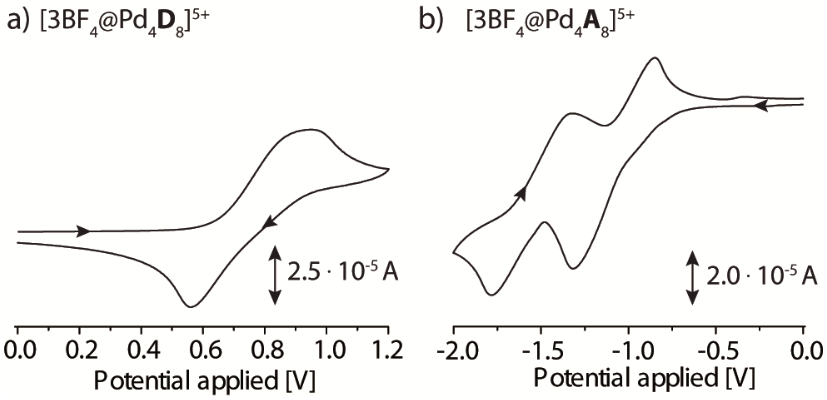

Figure VI.15 Cyclic voltammograms recorded at a glassy carbon working electrode against a $Ag/AgNO_3$

reference electrode of a) $[3BF_4@Pd_4\mathbf{D}_8]^{5+}$ (1 mM in CH_2Cl_2) and b) $[3BF_4@Pd_4\mathbf{A}_8]^{5+}$ (1 mM in CH_2Cl_2). Supporting electrolyte: 0.1 M $[NBu_4][PF_6]$. Scan rate: 100 mV·s^{-1}. Reproduced with permission from reference [136]. Copyright © 2016 American Chemical Society.

Clean UV/Vis spectra of radical double-cage species were not accessible by chemical oxidation/reduction due to the presence of waste products and the oxidation agent. Furthermore, no suitable reducing agent could be found for the chemical reduction of the acceptor-based double-cage $[3BF_4@Pd_4\mathbf{A}_8]^{5+}$. Therefore, the radical species were characterized by spectroelectrochemical measurements. For this, a thin layer cell (1 mm optical path length) including a Pt gauze and a $Ag/AgNO_3$ reference electrode together with a diode array spectrophotometer were applied for the experiment (for further experimental details and measured spectra see Appendix VI Section 6). The absorption spectrum of the donor double-cage $[3BF_4@Pd_4\mathbf{D}^{(\bullet+)}{}_8]^{13+}$ obtained via electrochemical oxidation was very similar to the spectrum obtained by chemical oxidation (see Figures VI.16). Characteristic peaks at around 525 nm (sharp peak) and around 680 nm (broad peak) were found by application of both oxidation methods. After the electrochemical reduction of the acceptor based double-cage $[3BF_4@Pd_4\mathbf{A}_8]^{5+}$ a broad absorption band around 700 nm appeared indicating the reduced $[3BF_4@Pd_4\mathbf{A}^{(\bullet-)}{}_8]^{3-}$ species (see Figure AP-VI.26). The UV/Vis spectrum of the electrochemically oxidized and reduced mixed-ligand double-cage $[3BF_4@Pd_4\mathbf{D}_m\mathbf{A}_{8\text{-}m}]$ was very similar (see Figure AP-VI.27) to those obtained for the homomeric double-cages. This observation supports the results from cyclic voltammetry, where the mixed-ligand double-cages showed the same redox behavior as the homomeric double-cages.

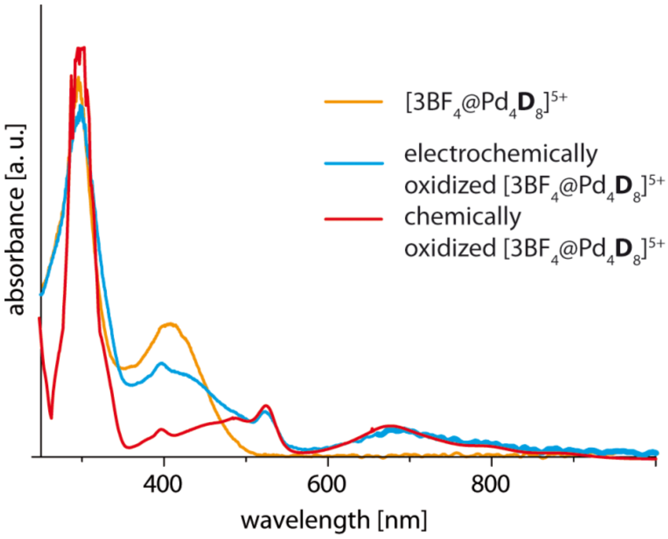

Figure VI.16 Comparison of UV/Vis spectra of electrochemically and chemically oxidized double-cage $[BF_4@Pd_4\mathbf{D}_8]^{5+}$. Reproduced with permission from reference [136]. Copyright © 2016 American Chemical Society.

Next,[137] femtosecond pump-probe spectroscopic analysis was performed for the homo-octameric double-cages, their mixture and the mixed-ligand double-cages. Pump pulses in the range 385-440 nm were chosen for the experiments which are in the absorption area of electron acceptor and donor components (see Figure VI.13). Time-resolved processes were monitored in the UV/Vis between 350 and 730 nm by measuring transient absorption changes using a white-light continuum (for further details see Appendix VI Section 7). The result of the transient absorption spectroscopic analysis for the excitation of the mixed-ligand double-cage $[3BF_4@Pd_4\mathbf{D}_m\mathbf{A}_{8-m}]^{5+}$ is shown in Figure VI.17. It is compared to the results obtained from the spectroelectrochemical experiments of the oxidized $[3BF_4@Pd_4\mathbf{D}^{(\bullet+)}{}_8]^{13+}$ and reduced $[3BF_4@Pd_4\mathbf{A}^{(\bullet-)}{}_8]^{3-}$ double-cages. Thereby, the absorption spectrum of the mixed-ligand double-cage measured 100 ps after excitation at 385 nm shows a similar absorption characteristics as the sum of radicals of the homomeric double-cages, thus indicating a charge separated state. Furthermore, the pump-probe transient absorption study showed that only in case of mixed-ligand double-cages a stable charge separated state was formed (see Appendix – Chapter VI Section 7).

---

[137] The femtosecond pump-probe studies were performed by Jennifer Ahrens and Prof. Dirk Schwarzer from Max-Planck-Institute for Biophysical Chemistry, Am Fassberg 11, 37077 Göttingen (Germany).

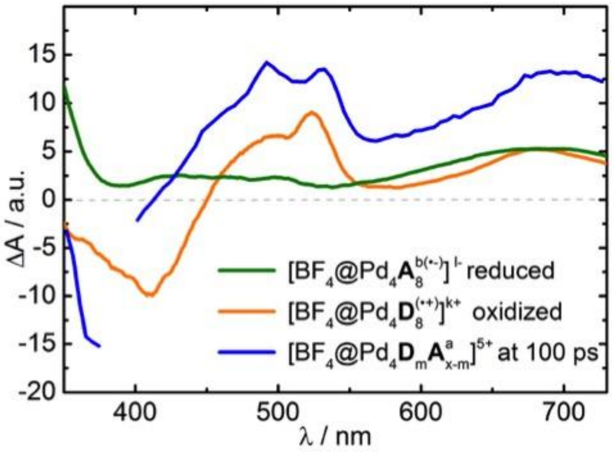

Figure VI.17 Electrochemically generated difference absorption spectra for the oxidized $[3BF_4@Pd_4\mathbf{D}^{(\bullet+)}{}_8]$ and reduced $[3BF_4@Pd_4\mathbf{A}^{(\bullet-)}{}_8]$ species are compared with a transient absorption spectrum measured 100 ps after 385 nm excitation of the mixed-ligand cage $[3BF_4@Pd_4\mathbf{D}_m\mathbf{A}_{8-m}]^{5+}$ (m = 0…8). Reproduced with permission from reference [136]. Copyright © 2016 American Chemical Society.

VI.4 Conclusion

Herein, a novel supramolecular mixed-ligand coordination architecture, which combines an electron donor and an electron acceptor unit within one densely packed interpenetrated double-cage, was presented. The steady state UV-Vis spectrum of the mixed-ligand double-cages provided first indication for interactions between the donor and acceptor units in the double-cage. On the other hand, no signs for electronic communication between the donor and acceptor components were observed for the mixture of the homomeric double-cages. Furthermore, it was shown that the donor homomeric double-cage, consisting of eight phenothiazine donors and four Pd(II) nodes, survives the oxidation of up to eight donor sites without immediate degradation. With the help of electrochemical and spectroelectrochemical analysis and femtosecond transient absorption spectroscopy it could be shown that a light-induced charge transfer occurs in mixtures which contain donor and acceptor units. Furthermore, it was demonstrated that only in case of the mixed-ligand double-cages with close proximity of the donor and acceptor units a stable charge separated state was feasible. The herein presented design of donor/acceptor double-cages may be further attractive for the development of photoactive materials with controlled morphology.

Chapter VII

Stability of Double-Cages on Surfaces

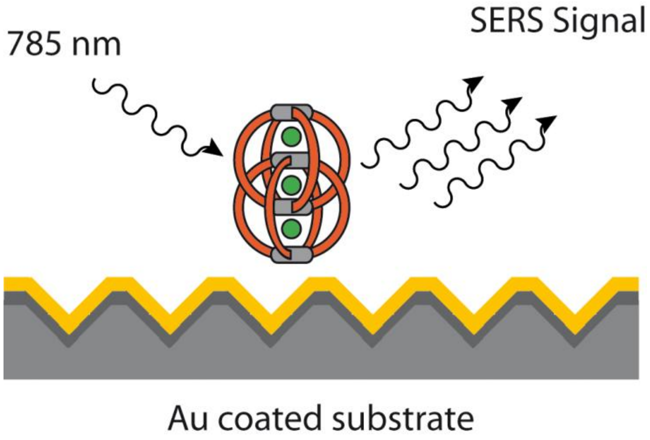

Reproduced with permission from reference [143]. Copyright © 2014 PCCP Owner Societies.

This chapter corresponds to the following publication:

- 'SERS spectroscopic evidence for the integrity of surface-deposited self-assembled coordination cages', M. Frank, S. Funke, H. Wackerbarth and G. H. Clever*, Phys. Chem. Chem. Phys.* **2014***, 16,* 21930-21935.

VII. STABILITY OF DOUBLE-CAGES ON SURFACES

VII.1 Introduction

The supramolecular self-assembled systems are usually studied in solution phase or as bulk materials. Nevertheless, for some applications such as electrochemical devices the mounting of the supramolecular assemblies as thin films on surfaces can result in beneficial properties.[138]

SERS (Surface Enhanced Raman Scattering) can be a very helpful tool for analysis of surface deposited analyte molecules due to characteristic signal patterns and high sensitivity compared to other techniques such as conventional Raman spectroscopy.[139] The enhancement factor of SERS spectroscopy is based on two contributions: one is the electromagnetic enhancement mechanism (EM) and the other is the chemical enhancement mechanism (CE) (see Figure VII.1). The electromagnetic enhancement results from the interaction of photons with the rough metal surface inducing an excitation of localized plasmons on the surface. Thus, the adsorbate should be positioned within a certain distance in respect to the nanostructured surface. This can be achieved by either drop coating the analyte directly on the bare metal surface or by adsorption via chemical interactions on a functionalized surface. The intensity of Raman scattering is directly proportional to the square of the induced dipole moment, which is the product of the Raman polarizability and the magnitude of the magnetic field. In total, the electromagnetic enhancement scales to the fourth power of the electromagnetic field, which results in an enhancement in the range of 10^3-10^{10}. This electromagnetic enhancement is a purely physical effect, which accounts by far the most dominant contribution part of the enhancement. The EM enhancement is strictly dependent on the nanostructure properties

---

[138] (a) T. D. Nguyen, H. R. Tseng, P. C. Celestre, A. H. Flood, Y. Liu, J. F. Stoddart, J. I. Zink, *Proc. Natl. Acad. Sci. U. S. A.*, **2005**, *102*, 10029. (b) N. Miyashita, D. G. Kurth, *J. Mater. Chem.*, **2008**, *18*, 2636. (c) N. Lin, S. Stepanow, M. Ruben, J. V. Barth, *Top. Curr. Chem.*, Springer Verlag Berlin Heidelberg **2008**. (d) T. Kudernac, S. Lei, J. A. A. W. Elemans, S. De Feyter, *Chem. Soc. Rev.*, **2009**, *38*, 402. (e) A. G. Slater, P. H. Beton, N. R. Champness, *Chem. Sci.*, **2011**, *2*, 1440. (f) Y. Ishida, R. Kulasekharan, T. Shimada, V. Ramamurthy, S. Takagi, *J.Phys. Chem. C* **2014**, *118*, 10198.

[139] (a) K. Kneipp, H. Kneipp, I. Itzkan, R. R. Dasari, M. S. Feld, *J. Phys.: Condens. Matter* **2002**, *14*, R597. (b) M. Moskovits, *J. Raman Spectrosc.*, **2005**, *36*, 485. (c) Z. Q. Tian, *J. Raman Spectrosc.*, **2005**, *36*, 466. (d) W. E. Smith, *Chem. Soc. Rev*. **2008**, *37*, 955.

(shape, size and dielectric properties of the metal) and indifferently applies to all analytes. The chemical enhancement accounts for an enhancement of up to 10^3. The chemical enhancement can have its origins in charge transfer (CT) between the electronic ground state of the adsorbate and the metal surface, which results in a change of polarizability of the molecule and thus a change of the Raman scattering. Another possible chemical enhancement contribution may arise from the resonant excitation of electronic transitions of the adsorbate coupled with the photoinduced charge transfer mechanism. Further technical developments allowed for detection of even single molecules on the surface, which drove forward the industrial applications of SERS due to its high sensivity. The nanostructured surface should fulfill some requirements such as chemical stability, easy of preparation, reproducibility and spatial uniformity. Silver and gold surfaces were proven to give the best results since they provide broad and intense plasmon resonances in the visible infrared region, which is the wavelength of interest for Raman spectroscopy.[140] The accessibility of well-defined SERS substrates, either via the top-down approach involving nanolithography techniques or the bottom-up methods involving chemical synthesis of nanoparticles capable of assembling into well-defined substrates, made this analytical tool also well reproducible resulting in a broad range of analytical applications.[141]

---

[140] L. Guerrini, D. Graham, *Chem. Soc. Rev.* **2012**, *41*, 7085.

[141] (a) P. L. Stiles, J. A. Dieringer, N. C. Shah, R. P. Van Duyne, *Annu. Rev. Anal. Chem.*, **2008**, *1*, 60. (b) S. Schlücker, *Angew. Chem. Int. Ed.*, **2014**, *53*, 4756.

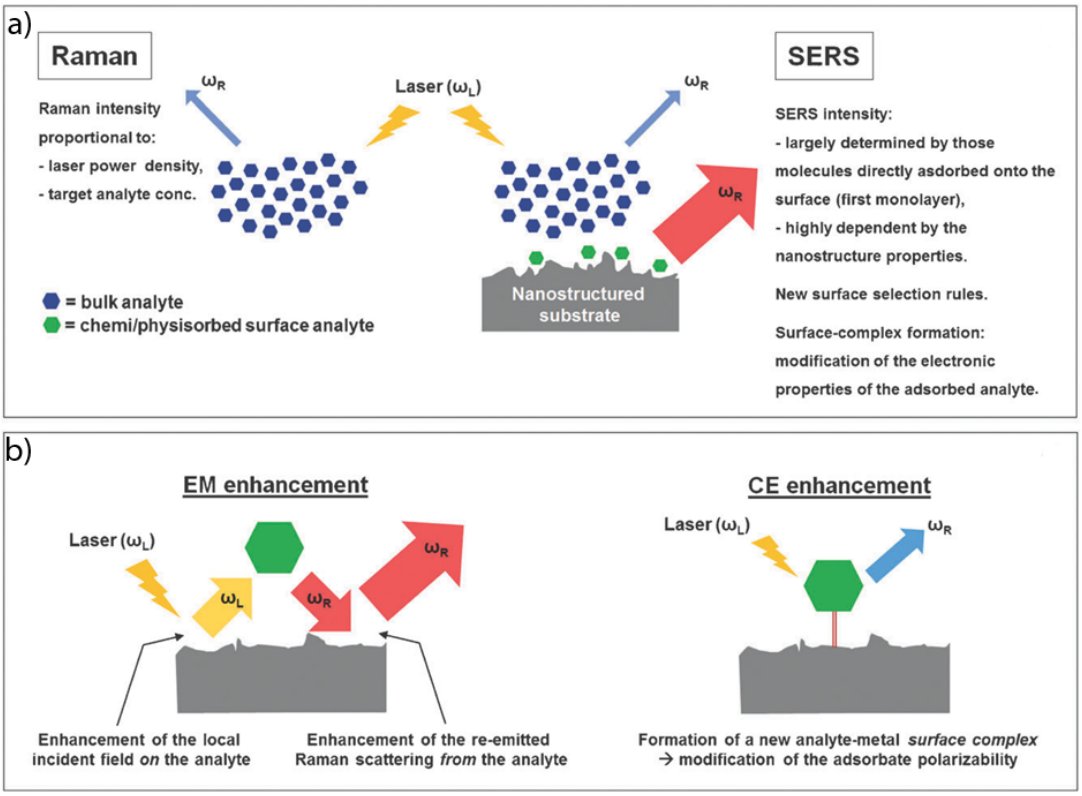

Figure VII.1 (a) Schematic comparative representation of the Raman and SERS phenomena. (b) Schematic representation of the electromagnetic and chemical enhancements in SERS. Reproduced with permission from reference [140]. Copyright © 2012 Royal Society of Chemistry.

Apart from the developments of the analytical tools, the examples of self-assembled three-dimensional and highly charged coordination compounds on surfaces or even surface-supported self-assembly are still rare. One example was reported by Reinhoudt and co-workers.[142] They showed the surface-supported self-assembly of a coordination cavitand comprising four alkylthioether groups at the lower rim and four tolylpyridine groups at the upper rim, which coordinated either to a Pd or a Pt metal source via pyridine arms (see Figure VII.2a). The attachment of alkyl chains to the ligands was necessary for binding the analyte cages to the modified gold surface in order to analyze them via the TM-AFM (Tapping Mode Atomic Force Microscopy) spectroscopy (see Figure VII.2b). They could show that it is not only possible to deposit these assemblies on a surface, but it is also possible to assemble the coordination compounds on a surface in a stepwise manner. Additionally they

---

[142] E. Menozzi, R. Pinalli, E. A. Speets, B. J. Ravoo, E. Dalcanale, D. N. Reinhoudt, *Chem. – Eur. J.*, **2004**, *10*, 2199.

could show that with this method, they can obtain heterodimeric capsules with different substituents in the upper and lower rim.

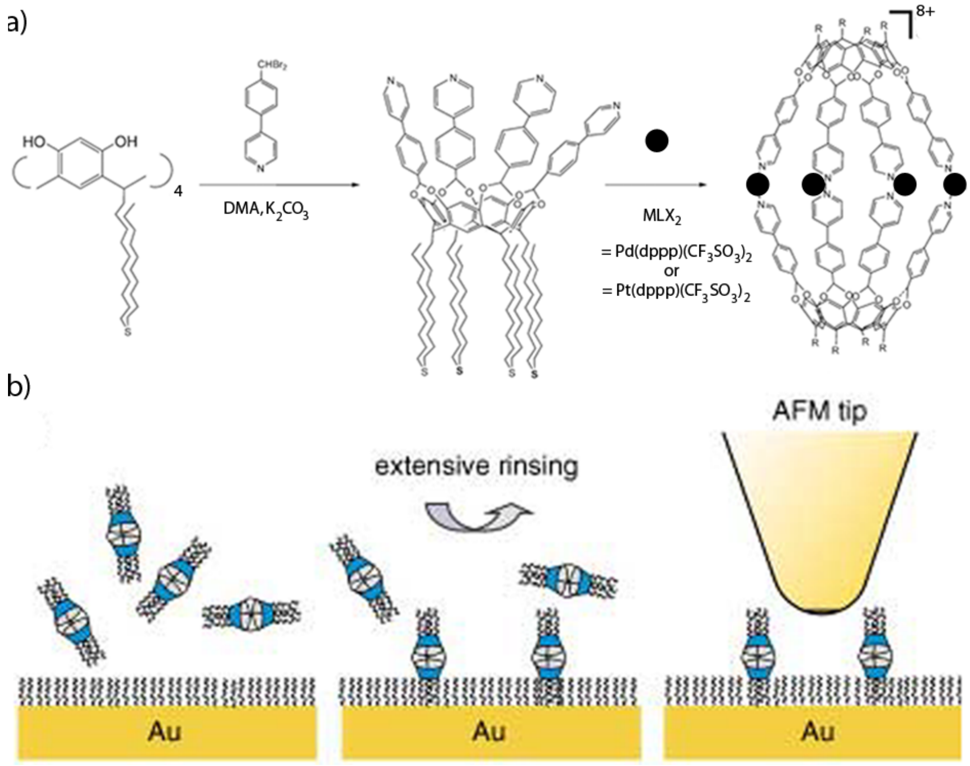

Figure VII.2 a) Synthesis of the cavitand ligand and self-assembly of nanosize coordination cages. b) Schematic representation of the deposition of the cages on the modified gold surface. Reproduced with permission from reference [142]. Copyright © 2004 WILEY-VCH Verlag GmbH & Co.

VII.2 Project Target

The study of the stability of double-cages after deposition on surfaces is of particular interest considering possible applications of double-cages in surface–mounted functional supramolecular materials. For this purpose, spectroscopic analysis via SERS (Surface Enhanced Raman Scattering) is a suitable tool to give insights into structural features of the double-cages. To proof the integrity of double-cages deposited on a surface, the SERS spectra should be compared to the Raman spectra in solution, where the integrity was previously confirmed via ^{1}H NMR spectroscopy. Also the comparison to the Raman and SERS spectra of the free ligand can be helpful to exclude the decomposition of the double-cage into the metal ions and free ligands.

VII.3 Results and Discussion[143]

For the study on the integrity of double-cages, the double-cages $[3BF_4@Pd_4\mathbf{L}^n{}_8]^{5+}$ with n = 1, 2, 3 were prepared from corresponding ligands $\mathbf{L}^2$, $\mathbf{L}^3$ and $\mathbf{L}^4$ via previously described procedure (see Chapter III). After the synthesis of double-cages in solution (acetonitrile as solvent), the double-cage solutions were deposited on a gold coated silicon substrate comprising a nanostructured surface (Klarite, Renishaw Diagnostics Ltd.). The nanostructured motif consists of periodic ordered inverted pyramids (~1.5 µm wide and ~1 µm deep) (see Figure VII.1).[144,145] After complete evaporation of the solvent, indicated by the lack of acetonitrile signals in the spectra, the double-cages remained as a thin film on the surface. Subsequently SERS spectra were recorded via application of a 785 nm (line width 0.06 nm) GaAlAs diode laser. The amplifying effect of the nanostructured surface was proven by control measurements on a planar Au surface (see Appendix AP-VII.2).

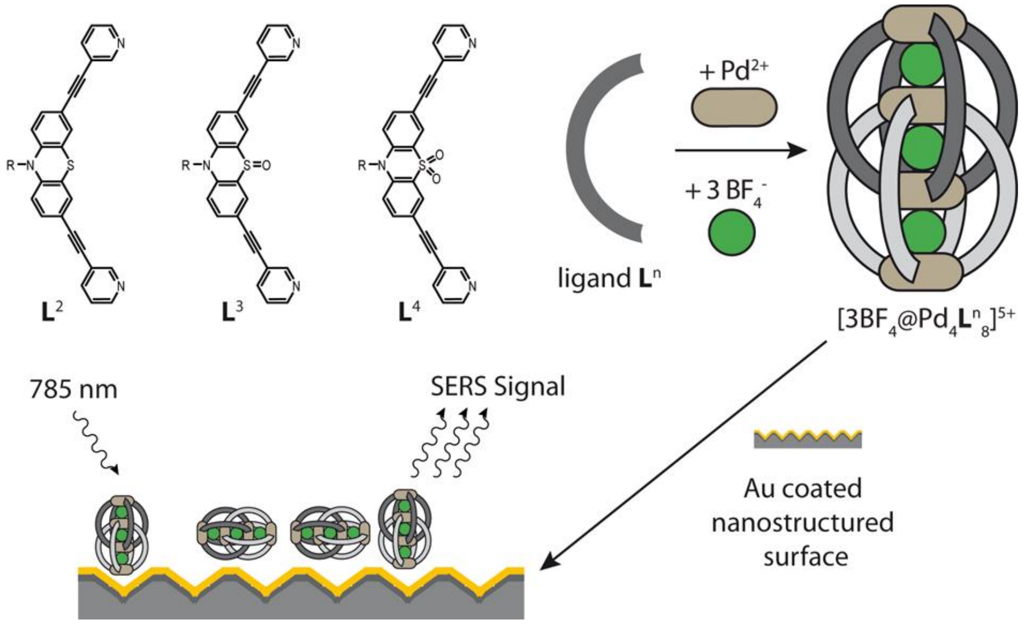

Figure VII.3 Structure of phenothiazine based ligands $\mathbf{L}^n$ and their reaction to the corresponding double-cage $[3BF_4@Pd_4\mathbf{L}^n{}_8]^{5+}$ with n = 1, 2, 3. Schematic representation of the random deposition of double-cages on a gold

---

[143] M. Frank, S. Funke, H. Wackerbarth and G. H. Clever*, Phys. Chem. Chem. Phys.* **2014***, 16,* 21930.

[144] H. Wackerbarth, C. Salb, L. Gundrum, M. Niederkrüger, K. Christou, V. Beushausen, W. Viöl, *Appl. Opt*. **2010**, *49*, 4362.

[145] N. M. B. Perney, J. J. Baumberg, M. E. Zoorob, M. D. B. Charlton, S. Mahnkopf, C. M. Netti, *Opt. Express* **2006**, *14*, 847.

coated nanostructured surface. The size of the double-cages (length 2.5 – 2.6 nm) is enlarged compared to the size of the inverted pyramidal (ground square 1.4 x 1.4 µm) structured surface of the metal. Reproduced with permission from reference [143]. Copyright © 2014 PCCP Owner Societies.

Figure VII.4 shows the results of the SERS measurement for the double-cage $[3BF_4@Pd_4\mathbf{L}^2{}_8](BF_4)_5$. The SERS spectra were compared to the Raman spectra recorded in acetonitrile solution. Both spectra show a very similar signal pattern with similar signal intensities and width. Similar results were obtained for the double-cages $[3BF_4@Pd_4\mathbf{L}^3{}_8](BF_4)_5$ and $[3BF_4@Pd_4\mathbf{L}^4{}_8](BF_4)_5$ (see Appendix AP-VII.5). The small differences between the SERS and solution Raman spectra may be contributed to the different distribution of guest and counteranions in the solid state and in solution. While in the solution state the encapsulated BF_4^- anions can exchange with the anions in the bulk solution, this anion interchange is restricted in the solid state. Also electrostatic interaction with the solvent molecules may affect the vibrations of the double-cage in solution state. For this reason, Raman spectra in a different solvent (acetone) were recorded and compared to the spectra obtained in acetonitrile and in SERS measurements. Although the spectra in acetone were accompanied with a low noise to signal ratio, they showed a similar signal pattern with similar intensities indicating that the observed signals are characteristic to the compound in study and the contribution effects from the solvent (acetonitrile or acetone) is rather small in this case. The deposition of the analyte molecules on the Au surface can also lead to a shift in Raman frequencies. This shifting can be attributed to strong interactions for example between a non-bonding orbital of the molecule and the Au surface. If such interactions are present in the system, even new bands due to formation of charge transfer complexes can arise in the SERS spectrum compared to the spectrum in solution. The lack of such interactions is indicated by very similar spectra in solution and on an Au substrate.[144,146] Also some vibrational modes, which belong to polar molecules with a component normal pointing to the surface, can be enhanced in intensity in the SERS spectrum compared to the solution state. In this case the molecules would have a certain orientation on the surface. Comparison of the herein studied SERS spectra with the Raman spectra in solution showed that the relative intensities are very similar to each other, which indicates weak intermolecular interactions between the analyte molecules and the surface.

---

[146] H. Wackerbarth, L. Gundrum, C. Salb, K. Christou, W. Viöl, *Appl. Opt.*, **2010**, *49*, 4367.

Weak interactions with the surface lead to a non-specific orientation of the molecules and they supposed to be randomly distributed.

Even though the spectra in the solid and solution state are very similar, the decomposition into the free metal and free ligand cannot be excluded yet. Therefore, additionally Raman and SERS spectra of the corresponding ligands have been recorded and compared to the spectra of the double-cages (see Figure VII.4). Significant differences in intensity distribution as well as in the frequencies of the vibrational bands between the double-cages and the corresponding ligands have been observed. For example the vibrational bands at 2210 cm^{-1}, 1163 cm^{-1} and 1031 cm^{-1} are shifted by a value of 6-9 cm^{-1} to higher wavenumbers as compared to the corresponding free ligand $\mathbf{L}^2$. On the other hand, the three bands at 1568 cm^{-1}, 1578 cm^{-1} and 1595 cm^{-1} are shifted to lower wavenumbers by a value of 2-8 cm^{-1}. Similar observations were made for the monooxygenated double-cage $[3BF_4@Pd_4\mathbf{L}^3{}_8](BF_4)_5$ and ligand $\mathbf{L}^3$ derivatives (see Appendix VII Section 1). For the dioxygenated derivative $[3BF_4@Pd_4\mathbf{L}^4{}_8](BF_4)_5$ the difference to the spectra of the corresponding ligand was not as pronounced as in the two other cases, but still the spectra were clearly differentiable. These examinations allow for the conclusion that the double-cages do not disassemble at least into the free ligands and metal nodes upon deposition on a surface and extraction of solvent molecules, which is an intriguing observation for such big and highly charged molecules.

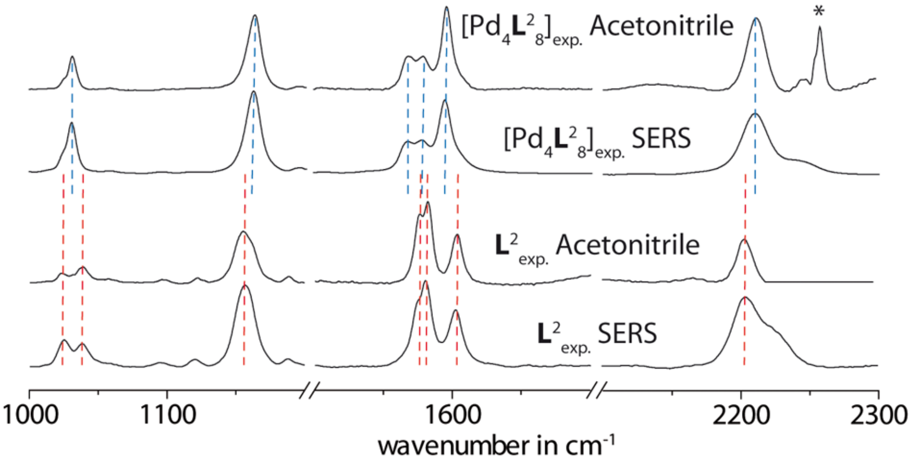

Figure VII.4 Comparison of the experimental Raman spectrum measured in acetonitrile solution and the Raman spectrum measured after deposition on the Au surface (SERS) for the double-cage $[3BF_4@Pd_4\mathbf{L}^2{}_8](BF_4)_5$ and the free ligand $\mathbf{L}^2$. Vibrational maxima of the signals are highlighted by doted lines (blue for

$[3BF_4@Pd_4\mathbf{L}^2_8](BF_4)_5$ and red for ligand $\mathbf{L}^2$). * Artefact. Reproduced with permission from reference [143]. Copyright © 2014 PCCP Owner Societies.

Comparing the spectra of ligand derivatives $\mathbf{L}^2$, $\mathbf{L}^3$ and $\mathbf{L}^4$, which only differ in their oxygenation state at the sulfur atom, show that they are although very similar still differentiable (see Figure VII.5). Some bands show a slight shifting, for example the band at 2203 cm^{-1} ($\mathbf{L}^2$) is shifted to 2209 cm^{-1} ($\mathbf{L}^3$) and 2216 cm^{-1} ($\mathbf{L}^4$). Furthermore the signal around 1142 cm^{-1} in the spectrum of $\mathbf{L}^2$ is split into two signals for the dioxygenated ligand derivative $\mathbf{L}^4$. The spectra of the corresponding double-cages $[3BF_4@Pd_4\mathbf{L}^n_8]^{5+}$ are similar to the spectra of the constituting ligands, showing that the resonances arise from the ligand skeletons incorporated into the double-cage structure. Nevertheless, the spectra of the double-cages show significant differences, for example the shifting and intensity distribution of the bands around 1050 and 1600 cm^{-1}. Also the band at 2210 cm^{-1} for $[3BF_4@Pd_4\mathbf{L}^2_8]^{5+}$ shows a slight shifting to 2214 cm^{-1} for $[3BF_4@Pd_4\mathbf{L}^2_8]^{5+}$ and 2215 cm^{-1} for $[3BF_4@Pd_4\mathbf{L}^4_8]^{5+}$.

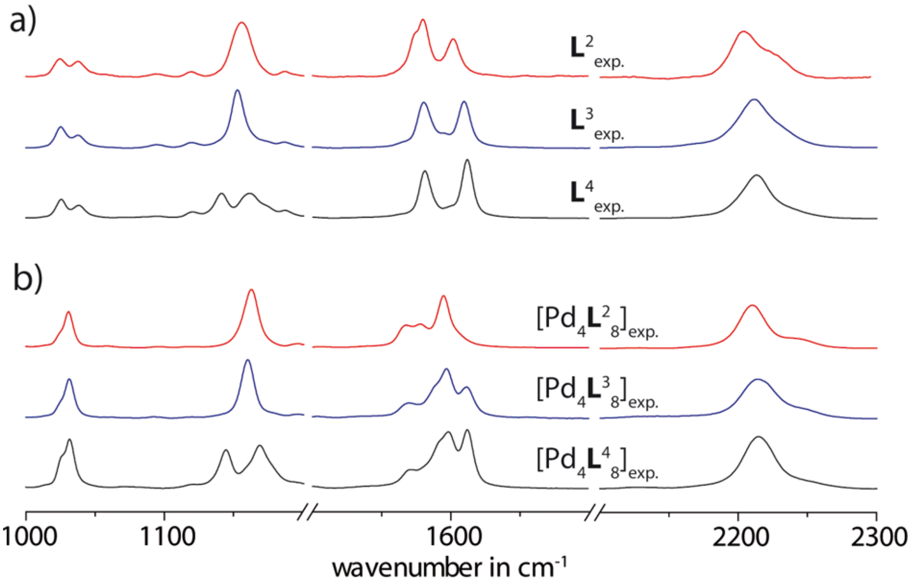

Figure VII.5 Comparison of the experimental spectra between a) free ligand derivatives $\mathbf{L}^n$ with n = 1, 2, 3 and b) corresponding double-cages $[3BF_4@Pd_4\mathbf{L}^n_8](BF_4)_5$. All spectra were recorded in solution with acetonitrile as the solvent. Reproduced with permission from reference [143]. Copyright © 2014 PCCP Owner Societies.

In order to assign the vibrational bands to vibration modes of the ligands, a DFT calculation on the B3LYP/6-31G* level of theory was performed in Gaussian 09.[72] The resulting calculated vibrational frequencies were systematically overestimated by the applied calculation method and needed to be corrected in order to be comparable to experimental vibrational frequencies. Due to a variety of reported scaling methods, three of them have been selected to correct the calculated frequencies: scaling with a functional- and basis-set-specific constant factor ($\omega_{\text{corr..}}$ = 0.9614 x $\omega_{\text{calc.}}$)[147], a reported scaling equation for phenothiazine derivatives ($\omega_{\text{corr..}}$ = 0.9519 x $\omega_{\text{calc.}}$ + 23.3)[148] and a scaling equation found via the try and error approach ($\omega_{\text{corr..}}$ = 0.9377 x $\omega_{\text{calc.}}$ + 45.2). The first two scaling equation gave good agreements for the middle part of the spectra, but for short and long wavelength the overlap between the calculated and measured spectra was not satisfying. The latter scaling approach with a linear scaling equation gave the best agreement between the measured and the calculated spectra with an error of less than 1 % (see Table VII.1).

Figure VII.6 shows the assignment of the calculated vibrational modes highlighted with red arrows for ligand $\mathbf{L}^2$ of the six bands with the highest relative intensities. The alkyne vibrational band is degenerated and is constructed from two frequencies at 2209.0 cm^{-1} and 2209.4 cm^{-1}, which give one vibrational band due to simulated line broadening effect of 4 cm^{-1}. The next less intense bands were calculated at 1597.9 cm^{-1}, 1579.1 cm^{-1}, 1569.9 cm^{-1} and 1150.0 cm^{-1} and are assigned to group vibrations of the phenothiazine backbone and the pyridine moieties. These vibrational modes are consistent with the ones reported in literature for similar compounds.[149] Similar vibrational modes have been calculated for the two oxygenated derivatives $\mathbf{L}^3$ and $\mathbf{L}^4$ (see Figure VII.6b and Appendix VII Section 2). For the monoxygenated derivative two ligand models were considered in the calculation, one model containing the oxygen in equatorial position and the other in the axial (see Chapter III). The sulfoxide stretching bands were found at 1034 cm^{-1} and 1060 cm^{-1} for axial isomer of ligand $\mathbf{L}^3$ and 1038 cm^{-1} and 1069 cm^{-1} for the equatorial isomer. Unfortunately the sulfoxide stretching bands are of very low relative intensity and they are not isolated from other group vibrations of the phenothiazine backbone. The vibrational modes of the

---

[147] A. P. Scott, L. Radom, *J. Phys. Chem.*, **1996**, *100*, 16502.

[148] M. Alcolea Palafox, M. Gil, J. L. Núñez, G. Tardajos, *Int. J. Quantum Chem.*, **2002**, *89*, 147.

[149] (a) D. Pan, D. L. Phillips, *J. Phys. Chem. A*, **1999**, *103*, 4737. (b) D. Pan, L. C. T. Shoute, D. L. Phillips, *J. Phys. Chem. A*, **1999**, *103*, 6851. (c) G. Sarata, M. Sakai, H. Takahashi, *J. Raman Spectrosc*. **2000**, *31*, 785. (d) R. Millen, D. de Faria, M. Temperini, *Vib. Spectrosc.*, **2001**, *27*, 89. (e) H. Jian, J. Xiang, K. Sun, J. Sun, C. Chen, B. Zhou, Y. Liu, G. Xu, *J. Colloid Interface Sci.*, **2000**, *229*, 212. (f) K. R. Ackermann, T. Henkel, J. Popp, *ChemPhysChem* **2007**, *8*, 2665. (g) M. Snehalatha, I. Hubert Joe, C. Ravikumar, V. S. Jayakumar *J. Raman Spectrosc.* **2009**, *40*, 176.

sulfoxide for the dioxygenated derivative were found at 1046 cm^{-1} and 1254 cm^{-1}. Also in this case the sulfoxide vibrations are of very low intensity and thus they are not suitable to guide the differentiation between the ligand derivatives. Nevertheless the calculated sulfoxide vibration modes are in good agreement with the ones reported for oxygenated phenothiazine derivatives.[150]

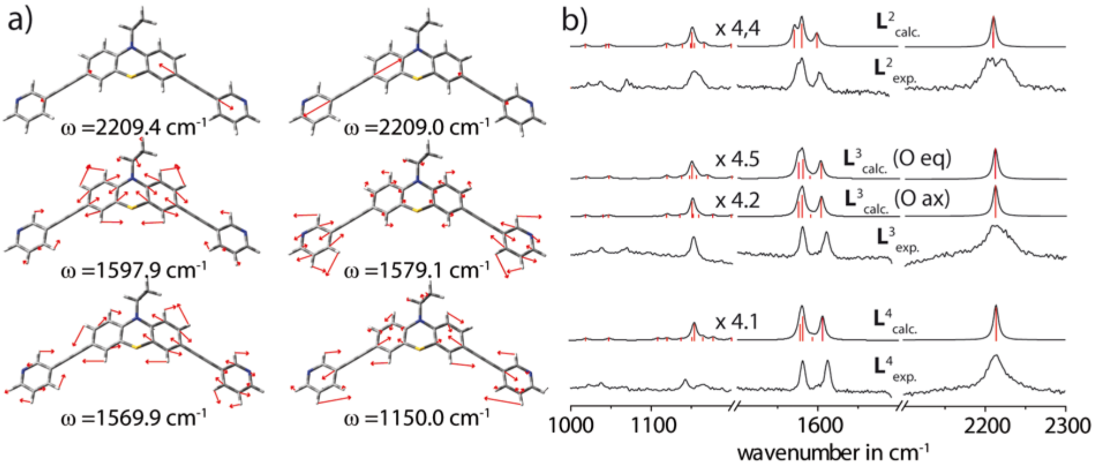

Figure VII.6 a) Calculated vibrational modes with the highest intensity for ligand **L**^{2}. For the calculation the hexyl chain was truncated to an ethyl chain. The values of the frequencies have been corrected with a scaling factor. b) Comparison of the experimental Raman spectra in solution (solvent acetone) and the calculated vibrational Raman spectra for the free ligands **L**^{n}. Calculated frequencies were treated with a gaussian peak broadening of 4 cm^{-1} in order to obtain spectra comparable the spectra obtained experimentally. The intensities of the calculated spectra below 1800 cm^{-1} were scaled by appropriate factors (assigned in the spectrum). Reproduced with permission from reference [143]. Copyright © 2014 PCCP Owner Societies.

---

[150] (a) M. Bolboaca, T. Iliescu, C. Paizs, F. D. Irimie, W. Kiefer, *J. Phys. Chem. A*, **2003**, *107*, 1811. (b) M. Bolboaca, T. Iliescu, W. Kiefer, *Chem. Phys*., **2004**, *298*, 87.

Table VII.1 Vibrational wavenumbers and intensities calculated at the DFT B3LYP/6-31G* level and experimental data for the ligands **L**$^{1-3}$. Reproduced with permission from reference [143]. Copyright © 2014 PCCP Owner Societies.

ligand **L**^{1}				ligand **L**^{2}						ligand **L**^{3}			
Experimental frequencies^a in cm^{-1}		Raman calculated frequencies^b in cm^{-1}		Experimental frequencies^a in cm^{-1}		Raman calculated frequencies^b in cm^{-1} for O$_{ax}$		Raman calculated frequencies^b in cm^{-1} for O$_{eq}$		Experimental frequencies^a in cm^{-1}		Raman calculated frequencies^b in cm^{-1}	
Raman	SERS	ω_{corr}	relative intensity	Raman	SERS	ω_{corr}	relative intensity	ω_{corr}	relative intensity	Raman	SERS	ω_{corr}	relative intensity
1021.8 m	1024.5 m	1017.5	1	1024.2 w	1025.1 m	1017.7	1	750.1	1	1022.1 w	1025.4 m	1017.9	1
1036.8 m	1037.7 m	1042.9	1	1038.3 m	1037.4 m	1046.4	1	1017.7	1	1037.7 w	1038.3 m	1046.4	1
	1057.2 sh	1046.6	1		1119.6 w	1118.4	1	1045.8	2			1107.4	2
	1119.6 vw	1118.3	1			1118.5	2	1118.1	1		1120.5 w	1119.1	1
		1118.5	2			1135.0	1	1118.2	2			1136.4	1
		1138.0	1	1152.3 s	1152.9 vs	1150.1	15	1136.1	1			1150.0	2
		1148.4	2			1151.5	3	1146.0	1	1142.4 m	1141.5 m	1152.8	13
1153.8 s	1155.9 vs	1150.0	13			1158.4	1	1149.1	13	1165.8 w	1161.6 m	1163.6	2
		1153.1	3		1172.4 w	1175.8	2	1154.6	4		1172.4 sh	1176.2	2
		1165.0	3		1186.8 w	1198.8	1	1168.7	3		1187.4 w	1199.2	1
	1187.1 vw	1198.7	1			1198.9	1	1198.6	1			1199.3	1
	1248.3 w	1249.2	2			1246.6	1	1249.1	2		1275.6 vw	1242.4	1
	1500.3 vw	1496.5	1		1301.7 vw	1302.5	1	1321.0	1		1297.5 w	1301.6	1
1575.9 sh	1574.7 vs	1569.9	16		1325.6 vw	1326.1	2	1470.4	1		1329.9 w	1326.2	2
1580.1 vs	1579.8 vs	1579.1	25			1493.9	1	1493.1	1		1473.0 vw	1470.7	1
1601.4 s	1601.7 s	1597.9	12	1580.7 vs	1580.4 vs	1575.2	14	1574.3	18		1499.7 vw	1494.0	1
2203.2 vs	2204.1 vs	2209.0	44			1579.7	25	1579.7	23			1577.0	13
		2209.4	100		1595.1 w	1590.3	1	1588.5	1	1581.3 vs	1581.3 vs	1580.4	23
		3070.7	1	1610.4 vs	1609.5 vs	1603.2	2	1602.3	16			1592.3	2
				2208.6 vs	2211.6 vs	2211.5	55	2211.3	53	1612.2 vs	1611.9 vs	1605.0	21
						2211.6	100	2211.5	100	2215.5 vs	2213.1 vs	2213.8	100
								3071.3	1			2213.9	50
						SO frequencies						SO frequencies	
						1034.5	< 1	1037.9	< 1			1046.4	< 1
						1060.2	< 1	1069.4	< 1			1254.0	< 1

Experimental intensity description: vs = very strong; s = strong; m = medium; w = weak; vw = very weak; sh = shoulder. ^{a} This work. ^{b} Scaled frequencies with the scaling equation $\omega_{corr} = 45.2 + 0.9377\omega_{calc}$.

VII.4 Conclusion

The comparison of the Raman spectra in solution and the SERS spectra on Au surface showed a very similar signal pattern, which indicated that the integrity of the self-assembled double-cages is maintained upon deposition on a surface. The double-cages survived the evaporation of the solvent without suffering from disintegration, e. g. by a coulombic explosion. It was shown that the double-cages do not disassemble under release of the metal cations and the free ligands at least within the limited time from sample preparation to measurement (hours to days). The spectra of the ligands $\mathbf{L}^n$ were clearly differentiable from the corresponding double-cages $[3BF_4@Pd_4\mathbf{L}^n{}_8](BF_4)_5$ and also amongst each other. Thus, Raman spectroscopy allows for differentiation of very closely related species, which either differ by the oxygenation state at the sulfur atom or the coordination to a metal ion.

APPENDIX

Materials and Instrumentation

General experimental procedure

All reagents and solvents were purchased from ABCR, Sigma Aldrich, TCI or Acros and used for the synthesis without further purification. Thin-layer chromatography was performed on Merck aluminium-based plates with silica gel and fluorescent indicator 254 nm.

Nuclear magnetic resonance spectroscopy

NMR spectra were recorded using *Bruker Avance III 300 MHz, Bruker Avance III 400 MHz, Bruker Avance III HD 400 MHz, Bruker Avance III HD 500 MHz* or *Bruker Avance I 900 MHz* spectrometers. The chemical shifts are given with respect to the signal of the deuterated solvent ($CDCl_3$: δ_H = 7.26 ppm, δ_C = 77.16 ppm; CD_3CN: δ_H = 1.94 ppm, δ_C = 1.32 and 118.26 ppm). The coupling constants *J* are given in Hz. The signals are assigned with the following abbreviations: s (singlet), s_{br} (broad singlet), d (doublet), dd (doublet of doublets), t (triplet), q (quartet), m (multiplet). The data were analyzed via the MNova (Mestrelab Research) software.

Mass spectrometry

Mass spectra were recorded on *Bruker FTICR-MS APEX IV* (ESI-HR-MS), *Bruker maXis* (ESI-HR-MS), *Bruker micrOTOF* (HR-ESI-MS), *Bruker HTC Ultra* (ESI-MS). Isotopic distribution and exact masses were calculated with *Bruker Compass DataAnalysis* Software.

UV-Vis spectroscopy

UV-Vis spectra were recorded on *Agilent 8453 UV-Visible* Spectrophotometer.

Fluorescence spectroscopy

The fluorescence measurements were carried out on a *Horiba Jobin-Yvon Fluoromax-4* spectrometer.

Cyclic voltammetry

The cyclic voltammograms were measured via application of a potentiostat PGSTAT101. The data were recorded with the help of the NOVA electrochemistry software (Version 1.9) included in Metrohm Autolab. A homemade electrochemical cell was used for the electrochemical measurements with a minimum sample volume of 3 mL. The sample and electrolyte salt were dissolved in dry and degassed acetonitrile. The electrochemical cell was kept under N_2-atmosphere during the measurements. A glassy carbon electrode was used as working electrode and a Pt wire as counter electrode. After each measurement the glassy carbon electrode and the Pt counter electrode were carefully polished with an appropriate polishing powder and rinsed with acetone and acetonitrile. As reference electrode the non-aqueous electrode $Ag/AgNO_3$ was utilized. For this, a solution of 0.01 M $AgNO_3$ and 0.1 M tetrabutylammonium perchlorate of electrochemical purity grade was prepared in dry and degassed acetonitrile and filled inside the electrode. The reference electrode was kept in acetonitrile/0.1 M tetrabutylammonium perchlorate solution between the measurement and it was rinsed with acetonitrile prior to every measurement. All measurements were performed at room temperature.

Spectroelectrochemistry

For the spectroelectrochemical measurements a thin layer quartz glass spectroelectrochemical cell was used with an optical path length of 1.0 mm. Instead of a glassy carbon working electrode a Pt mesh electrode was applied. As counter electrode a Pt wire was used. As reference electrode the aforementioned $Ag/AgNO_3$ (0.01 M) electrode was used. All spectra were recorded at room temperature. An AvaLight Deuterium-Halogen light source (200 nm - 1000 nm) was used for the UV/VIS measurements. The light was conducted via fiber optic cable (200 µm diameter) to the spectroelectrochemical cell and further to the spectrometer. With every voltage step with a scan rate of 0.01 V/s, the potentiostat PGSTAT101 sends a trigger signal to the DAD-spectrometer AVA-SPEC 2048. The data were stored on the RAM of the spectrometer and were finally sent to the AVASOFT 7.5 software.

Appendix-Chapter III

1. Synthesis and characterization of ligands L^{1-4} and cages $[Pd_2L^1_4](BF_4)_4$, $[3BF_4@Pd_4L^{2-4}_8](BF_4)_5$

a) Synthesis of Ligand $\mathbf{L}^1$:

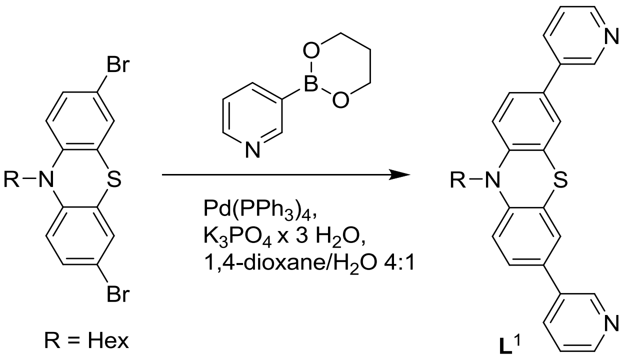

Scheme AP-III.1 Synthetic route to ligand $\mathbf{L}^1$.

A mixture of 3,7-dibromo-10-hexyl-10*H*-phenothiazine[71] (1.00 g, 2.27 mmol, 1.00 eq.), (3-Pyridyl)boronic acid propane-1,3-diol ester (1.08 g, 6.63 mmol, 2.92 eq.) and $K_3PO_4\cdot 3H_2O$ (15 g, 65.14 mmol, 28.75 eq.) were suspended in a mixture of 1,4-dioxane/H_2O (4:1). The mixture was degassed and $Pd(PPh_3)_4$ (0.13 g, 0.11 mmol, 0.05 eq.) was added. The mixture was stirred for 48 h at 90 °C. CH_2Cl_2 (300 mL) was added to the mixture and the organic phase was washed with H_2O (3 x 50 mL), dried over $MgSO_4$, filtrated and the solvent was evaporated under reduced pressure. The crude residue was purified by flash chromatography on silica gel ($CHCl_3$: MeOH = 50 : 1) and the product was isolated as a yellow oil (0.90 g, 2.06 mmol, 91 %).

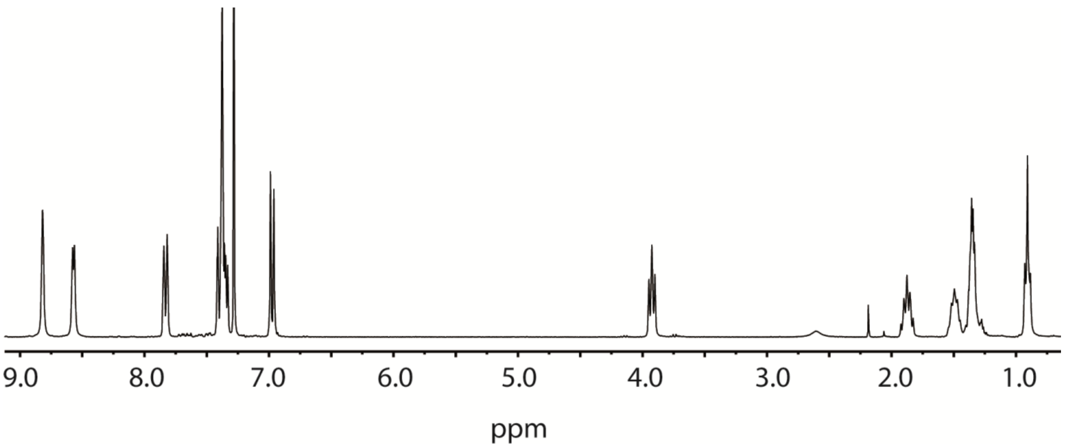

Figure AP-III.1 ^{1}H NMR (298 K, 300 MHz, $CDCl_3$) of ligand **L**^{1}.

^{1}H NMR (300 MHz, $CDCl_3$): δ [ppm] = 8.80 (s, 2 H), 8.55 (dd, J = 4.3 Hz, 2 H), 7.81 (d, J = 7.9 Hz, 2 H), 7.36 (m, 6 H), 6.95 (d, J = 8.3, 2 H), 3.90 (t, J = 7.2 Hz, 2 H), 1.92-178 (m, 2 H), 1.53 – 1.42 (m, 2 H), 1.40 – 1.29 (m, 4 H), 0.94 – 0.84 (m, 3 H).

ESI-FTICR-HRMS ($[C_{28}H_{27}N_3S]^+$):	found:	437.1934
	calc.:	437.1920

b) Synthesis of monomeric cage $[Pd_2\mathbf{L}^1_4](BF_4)_4$:

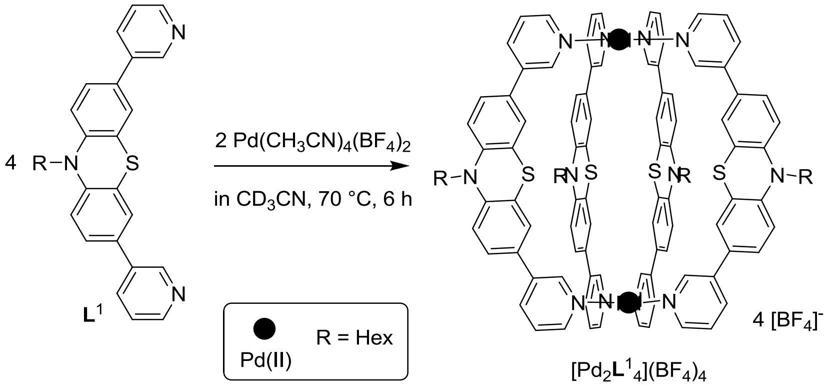

Scheme AP-III.2 Synthetic route to monomeric cage $[Pd_2\mathbf{L}^1_4](BF_4)_4$.

Cage $[Pd_2\mathbf{L}^1_4](BF_4)_4$ was formed in quantitative yield by heating a mixture of the ligand $\mathbf{L}^1$ (450 µL, 0.6 mg, 2.8 µmol) in CD_3CN and a solution of $[Pd(CH_3CN)_4(BF_4)_2]$ (0.68 µmol, 45 µL of a 15 mM solution in CD_3CN) at 70 °C for 6 h to give a solution/suspension of $[Pd_2\mathbf{L}^1_4](BF_4)_4$ (the solubility in CD_3CN is very low).

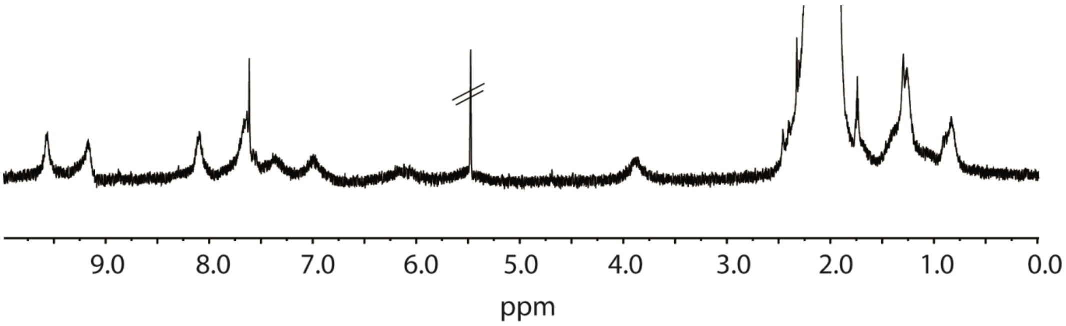

Figure AP-III.2 ^1H NMR (298 K, 300 MHz, MeCN-d_3) of monomeric cage $[Pd_2\mathbf{L}^1_4](BF_4)_4$.

^{1}H NMR (300 MHz, CD_3CN): δ [ppm] = 9.58 (s, 2 H), 9.29 – 9.07 (m, 2 H), 8.18 – 7.96 (m, 2 H), 7.78 – 7.21 (m, 6 H), 7.51 – 6.70 (m, 2 H), 4.04 – 3.61 (m, 2 H), 2.53 – 1.59 (m, 4 H), 1.51 – 1.14 (m, 4 H), 1.0 – 0.67 (m, 3 H).

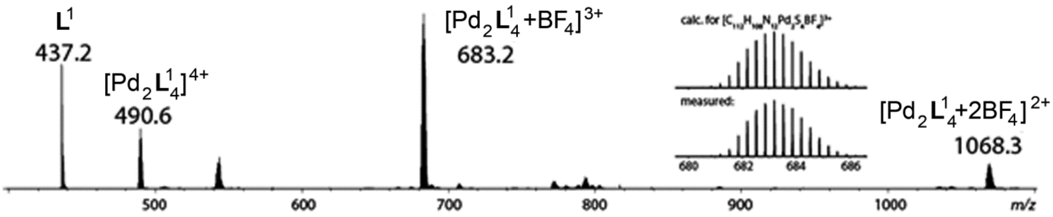

Figure AP-III.3 ESI-MS of monomeric cage $[Pd_2\mathbf{L}^1_4](BF_4)_4$.

ESI-FTICR-HRMS ($[C_{112}H_{108}N_{12}S_4Pd_2+BF_4]^{3+}$): found: 683.1957

calc.: 683.1946

c) Synthesis of ligand $\mathbf{L}^2$

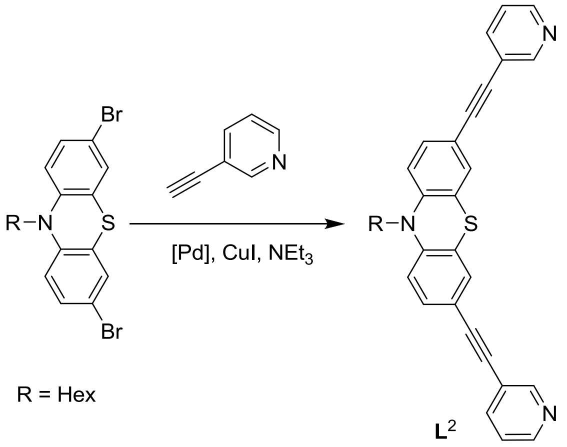

Scheme AP-III.3 Synthetic route leading to ligand $\mathbf{L}^2$.

A mixture of 3,7-dibromo-10-hexyl-10*H*-phenothiazine (1.328 g, 3.01 mmol, 1.00 eq.), 3-ethynylpyridine (0.931 g, 9.03 mmol, 3.00 eq.) and copper(I) iodide (0.060 g, 0.31 mmol, 0.10 eq.) in triethylamine (10 mL) was thoroughly degassed and $Pd(PPh_3)_2Cl_2$ (0.100 g, 0.14 mmol, 0.05 eq.) was added. The mixture was heated under nitrogen gas atmosphere at 90 °C for 48 h. Next, the mixture was cooled to room temperature and the solvent was evaporated under reduced pressure. A saturated NH_4Cl-solution was added to the residue and the organic components were extracted with $CHCl_3$. The organic layer was washed with water and brine, dried over $MgSO_4$, filtrated and the solvent was evaporated under reduced pressure. The crude residue was purified by flash chromatography on silica gel (n-hexane : EtOAc = 3 : 2) and the final product was isolated as a yellow oil (0.896 g, 1.79 mmol, 59 %).

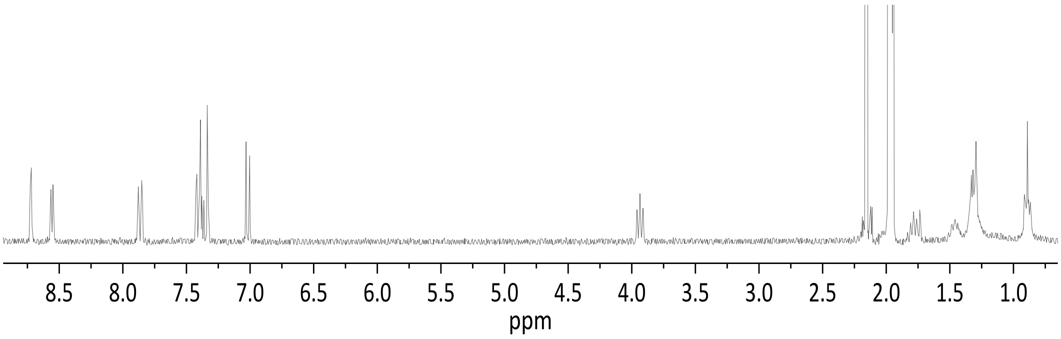

Figure AP-III.4 ^1H NMR (298 K, 300 MHz, CD_3CN) of ligand $\mathbf{L}^2$.

^{1}H NMR (300 MHz, CD_3CN): δ [ppm] = 8.72 (dd, J = 2.2, 0.9 Hz, 2 H), 8.55 (dd, J = 4.8, 1.7 Hz, 2 H), 7.86 (dt, J = 8.2, 2.0 Hz, 2 H), 7.41 (dd, J = 8.5, 2.0 Hz, 2 H), 7.38 (ddd, J = 8.4, 4.9, 0.9 Hz, 2 H), 7.33 (d, J = 1.9 Hz, 2 H), 7.02 (d, J = 8.5 Hz, 2 H), 3.94 (t, J = 7.8 Hz, 2 H), 1.87 – 1.75 (m, 2 H), 1.53 – 1.40 (m, 2H), 1.39 – 1.26 (m, 4 H), 0.95 – 0.83 (m, 3 H).

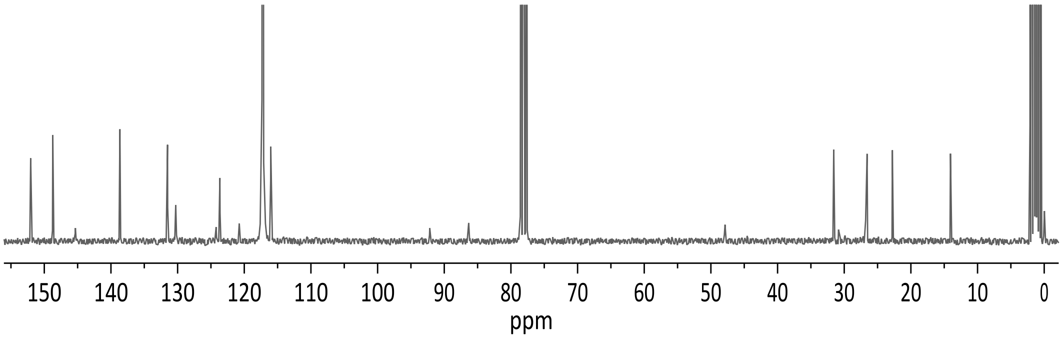

Figure AP-III.5 ^{13}C NMR (298 K, 75 MHz, CD_3CN) of ligand **L**^{2}.

^{13}C NMR (75 MHz, CD_3CN): δ [ppm] = 152.06, 148.75, 145.39, 138.71, 131.58, 130.30, 124.24, 123.72, 120.77, 116.90, 116.02, 92.22, 86.34, 47.87, 31.58, 26.83, 26.58, 22.80, 14.12.

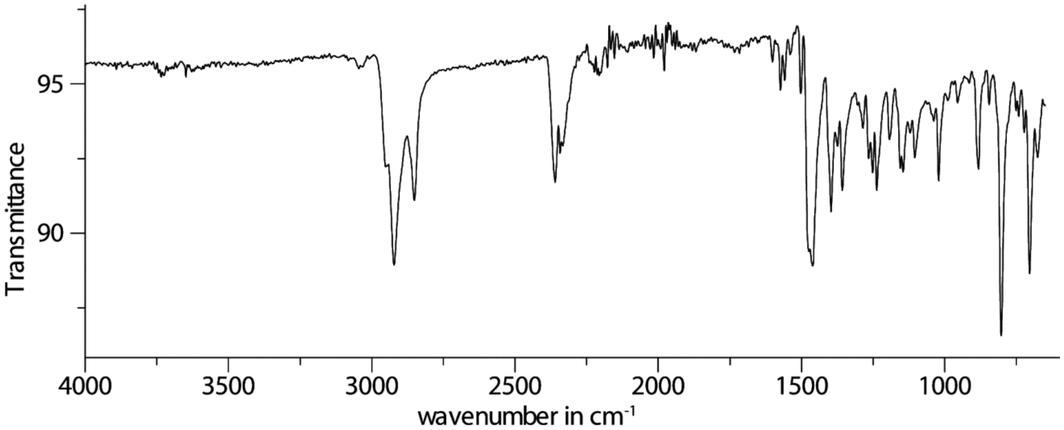

Figure AP-III.6 Attenuated total reflectance infrared spectrum (ATR-IR) (resolution 4 cm^{-1}; 40 spectra accumulated) of ligand **L**^{2}.

IR (ATR): ν [cm^{-1}] = 676, 704, 845, 882, 1021, 1105 1145, 1193, 1237, 1253, 1285, 1358, 1397, 1461, 1503, 1574, 2851, 2922.

ESI-FTICR-HRMS ($[C_{32}H_{27}N_3S+H]^+$): found: 486.1995

calc.: 486.1998

d) Synthesis of double-cage $[3BF_4@Pd_4\mathbf{L}^2_8](BF_4)_5$:

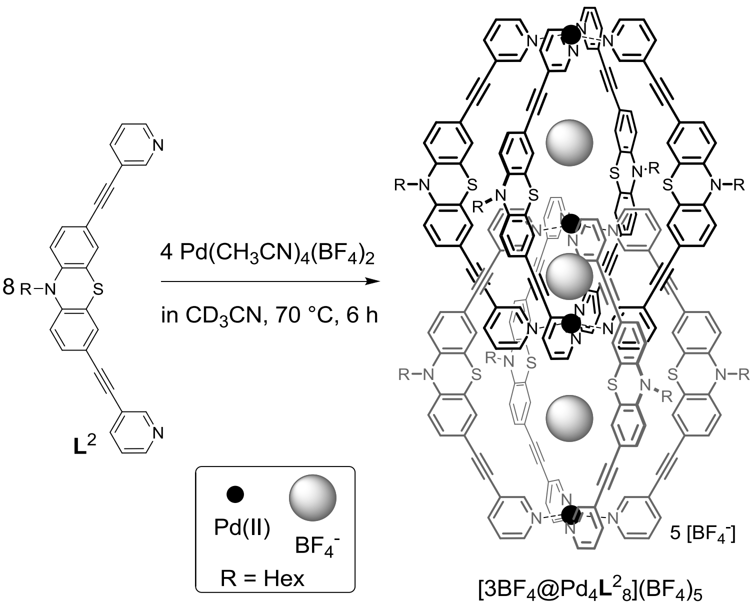

Scheme AP-III.4 Synthetic route leading to interpenetrated double-cage $[3BF_4@Pd_4\mathbf{L}^2_8](BF_4)_5$.

Cage compound $[3BF_4@Pd_4\mathbf{L}^2_8](BF_4)_5$ was formed in quantitative yield by heating a mixture of the ligand $\mathbf{L}^2$ (930 µL, 1.36 mg, 2.8 µmol) in CD_3CN and a solution of $[Pd(CH_3CN)_4(BF_4)_2]$ (1.4 µmol, 93 µL of a 15 mM solution in CD_3CN) at 70 °C for 6 h to give a 0.35 mM solution of $[3BF_4@Pd_4\mathbf{L}^2_8](BF_4)_5$.

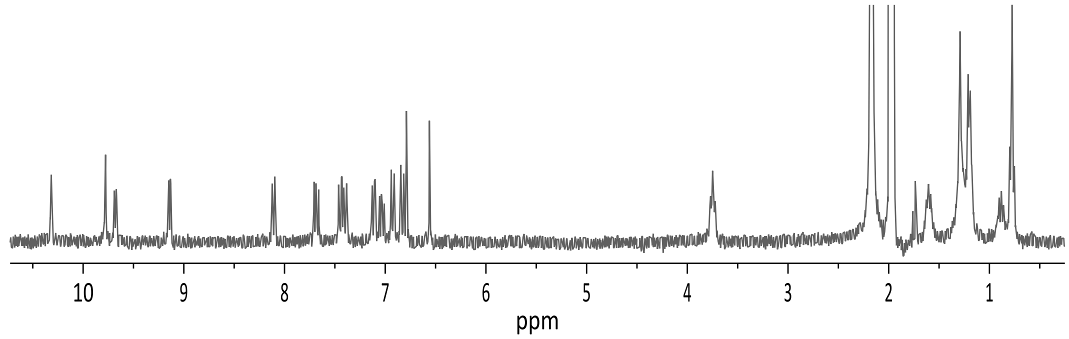

Figure AP-III.7 ^{1}H NMR (298 K, 300 MHz, CD_3CN) of double-cage $[3BF_4@Pd_4\mathbf{L}^2_8](BF_4)_5$.

^{1}H NMR (300 MHz, CD_3CN): *δ* [ppm] = 10.29 (s, 8 H), 9.75 (d, *J* = 1.4 Hz, 8 H), 9.65 (dd, *J* = 5.8, 0.8 Hz, 8 H), 9.12 (dd, *J* = 5.8, 1.4 Hz, 8 H), 8.09 (dt, *J* = 7.6, 1.4 Hz, 8 H), 7.66 (ddd, *J* = 8.7, 7.9, 0.5 Hz, 8 H), 7.42 (dd, *J* = 8.5, 2.0 Hz, 8 H), 7.37 (d, *J* = 8.2 Hz, 8 H), 7.09 (dd, *J* = 8.4, 1.9 Hz, 8 H), 7.01 (ddd, *J* = 8.2, 8.0, 0.6 Hz, 8 H), 6.90 (d, *J* = 8.6 Hz, 8 H), 6.80 (d, *J* = 8.6 Hz, 8 H), 6.76 (d, *J* = 1.9 Hz, 8 H), 6.53 (d, *J* = 1.9 Hz, 8 H), 3.72 (t, *J* = 7.1 Hz, 16 H), 1.64 – 1.51 (m, 16 H), 1.40 – 1.11 (m, 32 H), 0.90 – 0.82 (m, 16 H), 0.80 – 0.70 (m, 24 H).

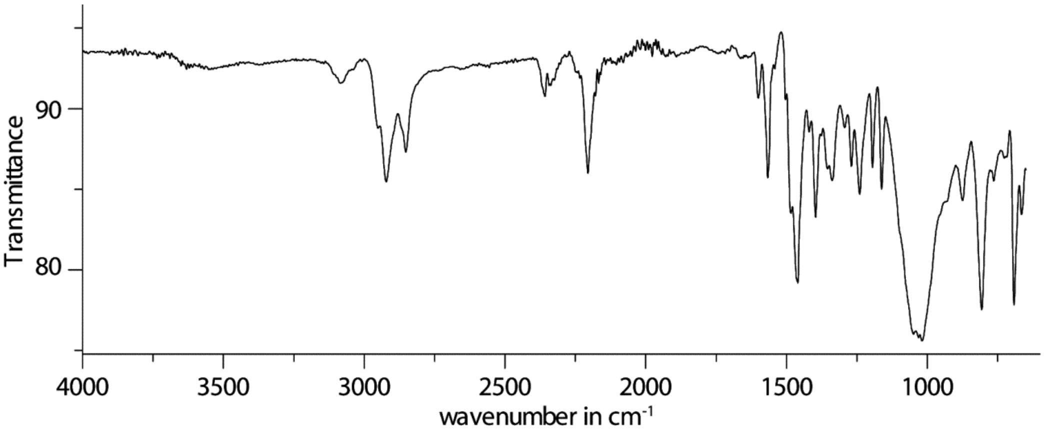

Figure AP-III.8 Attenuated total reflectance infrared spectrum (ATR-IR) (resolution 4 cm^{-1}; 40 spectra accumulated) of double-cage $[3BF_4@Pd_4\mathbf{L}^2{}_8](BF_4)_5$.

IR (ATR): ν [cm^{-1}] = 665, 692, 807, 875, 1018, 1162, 1195, 1240, 1270, 1338, 1396, 1460, 1567, 1601, 2205, 2852, 2922.

ESI-FTICR-HRMS ($[C_{256}H_{216}N_{24}S_8Pd_4+B_3F_{12}]^{5+}$): found: 914.2382

calc.: 914.2345

e) Synthesis of ligand **L**^{3}

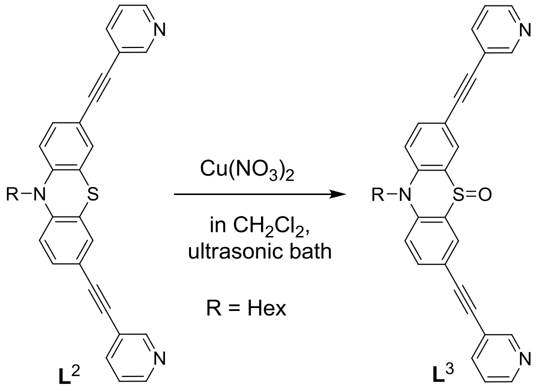

Scheme AP-III.5 Synthetic route leading to ligand **L**^{3}.

To a solution of **L**^{2} (25 mg, 0.05 mmol, 1.00 eq.) in CH_2Cl_2 (10 mL), $Cu(NO_3)_2 \cdot 3H_2O$ (40 mg, 0.17 mmol, 3.31 eq.) was added and the mixture was sonificated in an ultrasonic bath for 1 h at room temperature. After completion of the reaction, the mixture was washed with H_2O (2 x 10 mL). The solvent was evaporated under reduced pressure. The residue was purified by flash chromatography on silica gel ($CHCl_3$: MeOH = 25 : 1) to give **L**^{3} as a yellow product (17.7 mg, 0.04 mmol, 68 %).

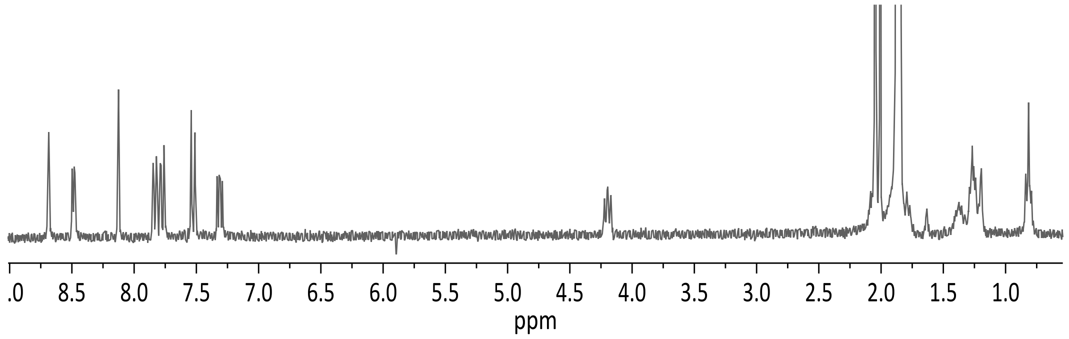

Figure AP-III.9 ^{1}H NMR (298 K, 500 MHz, CD_3CN) of ligand **L**^{3}.

^{1}H NMR (500 MHz, CD_3CN): δ [ppm] = 8.69 (d, J = 2.1 Hz, 2 H), 8.49 (dd, J = 5.0, 1.6 Hz, 2 H), 8.13 (d, J = 2.1 Hz, 2 H), 7.83 (dt, J = 7.8, 1.9 Hz, 2 H), 7.77 (dd, 8.9, 2.1 Hz, 2 H), 7.53 (d, J = 9.0 Hz, 2 H), 7.31 (ddd, J = 7.9, 4.9, 0.9 Hz, 2 H), 4.20 (t, J = 8.0 Hz, 2 H), 1.82 – 1.73 (m, 2 H), 1.45 – 1.31 (m, 2 H), 1.31 – 1.17 (m, 4 H), 0.87 – 0.76 (m, 3 H).

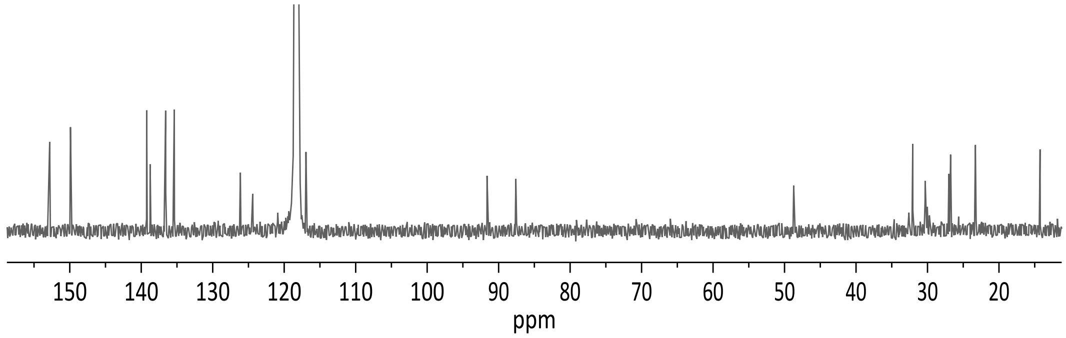

Figure AP-III.10 ^{13}C NMR (298 K, 100 MHz, CD_3CN) of ligand **L**^{3}.

^{13}C NMR (100 MHz, CD_3CN): *δ* [ppm] = 152.82, 149.87, 139.17, 138.72, 136.56, 135.34, 126.08, 124.41, 116.92, 91.59, 87.55, 48.73, 32.04, 27.00, 26.74, 23.27, 14.23 (not all C_{quart} were found).

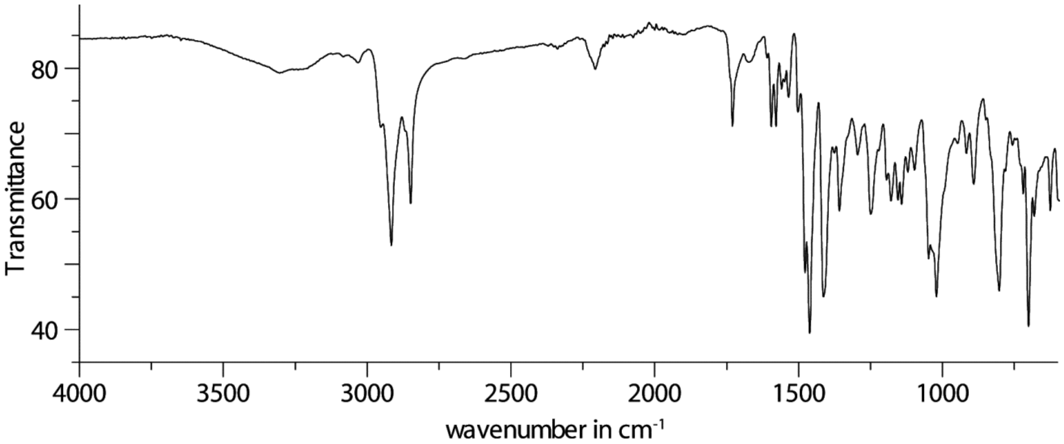

Figure AP-III.11 Attenuated total reflectance infrared spectrum (ATR-IR) (resolution 4 cm^{-1}; 40 spectra accumulated) of ligand **L**^{3}.

IR (ATR): *ν* [cm^{-1}] = 519, 555, 594, 625, 681, 701, 803, 891, 917, 1021, 1048, 1097, 1120, 1142, 1155, 1178, 1194, 1250, 1295, 1358, 1413, 1461, 1478, 1502, 1535, 1559, 1579, 1595, 1730, 2207, 2849, 2915.

ESI-FTICR-HRMS ($[C_{32}H_{27}N_3SO+H]^+$): found: 502.1934

calc.: 502.1948

f) Synthesis of double-cage $[3BF_4@Pd_4\mathbf{L}^3_8](BF_4)_5$:

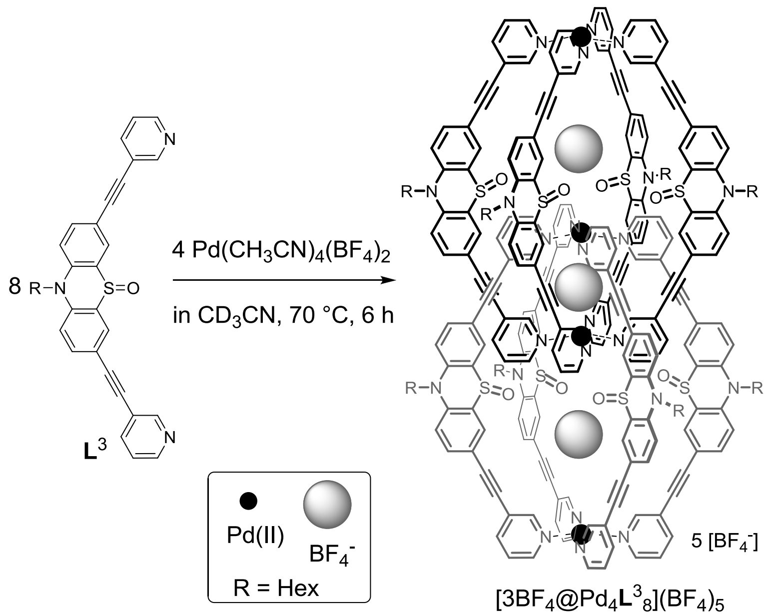

Scheme AP-III.6 Synthetic route leading to interpenetrated double-cage $[3BF_4@Pd_4\mathbf{L}^3_8](BF_4)_5$.

Cage compound $[3BF_4@Pd_4\mathbf{L}^3_8](BF_4)_5$ was formed in quantitative yield by heating a mixture of the ligand $\mathbf{L}^3$ (930 µL, 1.40 mg, 2.8 µmol) in CD_3CN and a solution of $[Pd(CH_3CN)_4(BF_4)_2]$ (1.4 µmol, 93 µL of a 15 mM solution in CD_3CN) at 70 °C for 6 h to give a 0.35 mM solution of $[3BF_4@Pd_4\mathbf{L}^3_8](BF_4)_5$.

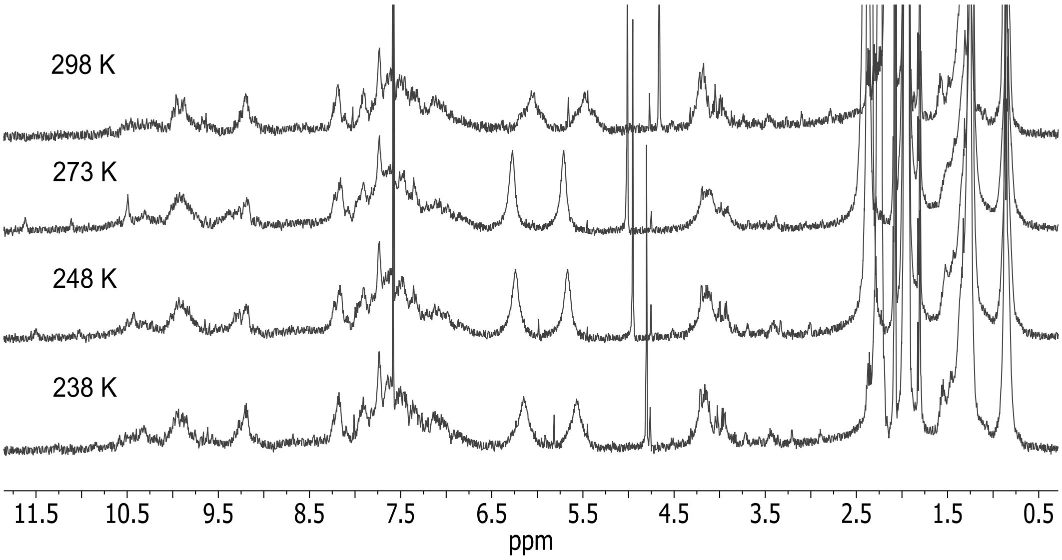

Figure AP-III.12 ^1H NMR (500 MHz, CD_3CN) of double-cage $[3BF_4@Pd_4\mathbf{L}^3_8](BF_4)_5$ at different temperatures.

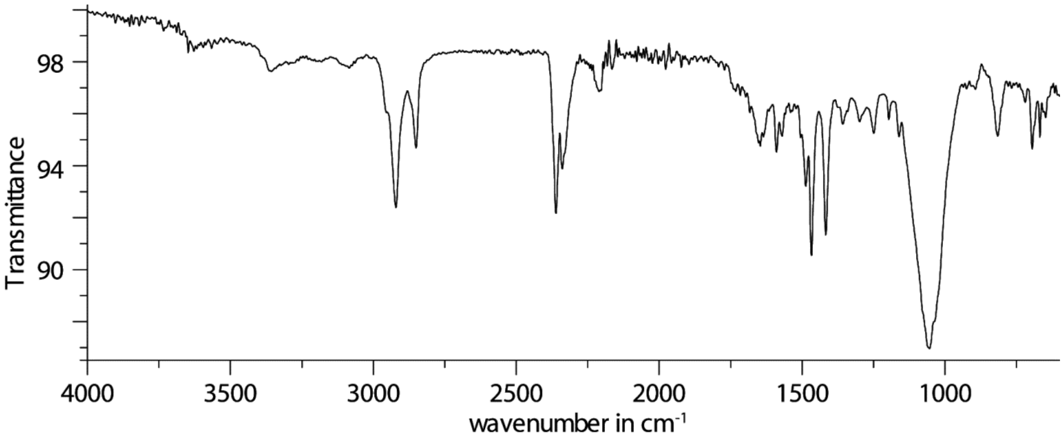

Figure AP-III.13 Attenuated total reflectance infrared spectrum (ATR-IR) (resolution 4 cm^{-1}; 40 spectra accumulated) of double-cage $[3BF_4@Pd_4\mathbf{L}^3_8](BF_4)_5$.

IR (ATR): v [cm^{-1}] = 520, 668, 695, 816, 1055, 1197, 1250, 1368, 1417, 1468, 1487, 1589, 1645, 2850, 2921.

ESI-FTICR-HRMS ($[C_{256}H_{216}N_{24}S_8Pd_4O_8+B_3F_{12}]^{5+}$):	found:	939.8297
	calc.:	939.8263

g) Synthesis of ligand **L**^{4}

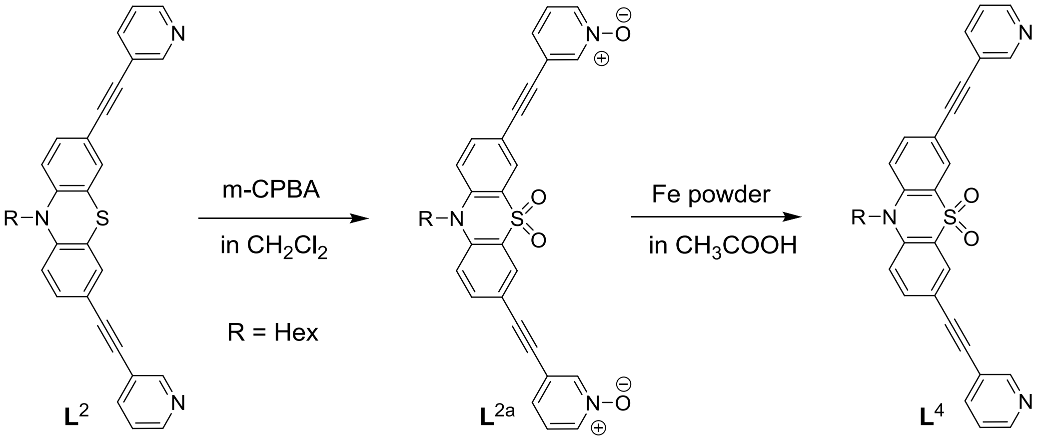

Scheme AP-III.7 Synthetic route leading to ligand **L**^{4}.

To a solution of **L**^{2} (25 mg, 0.05 mmol, 1.00 eq.) in CH_2Cl_2 (10 mL) *m*-CPBA (100 mg, 0.58 mmol, 11.58 eq.) was added at 0 °C and the mixture was stirred for 24 h at room temperature.[76] After completion of the reaction the solvent was evaporated under reduced pressure. The residue was purified by flash chromatography on silica gel ($CHCl_3$: MeOH = 25 : 1) to give the *N*-oxygenated ligand **L**^{2a} as a yellow solid (26.7 mg, 0.05 mmol, 97 %).

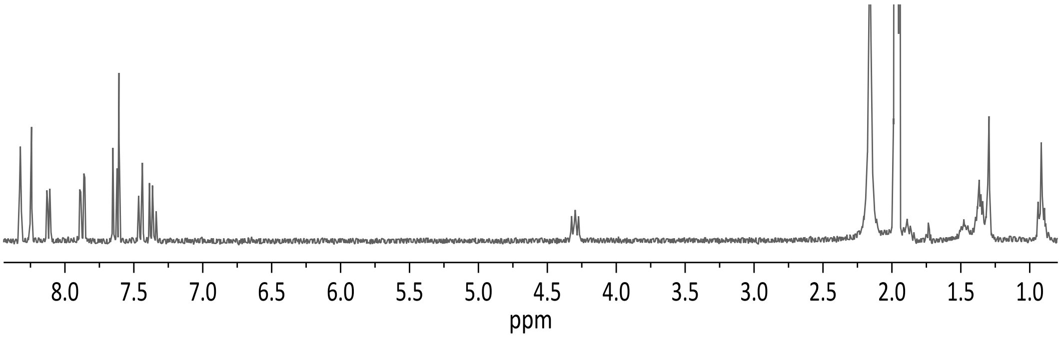

Figure AP-III.14 ^{1}H NMR (298 K, 300 MHz, CD_3CN) of *N*-oxygenated ligand **L**^{2a}.

^{1}H NMR (300 MHz, CD_3CN): δ [ppm] = 8.34–8.26 (m, 2 H), 8.22 (d, *J* = 2.1 Hz, 2 H), 8.09 (ddd, *J* = 6.4, 1.8, 1.1 Hz, 2 H), 7.85 (dd, *J* = 9.0, 2.1 Hz, 2 H), 7.61 (d, *J* = 9.0 Hz, 2 H), 7.43 (dt, *J* = 8.0, 1.2 Hz, 2 H), 7.34 (dd, *J* = 7.9, 6.5 Hz, 2 H), 4.27 (t, *J* = 7.6 Hz, 2 H), 1.91–1.80 (m, 2 H), 1.50–1.40 (m, 2 H), 1.39–1.30 (m, 4 H), 0.94–0.84 (m, 3 H).

ESI-MS ($[C_{32}H_{27}N_3SO_4+Na]^+$) = 572.20

To a solution of *N*-oxygenated ligand **L**^{2a} (5 mg, 0.01 mmol, 1.00 eq.) in acetic acid (1 mL) Fe powder (100 mg, 1.79 mmol, 179 eq.) was added and the mixture was stirred for 24 h at 70 °C.[151] After completion of the reaction, the mixture was washed with H_2O (2 x 5 mL). The solvent was evaporated under reduced pressure. The residue was purified by flash chromatography on silica gel ($CHCl_3$: MeOH = 10 : 1) to give the ligand **L**^{4} as a pale yellow solid (3 mg, 0.01 mmol, 64 %).

---

[151] US Patent, WO **2010**/001185 A1.

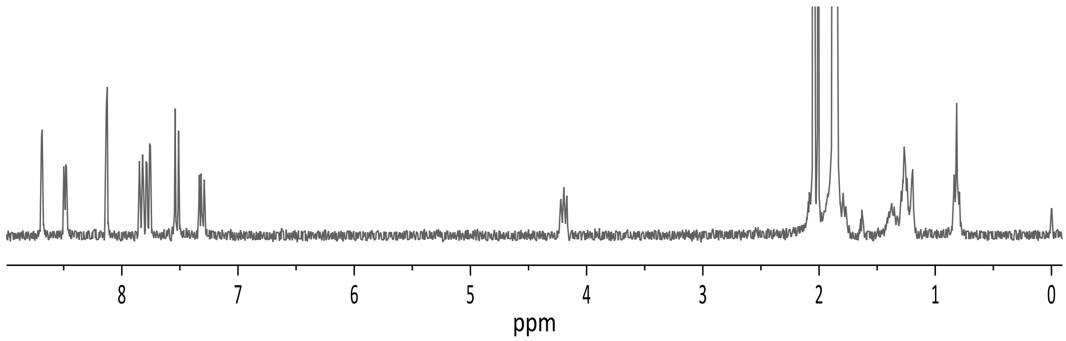

Figure AP-III.15 ^{1}H NMR (298 K, 300 MHz, CD_3CN) of ligand **L**^{4}.

^{1}H NMR (300 MHz, CD_3CN): δ [ppm] = 8.77 (d, J = 2.1 Hz, 2 H), 8.57 (dd, J = 5.0, 1.6 Hz, 2 H), 8.21 (d, J = 2.1 Hz, 2 H), 7.91 (dt, J = 7.8, 1.9 Hz, 2 H), 7.85 (dd, J = 8.9, 2.1 Hz, 2 H), 7.61 (d, J = 9.0 Hz, 2 H), 7.39 (ddd, J = 7.9, 4.9, 0.9 Hz, 2 H), 4.28 (t, J = 7.3 Hz, 2 H), 1.90 –1.80 (m, 2 H), 1.53 – 1.40 (m, 2 H), 1.39 – 1.24 (m, 4 H), 0.94 – 0.84 (m, 3 H).

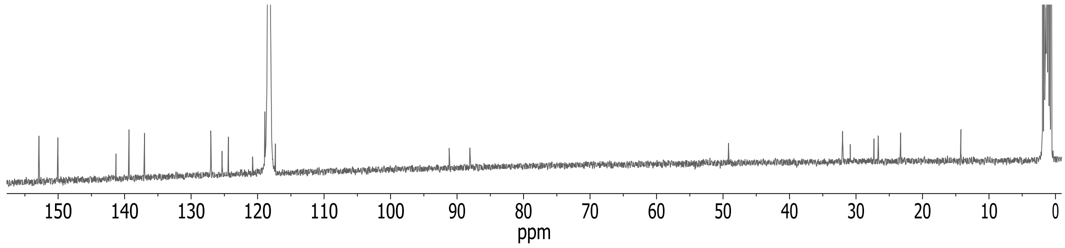

Figure AP-III.16 ^{13}C NMR (298 K, 100 MHz, CD_3CN) of ligand **L**^{4}.

^{13}C NMR (100 MHz, CD_3CN): δ [ppm] = 152.90, 150.04, 141.30, 139.28, 137.02, 127.02, 125.30, 124.35, 120.77, 118.94, 117.34, 91.19, 88.02, 49.15, 31.98, 27.30, 26.64, 23.25, 14.20.

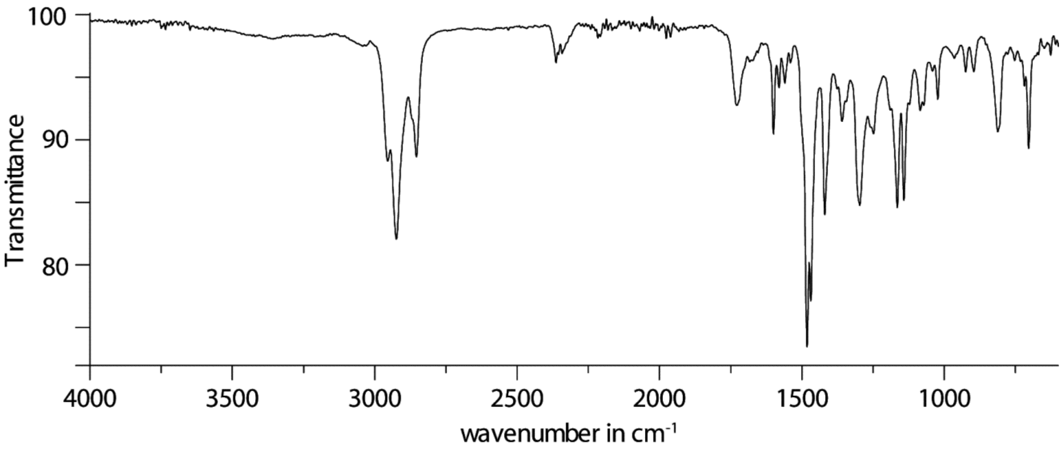

Figure AP-III.17 Attenuated total reflectance infrared spectrum (ATR-IR) (resolution 4 cm^{-1}; 40 spectra accumulated) of ligand **L**^{4}.

IR (ATR): ν [cm^{-1}] = 539, 565, 587, 704, 812, 896, 925, 1023, 1084, 1142, 1165, 1249, 1297, 1360, 1419, 1469, 1482, 1560, 1580, 1600, 1727, 2854, 2923.

ESI-FTICR-HRMS ([$C_{32}H_{27}N_3SO_2$+H]$^+$):	found:	518.1899
	calc.:	518.1897

h) Synthesis of double-cage $[3BF_4@Pd_4\mathbf{L}^4_8](BF_4)_5$:

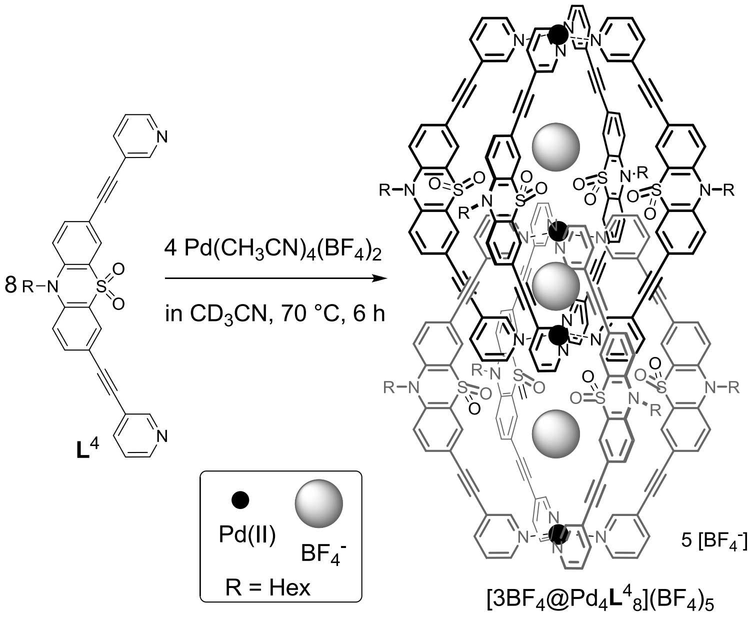

Scheme AP-III.8 Synthetic route leading to interpenetrated double-cage $[3BF_4@Pd_4\mathbf{L}^4_8](BF_4)_5$.

Cage compound $[3BF_4@Pd_4\mathbf{L}^4_8](BF_4)_5$ was formed in quantitative yield by heating a mixture of the ligand $\mathbf{L}^4$ (930 µL, 1.45 mg, 2.8 µmol) in CD_3CN and a solution of $[Pd(CH_3CN)_4(BF_4)_2]$ (1.4 µmol, 93 µL of a 15 mM solution in CD_3CN) at 70 °C for 6 h to give a 0.35 mM solution of $[3BF_4@Pd_4\mathbf{L}^4_8](BF_4)_5$.

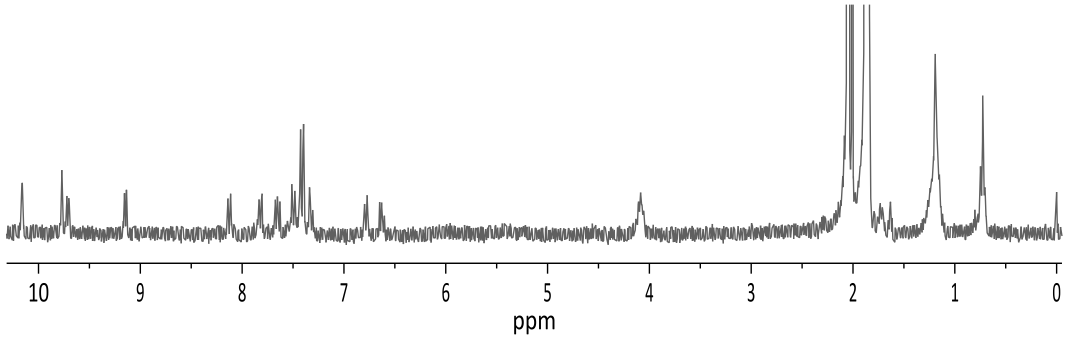

Figure AP-III.18 ^1H NMR (298 K, 300 MHz, CD_3CN) of double-cage $[3BF_4@Pd_4\mathbf{L}^4_8](BF_4)_5$.

^{1}H NMR (300 MHz, CD_3CN): δ [ppm] = 10.24 (s, 8 H), 9.85 (s, 8 H), 9.79 (d, J = 5.9 Hz, 8 H), 9.23 (d, J = 6.1 Hz, 8 H), 8.21 (d, J = 7.8 Hz, 8 H), 7.90 (d, J = 9.1 Hz, 8 H), 7.78 – 7.68 (m, 8 H), 7.58 (d, J = 9.1 Hz, 8 H), 7.49 (m, 24 H), 7.40 (d, J = 9.8 Hz, 8 H), 6.87 (d, J = 7.7 Hz, 8 H), 6.72 (d, J = 6.1 Hz, 8 H), 4.18 (t, J = 7.1 Hz, 16 H), 1.75 – 1.60 (m, 16 H), 1.40 – 1.10 (m, 48 H), 0.80 – 0.70 (m, 24 H).

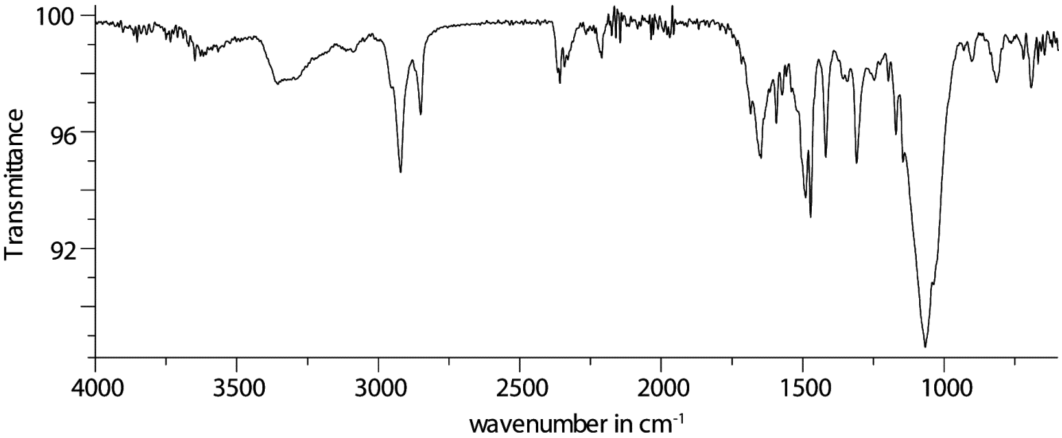

Figure AP-III.19 Attenuated total reflectance infrared spectrum (ATR-IR) (resolution 4 cm^{-1}; 40 spectra accumulated) of double-cage $[3BF_4@Pd_4\mathbf{L}^4_8](BF_4)_5$.

IR (ATR): ν [cm^{-1}] = 692, 815, 1067, 1171, 1309, 1418, 1472, 1490, 1573, 1593, 1647, 2850, 2921.

ESI-FTICR-HRMS ($[C_{256}H_{216}N_{24}S_8Pd_4O_{16}+B_3F_{12}]^{5+}$):	found:	965.4196
	calc.:	965.4182

2. X-ray data of double-cages $[3BF_4@Pd_4L^{2\text{-}4}{}_8]^{5+}$ and modeling of monomeric cage $[Pd_2L^1{}_4]^{4+}$

a) X-Ray structural data of double-cage $[3BF_4@Pd_4\mathbf{L}^2{}_8](BF_4)_5$[152]

The crystals were grown by a slow diffusion of diethylether into an acetonitrile solution of the double-cage $[3BF_4@Pd_4\mathbf{L}^2{}_8](BF_4)_5$. A crystal of a size of 0.2 x 0.1 x 0.05 mm^3 was selected from a batch of crystals using the X-TEMP 2 device.[153] The crystal was mounted on top of a glass fiber using inert perfluorinated polyether oil and placed in the cold gas stream of an Oxford Cryosystems low-temperature device on a Bruker D8 three circle diffractometer. The diffractometer was equipped with a SMART APEX2 CCD detector. Synchrotron radiation was used for data collection (source: undulator; monochromator: silicon [1 1 1]; wavelength: λ = 0.3936 Å). Data were collected in phi-scan mode at different detector 2ϑ angles ranging between 0° and 10°. The level of attenuation of the primary beam was varied depending on the desired reflection 2ϑ angles. The scan width was set to 0.3°. Exposure times were varied from run to run in the range between 0.3 s and 1.0 s. Data integration was done with SAINT 7.68A.[154] Each run with constant 2ϑ and ω settings was integrated using a separate orientation matrix. Data scaling and absorption correction was done with SADABS 2012/1.[155] The space group was determined with the program XPREP.[156] The structure was solved by direct methods using SHELXS-97.[157] Refinement by full-matrix least-squares procedures was done with SHELXL-97[157]. The double-cage structure is constructed from eight times the asymmetric unit, which consists of one ligand molecule, two fourths Pd atoms, two eights BF_4^- molecules and three fourths BF_4^- molecules. Two double-cages make up the contents of the unit cell.

---

[152] The X ray data for the double-cage $[3BF_4@Pd_4\mathbf{L}^2{}_8]^{5+}$ was measured, solved and refined by Dr. Jakob Hey (working group of Prof. Dr. D. Stalke, Georg-August University of Göttingen).

[153] T. Kottke, D. Stalke, *J. Appl. Crystallogr.* **1993**, *26*, 615-619.

[154] Bruker SAINT v7.68A, Madison, **2009**.

[155] G. M. Sheldrick, SADABS 2012/1, Göttingen, **2012**.

[156] G. M. Sheldrick, XPREP Version 2012/1 for Windows, Göttingen, **2005**.

[157] G. M. Sheldrick, *Acta Crystallogr., Sect. A.* **2008**, *64*, 112.

Table AP-III.1: Crystallographic data of $[3BF_4@Pd_4\mathbf{L}^2_8](BF_4)_5$.

CCDC number	**904005**
Empirical formula	$C_{304}H_{336}B_8F_{32}N_{24}O_{12}Pd_4S_8$
Formula weight	5894.53 g mol^{-1}
Temperature	15(2)
Wavelength	0.3936
Crystal system	Tetragonal
Space group	*P*4/*nnc*
Unit cell dimensions	a = b = 21.122(2) Å
	c = 34.263(3) Å
Volume	15286(2) Å^3
Z	2
Density (calculated)	1.281 Mg m^{-3}
Absorption coefficient	0.324 mm^{-1}
F(000)	6128
Crystal size	0.20 x 0.10 x 0.05 mm^3
Theta range for data collection	0.63 to 16.31 °
Index ranges	−21≤h≤30, −24≤k≤27, −48≤l≤42
Reflections collected	219452
Independent reflections	11661 [R(int) = 0.1010]
Completeness to theta = 60.18°	99.9 %
Max. and min. transmission	0.9840 and 0.9381
Refinement method	Full-matrix least-squares on F^2
Data / restraints / parameters	11661 / 2694 / 980
Goodness-of-fit on F^2	1.012
Final R indices [I>2sigma(I)]	R1 = 0.0529, wR2 = 0.1426
R indices (all data)	R1 = 0.0794, wR2 = 0.1671
Largest diff. peak and hole	1.041 and −1.219 e Å^{-3}

After refinement of the double-cages and the tetrafluoroborate anions, diffuse residual electron density was observed in the voids. Heavily disordered lattice solvent (diethylether) could be modeled into these voids (see Figures below). The BF_4^- ions are located at special positions, exhibiting disorder but not obeying the crystallographic symmetry. Due to the high resolution data, solvent as well as all expected tetrafluoroborate anions could be modeled, however only using distance and vibrational/U_{ij} restraints with lowered standard deviation. The main residue (the ligand) was described with a partly disordered model as well.

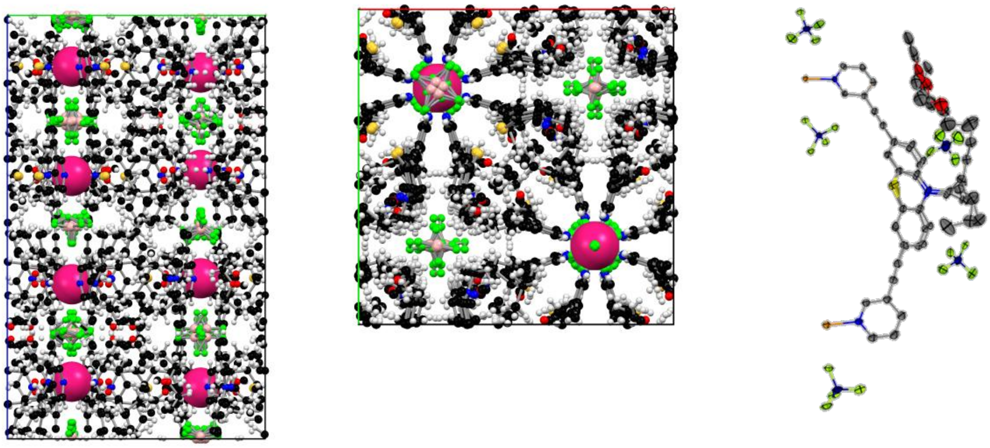

a) View along axis *a*.

b) View along axis *c*.

c) Asymmetric unit with atomic displacement parameters depicted at 50 % probability

Figure AP-III.20: Visualization of the structure of $[3BF_4@Pd_4\mathbf{L}^2_8](BF_4)_5$ in the unit cell. Double-cages and BF_4^- anions displayed as ball-and-stick-model; Pd atoms as large spheres colored in pink. The tunnel-like voids along axis *c* are filled with lattice solvent as can be seen in b).

b) X-Ray structural data of double-cage $[3BF_4@Pd_4\mathbf{L}^3_8](BF_4)_5$[158]

Suitable crystals of $[3BF_4@Pd_4\mathbf{L}^3_8](BF_4)_5$ were obtained after exposure of a crystalline sample of double-cage $[3BF_4@Pd_4\mathbf{L}^2_8](BF_4)_5$ for two month to air. A crystal of a size of 0.10 x 0.09 x 0.08 mm^3 was selected from a batch of low-quality crystals from completely

---

[158] The X ray data for the double-cage $[3BF_4@Pd_4\mathbf{L}^3_8]^{5+}$ was measured, solved and refined by Dr. Jakob Hey (working group of Prof. Dr. D. Stalke, Georg-August University of Göttingen).

evaporated mother liquor using the X-TEMP 2 device.[153] The crystal was mounted on top of a glass fiber using inert perfluorinated polyether oil and placed in the cold gas stream of a Bruker Kryoflex 2 low-temperature device on a Bruker D8 three circle diffractometer. The diffractometer was equipped with a SMART APEX2 CCD detector. Molybdenum K_α radiation was used for data collection (source: Bruker TXS rotating anode). The crystal diffracted very weakly. Data were collected in omega-scan mode in two runs at detector 2ϑ angles −10° and −17.5°. The scan width was set to 0.5°. The exposure time was 90 s per frame. After having collected frames with high exposure time after cell determination with initially lower exposure time, the crystal turned out to be a split crystal with a strong and a weak domain. Data integration was done with SAINT 7.68A taking into account both domains.[154] The data of the two domains were scaled and corrected for absorption with TWINABS 2012/1.[159] A deconvolution of the two domains was made and a HKLF4 file involving only reflections from the strong domain was used for structure solution and refinement. The space group *I*422 was determined using XPREP.[156] There is a pseudo mirror symmetry present in the structure that is caused by the Pd atoms residing on the principal fourfold axis at the special positions (0,0,z) and (0,0,−z). These positions have the site symmetry 4*mm* in space group *I*4/*mmm* and site symmetry 4 in space group *I*422. The remaining parts of the structure however do not obey the higher symmetry. The structure was solved by direct methods using SHELXS-97.[157] Refinement by full-matrix least-squares procedures was done with SHELXL-97.[157] Very much as in the case of $[3BF_4@Pd_4\mathbf{L}^2_8](BF_4)_5$, the double-cage structure is constructed from eight times the asymmetric unit, which consists of one ligand molecule, two fourths Pd atoms, two eights BF_4^- molecules and three fourths BF_4^- molecules. Two double-cages make up the contents of one unit cell. The refined Flack(x) parameter of 0.45(7) indicates racemic twinning, which is not unlikely because the (chiral) double-cages cannot be synthesized enantiomerically pure. If racemic twinning is taken into account, the batch scale factor refines to 0.48(7). The Pd atoms have by far the highest anomalous contribution. At the same time, their pseudo symmetry induces that the Flack(x) parameter as well as the batch scale factor in case of racemic twinning is of rather low significance. This is reflected in the standard uncertainty, which is unusually high for a structure

---

[159] G. M. Sheldrick, TWINABS 2012/1, Göttingen, **2012**.

containing Palladium atoms.

Table AP-III.2: Crystallographic data of $[3BF_4@Pd_4\mathbf{L}^3_8](BF_4)_5$.

CCDC number	**904004**
Empirical formula	$C_{256}H_{216}B_8F_{32}N_{24}O_8Pd_4S_8$
Formula weight	5133.09 g mol^{-1}
Temperature	100(2) K
Wavelength	0.71073 Å
Crystal system	Tetragonal
Space group	*I*422
Unit cell dimensions	a = b = 21.956(2) Å
	c = 32.713(4) Å
Volume	15771(3) Å^3
Z	2
Density (calculated)	1.081 Mg/m^3
Absorption coefficient	0.345 mm^{-1}
F(000)	5248
Crystal size	0.10 x 0.09 x 0.08 mm^3
Theta range for data collection	1.12 to 21.51 °
Index ranges	$-15 \le h \le 15$, $-22 \le k \le 22$, $-33 \le l \le 33$
Reflections collected	27054
Independent reflections	4548 [R(int) = 0.0532]
Completeness to theta = 21.51°	99.5 %
Max. and min. transmission	0.9729 and 0.9663
Refinement method	Full-matrix least-squares on F^2
Data / restraints / parameters	4548 / 513 / 467
Goodness-of-fit on F^2	0.946
Final R indices [I>2sigma(I)]	*R*1 = 0.0529, *wR*2 = 0.1453
R indices (all data)	*R*1 = 0.0758, *wR*2 = 0.1560
Absolute Structure Parameter	0.48(7)
Largest diff. peak and hole	1.058 and −0.555 e Å^{-1}

After refinement of the double-cages and the tetrafluoroborate anions, diffuse residual electron density was observed in the voids. Due to the low resolution of the data, it was not possible to model any lattice solvent into these voids and get a stable refinement. In order to extinguish the influence of the electron density present in the voids, the SQUEEZE routine of the PLATON program package[160,161] was used, which significantly enhanced the C−C bond length precision. The BF_4^- ions are located at special positions, exhibiting disorder but not obeying the crystallographic symmetry. They could be modeled, however only using distance and vibrational/U_{ij} restraints with lowered standard deviation.

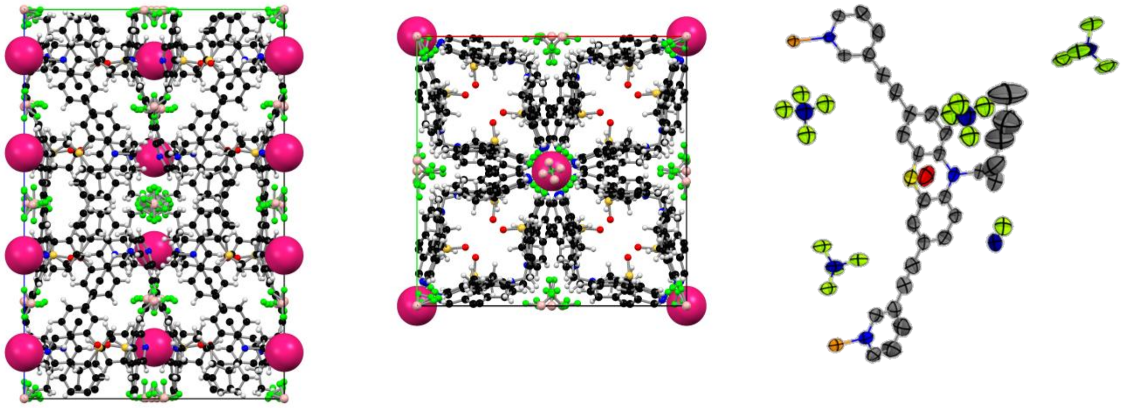

a) View along axis *a*.

b) View along axis *c*.

c) Asymmetric unit with atomic displacement parameters depicted at 50 % probability

Figure SI-III.21: Visualization of the structure of $[3BF_4@Pd_4\mathbf{L}^3_8](BF_4)_5$ in the unit cell. Double-cages and BF_4^- anions displayed as ball-and-stick-model; Pd atoms as large spheres colored in pink. The tunnel-like voids along axis *c* contain lattice solvent (not modeled) can be seen in b).

---

[160] A. L. Spek, *J. Appl. Cryst.* **2003**, *36*, 7.

[161] P. van der Sluis, A. L. Spek, *Acta Cryst.* **1990**, *A46*, 194.

c) X-Ray structure data of double-cage $[3BF_4@Pd_4\mathbf{L}^4{}_8](BF_4)_5$[162]

Suitable crystals of were grown by slow diffusion of ethanol into an acetonitrile solution of double-cage $[3BF_4@Pd_4\mathbf{L}^4{}_8](BF_4)_5$. A suitable yellow block shaped crystal of the size 0.09 x 0.08 x 0.06 mm^3 was selected from a batch of crystals using the X-TEMP 2 device.[153] The crystal was mounted on top of glass fiber using inert perfluorinated polyether oil and placed in the cold gas stream of a Bruker Kryoflex 2 low-temperature device with a cold stream at 100(2) K on a Bruker D8 three circle diffractometer. The diffractometer was equipped with a SMART APEX II CCD detector and a rotating anode source (Mo-Kα; λ = 0.71073 Å). Data were collected in omega-scan mode at different detector 2θ angles ranging between 0° and 90°. The scan width was set to 0.5°. Data integration was done with SAINT 8.30C.[163] Each run with constant 2θ and ϕ settings was integrated using a separate orientation matrix. Data scaling and absorption correction was done with SADABS 2012/1.[155] The space group was determined using XPREP.[156] The structure was solved by direct methods using SHELXS-97.[164] Refinement by full-matrix least-squares procedures was done with SHELXL-2013[157] within the SHELXLe-GUI.[165] The hydrogen atoms were refined isotropically on calculated positions using a riding model with their U_{iso} values constrained to 1.5 U_{eq} of their pivot atoms for terminal sp^3 carbon atoms and 1.2 times for all other carbon atoms. All non-hydrogen-atoms were refined with anisotropic displacement parameters. For the severely disordered solvent regions the SQUEEZE routine of the PLATON program was applied.

Table AP-III.3 Crystallographic data of $[3BF_4@Pd_4\mathbf{L}^4{}_8](BF_4)_5$. Reproduced with permission from reference [66]. Copyright © 2014 Royal Society of Chemistry.

CCDC number	**972251**
Empirical formula	$C_{512}H_{432}B_{14}Cl_2F_{56}N_{48}O_{32}Pd_8S_{16}$
Formula weight	8 x 1302.43 g mol^{-1}
Temperature	100(2) K
Wavelength	0.71073 Å
Crystal system	Tetragonal

---

[162] The X ray data for the double-cage $[3BF_4@Pd_4\mathbf{L}^4{}_8]^5$ was measured, solved and refined by Lennard Krause (working group of Prof. Dr. D. Stalke, Georg-August University of Göttingen).

[163] Bruker *SAINT v8.30C*, Madison, **2013**.

[164] G. M. Sheldrick, *Acta Crystallogr., Sect. A: Found. Crystallogr.* **1990**, *46*, 467.

[165] C. B. Hübschle, G. M. Sheldrick and B. Dittrich, *J. Appl. Crystallogr.* **2011**, *44*, 1281.

Space group	*P*4/*nnc*
Unit cell dimensions	a = b = 21.991(2) Å
	c = 31.800(3) Å
Volume	15378(2) $Å^3$
Z	8
Density (calculated)	1.125 Mg/m^3
Absorption coefficient	0.363 mm^{-1}
F(000)	5328
Crystal size	0.09 x 0.08 x 0.06 mm^3
Theta range for data collection	1.126 to 23.837°.
Index ranges	-25<=h<=24, -24<=k<=24, -
Reflections collected	166252
Independent reflections	5937 [R(int) = 0.0583]
Completeness to theta = 25.242°	85.0 %
Refinement method	Full-matrix least-squares on F^2
Data / restraints / parameters	5937 / 1104 / 682
Goodness-of-fit on F2	1.058
Final R indices	R1 = 0.0797, wR2 = 0.2565
R indices (all data)	R1 = 0.1049, wR2 = 0.3011
Largest diff. peak and hole	1.429 and -0.662 e.Å-3

After refinement of the double-cage, all necessary BF_4^- and Cl^- anions could be found in the fourier difference map. The BF_4^- are located on special positions, all but one exhibiting disorder and not obeying the crystallographic symmetry. They were modeled using distance restraints with lowered standard deviations. Diffuse residual electron density was observed in the crystal voids. Heavily disordered lattice solvent (ethanol) could be fitted into these voids (see figures below). However, a model containing a sufficient amount of solvent molecules to adequately describe the density did not converge.

with modeled solvent molecules	without modeled solvent molecules
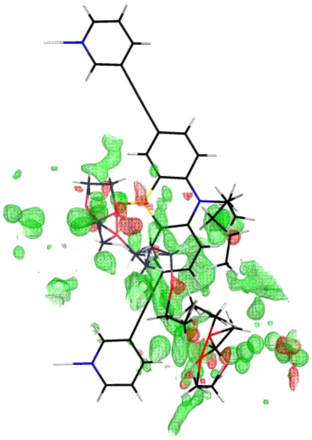	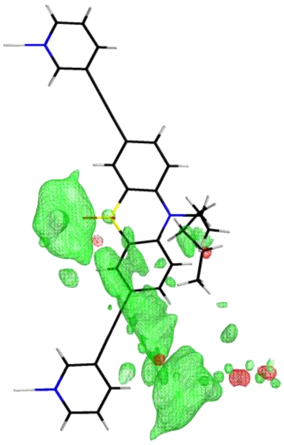
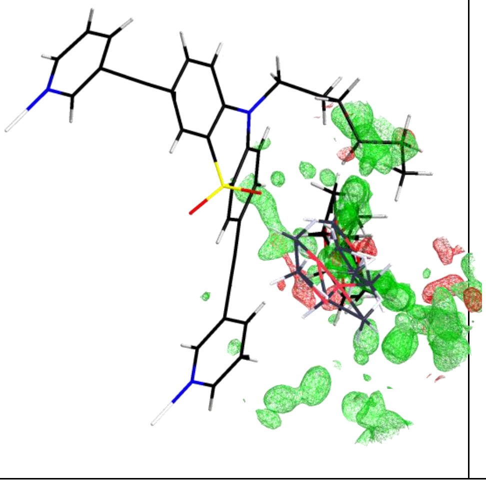	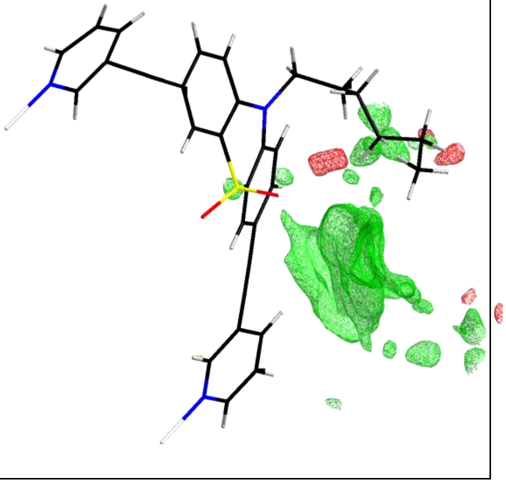

Figure AP-III.22 Exemplification of the solvent accessible crystal voids.

The pictures only show the residual electron density in the solvent channels of one asymmetric unit, the rest of the density and the BF_4^- ions are omitted for clarity. Due to the low resolution of the data, it was not possible to adequately model the lattice solvent into these voids and get a stable refinement. In order to extinguish the influence of the electron density present in the voids, the SQUEEZE routine of the PLATON program package was used.[160,161]

Table AP-III.4 Comparison of final model quality indicators.

	without solvent	with solvent	squeeze
R1	0.1158	0.0970	0.0797
wR2	0.3977	0.3804	0.3011
GooF*	1.360	1.612	1.010

*restrained GooF for all data

d) Comparison of crystal packing of $[3BF_4@Pd_4\mathbf{L}^2{}_8]^{5+}$, $[3BF_4@Pd_4\mathbf{L}^3{}_8]^{5+}$ and $[3BF_4@Pd_4\mathbf{L}^4{}_8]^{5+}$

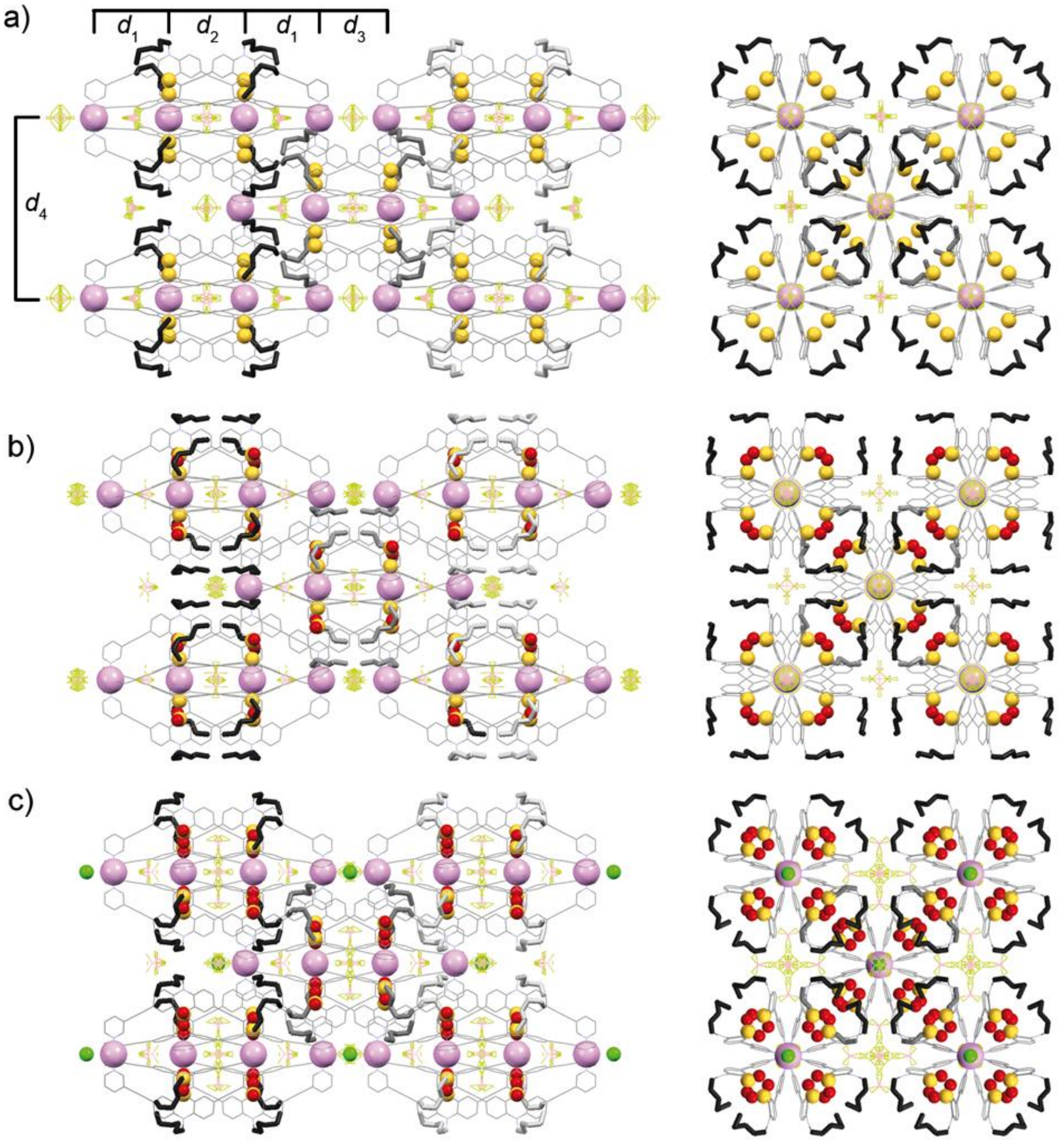

Figure AP-III.23 Side view (left) and view along (right) the Pd_n-axis of nine selected cages extracted from the X-ray crystal packing of (a) $[3BF_4@Pd_4\mathbf{L}^2{}_8]^{8+}$, (b) $[3BF_4@Pd_4\mathbf{L}^3{}_8]^{8+}$ and (c) $[3BF_4@Pd_4\mathbf{L}^4{}_8]^{8+}$ (only anions positioned on the Pd_n-axis are shown, other anions and solvent molecules were omitted for clarity. C: grey, N: blue, O: red, S: yellow, B: brown, F: light green, Cl: dark green, Pd: purple). The hexyl residues are highlighted in the colours black, grey and silver to indicate different planes in the packing.

Table AP-III.5 Parameters of the cage structures and packing extracted from the crystal structures.

	$[3BF_4@Pd_4\mathbf{L}^2_8]^{5+}$	$[3BF_4@Pd_4\mathbf{L}^3_8]^{5+}$	$[3BF_4@Pd_4\mathbf{L}^4_8]^{5+}$
d_1 (Pd_{outer}-Pd_{inner})	9.77 Å	8.16 Å	8.40 Å
d_2 (Pd_{inner}-Pd_{inner})	8.85 Å	8.63 Å	8.47 Å
d_3 (Pd_{outer}-Pd_{outer})	7.88 Å	7.77 Å	6.54 Å
d_4 (Pd_{Cage}-Pd_{Cage})	21.12 Å	21.96 Å	21.99 Å

The Pd-Pd distances for a BF_4^- enclosed between two $Pd(pyridine)_4$ planes is at least 7.77 Å. The minimum Pd-Pd distance for a Cl^- captured in between is considerably smaller. It was found to be 6.54 Å for the Pd_{outer}-Pd_{outer} distance in the $[3BF_4@Pd_4\mathbf{L}^4_8]^{5+}$ double-cage (for comparison: the distance between two inner Palladium cations enclosing a chloride anion of a previously reported double-cage based on the suberone backbone was found to be 6.26 Å[17]).

e) Structure of the monomeric cage $[Pd_2\mathbf{L}^1_4]^{4+}$

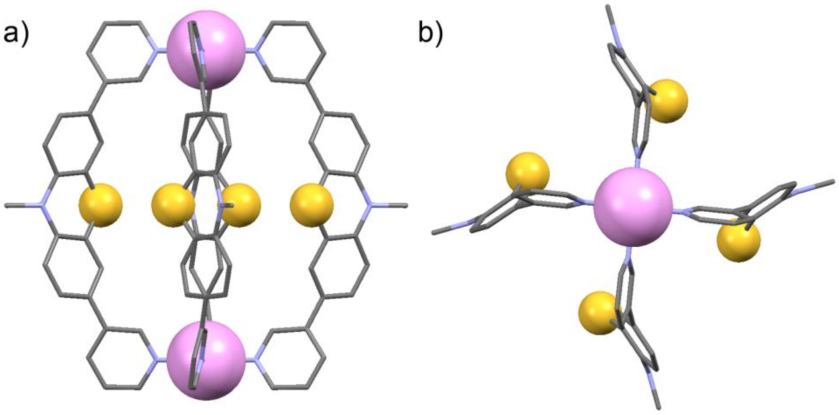

Figure SI-III.24 (a) Side view and (b) view along the Pd_2-axis of the monomeric cage $[Pd_2\mathbf{L}^1_4]^{4+}$ (C: grey, N: blue, S: yellow, Pd: purple). Palladium and sulphur atoms have been highlighted by space filling representation.

Since no single crystals suitable for X-ray crystallography could be obtained for the monomeric cage $[Pd_2\mathbf{L}^1_4]^{4+}$, the structure was calculated by a geometry optimization in Gaussian 09.[72] For this, an unconstrained geometry optimization on the PM6 semiempiric level of theory implemented in Gaussian 09[72] (charge: +4; spin-multiplicity: 1) was used. In order to reduce computational costs, the hexyl substituents were cut to methyl groups and no anions were considered in the calculation.

3. Oxygenation experiments

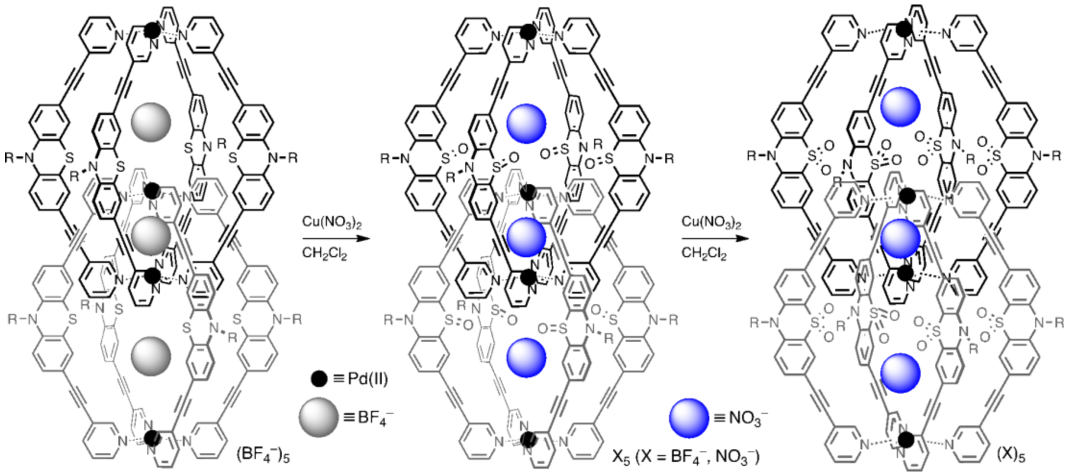

Scheme AP-III.9 Oxidation of cage $[3BF_4@Pd_4\mathbf{L}^2_8](BF_4)_5$ to the cage compounds $[3BF_4@Pd_4\mathbf{L}^3_8](BF_4)_5$ and $[3BF_4@Pd_4\mathbf{L}^4_8](BF_4)_5$.

The cage to cage oxidation was performed by adding an excess of solid $Cu(NO_3)_2{\cdot}3H_2O$ to a solution of cage $[3BF_4@Pd_4\mathbf{L}^2_8](BF_4)_5$ in CH_2Cl_2 (0.35 mM) and subsequent treatment in ultrasonic bath in a closed vial at room temperature (a slight warming of the sample due to the extended sonification was observed). The oxidation progress was monitored by ESI-MS (see Figure AP-III.25). Therefore, aliquots of the sample were taken in 30 min intervals. The samples were washed with water in order to remove the copper salt. Thereafter, the samples were diluted with acetonitrile and injected into the ESI-source of a Bruker APEX IV FTICR mass spectrometer.

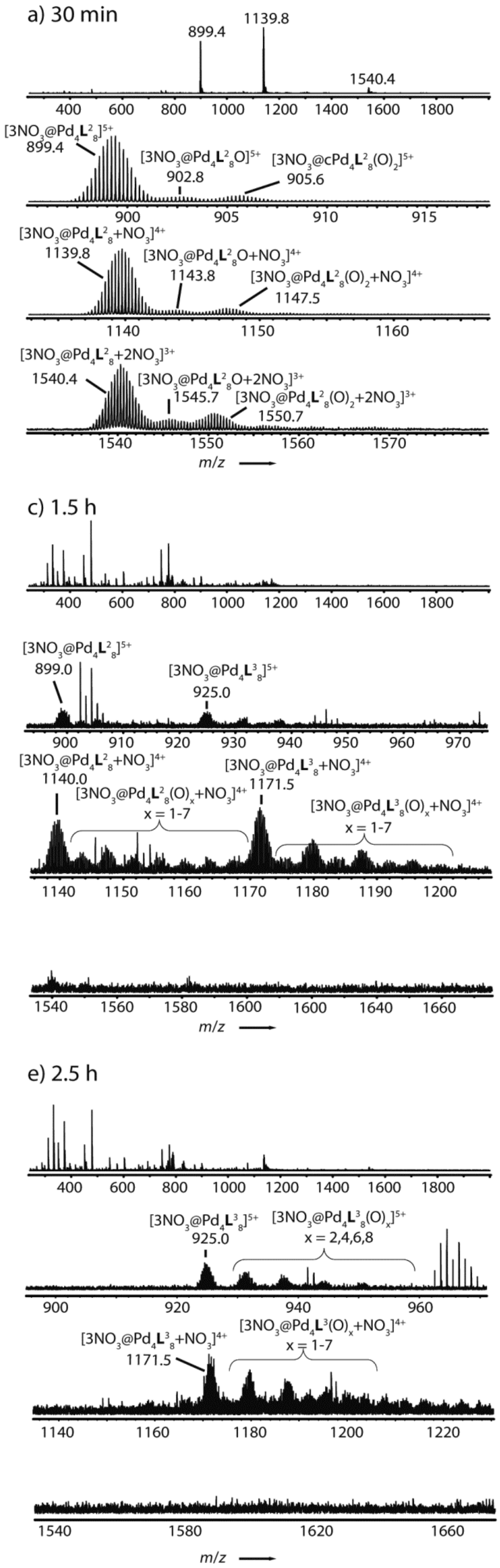

Figure AP-III.25 Time-dependent ESI-MS observation of the oxidation reaction of $[3BF_4@Pd_4\mathbf{L}^2_8]^{5+}$ to $[3X@Pd_4\mathbf{L}^3_8]^{5+}$ and $[3X@Pd_4\mathbf{L}^4_8]^{5+}$.

Mixing the ligands **L**^{2} and **L**^{3} in acetonitrile solution and subsequent addition of 0.5 equivalents of $[Pd(CH_3CN)_4](BF_4)_2$ and heating to 70 °C afforded a mixture of mixed-ligand double cages with the formula $[3BF_4@Pd_4\mathbf{L}^2{}_m\mathbf{L}^3{}_{8-m}]^{5+}$ (see Figure AP-III.26a). Heating the mixture of pre-assembled double-cages $[3BF_4@Pd_4\mathbf{L}^2{}_8]^{5+}$ and $[3BF_4@Pd_4\mathbf{L}^3{}_8]^{5+}$ over night at 70 °C show a very slow ligand exchange between the double cages (see Figure AP-III.26b).

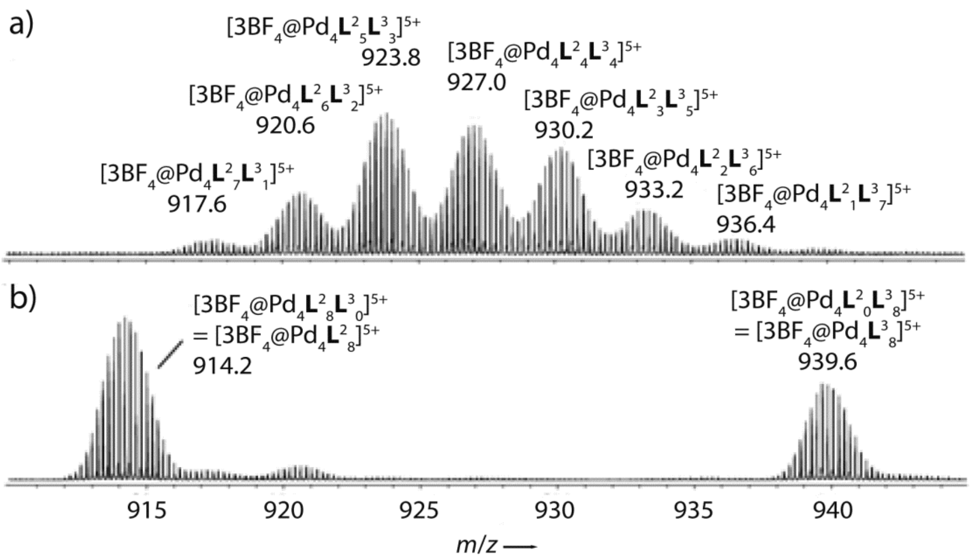

Figure AP-III.26 HR-ESI-MS measurements of a) the mixture of double-cage sample prepared by mixing of ligands **L**^{2} and **L**^{3} in acetonitrile, subsequent addition of Pd(II) and heating overnight and b) the mixture of the pre-formed double-cages $[3BF_4@Pd_4\mathbf{L}^2{}_8](BF_4)_5$ and $[3BF_4@Pd_4\mathbf{L}^3{}_8](BF_4)_5$ heated overnight at 70 °C.

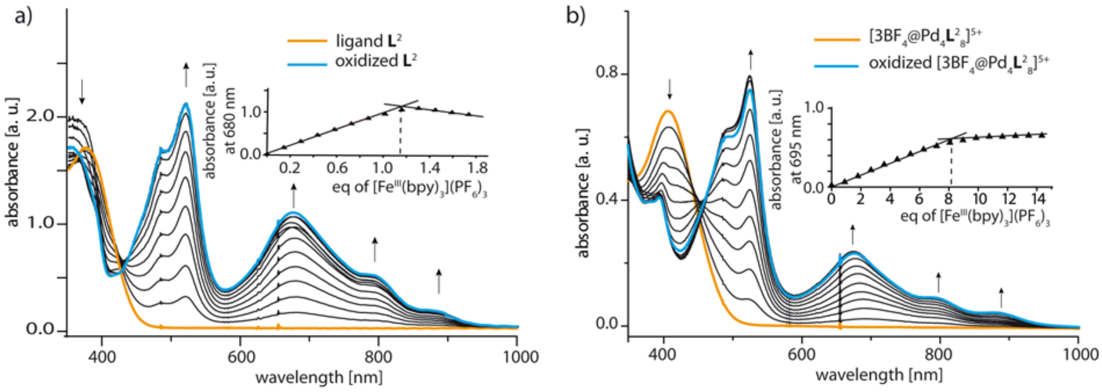

Figure AP-III.27 Titration of a) ligand **L**^{2} (c = 0.08 mM in CH_3CN) and b) $[3BF_4@Pd_4\mathbf{L}^2{}_8]^{5+}$ (c = 0.01 mM in CH_3CN) with $[Fe(III)(bpy)_3](PF_6)_3$.

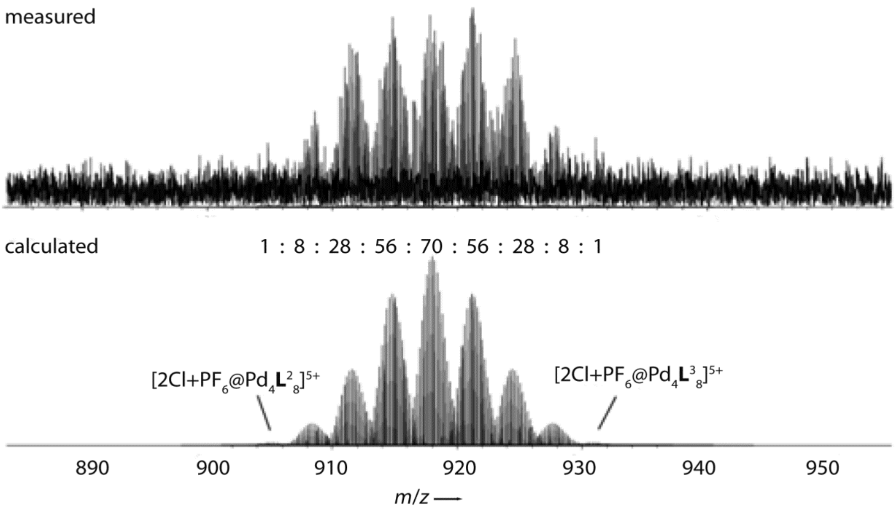

Figure AP-III.28 A non-statistical distribution of oxidation products [2Cl+PF$_6$@Pd$_4$**L**$^2_8$]$^{5+}$(O)$_n$] (n = 0 - 8) is observed in the ESI-FTICR mass spectrum of the reaction of the oxidized cage species [3BF$_4$@Pd$_4$**L**$^2_8$]$^{13\bullet+}$ with water (solvent: acetonitrile, oxidant: [Fe^{III}(bpy)$_3$](PF$_6$)$_3$, encapsulated chloride is captured in the mass spectrometer).

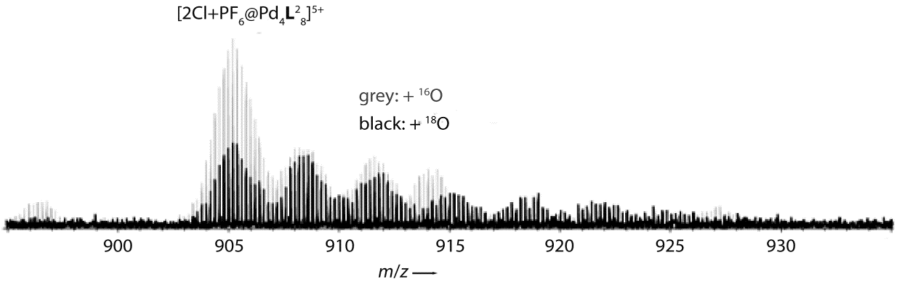

Figure AP-III.29 A comparison of the ESI-FTICR mass spectra of the reaction products of the oxidized cage species [3X@Pd$_4$**L**$^2_8$]$^{13\bullet+}$ with ^{16}O-water (grey) and ^{18}O-enriched water (black) shows that water is the source for the oxygenation of the sulfur atoms (solvent: acetonitrile, oxidant: [Fe^{III}(bpy)$_3$](PF$_6$)$_3$, encapsulated chloride is captured in the mass spectrometer).

Appendix-Chapter IV

1. Synthesis of double-cage compounds

Each cage compound $[3BF_4@Pd_4\mathbf{L}^{\mathbf{n}}_8](BF_4)_5$ with n = 2-5 was formed in quantitative yield by heating a mixture of the corresponding Ligand $\mathbf{L}^{\mathbf{n}}$ ($\mathbf{L}^{\mathbf{2}}$: 1.36 mg, 1.4 µmol; $\mathbf{L}^{\mathbf{3}}$: 1.40 mg, 1.4 µmol; $\mathbf{L}^{\mathbf{4}}$: 1.45 mg, 1.4 µmol and $\mathbf{L}^{\mathbf{5}}$: 0.57 mg, 1.4 µmol) and a solution of $[Pd(CH_3CN)_4](BF_4)_2$ (0.68 µmol, 45 µL of a 15 mM stock solution in CD_3CN) in CD_3CN (450 µL) at 70 °C for 24 h in a closed vial to give a 0.35 mM solution of $[3BF_4@Pd_4\mathbf{L}^{\mathbf{n}}_8](BF_4)_5$.

2. Titration experiments

The host-guest complexes were formed by titrating a solution of a halide salt (with tetrabutylammonium counter cations in CD_3CN, 17.5 mM) in steps of 1.0 eq or 2.0 eq (10 µL) into 500 µL of a 0.35 mM solution of double-cages in CD_3CN in an NMR tube. The NMR spectra were recorded immediately after briefly shaking the solution.

a) Titration experiments of double-cage $[3BF_4@Pd_4\mathbf{L}^2_8]^{5+}$

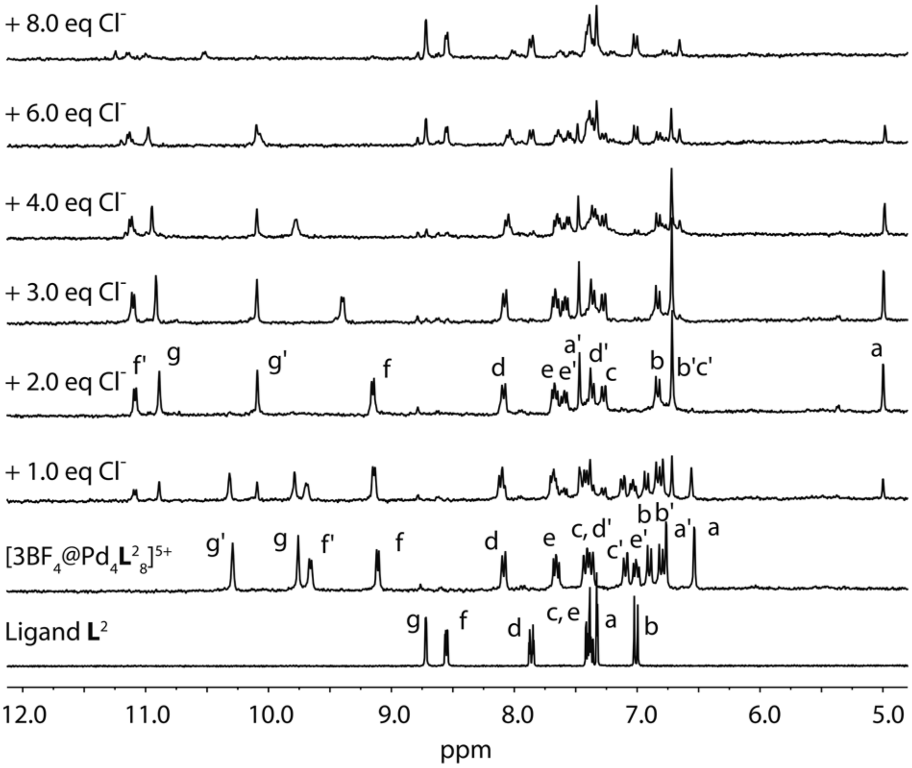

Figure AP-IV.1 ^{1}H NMR titration (300 MHz, 298 K, CD_3CN) of $[3BF_4@Pd_4\mathbf{L^2}_8]^{5+}$ with NBu_4Cl (17.5 mM). Upon addition of two equivalents of Cl^-, $[3BF_4@Pd_4\mathbf{L^2}_8]^{5+}$ transforms into $[2Cl+BF_4@Pd_4\mathbf{L^2}_8]^{5+}$. Further addition of excess halide results in decomplexation of Pd(II) under release of free ligand $\mathbf{L}^2$.

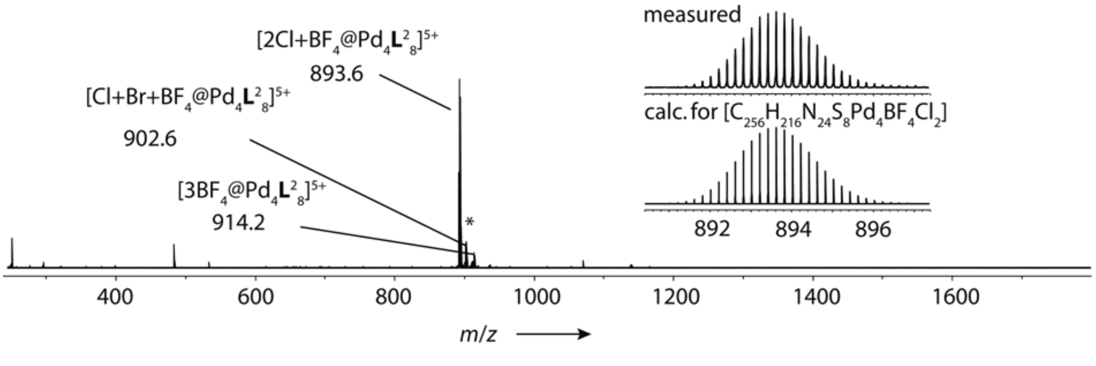

Figure AP-IV.2 ESI mass spectra (FTICR, positive mode, eluent CH_3CN) of the host-guest-complexes $[2Cl+BF_4@Pd_4\mathbf{L}^2_8]^{5+}$. * = contamination with Br^-.

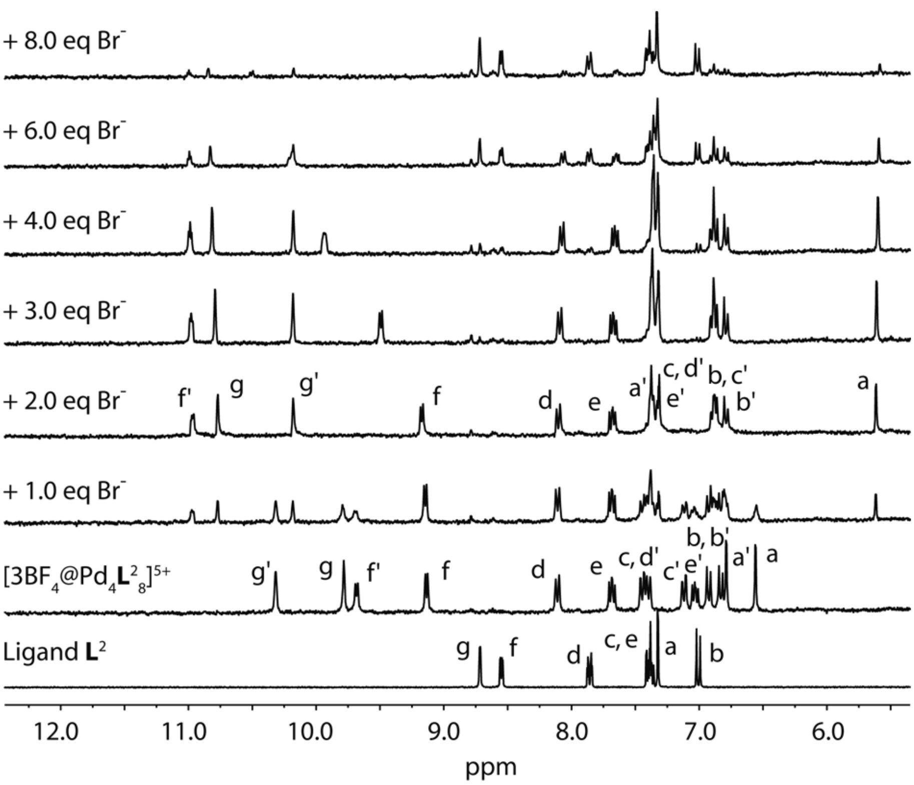

Figure AP-IV.3 ^{1}H NMR titration (300 MHz, 298 K, CD_3CN) of $[3BF_4@Pd_4\mathbf{L^2}_8]^{5+}$ with NBu_4Br (17.5 mM). Upon addition of two equivalents of Br^-, $[3BF_4@Pd_4\mathbf{L}^2{}_8]^{5+}$ transforms into $[2Br+BF_4@Pd_4\mathbf{L}^2{}_8]^{5+}$. Further addition of excess halide results in decomplexation of Pd(II) under release of free ligand $\mathbf{L}^2$.

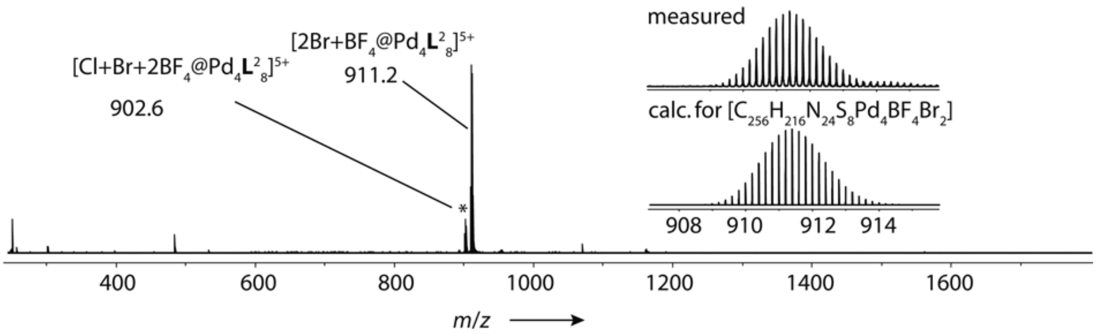

Figure AP-IV.4 ESI mass spectra (FTICR, positive mode, eluent CH_3CN) of the host-guest-complexes $[2Br+BF_4@Pd_4\mathbf{L}^2{}_8]^{5+}$. * = contamination with Cl^-.

b) Titration experiments of double-cage $[3BF_4@Pd_4\mathbf{L}^4{}_8]^{5+}$

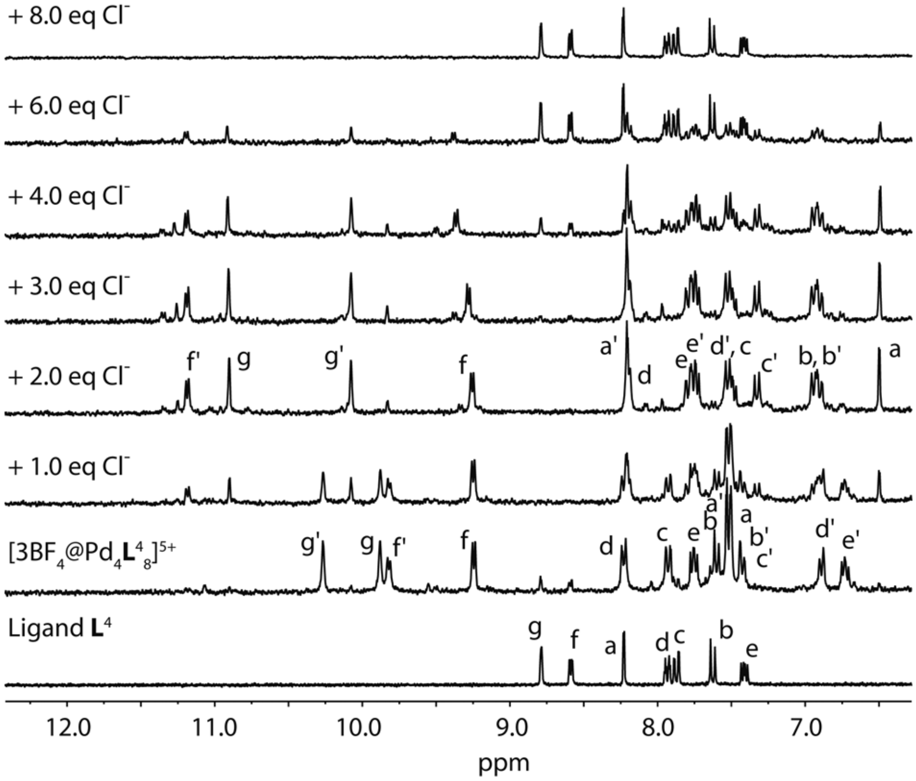

Figure AP-IV.5 ^{1}H NMR titration (300 MHz, 298 K, CD_3CN) of $[3BF_4@Pd_4\mathbf{L}^4{}_8]^{5+}$ with NBu_4Cl (17.5 mM). Upon addition of two equivalents of Cl^-, $[3BF_4@Pd_4\mathbf{L}^4{}_8]^{5+}$ transforms into $[2Cl+BF_4@Pd_4\mathbf{L}^4{}_8]^{5+}$. Further addition of excess halide results in decomplexation of Pd(II) under release of free ligand $\mathbf{L}^4$.

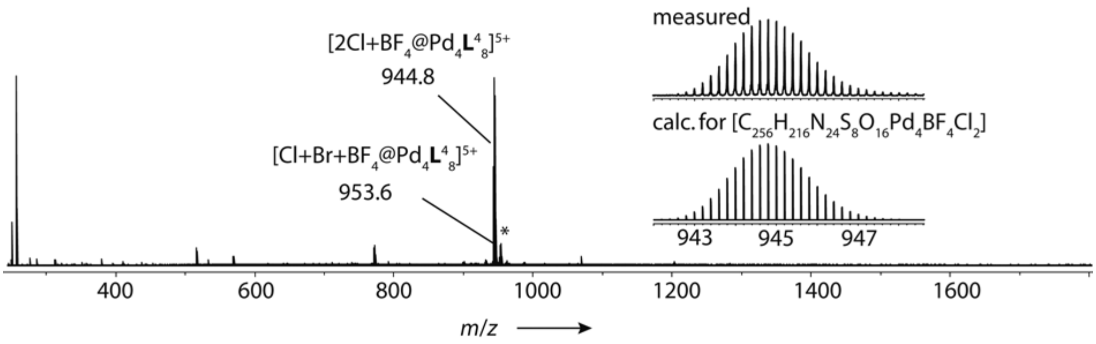

Figure AP-IV.6 ESI mass spectra (FTICR, positive mode, eluent CH_3CN) of the host-guest-complexes $[2Cl+BF_4@Pd_4\mathbf{L}^4{}_8]^{5+}$. * = contamination with Br^-.

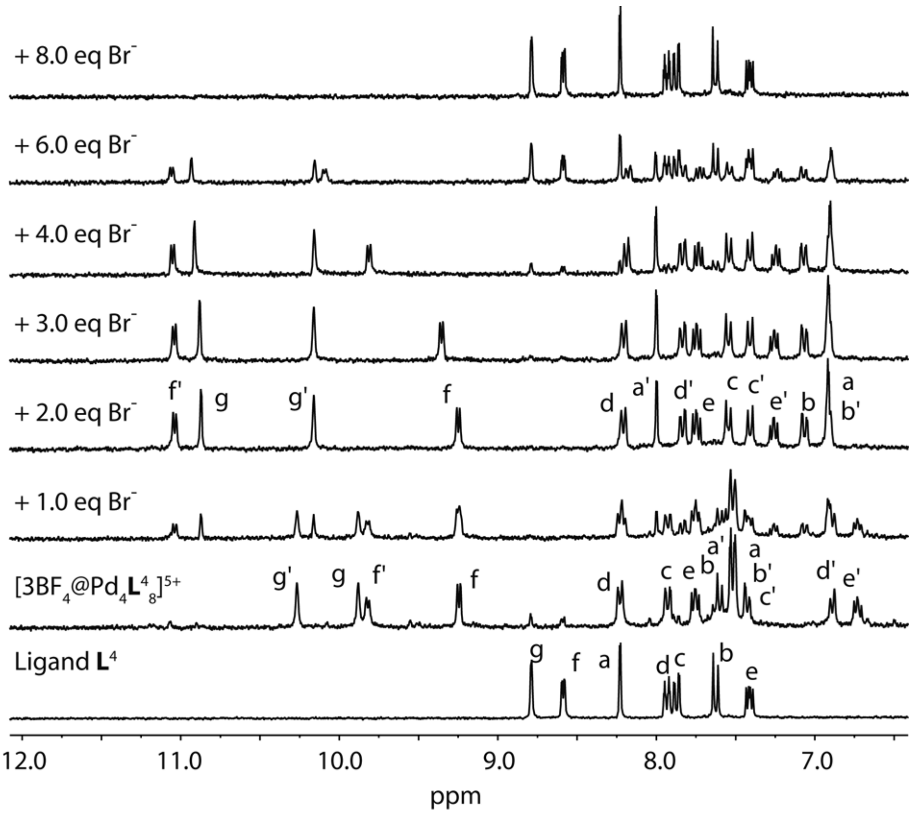

Figure AP-IV.7 ^{1}H NMR titration (300 MHz, 298 K, CD_3CN) of $[3BF_4@Pd_4\mathbf{L}^4_8]^{5+}$ with NBu_4Br (17.5 mM). Upon addition of two equivalents of Br^-, $[3BF_4@Pd_4\mathbf{L}^4_8]^{5+}$ transforms into $[2Br+BF_4@Pd_4\mathbf{L}^4_8]^{5+}$. Further addition of excess halide results in decomplexation of Pd(II) under release of free ligand $\mathbf{L}^4$.

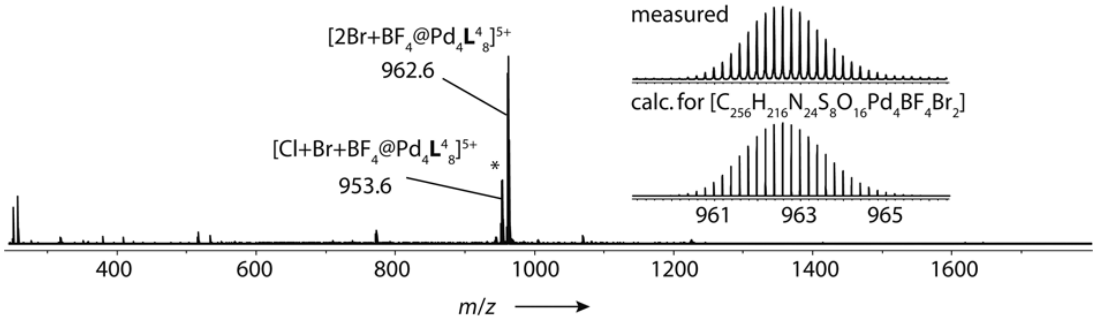

Figure AP-IV.8 ESI mass spectra (FTICR, positive mode, eluent CH_3CN) of the host-guest-complexes $[2Br+BF_4@Pd_4\mathbf{L}^4_8]^{5+}$. * = contamination with Cl^-.

3. Calculations of the NMR shifts after binding of halide anions

^{1}H NMR shifts of the protons H_a and $H_{a'}$ were calculated using the GIAO method implemented in Gaussian '09.[72] A fragment of the double-cage structure containing one inner Pd(II) ion and two BF_4^- anions was used for the calculations (see Figure AP-IV.9). In order to reduce computational costs, the hexyl substituents were cut to methyl groups. The DFT computation was performed on the B3LYP/LANL2DZ level of theory using the default solvation model (IEFPCM) with the solvent acetonitrile.

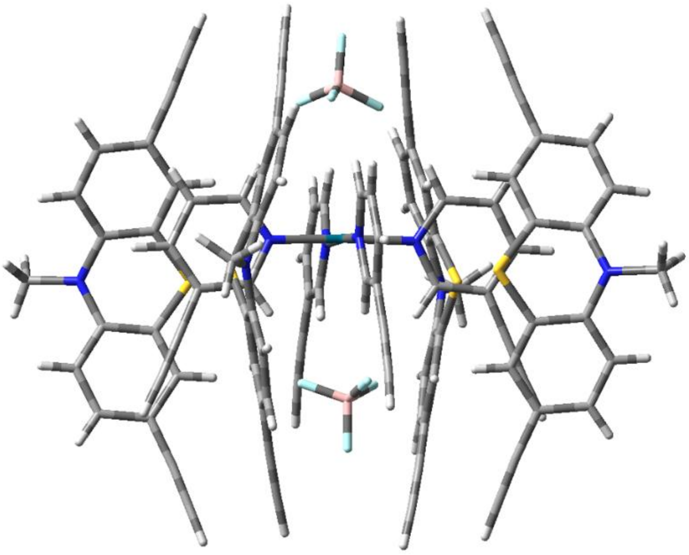

Figure AP-IV.9 Fragment used for the spin-spin coupling computation by Gaussian '09[72].

The results of the ^{1}H NMR shift computations of the protons H_a and $H_{a'}$ for all four coordination cages [$3BF_4@Pd_4\mathbf{L^n}_8$] with n = 2-5 and the experimental values[166] are shown in Figure AP-IV.10 and Table AP-IV.1. The $\Delta\delta$ value indicates the difference between the ^{1}H NMR signals of [$3BF_4@Pd_4\mathbf{L^n}_8$] and [$2X{+}BF_4@Pd_4\mathbf{L^n}_8$] with X = Cl^-, Br^-.

---

[166] measured at 300 MHz, 298 K, CD_3CN.

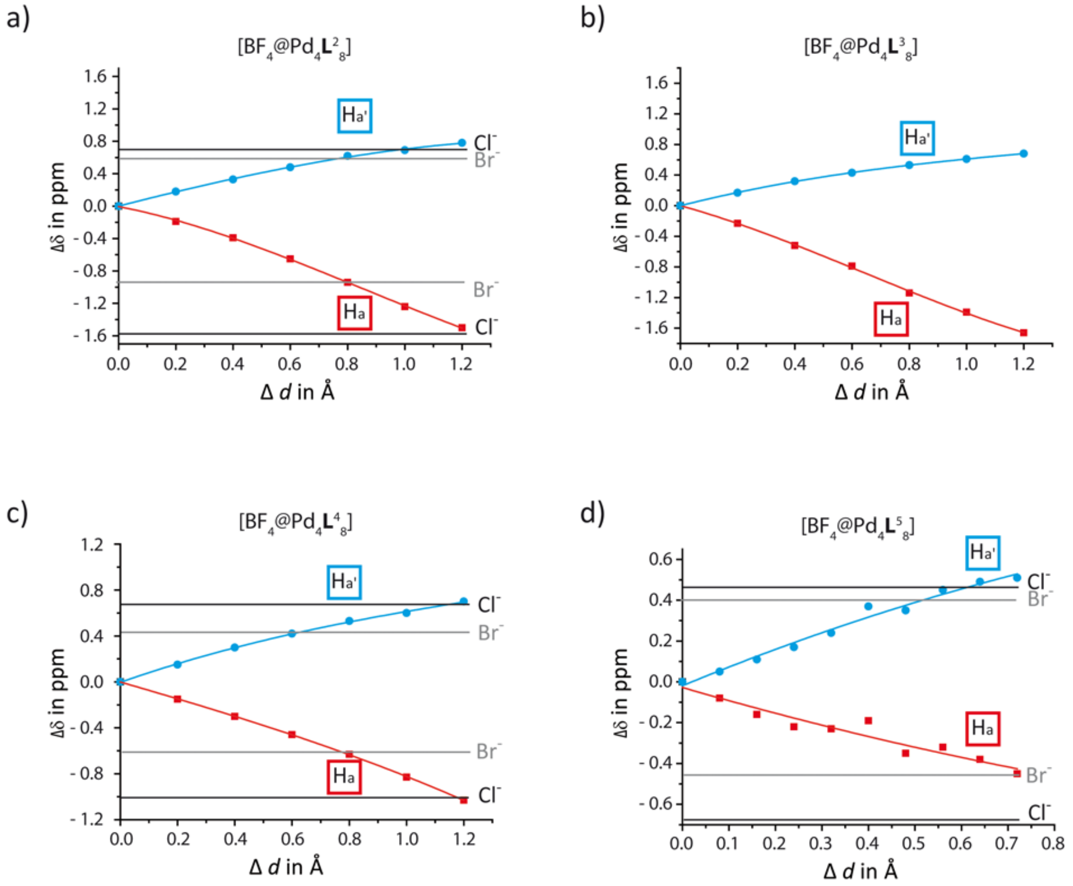

Figure AP-IV.10 Results of the computation for Δ*δ* of a) $[BF_4@Pd_4\mathbf{L}^{2}_{8}]$, b) $[BF_4@Pd_4\mathbf{L}^{3}_{8}]$, c) $[BF_4@Pd_4\mathbf{L}^{4}_{8}]$ and d) $[BF_4@Pd_4\mathbf{L}^{5}_{8}]$. The straight horizontal lines assign the experimental values of Δ*δ*. No experimental values could be obtained for $[2X+BF_4@Pd_4\mathbf{L}^{3}_{8}]$ since the compound shows very broad signals in the ^{1}H NMR.

Table AP-IV.1 Summary of the differences in chemical shifts of the protons H_a and $H_{a'}$ upon anion binding extracted from ^{1}H NMR measurements.

		Δ*δ* in ppm for H_a	Δ*δ* in ppm for $H_{a'}$
Cl	$[2Cl+BF_4@Pd_4\mathbf{L}^{2}_{8}]^{5+}$	- 1.57	0.70
	$[2Cl+BF_4@Pd_4\mathbf{L}^{3}_{8}]^{5+}$	x	x
	$[2Cl+BF_4@Pd_4\mathbf{L}^{4}_{8}]^{5+}$	- 1.01	0.68
	$[2Cl+BF_4@Pd_4\mathbf{L}^{5}_{8}]^{5+}$	- 0.70	0.44
Br	$[2Br+BF_4@Pd_4\mathbf{L}^{2}_{8}]^{5+}$	- 0.94	0.59
	$[2Br+BF_4@Pd_4\mathbf{L}^{3}_{8}]^{5+}$	x	x
	$[2Br+BF_4@Pd_4\mathbf{L}^{4}_{8}]^{5+}$	-0.62	0.44
	$[2Br+BF_4@Pd_4\mathbf{L}^{5}_{8}]^{5+}$	-0.49	0.38

4. Model calculations for the $[2X+BF_4@Pd_4L_8]^{5+}$ systems[167]

In order to calculate optimal Δ*d* and *R* values for the cage systems interacting with halide anions in the outer pockets, a push-and-pull model was constructed according to previous study of **L^5**.[168] The fitting range for the anion Cl^- was expanded up to 10.5 Å, BF_4^- to 9.8 Å, and the same distance range as in Cl^- was adopted for Br^-. Figure AP-IV. 11 shows a simplified model for the host-guest interactions. The only variable is the distance r_2 in the inner pocket (*R* is fixed to a constant value). The interaction energies are computed by splitting the total potential into three separate terms, each being calculated at the DF-MP2/cc-pVTZ level of theory (cc-pVTZ-PP for Pd, in combination with the ECP28MDF pseudopotential).[169,170] Each subsystem consists of two Pd(II) complexes with four pyridines, with the anion being placed in the middle of the two planes. The distance *r* between the two planes is varied and the interaction energy calculated. In the case of BF_4^-, since the anion is not perfectly spherical, the structure was optimized, keeping the planes fixed. The optimizations were carried out at the BP86/def2-SVP level of theory with the ORCA program package.[171] The wave function calculations were carried out with Molpro2010.1.[172] The resulting calculated r_2 distances are summarized in Table AP-IV.2.

The potential profiles were calculated for each of the three different anions and were then fitted to a linear combination of gaussian functions through the use of the OGOLEM program.[173] In the case of the halides, 7 Gaussian functions were used. For BF_4^- only 4 Gaussians were applied to avoid overfitting of the profile. The results are shown in Figure AP-IV.12.

---

[167] The calculations were performed and analyzed by Dr. Johannes M. Dieterich and Prof. Dr. Ricardo A. Mata, Department of Physical Chemistry, University of Göttingen

[168] J. M. Dieterich, G. H. Clever and R. A. Mata, *Phys. Chem. Chem. Phys.*, **2012**, *14*, 12746.

[169] T. H. Dunning, *J. Chem. Phys.*, **1989**, *90*, 1007.

[170] K. Peterson, D. Figgen, M. Dolg and H. Stoll, *J. Chem. Phys.*, **2007**, *126*, 124101.

[171] F. Neese, Orca: An Ab Initio, DFT and Semiempirical electronic structure package v2.8, **2011**.

[172] H.-J. Werner, P. J. Knowles, G. Knizia, F. R. Manby and M. Schütz, et al., MOLPRO, version 2010.1, a package of ab initio programs, **2010**, see http://www.molpro.net.

[173] (a) J. M. Dieterich, B. Hartke, Mol. Phys. **2010**, *108*, 279. (b) J. M. Dieterich, B. Hartke, *J. Comput. Chem.* **2011**, *32*, 1377.

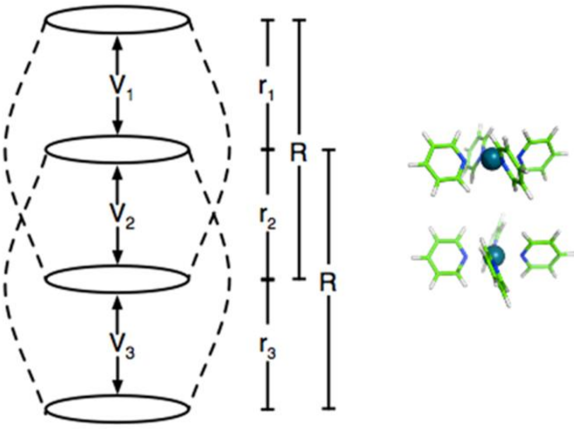

Figure AP-IV.11 Push-and-pull model for anion binding. The three pockets are represented by three different subsystems. The total potential is given by $V=V_1+V_2+V_3$, which upon fixing the distance *R*, is dependent on a single variable (in our case, the distance r_2).

Table AP-IV.2 Calculated distances $r_2 = \mathrm{Pd_{inner}}$-$\mathrm{Pd_{inner}}$.

	$\mathbf{L^2}$	$\mathbf{L^3}$	$\mathbf{L^4}$	$\mathbf{L^5}$
BF_4^-	9.17±0.17	8.39±0.14	8.20±0.20	8.09±0.25
Br^-	9.80±0.09	9.46±0.32	9.28±0.33	9.01±0.41
Cl^-	9.80±0.06	9.78±0.18	9.63±0.26	9.07±0.33

The theoretical error bars are based on a 1 kcal/mol tolerance for each given minimum. The estimated errors for the distance are computed as the average deviation of the upper and lower values.

Table AP-IV.3 Pd-Pd distances in coordination double-cages of $[3BF_4@Pd_4\mathbf{L}^2{}_8]^{5+}$, $[3BF_4@Pd_4\mathbf{L}^3{}_8]^{5+}$, $[3BF_4@Pd_4\mathbf{L}^4{}_8]^{5+}$ and $[3BF_4@Pd_4\mathbf{L}^5{}_8]^{5+}$ obtained from the X-ray structure.

	d (Pd-Pd)$_{\mathrm{monocage}}$ in	*d* (Pd$_{\mathrm{outer}}$-Pd$_{\mathrm{inner}}$)	*d* (Pd$_{\mathrm{inner}}$-Pd$_{\mathrm{inner}}$) in
$[3BF_4@Pd_4\mathbf{L}^2{}_8]^{5+}$	17.62	8.77	8.85
$[3BF_4@Pd_4\mathbf{L}^3{}_8]^{5+}$	16.77	8.16	8.63
$[3BF_4@Pd_4\mathbf{L}^4{}_8]^{5+}$	16.87	8.40	8.47
$[3BF_4@Pd_4\mathbf{L}^5{}_8]^{5+}$	16.34	8.09	8.25

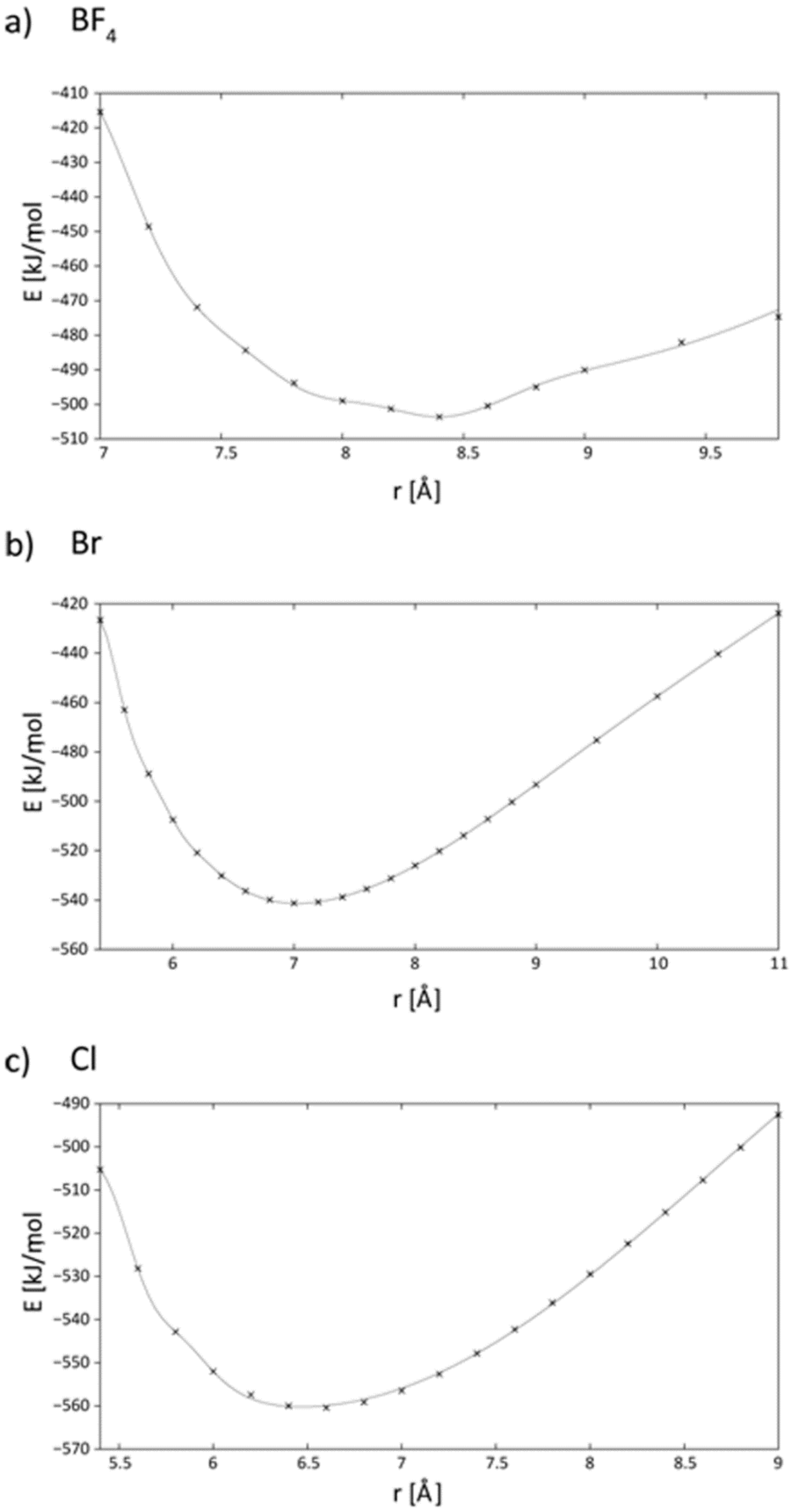

Figure AP-IV.10 DF-MP2 interaction energy profile (in kJ/mol) for a) BF_4^-, b) Br^- and c) Cl^- interacting with two Pd(II) planes.

5. ^{1}H,^{1}H-NOESY correlations[174]

General procedure: First, the NOESY spectra of the coordination double-cages $[3BF_4@Pd_4\mathbf{L}^n{}_8](BF_4)_5$ with n = 2,4,5 were measured. Next, some prominent signals in the spectrum were chosen for integration. Thereby all the integrals were correlated to one diagonal signal peak (integral was set to *I* = 1). In the next step, these integrals were correlated to the corresponding distances obtained from the X-ray structures. Having this correlation in hand, the NOESY intensities of halide containing double-cages $[2X+BF_4@Pd_4\mathbf{L}^2{}_8]^{5+}$ (X^- = Cl^-, Br^-) could be converted to distances.

Here an example for the calculation performed for the double-cage $[3BF_4@Pd_4\mathbf{L}^2{}_8]^{5+}$:

The relative integral I_rel of an NOE signal depends on the interatomic distance *d* (*a* = proportionality factor).

$$I_\text{rel} = a \cdot d^{-6}$$

In order to calculate the atomic distances, the interatomic distance *d* was written as a function of the measured integral.

$$d = a \cdot I_\text{rel}{}^{-1/6}$$

The experimental conditions for the measurement of all NOESY spectra were held as constant as possible in order to obtain reliable distances. The proton-proton crosspeaks in the NOESY spectra of $[3BF_4@Pd_4\mathbf{L}^2{}_8]^{5+}$ and $[2X+BF_4@Pd_4\mathbf{L}^2{}_8]^{5+}$ with X = Cl^-, Br^- were measured and correlated to one of the diagonal signal's. The two cross-peak signal integrals I_1 and I_2 were averaged. The distances d_X in $[2X+BF_4@Pd_4\mathbf{L}^2{}_8]^{5+}$ were calculated according to the following equation:

$$d_\text{X} = d_{\text{BF}_4} \cdot \frac{I_\text{rel,X}{}^{-1/6}}{I_{\text{rel,BF}_4}{}^{-1/6}}$$

All signals used for correlation show contribution of two protons to the observed integral I_rel, that the NOE signal integrals could not be directly compared to the distances in the crystal structure. Artificial distances *d'* were calculated from the two contributing distances

---

[174] The NOESY spectra (900 MHz, CD_3CN) of the chloride containing cages $[BF_4@Pd_4\mathbf{L}^n{}_8]$ with n = 2,4,5 were measured by Dr. Michael John, University of Göttingen.

d_1 and d_2 using the following equation.

$$d' = (d_1^{-6} + d_2^{-6})^{-1/6}$$

An analogous distance d'^* was extracted from a series of molecular models and compared to the distances d'.

Errors for the distances Δd_X were calculated using the integral dependent maximum error. The integral error ΔI_{rel} was obtained from the standard deviation of the two averaged integral values and the contribution of the noise. $\Delta I_{rel,\ noise} = 0.0004$ was obtained from the noise level of the NOESY spectra.

$$\Delta d_{\mathrm{X}} = \left|\frac{\partial d_{\mathrm{X}}}{\partial I_{\mathrm{rel,BF_4}}} \cdot \Delta I_{\mathrm{rel,BF_4}}\right| + \left|\frac{\partial d_{\mathrm{X}}}{\partial I_{\mathrm{rel,X}}} \cdot \Delta I_{\mathrm{rel,X}}\right|$$

$$\Delta d_{\mathrm{X}} = \left|-\frac{1}{6} \cdot d_{\mathrm{BF_4}} \cdot \frac{I_{\mathrm{rel,X}}{}^{-7/6}}{I_{\mathrm{rel,BF_4}}{}^{-1/6}} \cdot \Delta I_{\mathrm{rel,BF_4}}\right| + \left|\frac{1}{6} \cdot d_{\mathrm{BF_4}} \cdot \frac{I_{\mathrm{rel,X}}{}^{-1/6}}{I_{\mathrm{rel,BF_4}}{}^{5/6}} \cdot \Delta I_{\mathrm{rel,X}}\right|$$

For the halide-containing double-cage $[2X{+}BF_4@Pd_4\mathbf{L}^2_8]^{5+}$ a translation model was generated by using the crystal structure of $[3BF_4@Pd_4\mathbf{L}^2_8]^{5+}$. In order to identify a suitable model for $[2X{+}BF_4@Pd_4\mathbf{L}^2_8]^{5+}$, the deviations of these distances from those obtained from the NOESY correlation were quantified by calculation of the Q-factor for each model.

$$Q = \left\{\frac{\sum_{i=1}^{N}\left(d_{\mathrm{i}}^{\mathrm{exp}} - d_{\mathrm{i}}^{\mathrm{calc}}\right)^2}{\sum_{i=1}^{N}\left(d_{\mathrm{i}}^{\mathrm{exp}}\right)^2}\right\}^{1/2}$$

A perfect agreement of the model and the experiment would result in $Q = 0$.

Table AP-IV.4 NOE signal intensities and proton proton distances for $[3BF_4@Pd_4\mathbf{L^2}_8]^{5+}$, $[2Cl{+}BF_4@Pd_4\mathbf{L^2}_8]^{5+}$ and $[2Br{+}BF_4@Pd_4\mathbf{L^2}_8]^{5+}$.

$[3BF_4@Pd_4\mathbf{L^2}_8]^{5+}$									
	NOE						Crystal		
Protons	I_1	I_2	I	ΔI			d_1 [Å]	d_2 [Å]	d' [Å]
g -> f'	0,0155	0,0108	0,013	0,0033			4,948	5,340	5,405
g -> e'	0,0027	0,0025	0,002	0,0001			5,817	6,419	4,559
f' -> a	0,0377	0,0324	0,035	0,0037			3,017	3,320	2,800
e' -> a	0,0239	0,0269	0,025	0,0021			3,377	3,716	3,135
$[2Cl{+}BF_4@Pd_4\mathbf{L^2}_8]$									
	NOE				Correlation		Model	Model	Model
Protons	I_1	I_2	I	ΔI	d' [Å]	$\Delta d'$ [Å]	d_1* [Å]	d_1* [Å]	d_1*[Å]
g -> f'	0,0339	0,0298	0,0319	0,0029	4,664	0,252	4,220	4,674	3,926
g -> e'	0,0064	0,0058	0,0061	0,0004	3,955	0,123	5,860	5,194	4,863
f' -> a	0,0187	0,0248	0,0218	0,0043	3,032	0,149	2,934	3,245	2,728
e' -> a	0,0173	0,0128	0,0151	0,0032	3,420	0,152	3,274	3,623	3,045
$[2Br{+}BF_4@Pd_4\mathbf{L^2}_8]$									
	NOE				Correlation		Model	Model	Model
Protons	I_1	I_2	I	ΔI	d' [Å]	$\Delta d'$	d_1* [Å]	d_1* [Å]	d_1*[Å]
g -> f'	0,0148	0,0147	0,0148	0,0001	5,303	0,204	4,801	5,205	4,432
g -> e'	0,0045	0,0044	0,0045	0,0001	4,169	0,041	5,690	6,304	5,295
f' -> a	0,0271	0,0223	0,0247	0,0034	2,968	0,123	2,985	3,291	2,773
e' -> a	0,0202	0,0176	0,0189	0,0018	3,293	0,101	3,686	3,343	3,105

Table AP-VI.4 shows that the best model for $[2Cl{+}BF_4@Pd_4\mathbf{L^2}_8]^{5+}$ is found for the inner Pd-Pd distance of $d(Pd_{in}\text{-}Pd_{in})$ = 9.65 Å. This is a change of 0.80 Å compared to $[3BF_4@Pd_4\mathbf{L^2}_8]^{5+}$, where $d(Pd_{in}\text{-}Pd_{in})$ is 8.85 Å.

The best model for $[2Br{+}BF4@Pd_4\mathbf{L}^2_8]^{5+}$ is found for the inner Pd-Pd distance of $d(Pd_{in}\text{-}Pd_{in})$ = 9.05 Å. This is a change of 0.20 Å compared to $[3BF_4@Pd_4\mathbf{L}^2_8]^{5+}$, where $d(Pd_{in}\text{-}Pd_{in})$ is 8.85 Å.

6. Competition experiments

General procedure

A mixture of two different cages (250 µL, 0.35 mM in CD_3CN per cage) in a ratio of 1:1 was used for competition experiments. This solution was treated with one equivalent of halide salt (NBu_4Cl or NBu_4Br, 17.5 mM, 10 µL in CD_3CN). Subsequently after addition of halide, an ^1H NMR spectrum was measured. The samples were left to stand overnight and an an ^1H NMR spectrum was measured again, which did not show any changes compared to the first recorded spectrum.

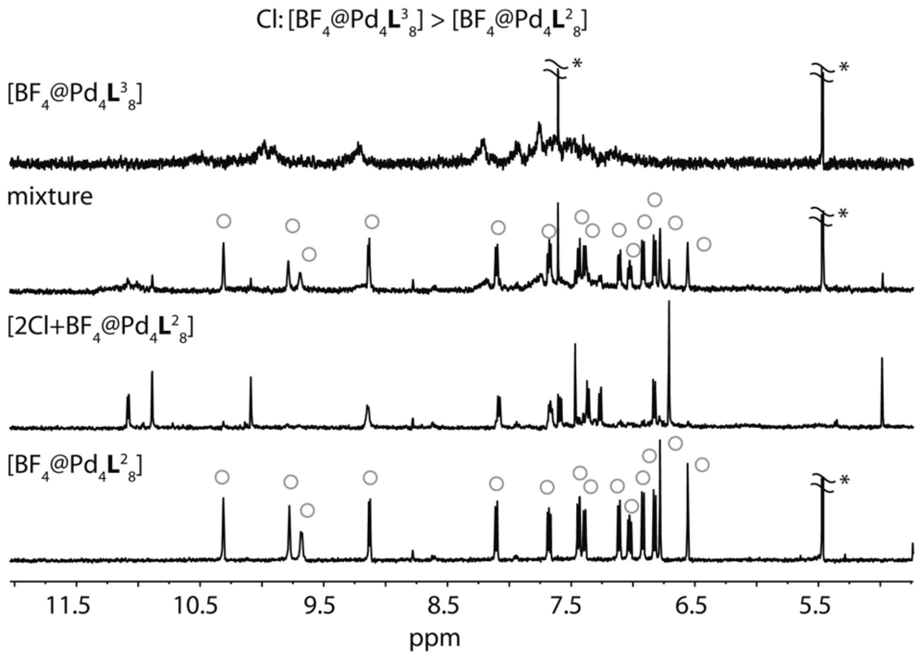

Figure AP-IV.13 ^{1}H NMR spectra (500 MHz, 298 K, CD_3CN) of the competition experiment between $[3BF_4@Pd_4\mathbf{L}^{2}_{8}]$ and $[BF_4@Pd_4\mathbf{L}^{3}_{8}]$ for the binding of chloride anions. ^{1}H NMR spectra of $[BF_4@Pd_4\mathbf{L}^{2}_{8}]$, $[2Br+BF_4@Pd_4\mathbf{L}^{2}_{8}]$, $[BF_4@Pd_4\mathbf{L}^{3}_{8}]$ are shown as reference.

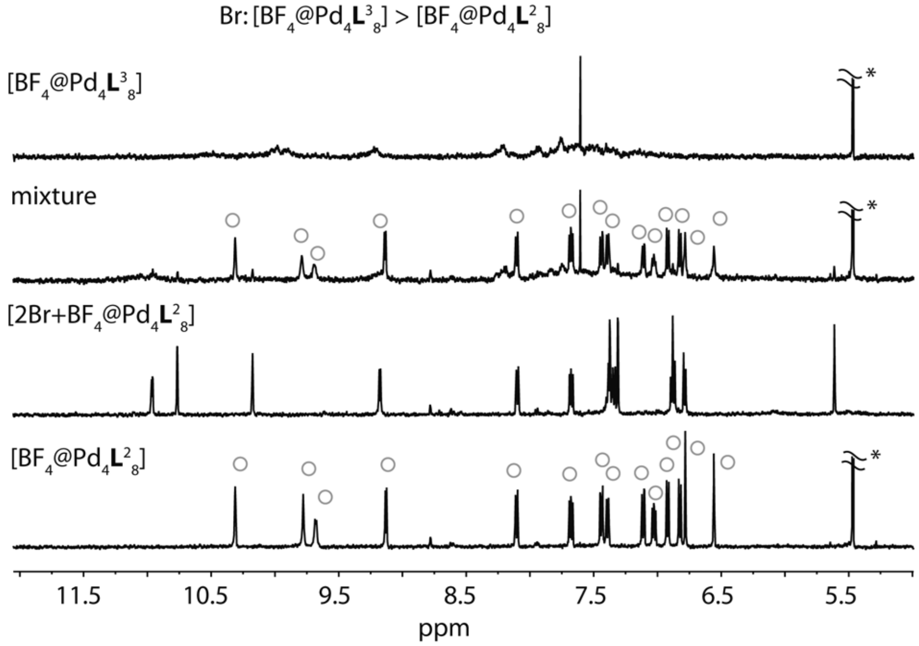

Figure AP-IV.14 ^{1}H NMR spectra (500 MHz, 298 K, CD_3CN) of the competition experiment between $[BF_4@Pd_4\mathbf{L}^{2}_{8}]$ and $[BF_4@Pd_4\mathbf{L}^{3}_{8}]$ for the binding of bromide anions. ^{1}H NMR spectra of $[BF_4@Pd_4\mathbf{L}^{2}_{8}]$, $[2Br+BF_4@Pd_4\mathbf{L}^{2}_{8}]$, $[BF_4@Pd_4\mathbf{L}^{3}_{8}]$ are shown as reference.

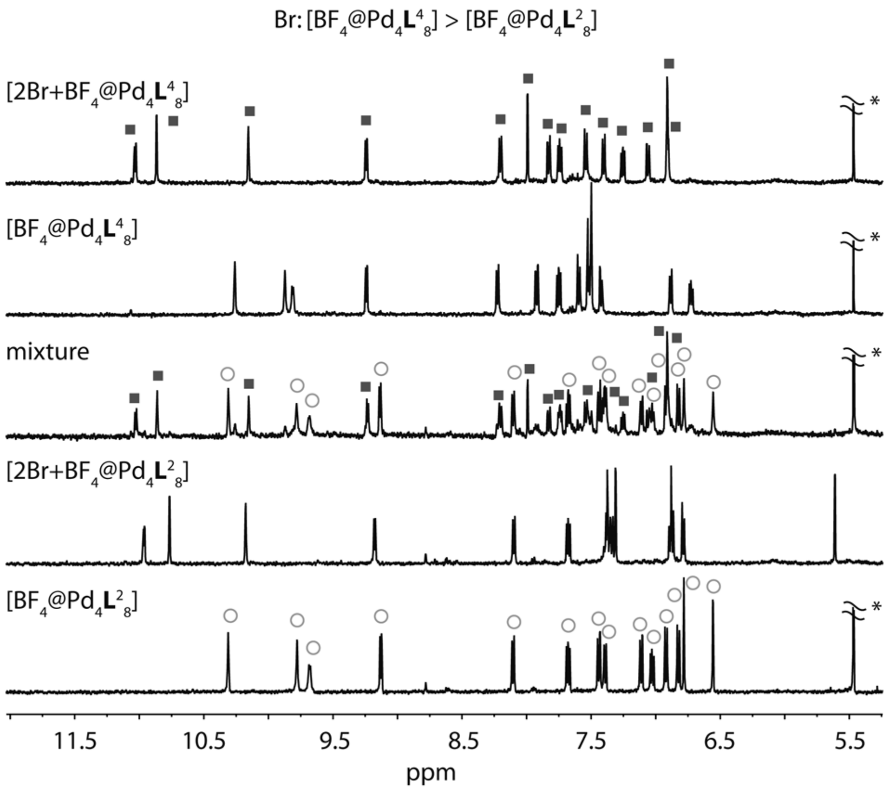

Figure AP-IV.15 ^{1}H NMR spectra (500 MHz, 298 K, CD_3CN) of the competition experiment between [BF_4@Pd_4**L**$^2_8$] and [BF_4@Pd_4**L**$^4_8$] for the binding of chloride anions. ^{1}H NMR spectra of [BF_4@Pd_4**L**$^2_8$], [2Br+BF_4@Pd_4**L**$^2_8$], [BF_4@Pd_4**L**$^4_8$] and [2Br+BF_4@Pd_4**L**$^4_8$] are shown as reference.

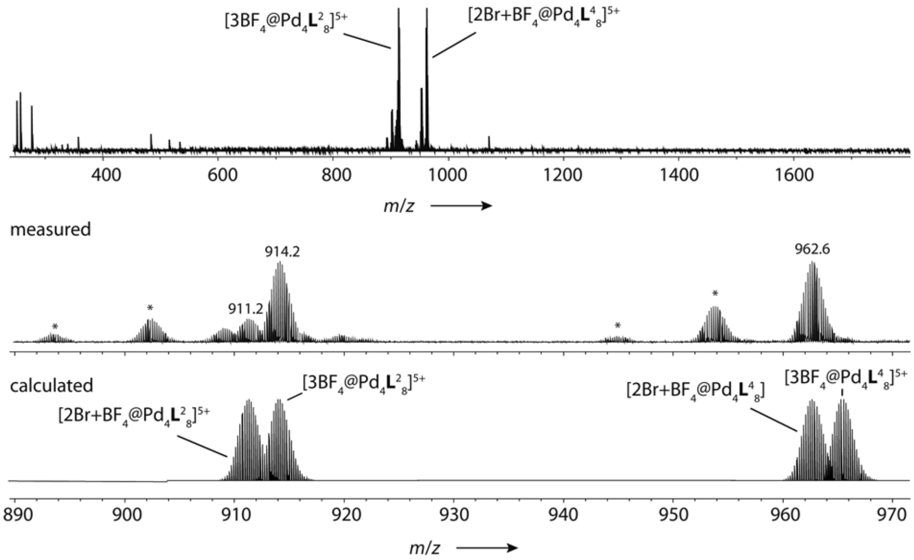

Figure AP-IV.16 ESI mass spectra (FTICR, positive mode, eluent CH_3CN) of the host-guest-complexes of the competition experiment between [BF_4@Pd_4**L**$^2_8$] and [BF_4@Pd_4**L**$^4_8$] for binding of bromide anions. * = contamination with Cl^-.

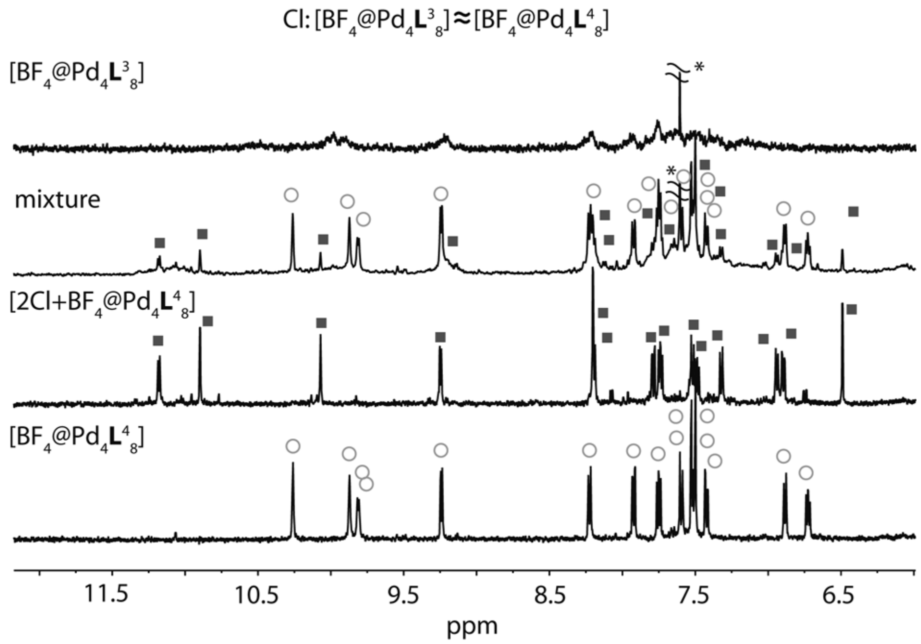

Figure AP-IV.17 ^{1}H NMR titration (500 MHz, 298 K, CD$_3$CN): Competition experiments of [BF$_4$@Pd$_4$**L**$^3_8$] and [BF$_4$@Pd$_4$**L**$^4_8$] for the binding of the chloride anion. ^{1}H NMR spectra of [BF$_4$@Pd$_4$**L**$^4_8$], [2Cl+BF$_4$@Pd$_4$**L**$^4_8$] and [BF$_4$@Pd$_4$**L**$^3_8$] are shown as reference.

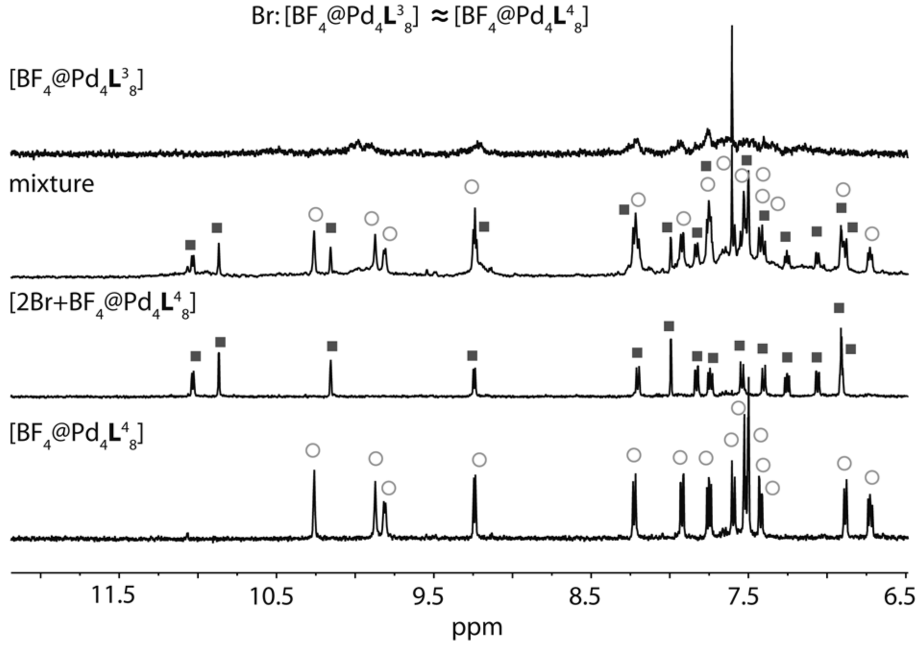

Figure AP-IV.18 ^{1}H NMR spectra (500 MHz, 298 K, CD$_3$CN) of the competition experiment between [BF$_4$@Pd$_4$**L**$^3_8$] and [BF$_4$@Pd$_4$**L**$^4_8$] for the binding of bromide anions. ^{1}H NMR spectra of [BF$_4$@Pd$_4$**L**$^4_8$], [2Br+BF$_4$@Pd$_4$**L**$^4_8$] and [BF$_4$@Pd$_4$**L**$^3_8$] are shown as reference.

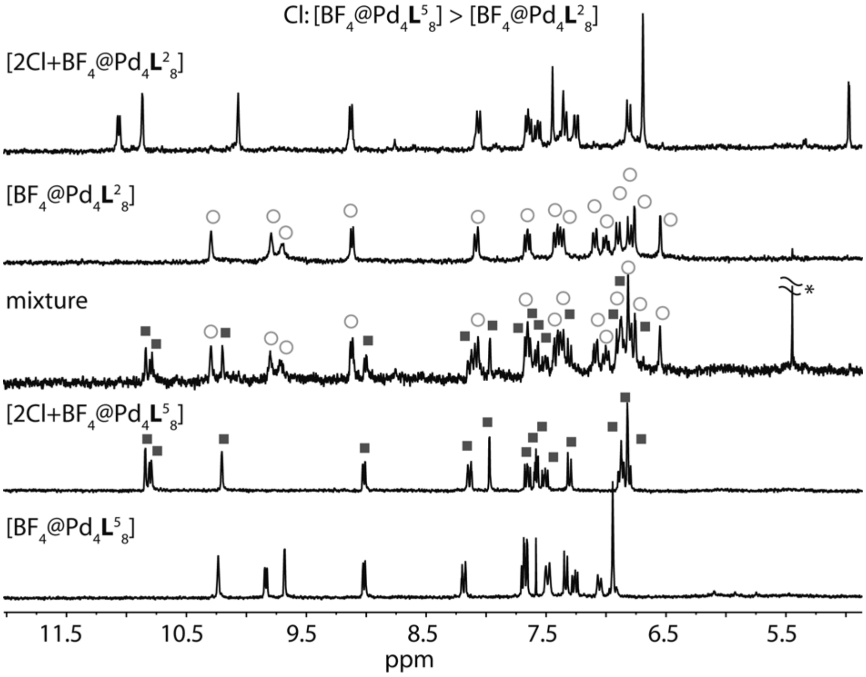

Figure AP-IV.19 ^{1}H NMR spectra (500 MHz, 298 K, CD_3CN) of the competition experiment between [BF_4@Pd_4**L**$^2_8$] and [BF_4@Pd_4**L**$^5_8$] for the binding of chloride anions. ^{1}H NMR spectra of [BF_4@Pd_4**L**$^5_8$], [2Cl+BF_4@Pd_4**L**$^5_8$], [BF_4@Pd_4**L**$^2_8$] and [2Cl+BF_4@Pd_4**L**$^2_8$] are shown as reference.

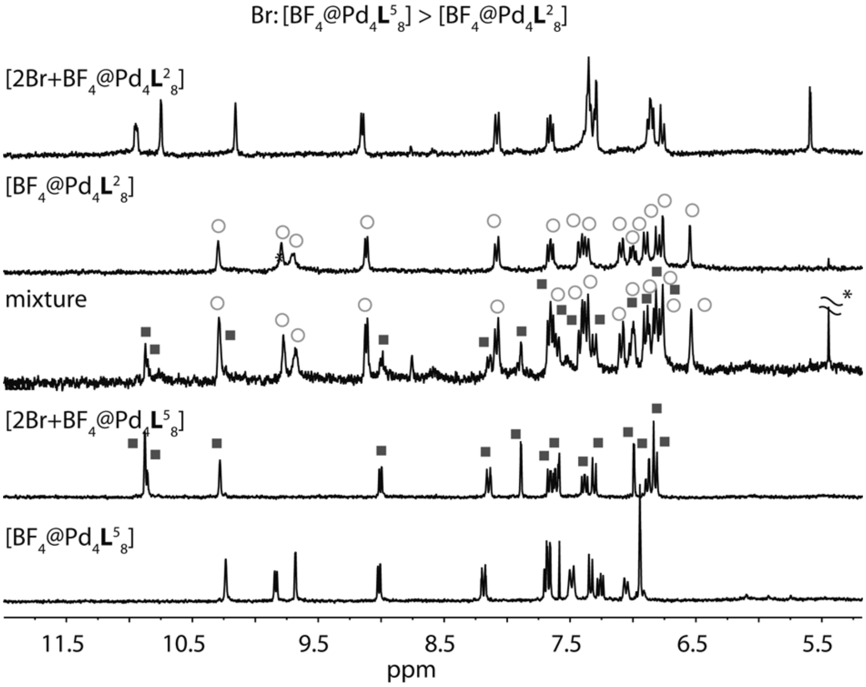

Figure AP-IV.20 ^{1}H NMR spectra (500 MHz, 298 K, CD_3CN) of the competition experiment between [BF_4@Pd_4**L**$^2_8$] and [BF_4@Pd_4**L**$^5_8$] for the binding of bromide anions. ^{1}H NMR spectra of [BF_4@Pd_4**L**$^5_8$], [2Br+BF_4@Pd_4**L**$^5_8$], [BF_4@Pd_4**L**$^2_8$] and [2Br+BF_4@Pd_4**L**$^2_8$] are shown as reference.

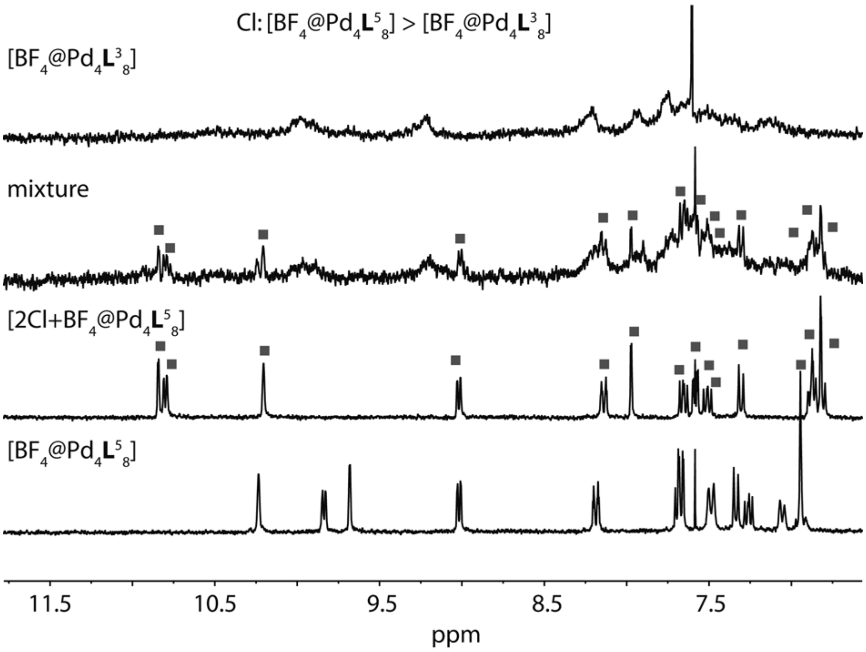

Figure AP-IV.21 ^{1}H NMR spectra (500 MHz, 298 K, CD_3CN) of the competition experiment between [BF_4@Pd_4**L**$^3_8$] and [BF_4@Pd_4**L**$^5_8$] for the binding of chloride anions. ^{1}H NMR spectra of [BF_4@Pd_4**L**$^5_8$], [2Cl+BF_4@Pd_4**L**$^5_8$] and [BF_4@Pd_4**L**$^3_8$] spectra are shown as reference.

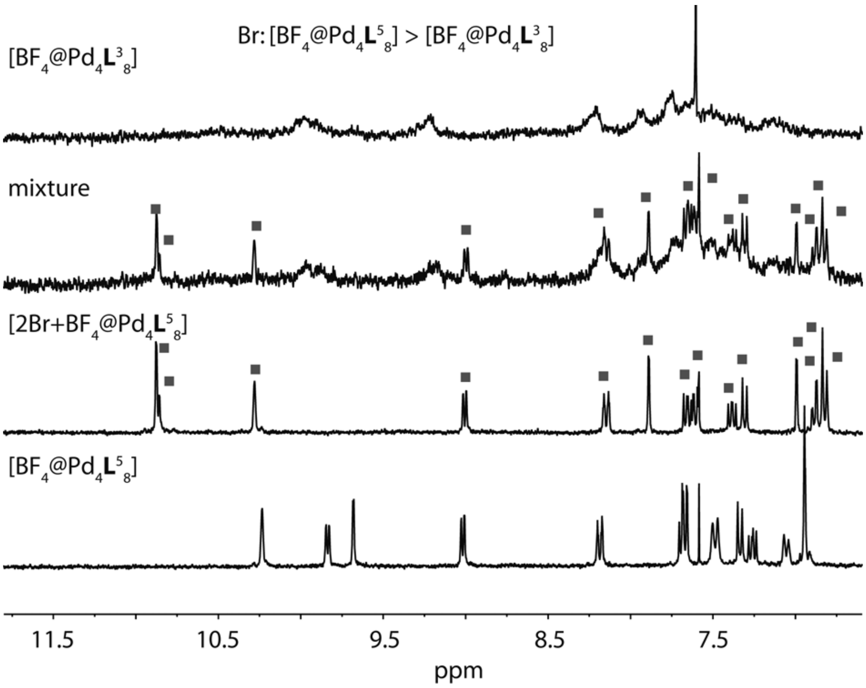

Figure AP-IV.22 ^{1}H NMR spectra (500 MHz, 298 K, CD_3CN) of the competition experiment between [BF_4@Pd_4**L**$^3_8$] and [BF_4@Pd_4**L**$^5_8$] for the binding of bromide anions. ^{1}H NMR spectra of [BF_4@Pd_4**L**$^3_8$], [BF_4@Pd_4**L**$^5_8$] and [2Br+BF_4@Pd_4**L**$^5_8$] are shown as reference.

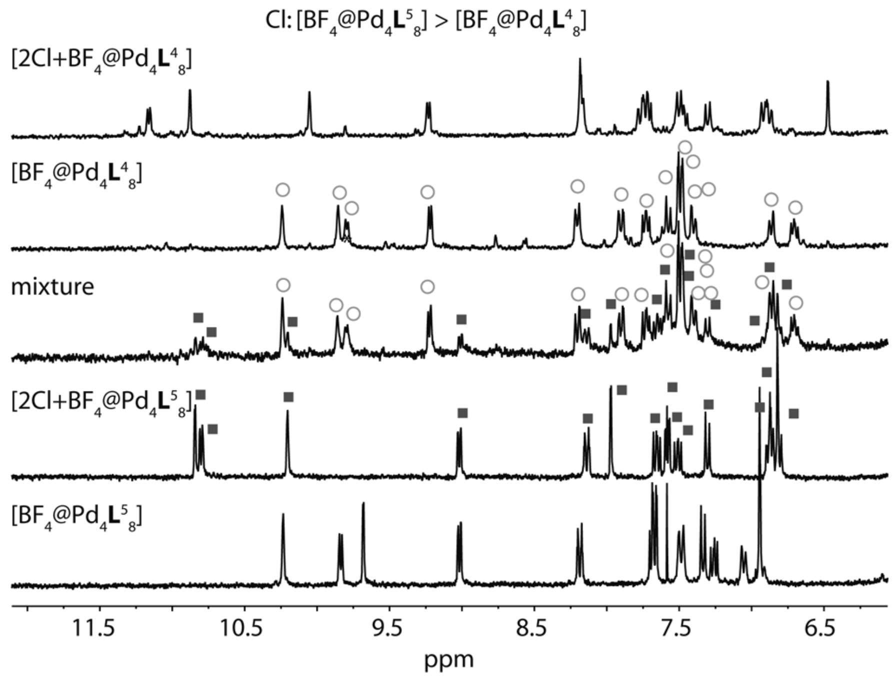

Figure AP-IV.23 ^1H NMR spectra (500 MHz, 298 K, CD_3CN) of the competition experiment between $[BF_4@Pd_4\mathbf{L}^4_8]$ and $[BF_4@Pd_4\mathbf{L}^5_8]$ for the binding of chloride anions. ^1H NMR spectra of $[BF_4@Pd_4\mathbf{L}^4_8]$, $[2Cl+BF_4@Pd_4\mathbf{L}^4_8]$, $[BF_4@Pd_4\mathbf{L}^5_8]$ and $[2Cl+BF_4@Pd_4\mathbf{L}^5_8]$ are shown as reference.

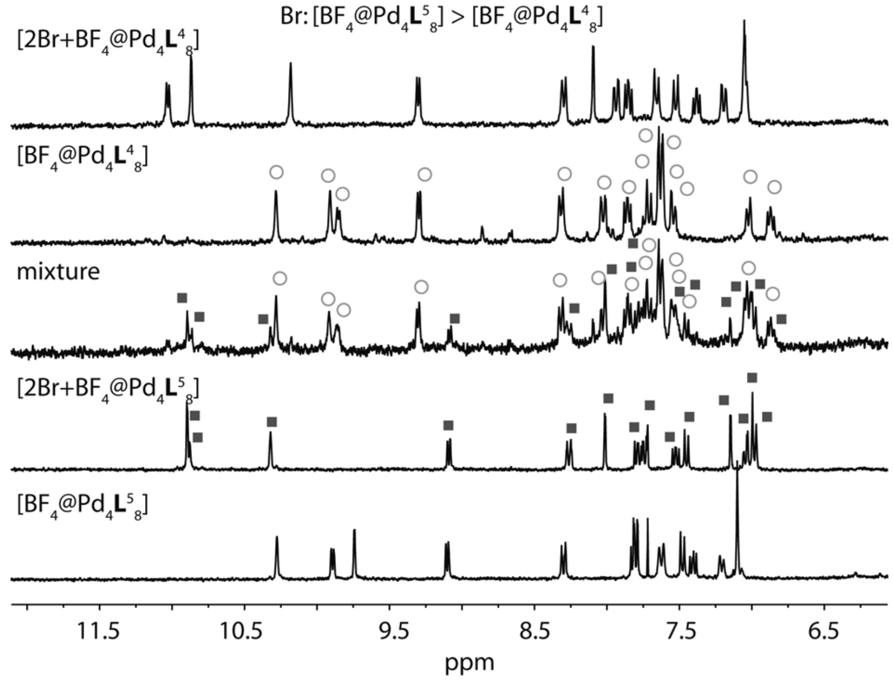

Figure AP-IV.24 ^1H NMR spectra (500 MHz, 298 K, CD_3CN) of the competition experiment between $[BF_4@Pd_4\mathbf{L}^4_8]$ and $[BF_4@Pd_4\mathbf{L}^5_8]$ for the binding of bromide anions. ^1H NMR spectra of $[BF_4@Pd_4\mathbf{L}^4_8]$, $[2Br+BF_4@Pd_4\mathbf{L}^4_8]$, $[BF_4@Pd_4\mathbf{L}^5_8]$ and $[2Br+BF_4@Pd_4\mathbf{L}^5_8]$ are shown as reference.

7. Titration experiments with AgBF$_4$ and competition experiments between Cl$^-$ and Br$^-$

General procedure – Titration with AgBF$_4$

To the solution of the chloride or bromide containing double-cage $[2X+BF_4@Pd_4\mathbf{L}^n{}_8]^{5+}$ n = 2, 4 (500 µL, 0.35 mM in CD_3CN) a solution of $AgBF_4$ (8.5 mM in CD_3CN) was added in 1.0 equivalent steps (20.5 µL). After addition an ^{1}H NMR spectrum was recorded.

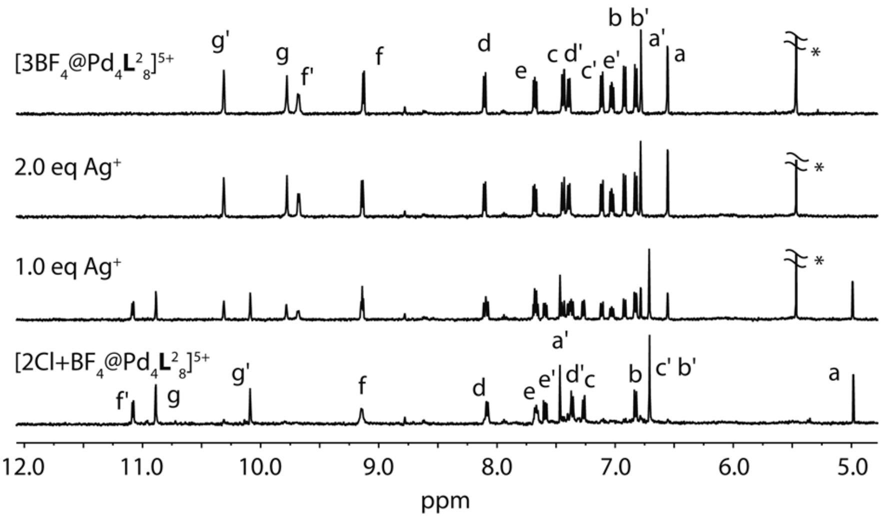

Figure AP-IV.25 ^{1}H NMR titration (500 MHz, 298 K, CD_3CN): Precipitation of encapsulated chloride from $[2Cl+BF_4@Pd_4\mathbf{L}^2{}_8]^{5+}$ with two equivalents of $AgBF_4$ under full recovery of $[3BF_4@Pd_4\mathbf{L}^2{}_8]^{5+}$ (top spectrum as reference).

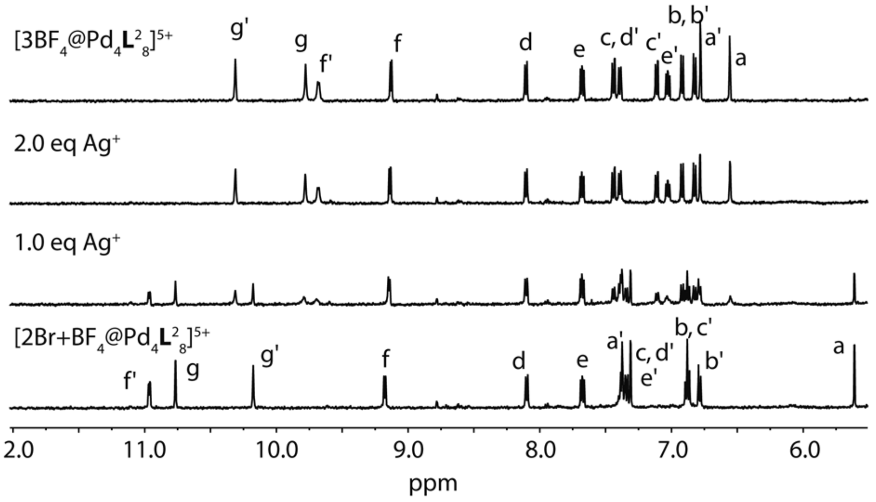

Figure AP-IV.26 ^{1}H NMR titration (500 MHz, 298 K, CD_3CN): Precipitation of encapsulated bromide from $[2Br+BF_4@Pd_4L^2{}_8]^{5+}$ with two equivalents of $AgBF_4$ under full recovery of $[3BF_4@Pd_4L^2{}_8]^{5+}$ (top spectrum as reference).

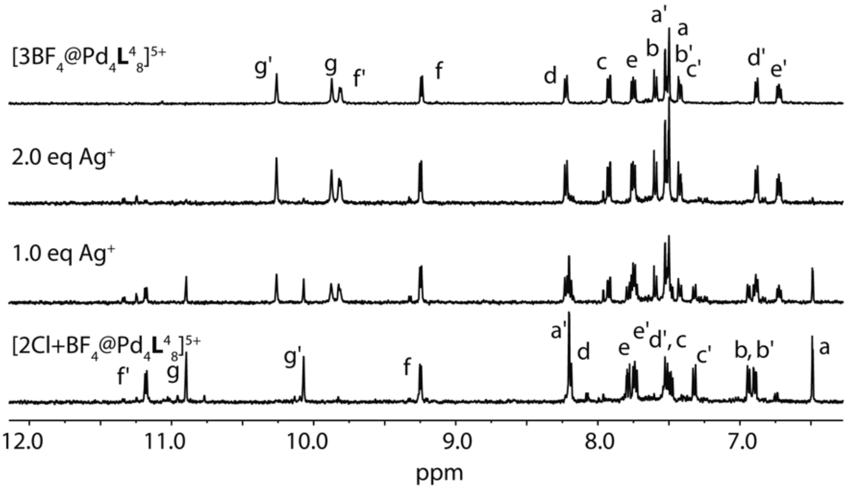

Figure AP-IV.27 ^{1}H NMR titration (500 MHz, 298 K, CD_3CN): Precipitation of encapsulated chloride from $[2Cl+BF_4@Pd_4\mathbf{L}^4{}_8]^{5+}$ with two equivalents of $AgBF_4$ under full recovery of $[3BF_4@Pd_4\mathbf{L}^4{}_8]^{5+}$ (top spectrum as reference).

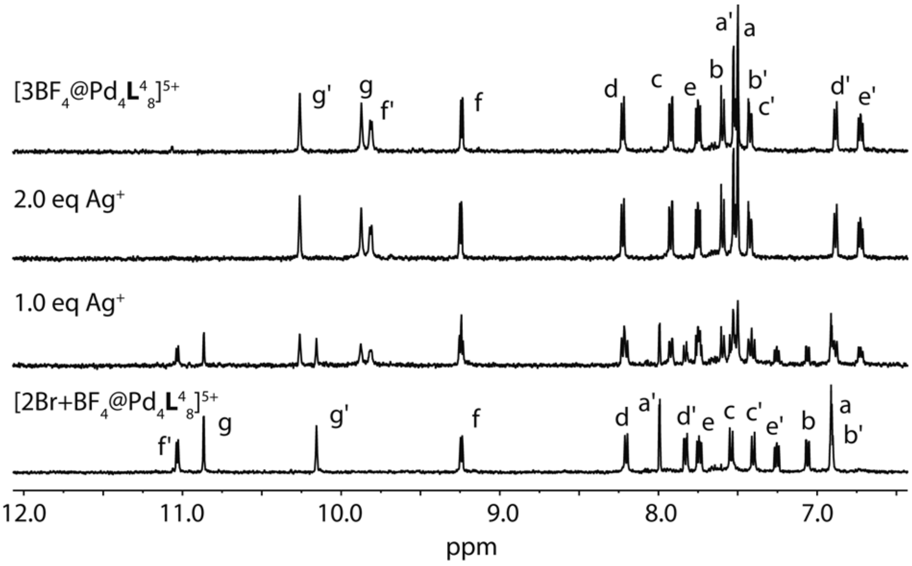

Figure AP-IV.28 ^{1}H NMR titration (500 MHz, 298 K, CD_3CN): Precipitation of encapsulated bromide from $[2Br+BF_4@Pd_4\mathbf{L}^4{}_8]^{5+}$ with two equivalents of $AgBF_4$ under full recovery of $[3BF_4@Pd_4\mathbf{L}^4{}_8]^{5+}$ (top spectrum as reference).

General procedure – Competition experiments between Cl^- and Br^-

To the solution of the double-cage $[3BF_4@Pd_4\mathbf{L}^n{}_8]^{5+}$ n = 2, 4 (500 µL, 0.35 mM in CD_3CN) solutions of NBu_4Cl (10 µL, 17.5 mM in CD_3CN) and NBu_4Br (10 µL, 17.5 mM in CD_3CN) were added simultaneously. After addition, an ^1H NMR and an ESI mass spectra were recorded.

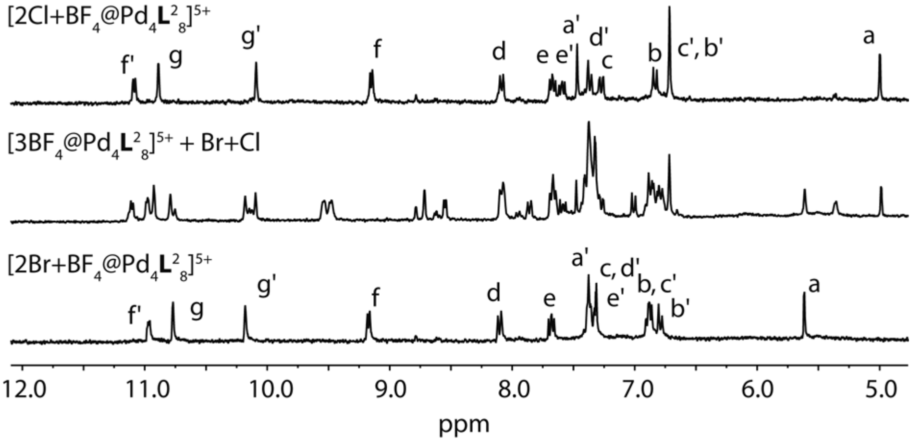

Figure AP-IV.29 ^1H NMR titration (300 MHz, 298 K, CD_3CN): Competition of two equivalents of bromide with chloride for $[3BF_4@Pd_4\mathbf{L}^2{}_8]^{5+}$. Signals of $[2Br+BF_4@Pd_4\mathbf{L}^2{}_8]^{5+}$ and $[2Cl+BF_4@Pd_4\mathbf{L}^2{}_8]^{5+}$ appear at almost the same intensity, indicating that the affinity of $[3BF_4@Pd_4\mathbf{L}^2{}_8]^{5+}$ is not preferred to one halide anion. Signals of free Ligand $\mathbf{L}^2$ appear.

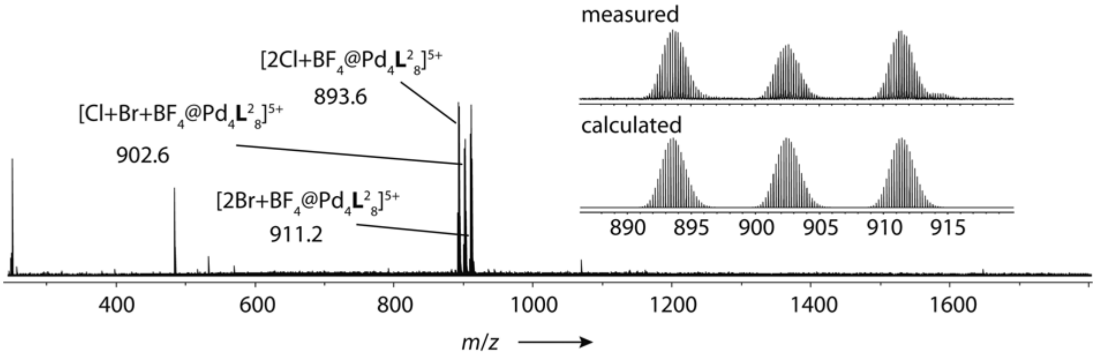

Figure AP-IV.30 ESI mass spectra (FTICR, positive mode, eluent CH_3CN) after addition of Cl^- and Br^- solutions to the double-cage $[3BF_4@Pd_4\mathbf{L}^2{}_8]^{5+}$.

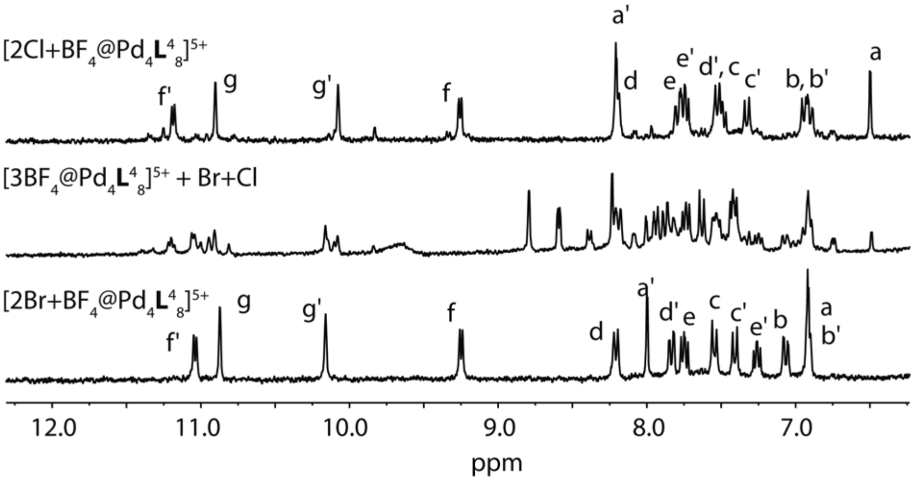

Figure AP-IV.31 ^{1}H NMR titration (300 MHz, 298 K, CD_3CN): Competition of two equivalents of bromide with chloride for [$3BF_4$@Pd_4**L**$^4_8$]$^{5+}$. Signals of [2Br+BF_4@Pd_4**L**$^4_8$]$^{5+}$ and [2Cl+BF_4@Pd_4**L**$^4_8$]$^{5+}$ appear at almost the same intensity, indicating that the affinity of [$3BF_4$@Pd_4**L**$^4_8$]$^{5+}$ is not preferred to one halide anion. Signals of free Ligand **L**^{4} appear.

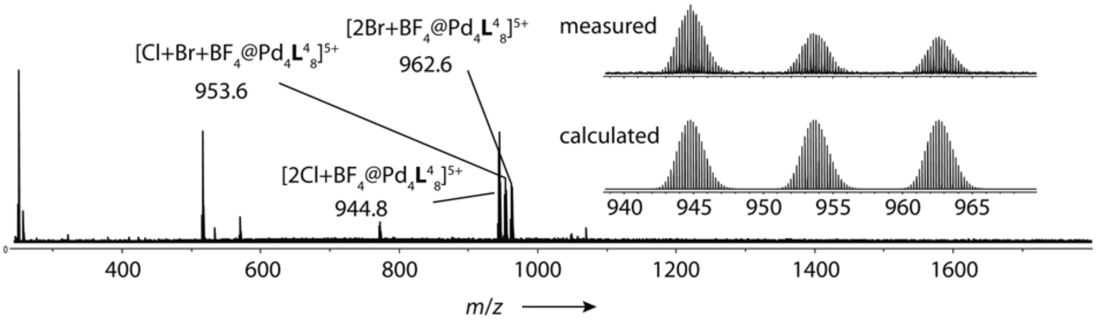

Figure AP-IV.32 ESI mass spectra (FTICR, positive mode, eluent CH_3CN) after addition of Cl^- and Br^- solutions to the double-cage [$3BF_4$@Pd_4**L**$^4_8$]$^{5+}$.

Appendix-Chapter V

1. Mixing Experiments

General procedure – Synthesis of cages

Cage compounds $[3BF_4@Pd_4\mathbf{L}^n{}_8]^{5+}$ with n = 2,3,4 and $[Pd_2\mathbf{L}^1{}_4]^{4+}$ were synthesized in quantitative yield by heating a solution of the ligand $\mathbf{L}^{1–4}$ (2.8 µmol) in 930 µL CD_3CN and a solution of $[Pd(CH_3CN)_4](BF_4)_2$ (1.4 µmol, 93 µL of a 15 mM solution in CD_3CN) at 70 °C for 6 h to give a 0.35 mM solution of $[3BF_4@Pd_4\mathbf{L}^n{}_8]^{5+}$ with n = 2,3,4 or a 0.7 mM solution of $[Pd_2\mathbf{L}^1{}_4]^{4+}$, respectively.

General procedure – Preparation of either mixed-ligand cages or mixed cages

Mixing experiment between ligands $\mathbf{L}^{2\text{-}4}$: A binary solution of two ligands was prepared by mixing the solutions of ligand $\mathbf{L}^x$ (250 µL, 2.8 mM) and $\mathbf{L}^y$ (250 µL, 2.8 mM) in CD_3CN. To this solution, $[Pd(CH_3CN)_4](BF_4)_2$ (0.75 µmol, 50 µL of a 15 mM solution in CD_3CN) was added and the mixture was heated at 70 °C to give $[3BF_4@Pd_4\mathbf{L}^x{}_m\mathbf{L}^y{}_{8–m}]^{5+}$ with $\mathbf{L}^x$, $\mathbf{L}^y = \mathbf{L}^{2–4}$; $\mathbf{L}^x \neq \mathbf{L}^y$; and m = 1 - 8.

Mixing experiment between $\mathbf{L}^{2\text{-}4}$ and $\mathbf{L}^1$: A binary solution of two ligands was prepared by mixing the solutions of ligand $\mathbf{L}^1$ (250 µL, 2.8 mM) and $\mathbf{L}^x$ (250 µL, 2.8 mM) in CD_3CN. To this solution, $[Pd(CH_3CN)_4](BF_4)_2$ (0.75 µmol, 50 µL of a 15 mM solution in CD_3CN) was added and the mixture was heated at 70 °C to give a mixture of the double-cage $[3BF_4@Pd_4\mathbf{L}^x{}_8]^{5+}$ with $\mathbf{L}^x = \mathbf{L}^{2–4}$ and the monomeric cage $[Pd_2\mathbf{L}^1{}_4]^{4+}$.

a) Mixing experiments for ligands **L**^{2} and **L**^{3}

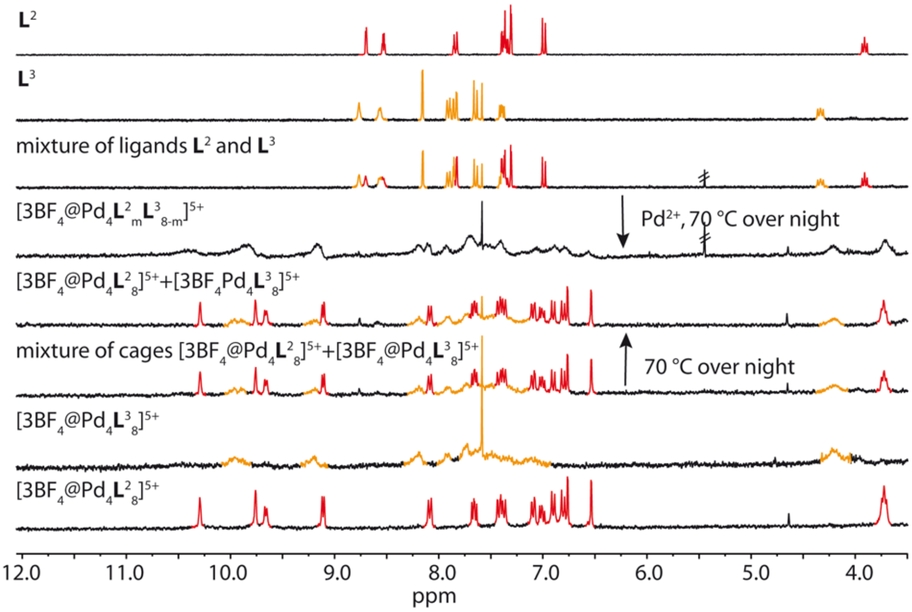

Figure AP-V.1 ^{1}H NMR spectra (300 MHz, 298 K, CD$_3$CN) of a binary system containing two different long ligands **L**^{2} + **L**^{3} (250 µL of a 2.8 mM solution for each ligand). The outcome of the self-assembly gives mixed-ligand double-cages $[3BF_4@Pd_4\mathbf{L}^2_m\mathbf{L}^3_{8\text{-}m}]^{5+}$ showing a statistical ligand distribution, when the ligands are mixed prior to the addition of palladium and heated at 70 °C over night. In contrast, combination of two preassembled homomeric double-cages $[3BF_4@Pd_4\mathbf{L}^2_8]^{5+}$ + $[3BF_4@Pd_4\mathbf{L}^3_8]^{5+}$ (250 µL of a 0.35 mM solution for each cage) leads to a mixture of coexisting homogeneous structures between which the ligand exchange is tremendously slowed down.

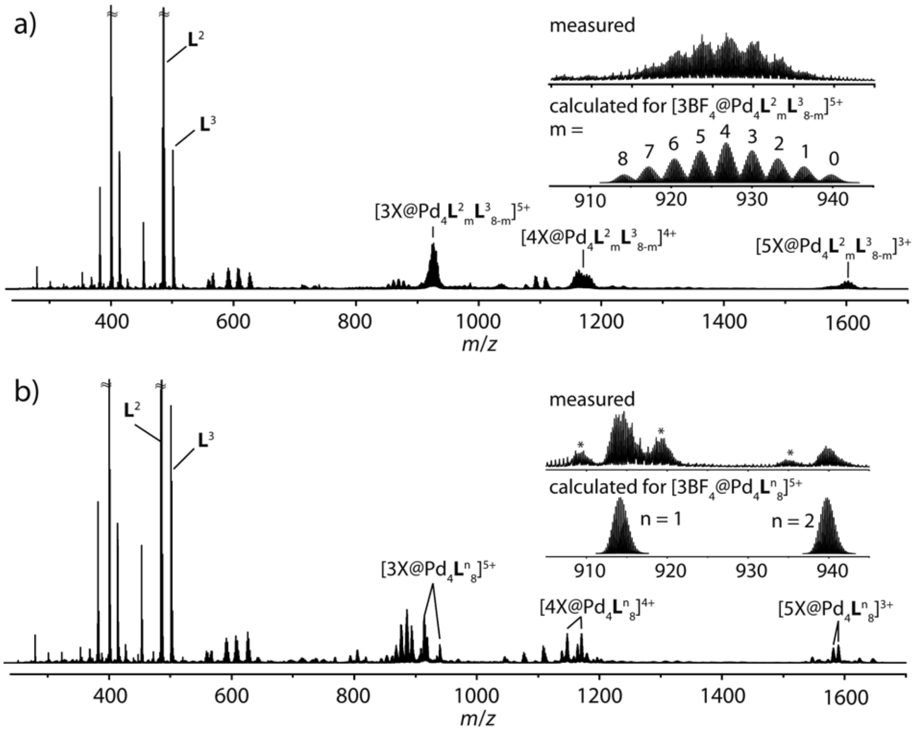

Figure AP-V.2 (a) ESI-TOF mass spectra in positive mode of the solution after addition of 0.5 eq $[Pd(CH_3CN)_4](BF_4)_2$ to premixed ligands $\mathbf{L}^2$ and $\mathbf{L}^3$ (250 μL of a 2.8 mM solution for each ligand) and heating in CD_3CN at 70 °C. The spectrum shows a statistical distribution of the ligands forming the double-cages $[3BF_4@Pd_4\mathbf{L}^2_m\mathbf{L}^3_{8-m}]^{5+}$ with m = 8-0. (b) ESI-TOF mass spectra in positive mode of the solution after mixing the double-cages $[3BF_4@Pd_4\mathbf{L}^2_8]^{5+}$ and $[3BF_4@Pd_4\mathbf{L}^3_8]^{5+}$ (250 μL of a 0.35 mM solution for each cage) and heating at 70 °C. * denotes other anion combinations with X = BF_4^-, F^-, NO_3^- and Cl^-.

b) Mixing experiments for ligands $\mathbf{L}^3$ and $\mathbf{L}^4$

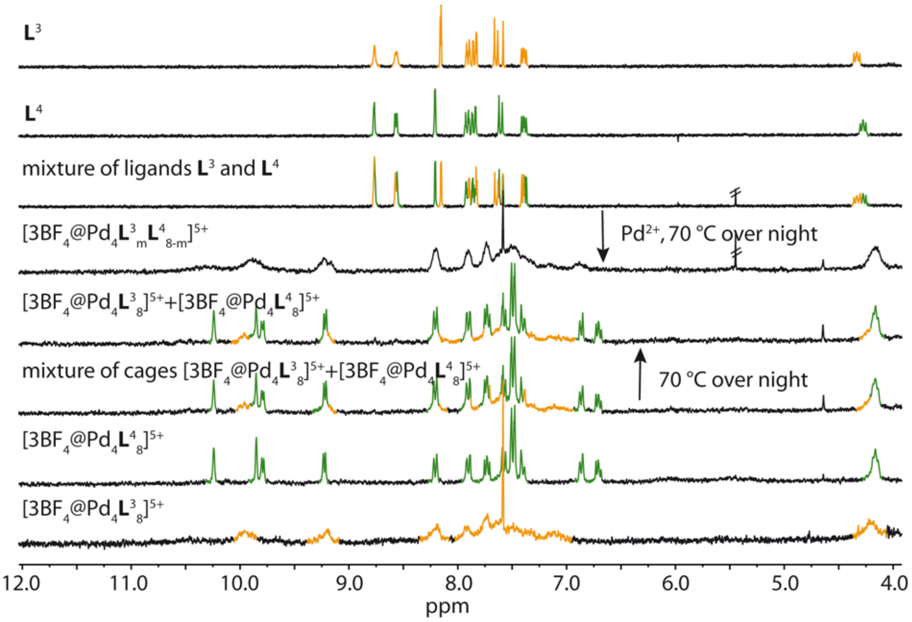

Figure AP-V.3 ^{1}H NMR spectra (300 MHz, 298 K, CD_3CN) of a binary system containing two different long ligands $\mathbf{L}^3$ + $\mathbf{L}^4$ (250 µL of a 2.8 mM solution for each ligand). The outcome of the self-assembly gives mixed-ligand double-cages $[3BF_4@Pd_4\mathbf{L}^3_m\mathbf{L}^4_{8-m}]^{5+}$ showing a statistical ligand distribution, when the ligands are mixed prior to the addition of palladium and heated at 70 °C over night. In contrast, combination of two preassembled homomeric double-cages $[3BF_4@Pd_4\mathbf{L}^3_8]^{5+}$ + $[3BF_4@Pd_4\mathbf{L}^4_8]^{5+}$ (250 µL of a 0.35 mM solution for each cage) leads to a mixture of coexisting homogeneous structures between which the ligand exchange is tremendously slowed down.

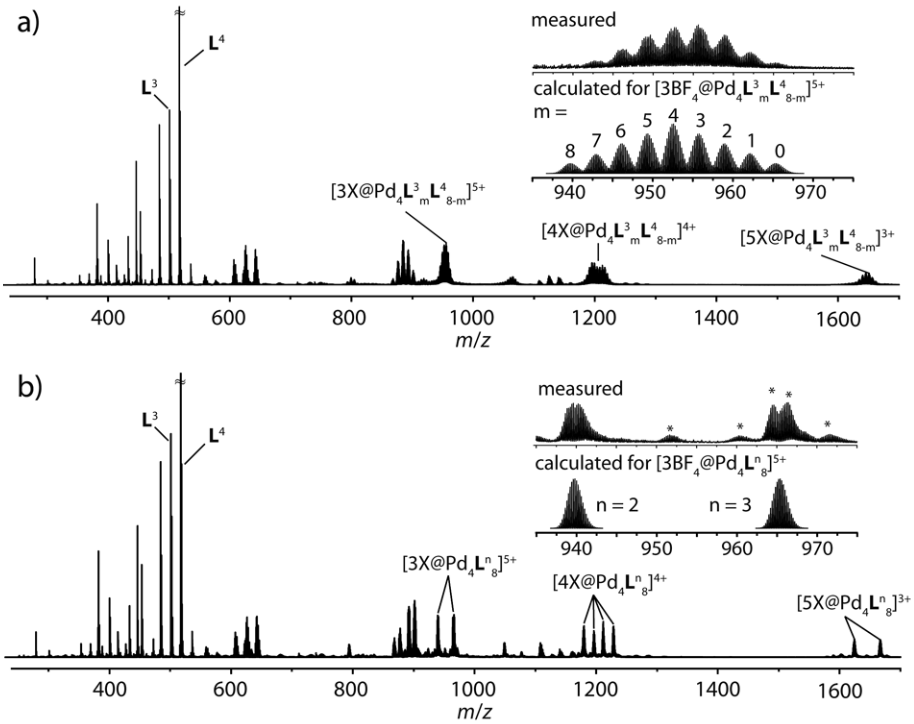

Figure AP-V.4 (a) ESI-TOF mass spectra in positive mode of the solution after addition of 0.5 eq $[Pd(CH_3CN)_4](BF_4)_2$ to premixed ligands $\mathbf{L}^3$ and $\mathbf{L}^4$ (250 µL of a 2.8 mM solution for each ligand) and heating in CD_3CN at 70 °C. The spectrum shows a statistical distribution of the ligands forming the double-cages $[3BF_4@Pd_4\mathbf{L}^3{}_m\mathbf{L}^4{}_{8\text{-}m}]^{5+}$ with m = 8-0. (b) ESI-TOF mass spectra in positive mode of the solution after mixing the double-cages $[3BF_4@Pd_4\mathbf{L}^3{}_8]^{5+}$ and $[3BF_4@Pd_4\mathbf{L}^4{}_8]^{5+}$ (250 µL of a 0.35 mM solution for each cage) and heating at 70 °C. * denotes other anion combinations with X = BF_4^-, F^-, NO_3^- and Cl^-.

c) Mixing experiments for ligands **L**^{3} and **L**^{1}

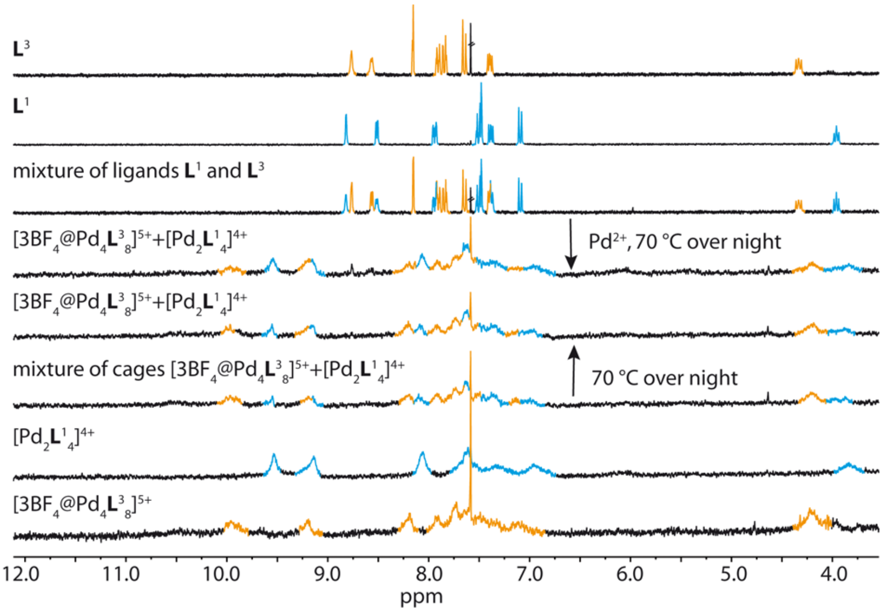

Figure AP-V.5 ^{1}H NMR spectra (300 MHz, 298 K, CD_3CN) of the binary system containing the long ligand **L**^{3} and the short ligand **L**^{1}. The outcome of the self-assembly is independent of the order of mixing of components. In both cases, this system shows narcissistic self-sorting behaviour yielding the mixture of cages $[3BF_4@Pd_4\mathbf{L}^3_8]^{5+}$ and $[Pd_2\mathbf{L}^1_4]^{4+}$.

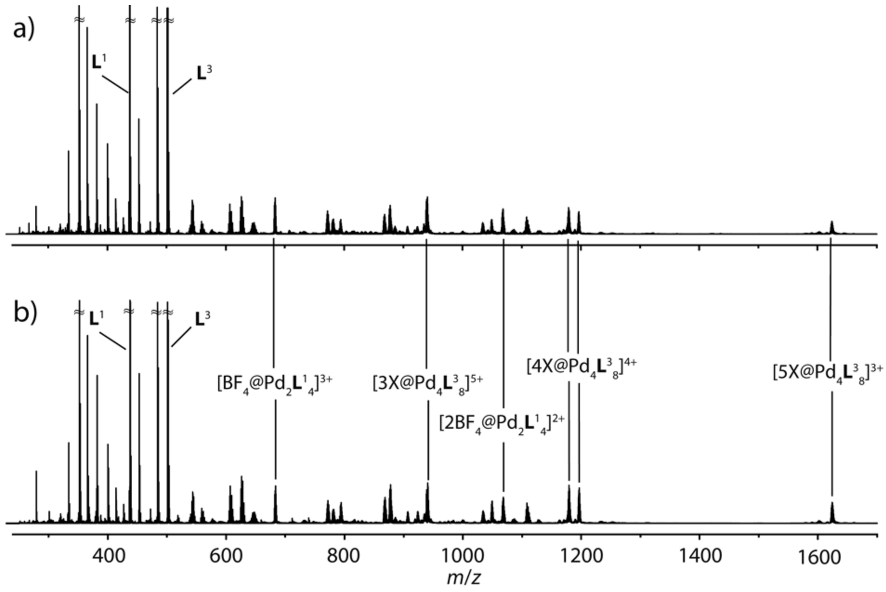

Figure AP-V.6 (a) ESI-TOF mass spectra in positive mode of the solution after addition of 0.5 eq $[Pd(CH_3CN)_4](BF_4)_2$ to premixed ligands **L**^{3} and **L**^{1} (250 µL of a 2.8 mM solution for each ligand) and heating in CD_3CN at 70 °C. (b) ESI-TOF mass spectra in positive mode of the solution of the mixture of preassembled double-cage $[3BF_4@Pd_4\mathbf{L}^3_8]^{5+}$ and monomeric cage $[Pd_2\mathbf{L}^1_4]^{4+}$ (250 µL of a 0.35 mM solution for each cage) after heating at 70 °C. The spectra show no exchange of the ligands. X = BF_4^-, F^-, NO_3^-.

d) Mixing experiments for ligands **L**^{4} and **L**^{1}

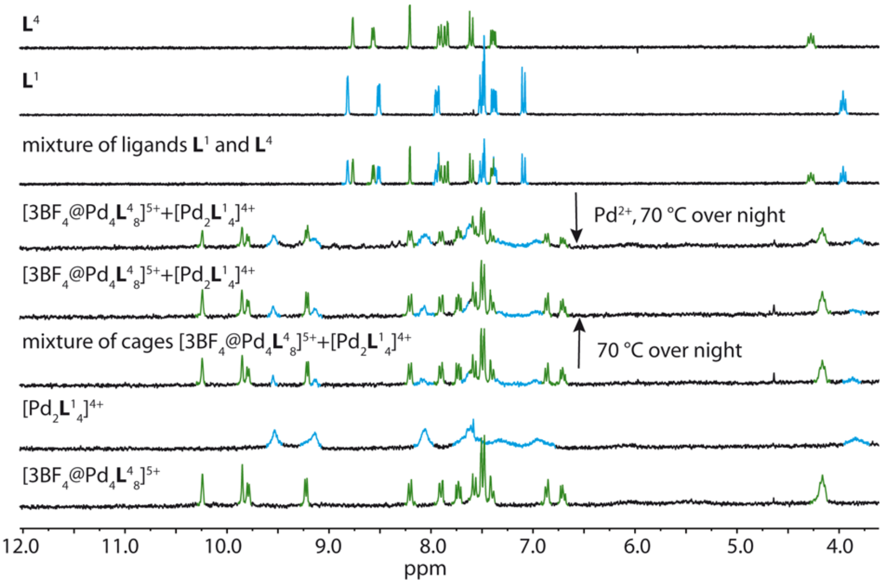

Figure AP-V.7 ^{1}H NMR spectra (300 MHz, 298 K, CD_3CN) of the binary system containing the long ligand **L**^{4} and the short ligand **L**^{1}. The outcome of the self-assembly is independent of the order of mixing of components. In both cases, this system shows narcissistic self-sorting behaviour yielding the mixture of cages $[3BF_4@Pd_4\mathbf{L}^4_8]^{5+}$ and $[Pd_2\mathbf{L}^1_4]^{4+}$.

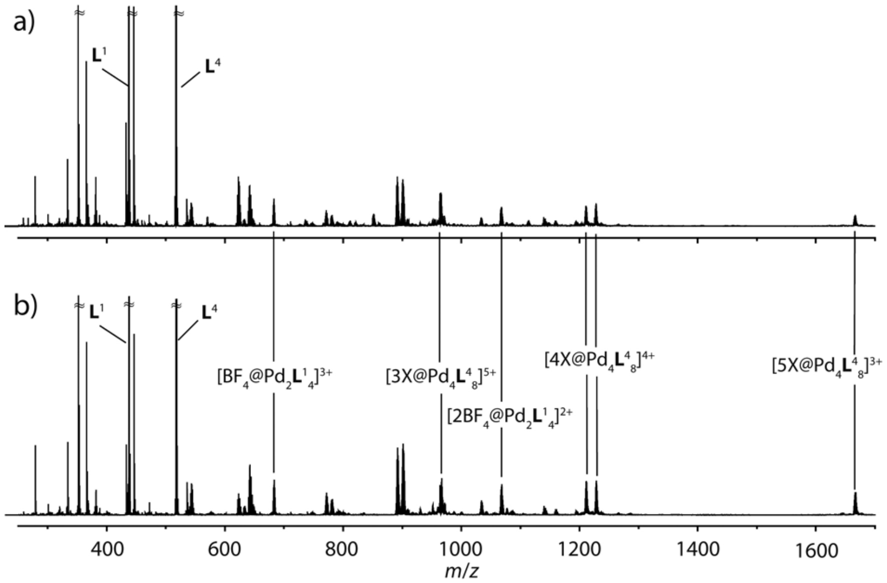

Figure AP-V.8 (a) ESI-TOF mass spectra in positive mode of the solution after addition of 0.5 eq $[Pd(CH_3CN)_4](BF_4)_2$ to premixed ligands **L**^{1} and **L**^{4} (250 μL of a 2.8 mM solution for each ligand) and heating in CD_3CN at 70 °C. (b) ESI-TOF mass spectra in positive mode of the solution of the mixture of preassembled double-cage $[3BF_4@Pd_4\mathbf{L}^4_8]^{5+}$ and monomeric cage $[Pd_2\mathbf{L}^1_4]^{4+}$ (250 μL of a 0.35 mM solution for each cage) after heating at 70 °C. The spectra show no exchange of the ligands. X = BF_4^-, F^-, NO_3^-.

e) Mixing of double-cages $[3BF_4@Pd_4\mathbf{L}^2{}_8]^{5+}$ and $[3BF_4@Pd_4\mathbf{L}^4{}_8]^{5+}$ and 2-Picoline

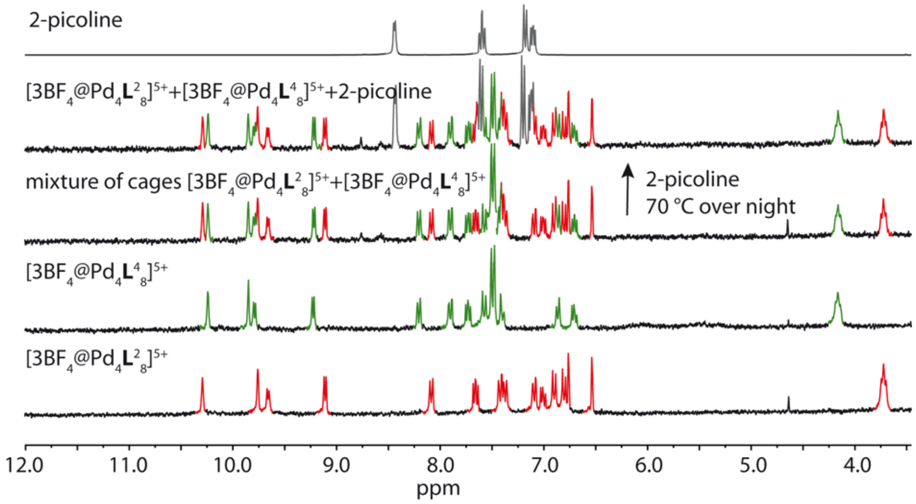

Figure AP-V.9 ^{1}H NMR spectra (300 MHz, 298 K, CD_3CN) of the mixture of double-cages $[3BF_4@Pd_4\mathbf{L}^2{}_8]^{5+}$ and $[3BF_4@Pd_4\mathbf{L}^4{}_8]^{5+}$ (250 µL of a 0.35 mM solution for each cage) and 2-picoline (8 eq per cage molecule, 13 µL of a 101 mM stock solution). The outcome shows no exchange of the ligands even after heating at 70 °C.

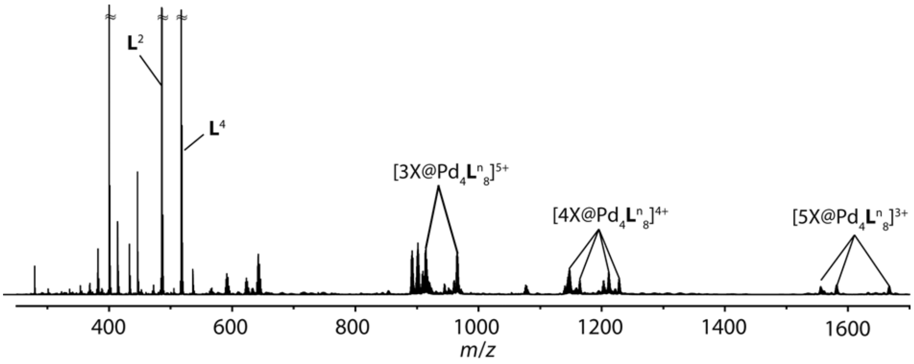

Figure AP-V.10 ESI-TOF mass spectra in positive mode of the solution of the mixture of preassembled double-cages $[3BF_4@Pd_4\mathbf{L}^2{}_8]^{5+}$ and $[3BF_4@Pd_4\mathbf{L}^4{}_8]^{5+}$ (250 µL of a 0.35 mM solution for each cage) and 2-picoline after heating at 70 °C. X = BF_4^-, F^-, NO_3^-.

2. Heating of the mixed-ligand double-cages $[3BF_4@Pd_4L^2{}_mL^4{}_{8-m}]^{5+}$ and the mixture of homomeric double-cages $[3BF_4@Pd_4L^2{}_8]^{5+}$ and $[3BF_4@Pd_4L^4{}_8]^{5+}$

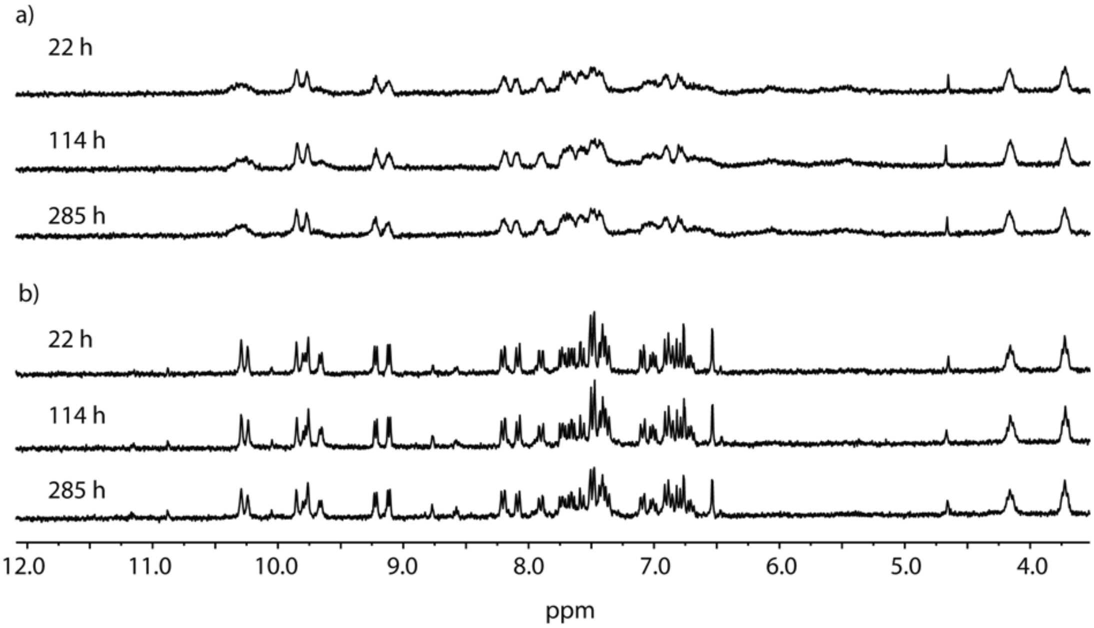

Figure AP-V.11 a) ^{1}H NMR spectra (300 MHz, 298 K, CD_3CN) of a binary system containing two different long ligands $\mathbf{L^2}$ + $\mathbf{L^4}$ (250 µL of a 2.8 mM solution for each ligand). The outcome of the self-assembly gives mixed cages $[3BF_4@Pd_4\mathbf{L}^2{}_m\mathbf{L}^4{}_{8-m}]^{5+}$ showing a statistical ligand distribution, when the ligands are mixed prior to the addition of palladium and heated at 70 °C. No significant changes were observed after heating for 22 h, 114 h and 285 h at 70 °C. b) Combination of two preassembled double-cages $[3BF_4@Pd_4\mathbf{L^2}_8]^{5+}$ + $[3BF_4@Pd_4\mathbf{L^4}_8]^{5+}$ (250 µL of a 0.35 mM solution for each cage) and heating at 70 °C leads to a mixture of coexisting homogeneous structures between which the ligand exchange is tremendously slowed down.

Appendix-Chapter VI

1. Synthesis

a) Synthesis of ligand **L**^{6}

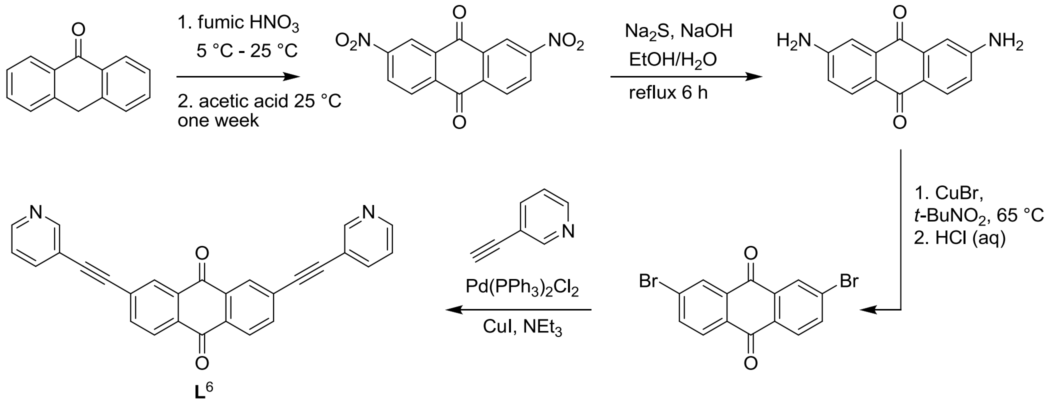

Scheme AP-VI.1 Synthetic route leading to ligand **L**^{6}.[175]

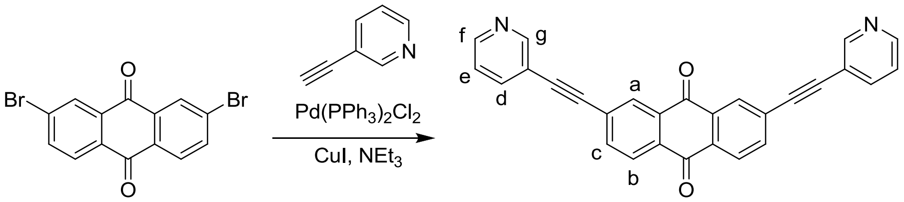

Scheme AP-VI.2 Synthetic route leading to ligand **L**^{6}.

A suspension of 2,7-Dibromo-9,10-anthraqinone (140 mg, 0.38 mmol, 1.00 eq.), 3-ethynylpyridine (118 mg, 1.15 mmol, 3.0 eq.), copper(I)iodide (7 mg, 0.04 mmol, 0.10 eq.) in NEt_3 (15 mL) was degassed using the “Pump and Freeze” method. $Pd(PPh_3)_2Cl_2$ (27 mg, 0.04 mmol, 0.10 eq.) was added and the reaction mixture was stirred for 18 h at 90 °C. After heating, the solvent was removed and the crude product was prepurified by column chromatography ($CHCl_3$:MeOH 50:1). After recrystallization from pyridine the ligand **L**^{6} was isolated as a pale yellow solid (92 mg, 0.22 mmol, 59 %).

---

[175] The building block 2,7-Dibromo-9,10-anthraqinone was obtained following the synthetic protocol described in reference [178].

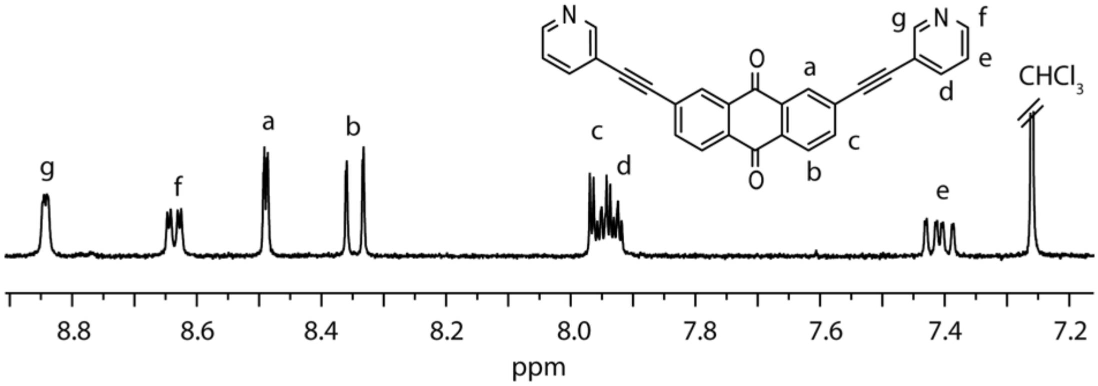

Figure AP-VI.1: ^{1}H NMR (300 MHz, 298 K, $CDCl_3$) of ligand **L**^{6}.

^{1}H NMR (300 MHz, $CDCl_3$) δ [ppm] = 8.83 (d, J = 1.9 Hz, 2H, H_g), 8.63 (dd, J = 5.0, 1.7 Hz, 2H, H_f), 8.48 (d, J = 1.7 Hz, 2H, H_a), 8.34 (d, J = 8.1 Hz, 2H, H_b), 7.94 (dd, J = 8.1, 1.8 Hz, 2H, H_c), 7.88 (dt, J = 8.0, 1.8 Hz, 2H, H_d), 7.36 (dd, J = 7.9, 5.0 Hz, 2H, H_e).

ESI-MS [m/z]: found 411.1 (100 %), 412.1 (31 %), 413.1 (6 %); calculated for $[C_{28}H_{15}N_2O_2]^+$ 411.1 (100 %), 412.1 (31 %), 413.1 (5 %).

b) Synthesis of double-cage $[3BF_4@Pd_4\mathbf{L}^6{}_8](BF_4)_5$

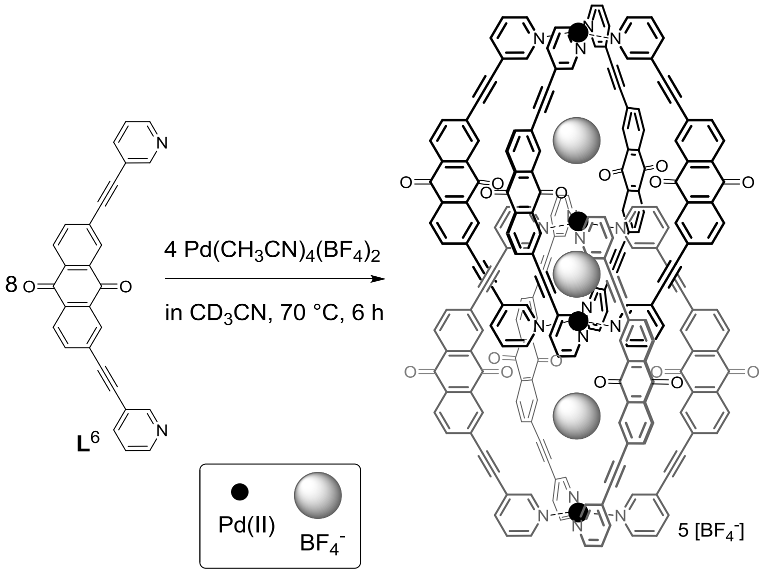

Scheme AP-VI.3 Synthetic route to double-cage $[3BF_4@Pd_4\mathbf{L}^6{}_8](BF_4)_5$.

Ligand **L**^{6} (1.15 mg. 2.8 µmol) was suspended in 1 mL CD_3CN and 95 µL of 15 mM $Pd(CH_3CN)_4(BF_4)_2$ stock solution in CD_3CN were added to the suspension. The reaction mixture was stirred at 70 °C for 18 h to obtain the double-cage in quantitative yield. Due to the low solubility of the double-cage in acetonitrile, a suspension the double-cage (0.35 mM) was obtained.

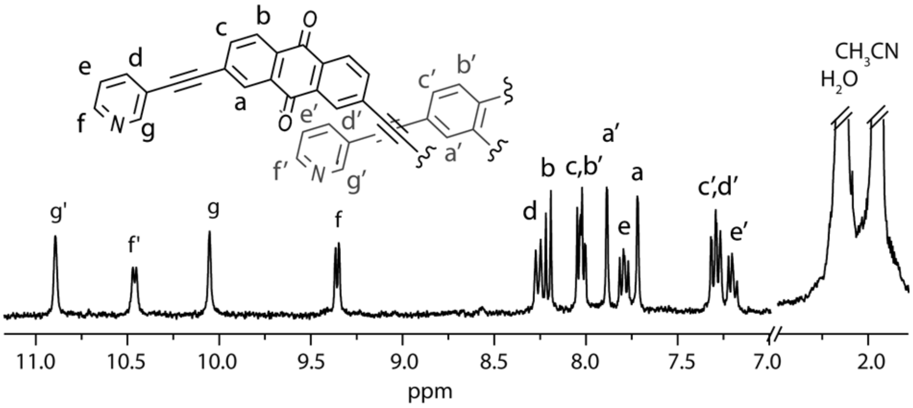

Figure AP-VI.2 ^{1}H NMR (300 MHz, 298 K, CD_3CN) of the double-cage $[3BF_4@Pd_4\mathbf{L}^6_8]^{5+}$.

^{1}H NMR (500 MHz, 298 K, CD_3CN) δ [ppm] = 10.88 (s, 8H, $H_{g'}$), 10.45 (d, J = 6.0 Hz, 8H, $H_{f'}$), 10.04 (s, 8H, H_g), 9.32 (d, J = 6.3 Hz, 8H, H_f), 8.25 (d, J = 8.1 Hz, 8H, H_d), 8.20 (d, J = 7.8 Hz, 8H, H_b), 8.06 – 7.98 (m, 16H, H_c, $H_{b'}$), 7.87 (s, 8H, $H_{a'}$), 7.82 – 7.75 (m, 8H, H_e), 7.71 (s, 8H, H_a), 7.33 – 7.24 (m, 16H, $H_{c'}$, $H_{d'}$), 7.23 – 7.15 (m, 8H, $H_{e'}$).

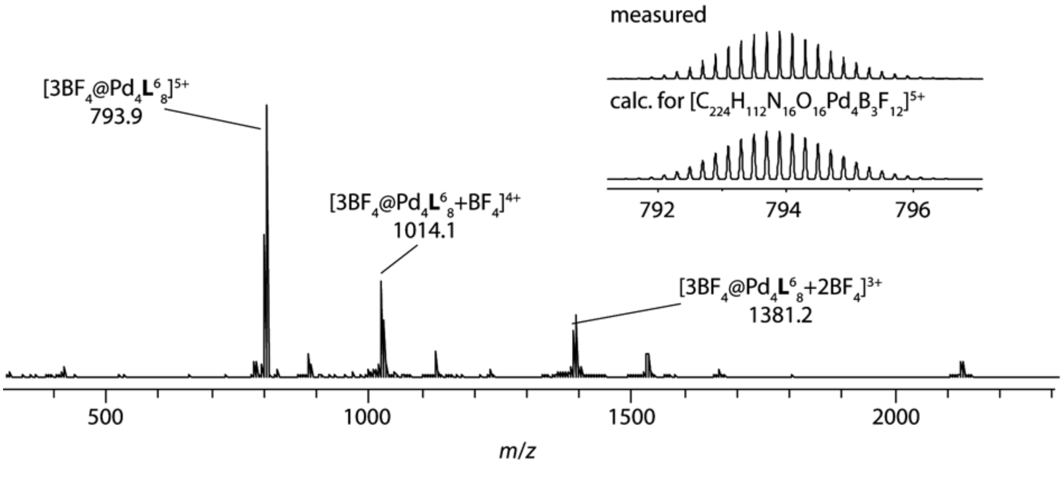

Figure AP-VI.3 ESI high resolution mass spectrum of the double-cage $[3BF_4@Pd_4\mathbf{L}^6_8]^{5+}$.

c) Preparation of the mixture of double-cages [$3BF_4@Pd_4\mathbf{L}^2_8](BF_4)_5$ + [$3BF_4@Pd_4\mathbf{L}^6_8](BF_4)_5$

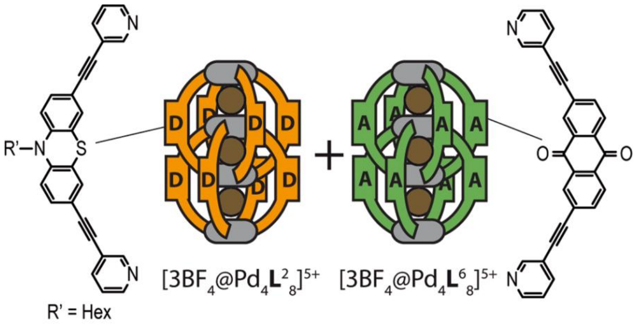

Scheme AP-VI.4 Mixture of preassembled double-cages [$3BF_4@Pd_4\mathbf{L}^2_8](BF_4)_5$ and [$3BF_4@Pd_4\mathbf{L}^6_8](BF_4)_5$.

The mixture of double-cages was prepared by mixing 250 µL of 0.35 mM double-cage [$3BF_4@Pd_4\mathbf{L}^2_8](BF_4)_5$ solution in CD_3CN with 250 µL of 0.35 mM double-cage [$3BF_4@Pd_4\mathbf{L}^6_8](BF_4)_5$ solution in CD_3CN.

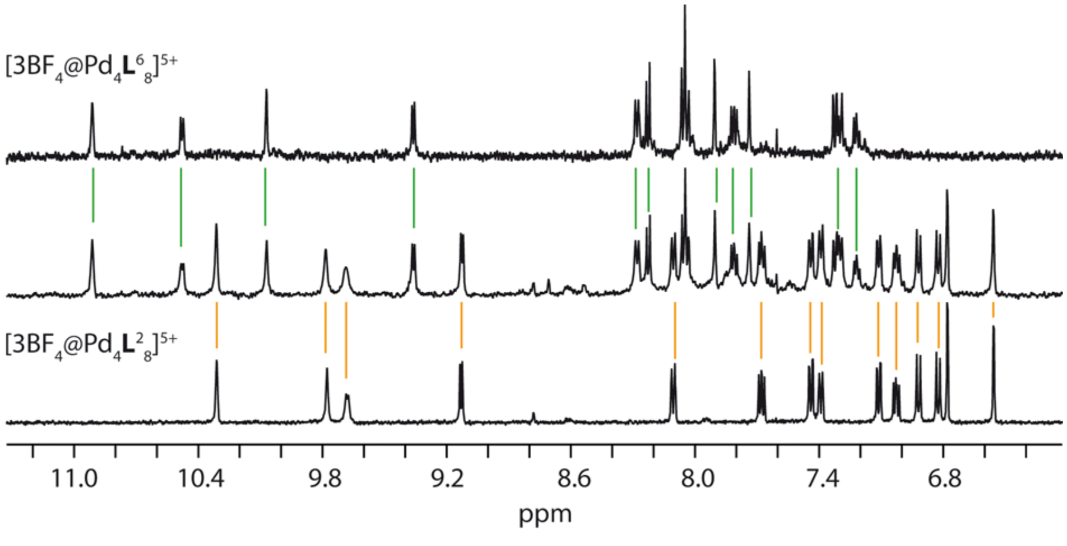

Figure AP-VI.4 ^{1}H NMR (500 MHz, 298 K, CD_3CN) of the double-cage mixture [$3BF_4@Pd_4\mathbf{L}^2_8]^{5+}$ and [$3BF_4@Pd_4\mathbf{L}^6_8]^{5+}$.

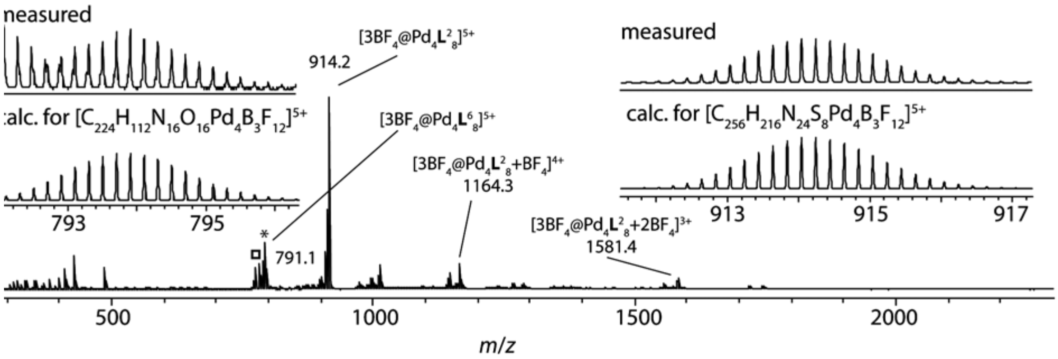

Figure AP-VI.5 ESI high resolution mass spectrum of the double-cage mixture $[3BF_4@Pd_4\mathbf{L}^2{}_8]^{5+}$ and $[3BF_4@Pd_4\mathbf{L}^6{}_8]^{5+}$. * denotes with bromide contaminated species $[2Br+BF_4@Pd_4\mathbf{L}^6{}_8]^{5+}$. □ denotes with chloride contaminated species $[2Cl+BF_4@Pd_4\mathbf{L}^6{}_8]^{5+}$.

d) Preparation of mixed-ligand cages $[3BF_4@Pd_4\mathbf{L}^2{}_m\mathbf{L}^6{}_{8\text{-}m}](BF_4)_5$

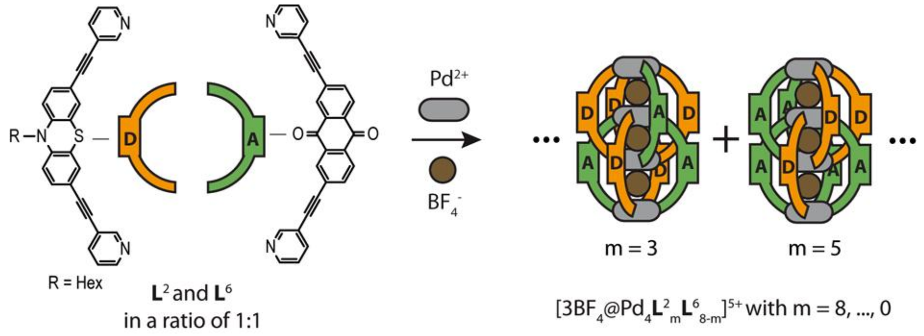

Scheme AP-VI.5 Mixture of ligands $\mathbf{L}^2$ and $\mathbf{L}^6$ and subsequent assembly into the mixed-ligand double-cages $[3BF_4@Pd_4\mathbf{L}^2{}_m\mathbf{L}^6{}_{8\text{-}m}](BF_4)_5$.

The mixed-ligand double-cages were prepared by mixing ligand $\mathbf{L}^2$ (1.36 mg) and ligand $\mathbf{L}^6$ (1.15 mg) in 2 mL of deuterated acetonitrile with 190 µL of 15 mM $Pd(CH_3CN)_4(BF_4)_2$ stock solution and heating the mixture at 70 °C for 18 h.

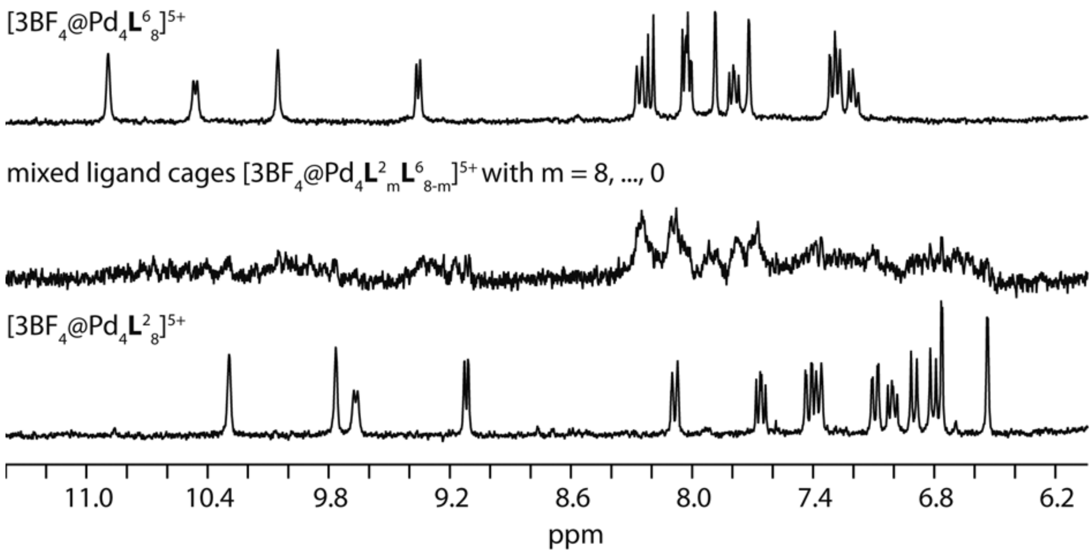

Figure AP-VI.6 ^{1}H NMR (300 MHz, 298 K, Acetonitrile-d_3) of the mixed-ligand double-cage $[3BF_4@Pd_4\mathbf{L}^2{}_m\mathbf{L}^6{}_{8-m}]^{5+}$ with m = 8,…,0.

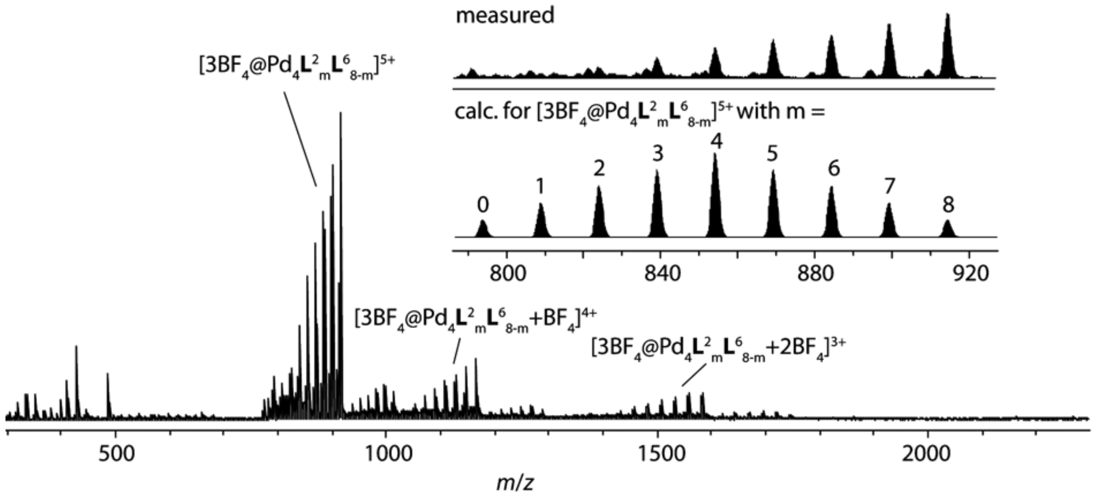

Figure AP-VI.7 ESI high resolution mass spectrum of the mixed-ligand double-cage $[3BF_4@Pd_4\mathbf{L}^2{}_m\mathbf{L}^6{}_{8-m}]^{5+}$ with m = 8,…,0.

e) Synthesis of ligand **L**^{7}

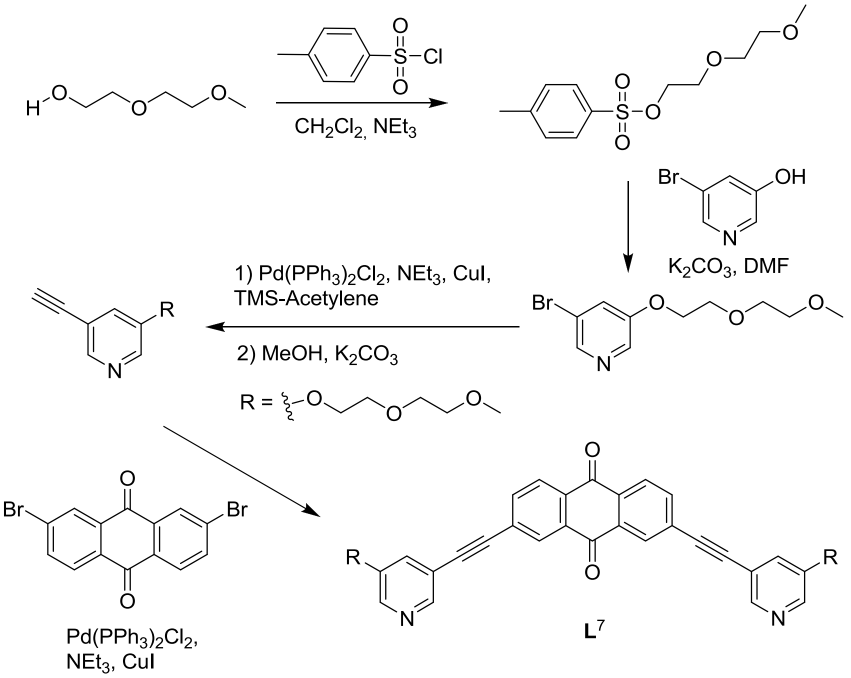

Scheme AP-VI.6 Synthetic route leading to the modified anthraquinone ligand **L**^{7}.

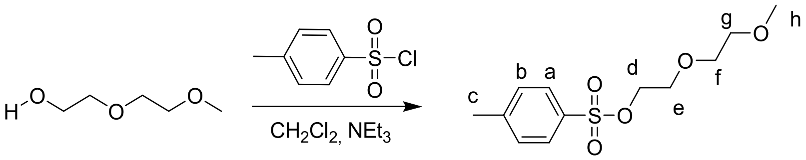

Scheme AP-VI.7 Synthesis of building block 2-(2-methoxyethoxy)ethyl 4-methylbenzenesulfonate.

2-(2-Methoxyethoxy)ethanol (15.0 g, 125 mmol, 1.00 eq.) was dissolved with Tosylchloride (23.8 g, 125 mmol, 1.00 eq.) in Triethylamine (60 mL) and CH$_2$CL$_2$ (100 mL). After 12 h of stirring a white precipitate was filtrated off and the residue was washed with ethyl acetate. The solvent was removed from the filtrate and the crude product was purified by column chromatography (Hexane:Ethylacetate 1:1). The clean product was obtained as a yellowish oily liquid (26.8 g, 98 mmol, 78 %).

^{1}H NMR (300 MHz, 298 K, Chloroform-*d*) δ [ppm] = 7.79 – 7.72 (m, 2H, H$_b$), 7.33 – 7.27 (m, 2H, H$_a$), 4.15 – 4.10 (m, 2H, H$_d$), 3.67 – 3.62 (m, 2H, H$_e$), 3.55 – 3.40 (m, 4H, H$_f$, H$_g$), 3.30 (s, 3H, H$_h$), 2.40 (s, 3H, H$_c$).

ESI-MS [*m/z*]: found 275.1; calculated for [C$_{12}$H$_{18}$SO$_5$+H]$^+$ 275.1.

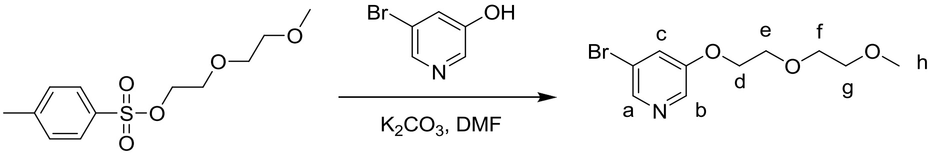

Scheme AP-VI.8 Synthesis of building block 3-bromo-5-(2-(2-methoxyethoxy)ethoxy)pyridine.

5-Bromo-3-pyridinole (1.00 g, 5.75 mmol, 1.00 eq.), 2-(2-methoxyethoxy)ethyl-4-methylbenzenesulfonate (2.36 g, 8.62 mmol, 1.50 eq.), K_2CO_3 (2.38 g, 17.24 mmol, 3.00 eq.) and DMF (20 mL) were mixed and heated to 70 °C for 18 h. After reaction has completed, the mixture was poured into 2 M NaOH and the product was extracted with EtOAc. The crude product was purified by column chromatography with Chloroform/Methanol 10:1 and it was isolated as brownish oil (2.20 g, 7.97 mmol, 92 %).

^{1}H NMR (300 MHz, 298 K, Chloroform-*d*) δ [ppm] = 8.33 – 8.26 (m, 2H), 7.52 (s, 1H), 4.24 – 4.17 (m, 2H), 3.90 – 3.82 (m, 2H), 3.74 – 3.65 (m, 2H), 3.59 – 3.52 (m, 2H), 3.38 (s, 3H).

ESI-MS [*m/z*]: found 276.0 (100), 277.0 (11), 278.0 (100), 279.0 (11); calculated for $[C_{10}H_{12}NO_3Br+H]^+$ 276.0 (100), 277.0 (11), 278.0 (100), 279.0 (11).

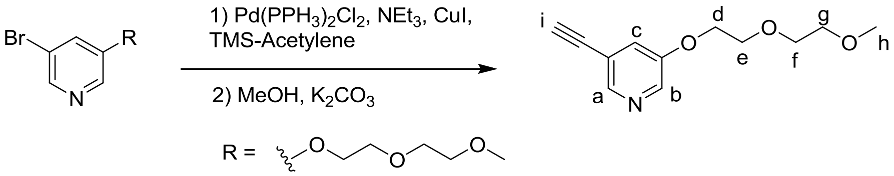

Scheme AP-VI.9 Synthesis of building block 3-ethynyl-5-(2-(2-methoxyethoxy)ethoxy)pyridine.

3-Bromo-5-(2-(2-methoxyethoxy)ethoxy)pyridine (2.20 g, 7.97 mmol, 1.00 eq.) was dissolved in 10 mL of NEt_3 and CuI (151 mg, 0.80 mmol, 0.10 eq.) was added. After the mixture was degassed by using the „Freeze and Pump“-method, $Pd(PPh_3)_2Cl_2$ (559 mg, 0.80 mmol, 0.10 eq.) and trimethylsilylacetylene (3.30 mL, 23.91 mmol, 3.00 eq.) were added. The reaction mixture was heated to 90 °C for 18 h. The solvent was removed and the crude product was purified by column chromatography. The TMS-protecting group was removed by stirring the product with K_2CO_3 (3 g, 21.43 mmol, 2.69 eq.) in methanol (10 mL).

^{1}H NMR (300 MHz, 298 K, Chloroform-*d*) δ [ppm] = 8.32 (d, *J* = 1.6 Hz, 1H, H_a), 8.29 (d, *J* = 2.8 Hz, 1H, H_b), 7.30 (dd, *J* = 2.9, 1.6 Hz, 1H, H_c), 4.21 – 4.15 (m, 2H, H_d), 3.90 – 3.84 (m, 2H, H_e), 3.74 – 3.68 (m, 2H, H_f), 3.60 – 3.54 (m, 2H, H_g), 3.39 (s, 3H, H_h), 3.19 (s, 1H, H_i).

ESI-MS [*m/z*]: found 222.1 (100), 223.1 (14); calculated for $[C_{12}H_{15}NO_3+H]^+$ 222.1 (100), 223.1 (14).

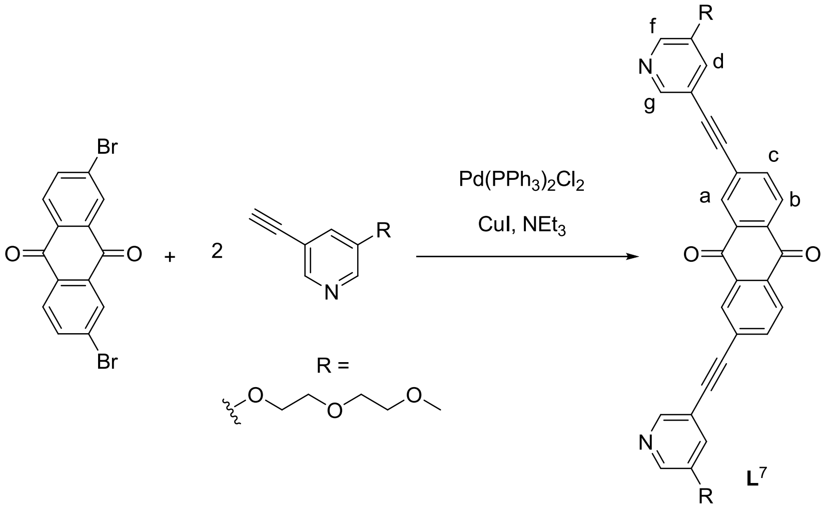

Scheme AP-VI.10 Synthetic route leading of ligand **L**^{7}.

2,7-Dibromoanthraquinone (100 mg, 0.27 mmol, 1.00 eq.) was mixed with 3-Ethynyl-5-(2-(2-methoxyethoxy)ethoxy)pyridine (121 mg, 0.55 mmol, 2.00 eq.), Copper(I)iodid (10 mg, 0.05 mmol, 0.19 eq.) in 10 mL triethylamine. The mixture was degassed by using the „Freeze and Pump“-method and $Pd(PPh_3)_2Cl_2$ (19 mg, 0.03 mmol, 0.10 eq.) was added. The reaction mixture was heated to 90 °C for 18 h. The solvent was removed and the crude product was purified by column chromatography (EtOAc -> 10 %MeOH in EtOAc). The product was isolated as yellow solid (110 mg, 0.17 mmol, 62 %).

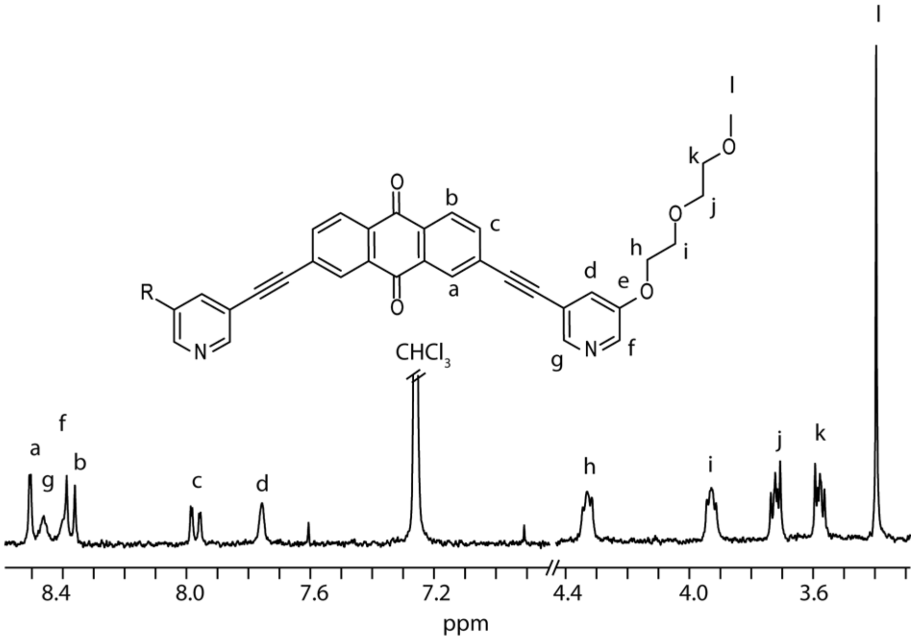

Figure AP-VI.8 ^{1}H NMR (300 MHz, 298 K, CDCl$_3$) of ligand **L**^{7}.

^{1}H NMR (300 MHz, 298 K, CDCl$_3$) δ [ppm] = 8.50 (s, 2H, H$_a$), 8.46 (s, 2H, H$_g$), 8.40 (s, 2H, H$_f$), 8.37 (d, *J* = 8.1 Hz, 2H, H$_b$), 7.97 (d, *J* = 8.8 Hz, 2H, H$_c$), 7.76 (s, 2H, H$_d$), 4.37 – 4.28 (m, 4H, H$_h$), 3.96 – 3.89 (m, 4H, H$_i$), 3.75 – 3.68 (m, 4H, H$_j$), 3.61 – 3.55 (m, 4H, H$_k$), 3.40 (s, 6H, H$_l$).

ESI-MS [*m/z*]: found 647.2 (100 %), 648.2 (41 %), 649.2 (8 %); calculated for [$C_{38}H_{34}N_2O_8$]$^+$ 647.2 (100 %), 648.2 (42 %), 649.2 (10 %).

f) Synthesis of double-cage [3BF$_4$@Pd$_4$**L**$^7{}_8$](BF$_4$)$_5$

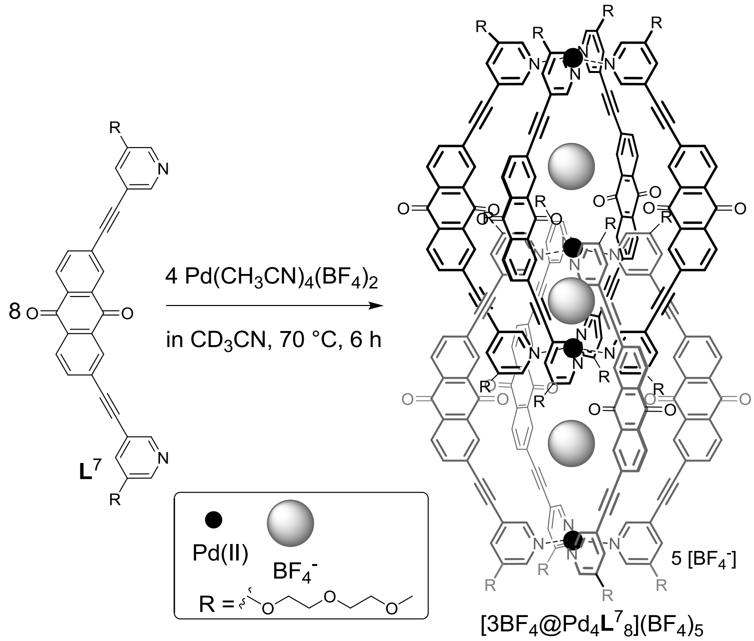

Scheme AP-VI.11 Synthetic route leading to double-cage [3BF$_4$@Pd$_4$**L**$^7{}_8$](BF$_4$)$_5$.

Ligand **L**^{7} (1.81 mg, 2.8 µmol) was suspended in 1 mL CD$_3$CN and 95 µL of 15 mM Pd(CH$_3$CN)$_4$(BF$_4$)$_2$ stock solution were added to the suspension. The reaction mixture was stirred at 70 °C for 18 h to obtain the double-cage in quantitative yield.

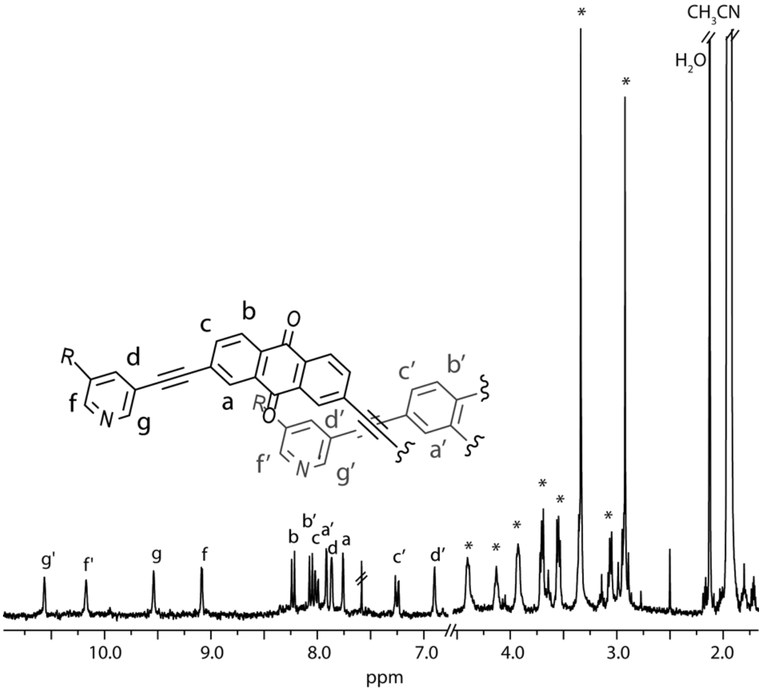

Figure AP-VI.9 ^{1}H NMR (300 MHz, 298 K, CD_3CN) of the double-cage $[3BF_4@Pd_4\mathbf{L}^7{}_8]^{5+}$. * denotes the PEG residue signals.

^{1}H NMR (300 MHz, 298 K, CD_3CN) δ [ppm] = 10.56 (s, 8H, $H_{g'}$), 10.17 (s, 8H, $H_{f'}$), 9.54 (s, 8H, H_g), 9.09 (d, J = 2.3 Hz, 8H, H_f), 8.23 (d, J = 8.0 Hz, 8H, H_b), 8.06 (d, J = 7.9 Hz, 8H, $H_{b'}$), 8.01 (dd, J = 8.0, 1.5 Hz, 8H, H_c), 7.91 (d, J = 1.3 Hz, 8H, H_a), 7.87 (d, J = 2.5 Hz, 8H, H_d), 7.76 (s, J = 1.4 Hz, 8H, H_a) 7.25 (dd, J = 8.6, 1.7 Hz, 8H, $H_{c'}$), 6.90 (s, 8H, $H_{d'}$), 4.40 (s, 16H), 4.13 (s, 16H), 3.93 (s, 16H), 3.77 – 3.59 (m, 32H), 3.58 – 3.52 (m, 8H, 16 H), 3.38 – 3.29 (m, 40H), 3.10 – 3.02 (m, 16H), 2.92 (s, 24H).

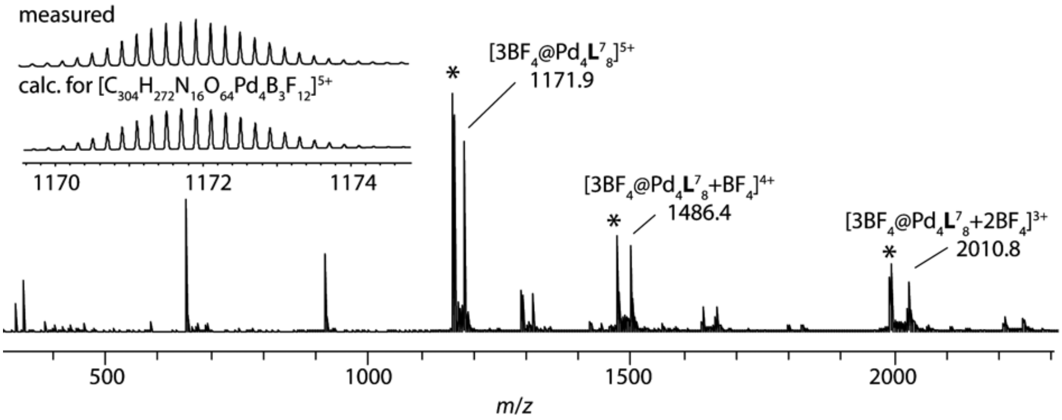

Figure AP-VI.10 ESI high resolution mass spectrum of the double-cage $[3BF_4@Pd_4\mathbf{L}^7{}_8]^{5+}$.

g) Preparation of the mixture of double-cages $[3BF_4@Pd_4\mathbf{L}^2{}_8](BF_4)_5$ + $[3BF_4@Pd_4\mathbf{L}^7{}_8](BF_4)_5$

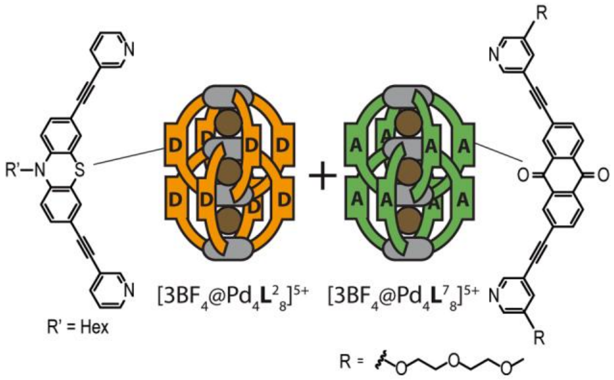

Scheme AP-VI.12 Mixture of preassembled double-cages $[3BF_4@Pd_4\mathbf{L}^2{}_8](BF_4)_5$ and $[3BF_4@Pd_4\mathbf{L}^7{}_8](BF_4)_5$.

The mixture of double-cages was prepared by mixing 250 µL of 0.35 mM double-cage $[3BF_4@Pd_4\mathbf{L}^2{}_8]^{5+}$ solution in CD_3CN with 250 µL of 0.35 mM double-cage $[3BF_4@Pd_4\mathbf{L}^7{}_8]^{5+}$ solution in CD_3CN.

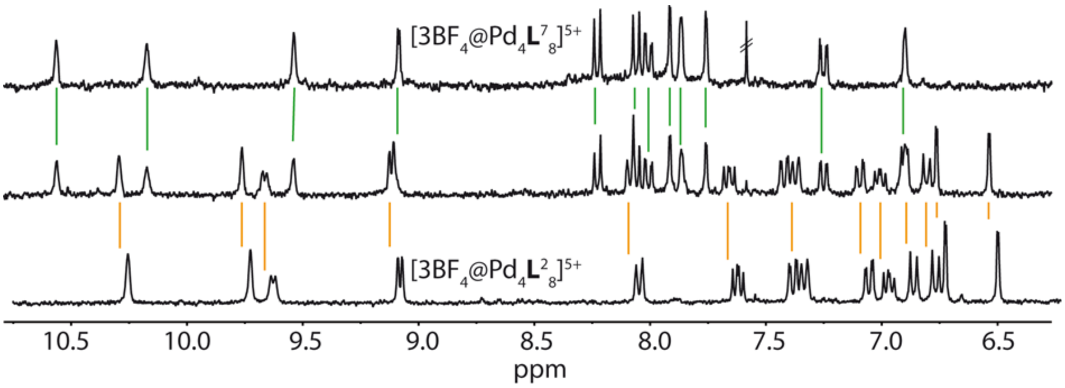

Figure AP-VI.11 ^1H NMR (300 MHz, 298 K, CD_3CN) of the double-cage mixture $[3BF_4@Pd_4\mathbf{L}^2{}_8]^{5+}$ and $[3BF_4@Pd_4\mathbf{L}^7{}_8]^{5+}$.

h) Preparation of mixed-ligand double-cages $[3BF_4@Pd_4\,\mathbf{L}^2_m\mathbf{L}^7_{8\text{-}m}](BF_4)_5$

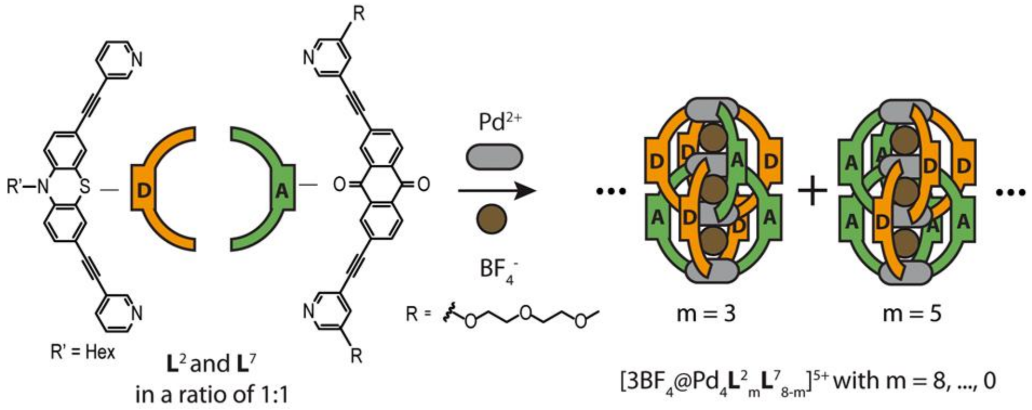

Scheme AP-VI.13 Mixture of ligands $\mathbf{L}^2$ and $\mathbf{L}^7$ and subsequent assembly into the mixed-ligand double-cages $[3BF_4@Pd_4\mathbf{L}^2_m\mathbf{L}^7_{8\text{-}m}](BF_4)_5$.

The mixed-ligand double-cages were prepared by mixing ligand $\mathbf{L}^2$ (1.36 mg) and ligand $\mathbf{L}^7$ (1.81 mg) in 2 mL of CD_3CN with 190 µL of 15 mM $Pd(CH_3CN)_4(BF_4)_2$ stock solution and heating the mixture at 70 °C for 18 h.

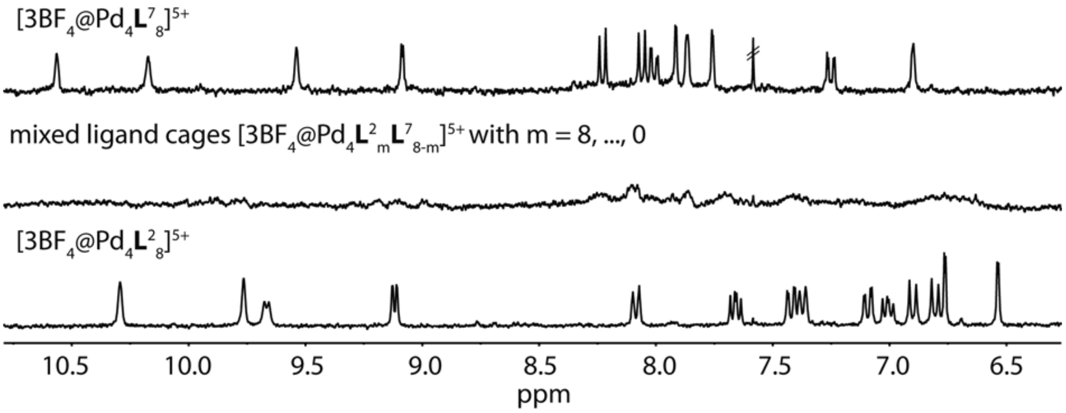

Figure AP-VI.12 ^1H NMR (300 MHz, 298 K, CD_3CN) of mixed-ligand double-cages $[3BF_4@Pd_4\mathbf{L}^2_m\mathbf{L}^7_{8\text{-}m}]^{5+}$ with m = 8,…,0.

2. Geometry optimization of double-cage structure [$3BF_4@Pd_4L^6{}_8$](BF_4)$_5$

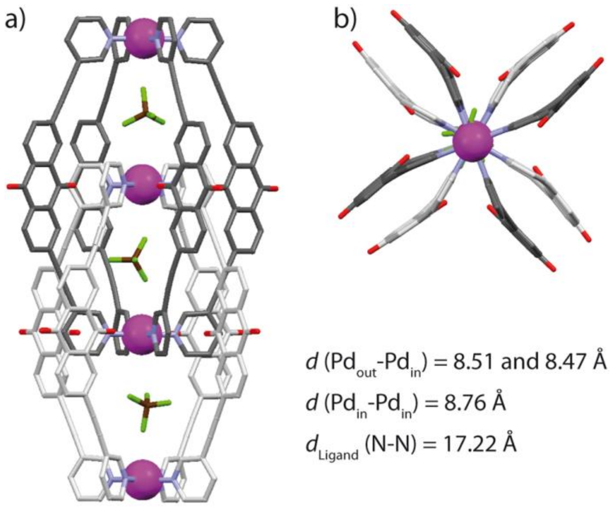

d (Pd_{out}-Pd_{in}) = 8.51 and 8.47 Å
d (Pd_{in}-Pd_{in}) = 8.76 Å
d_{Ligand} (N-N) = 17.22 Å

Figure AP-VI.13 DFT calculated model for [$3BF_4@Pd_4\mathbf{L}^6{}_8$]$^{5+}$ shown as a) side view and b) view along the Pd-Pd axis.

The structure of the double-cage [$3BF_4@Pd_4\mathbf{L}^6{}_8$]$^{5+}$ was constructed according to the previously reported X-ray structure of the acridone based double-cage.[18] The obtained structure was optimized on ωB97XD/def2-SVP DFT level (charge: +5, multiplicity: singlet, with three BF_4^- inside the three internal pockets, without constraints) using the dispersion-corrected ωB97XD functional implemented in Gaussian '09[72] and the Ahlrich def2-SVP basis set obtained from the EMSL basis set exchange website https://bse.pnl.gov/bse/portal.[176] Hydrogens are omitted for clarity.

---

[176] K. L. Schuchardt, B. T. Didier, T. Elsethagen, L. Sun, V. Gurumoorthi, J. Chase, J. Li, T. L. J. Windus, *Chem. Inf. Model.* **2007**, 47, 1045.

3. UV/VIS Spectra

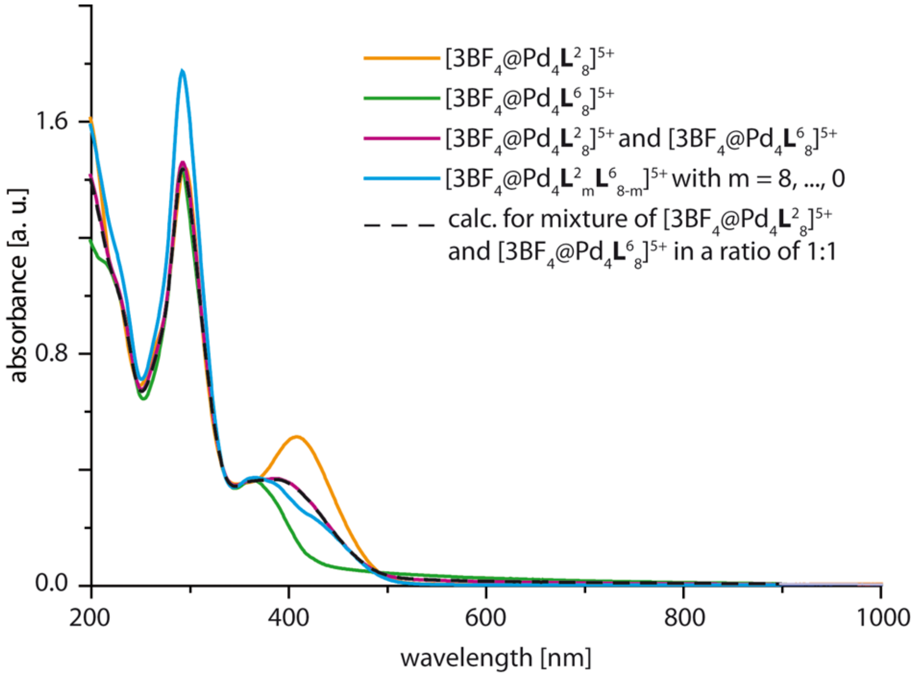

Figure AP-VI.14 UV/Vis spectra of double-cages $[3BF_4@Pd_4\mathbf{L}^2_8]^{5+}$ (20 µM in MeCN) and $[3BF_4@Pd_4\mathbf{L}^6_8]^{5+}$ (20 µM in MeCN), their mixture $[3BF_4@Pd_4\mathbf{L}^2_8]^{5+}$ + $[3BF_4@Pd_4\mathbf{L}^6_8]^{5+}$ (10 µM of each double-cage in MeCN) and the mixed-ligand double-cages $[3BF_4@Pd_4\mathbf{L}^2_m\mathbf{L}^6_{8-m}]^{5+}$ (20 µM in MeCN). The spectrum for the mixture of $[3BF_4@Pd_4\mathbf{L}^2_8]^{5+}$ and $[3BF_4@Pd_4\mathbf{L}^6_8]^{5+}$ in a ratio of 1:1 was calculated from experimental spectra of each double-cage. Light path: 0.2 cm.

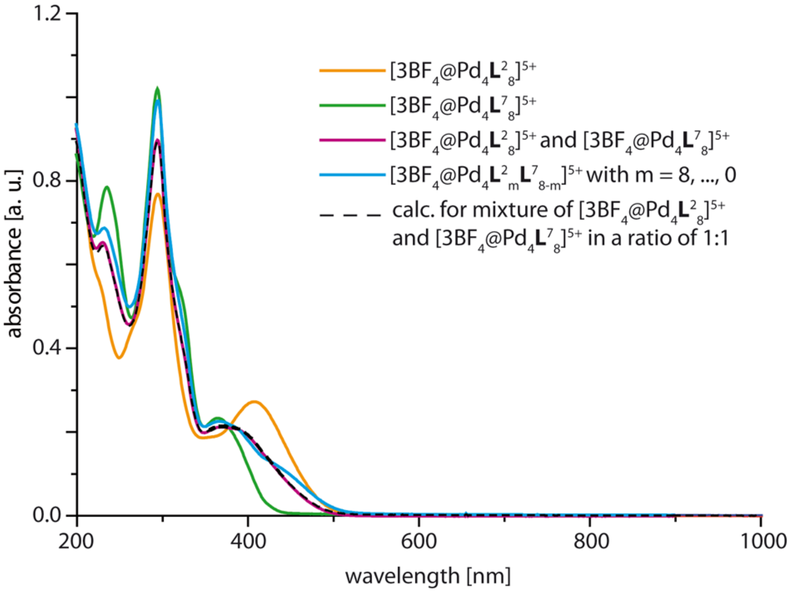

Figure SI-VI.15 UV/Vis spectra of double-cages $[3BF_4@Pd_4\mathbf{L}^2_8]^{5+}$ (20 µM in MeCN) and $[3BF_4@Pd_4\mathbf{L}^7_8]^{5+}$ (20 µM in MeCN), their mixture $[3BF_4@Pd_4\mathbf{L}^2_8]^{5+}$ + $[3BF_4@Pd_4\mathbf{L}^7_8]^{5+}$ (10 µM of each double-cage in MeCN) and the mixed-ligand double-cages $[3BF_4@Pd_4\mathbf{L}^2_m\mathbf{L}^7_{8-m}]^{5+}$ (20 µM in MeCN). The spectrum for the mixture of $[3BF_4@Pd_4\mathbf{L}^2_8]^{5+}$ and $[3BF_4@Pd_4\mathbf{L}^7_8]^{5+}$ in a ratio of 1:1 was calculated from experimental spectra of each double-cage. Light path: 0.1 cm.

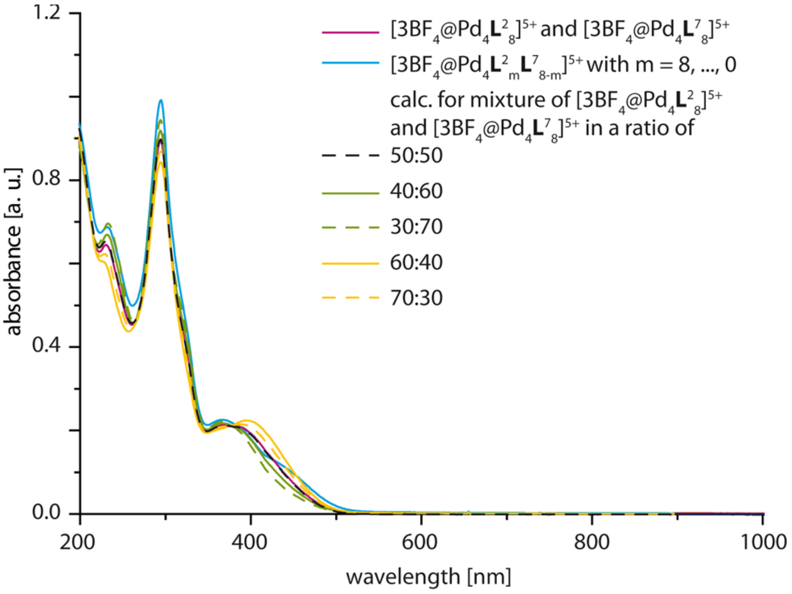

Figure AP-VI.16 UV/Vis spectra of the mixture $[3BF_4@Pd_4\mathbf{L}^2_8]^{5+}$ + $[3BF_4@Pd_4\mathbf{L}^7_8]^{5+}$ (10 µM of each double-cage in MeCN) and the mixed-ligand double-cages $[3BF_4@Pd_4\mathbf{L}^2_m\mathbf{L}^7_{8-m}]^{5+}$ (20 µM in MeCN). The spectra for the mixture of $[3BF_4@Pd_4\mathbf{L}^2_8]^{5+}$ and $[3BF_4@Pd_4\mathbf{L}^7_8]^{5+}$ in ratio of 50:50; 40:60; 30:70; 60:40 and 70:30 were calculated from experimental spectra of each double-cage. Light path: 0.1 cm.

4. Oxidation of the [$3BF_4@Pd_4L^2_8$](BF_4)$_5$ double-cage

a) UV/Vis

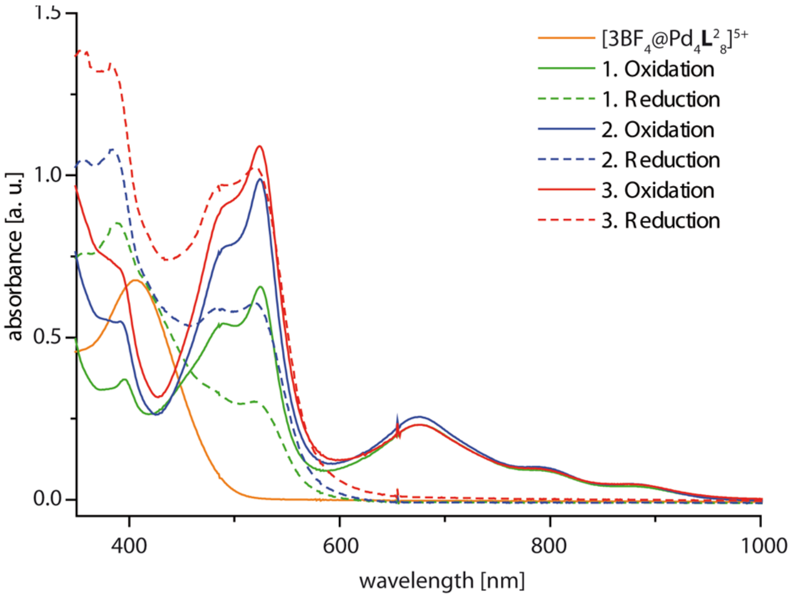

Figure AP-VI.17 Oxidation of double-cage [$3BF_4@Pd_4\mathbf{L}^2_8$]$^{5+}$ (45 µM in MeCN) with Fe(III)(bpy)$_3$(BF_4)$_3$ (2.3 mM in MeCN) and subsequent reduction with Zn powder followed by UV/Vis spectroscopy for three oxidation/reduction cycles.

b) ^{1}H NMR

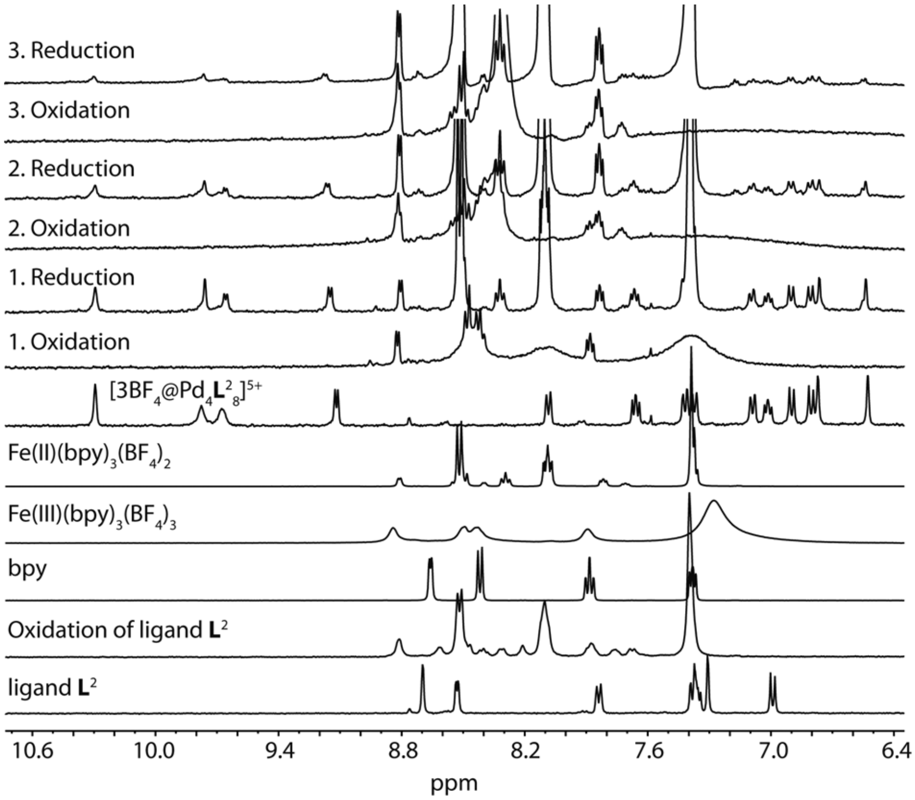

Figure AP-VI.18 ^{1}H NMR (400 MHz, 298 K, Acetonitrile-*d*$_3$) of free ligand **L**^{2}, ligand **L**^{2} + [Fe(III)bpy$_3$](BF$_4$)$_3$, free 2,2'-bipyridine, [Fe(III)bpy$_3$](BF$_4$)$_3$, [Fe(II)bpy$_3$](BF$_4$)$_2$, double-cage [3BF$_4$@Pd$_4$**L**$^2_8$]$^{5+}$ before starting the reaction, after first oxidation of [3BF$_4$@Pd$_4$**L**$^2_8$]$^{5+}$ by addition of [Fe(III)bpy$_3$](BF$_4$)$_3$, after first reduction by addition of Zn powder and second/third redox cycles.

c) ESI-HR-MS

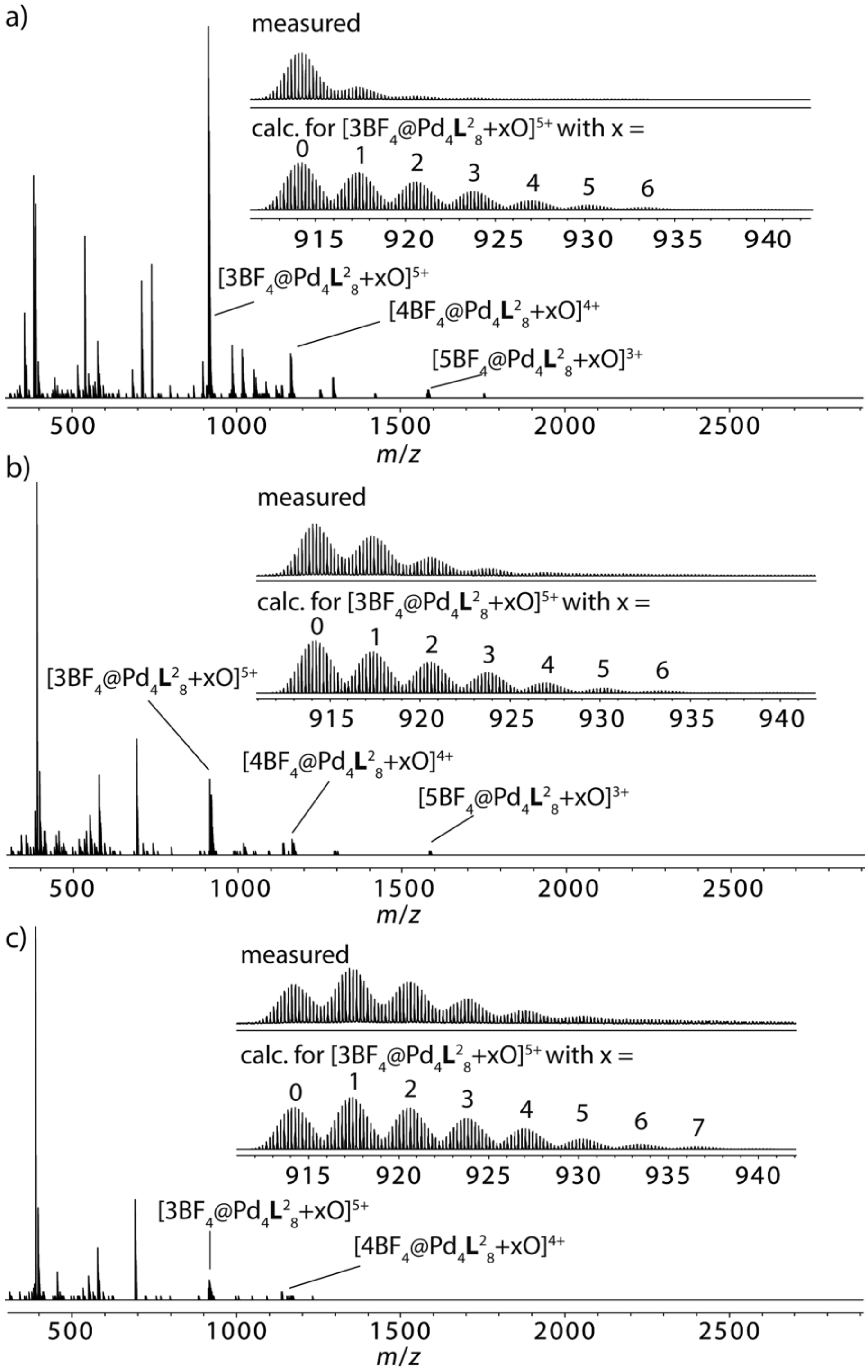

Figure AP-VI.19 ESI high resolution mass spectra of redox cycles of the double-cage $[3BF_4@Pd_4\mathbf{L}^2_8]^{5+}$ for oxidation with $[Fe(III)bpy_3](BF_4)_3$ and reduction with Zn powder. The spectra were measured after each reduction step: a) first, b) second and c) third redox cycle.

5. Cyclic Voltammetry Data

a) CV of ligand $\mathbf{L}^2$ and $\mathbf{L}^7$ and double-cages $[3BF_4@Pd_4\mathbf{L}^2_8](BF_4)_5$ and $[3BF_4@Pd_4\mathbf{L}^7_8](BF_4)_5$

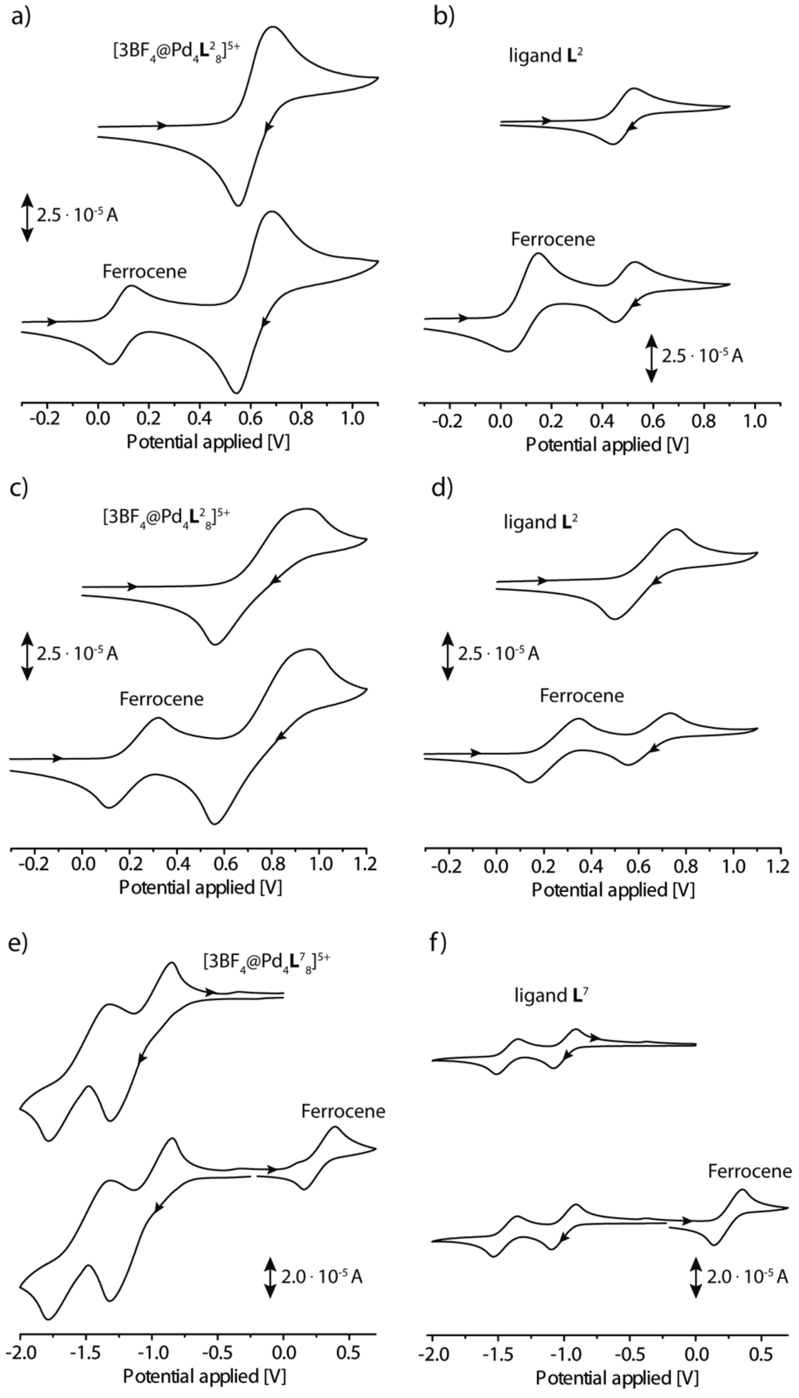

Figure AP-VI.20 Cyclic voltammograms recorded at a glassy carbon working electrode and Ag/AgNO$_3$ reference electrode of a) $[3BF_4@Pd_4\mathbf{L}^2_8]^{5+}$ (1 mM in CH$_3$CN), b) ligand $\mathbf{L}^2$ (1 mM in CH$_3$CN), c) $[3BF_4@Pd_4\mathbf{L}^2_8]^{5+}$ (1 mM in CH$_2$Cl$_2$), d) ligand $\mathbf{L}^2$ (1 mM in CH$_2$Cl$_2$), e) $[3BF_4@Pd_4\mathbf{L}^7_8]^{5+}$ (1 mM in CH$_2$Cl$_2$), f) ligand $\mathbf{L}^7$ (1 mM in CH$_2$Cl$_2$). Supporting electrolyte: 0.1 M [NBu$_4$][PF$_6$]. Scan rate: 0.1 V·s^{-1}.

b) CV of mixed-ligand cage [$3BF_4@Pd_4\mathbf{L}^2{}_m\mathbf{L}^7{}_{8\text{-}m}$]($BF_4$)$_5$

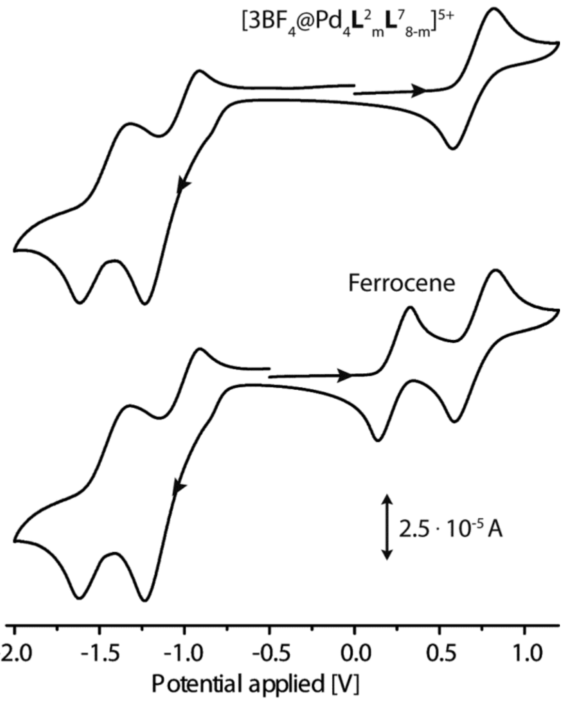

Figure AP-VI.21 Cyclic voltammograms recorded at a glassy carbon working electrode and Ag/AgNO$_3$ reference electrode of [$3BF_4@Pd_4\mathbf{L}^2{}_m\mathbf{L}^7{}_{8\text{-}m}$]$^{5+}$ (1 mM in CH_3CN). Supporting electrolyte: 0.1 M [NBu_4][PF_6]. Scan rate: 0.1 V·s^{-1}.

Table AP-VI.1: Cyclic voltammetry parameters.

Compound	scan rate [mV/s]	Solvent	E_f vs. $E_{1/2}$(Fc/Fc$^+$) [V]	E_r vs. $E_{1/2}$(Fc/Fc$^+$) [V]	$E_{1/2}$ vs. $E_{1/2}$(Fc/Fc$^+$) [V]	ΔE [mV]
Ligand $\mathbf{L}^2$	100	CH_3CN	0.43	0.36	0.39	71
	100	CH_2Cl_2	0.49	0.32	0.41	168
[$3BF_4@Pd_4\ \mathbf{L}^2{}_8$]$^{5+}$	100	CH_3CN	0.59	0.46	0.52	127
	100	CH_2Cl_2	0.70	0.35	0.53	347
Ligand $\mathbf{L}^7$	100	CH_2Cl_2	-1.35 (1) and -1.78 (2)	-1.16 (1) and -1.61 (2)	-1.25 (1) and -1.70 (2)	178 (1) and 171 (2)
[$3BF_4@Pd_4\ \mathbf{L}^7$]$^{5+}$	100	CH_2Cl_2	-1.58 (1) and -2.05 (2)	-1.12 (1) and -1.63 (2)	-1.35 (1) and -1.84 (2)	452 (1) and 420 (2)
[$3BF_4@Pd_4\ \mathbf{L}^2{}_m\ \mathbf{L}^7{}_{8\text{-}m}$]$^{5+}$	100	CH_2Cl_2	0.59; -1.45; -1.85	0.37; -1.15; -1.59	0.48; -1.30; -1.72	227; 298; 266

ΔE(Ferrocene): (204±15) mV in CH_2Cl_2 and (85±10) mV in CH_3CN. E_f = forward peak, E_r = reverse peak. (1) first reduction, (2) second reduction step

6. Spectroelectrochemical data

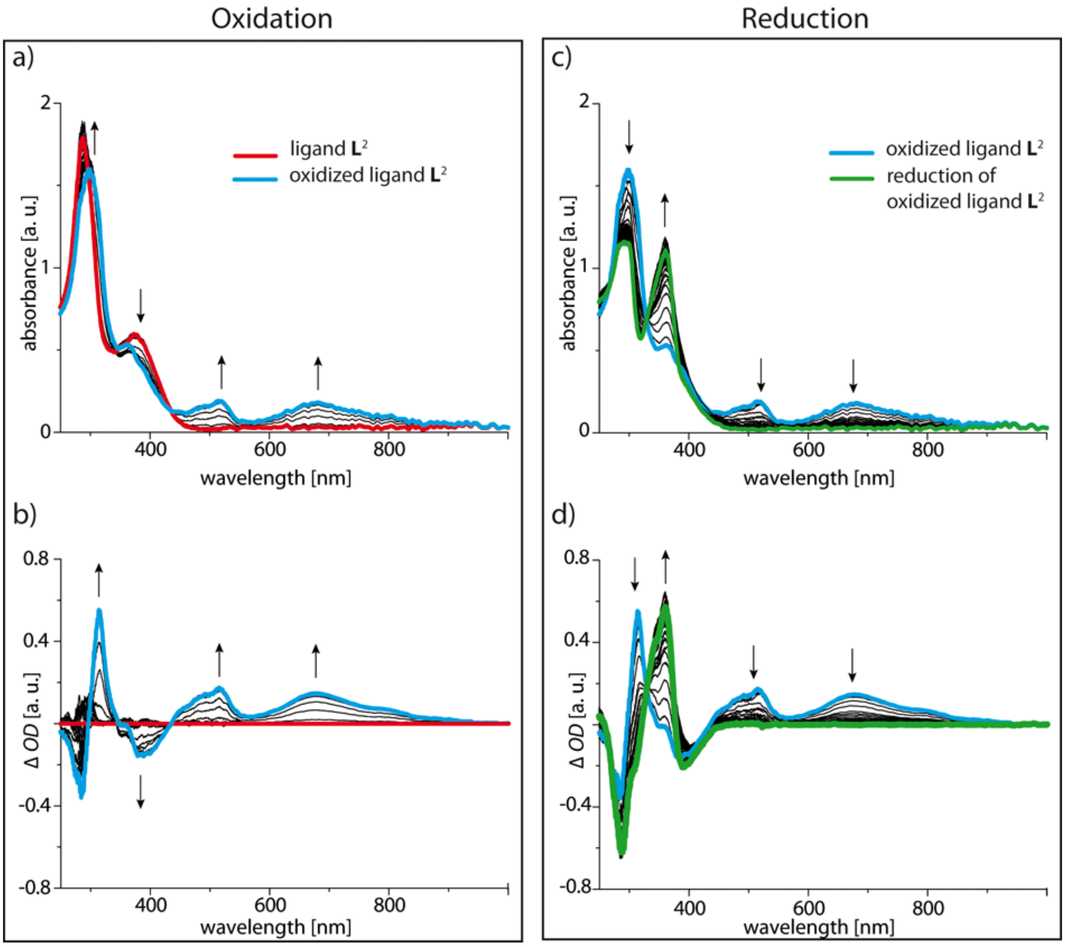

Figure AP-VI.22 UV/Vis spectra of ligand **L**^{2} (0.28 mM in CH_3CN, 0.1 M NBu_4BF_4) recorded during cyclic voltammetry with a scan rate of 0.01 V·s^{-1}, Pt gauze as working electrode and $Ag/AgNO_3$ as reference electrode. UV/Vis spectra of a) oxidation and c) reduction processes. Optical difference spectra (related to the spectrum of the non-oxidized ligand **L**^{2}) are shown for b) oxidation and d) reduction processes.

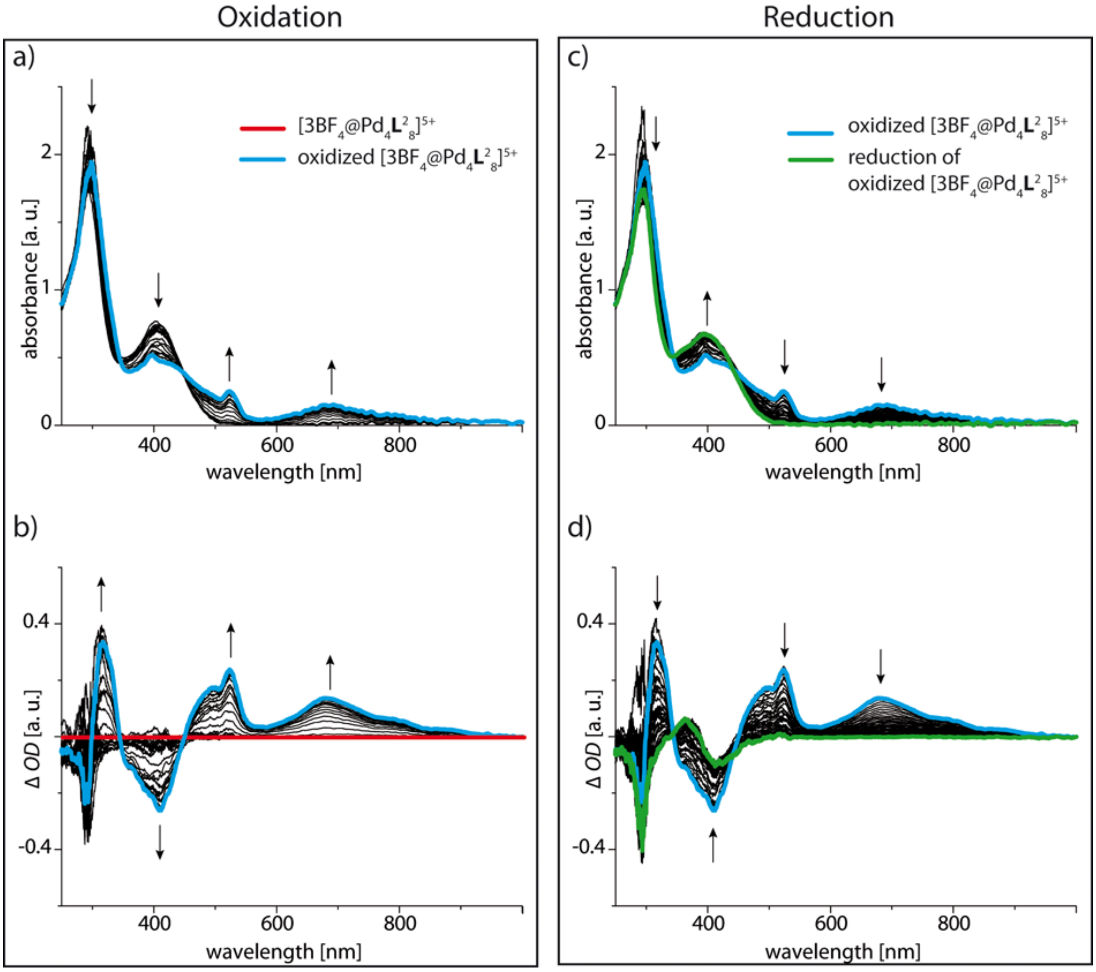

Figure AP-VI.23 UV/Vis spectra of double-cage $[3BF_4@Pd_4\mathbf{L}^2_8]^{5+}$ (0.04 mM in CH_3CN, 0.1 M NBu_4BF_4) recorded during cyclic voltammetry with a scan rate of 0.01 V·s^{-1}, Pt gauze as working electrode and Ag/AgNO$_3$ as reference electrode. UV/Vis spectra of a) oxidation and c) reduction processes. Optical difference spectra (related to the spectrum of the non-oxidized double-cage $[3BF_4@Pd_4\mathbf{L}^2_8]^{5+}$) are shown for b) oxidation and d) reduction processes.

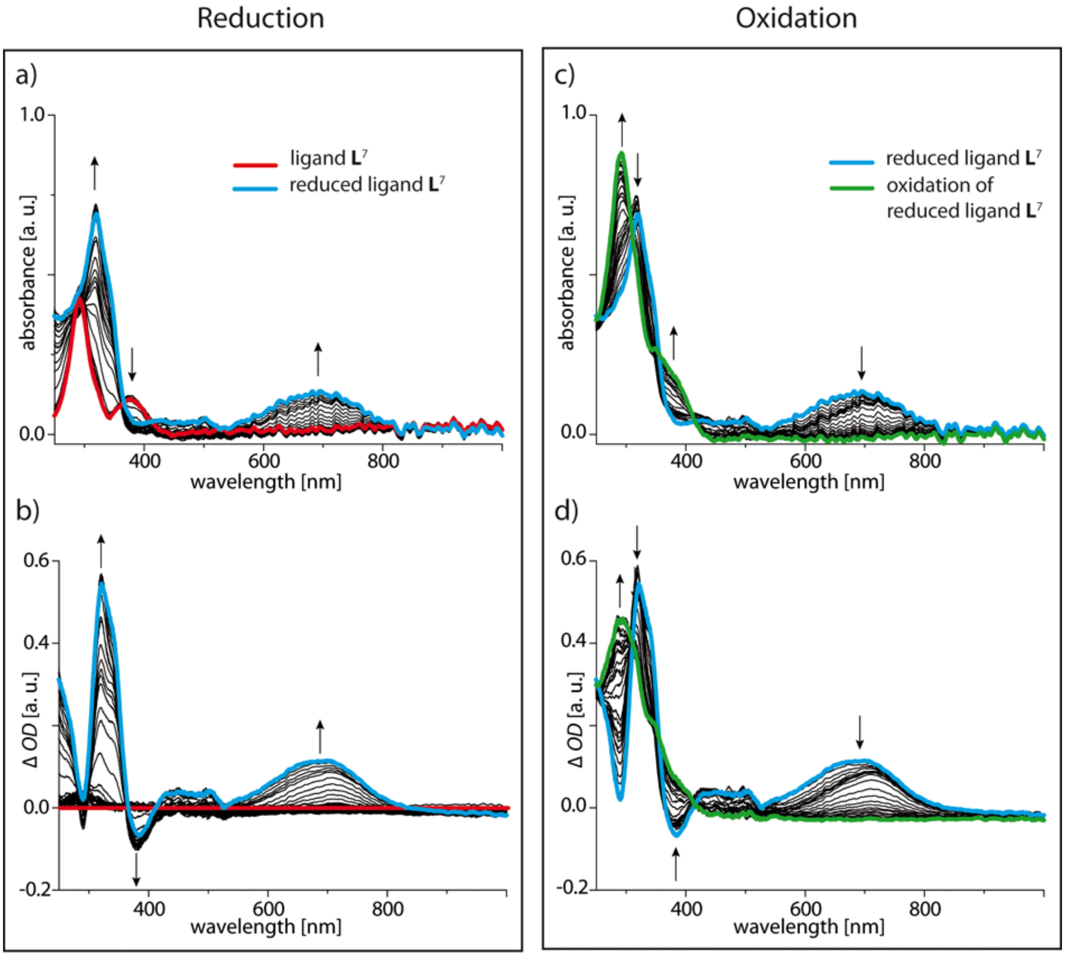

Figure AP-VI.24 UV/Vis spectra of ligand **L**^{7} (0.30 mᴍ in CH_3CN, 0.1 ᴍ NBu_4BF_4) recorded during cyclic voltammetry with a scan rate of 0.01 V·s^{-1}, Pt gauze as working electrode and Ag/$AgNO_3$ as reference electrode. UV/Vis spectra of a) oxidation and c) reduction processes. Optical difference spectra (related to the spectrum of the non-oxidized of the ligand **L**^{7}) are shown for b) oxidation and d) reduction processes.

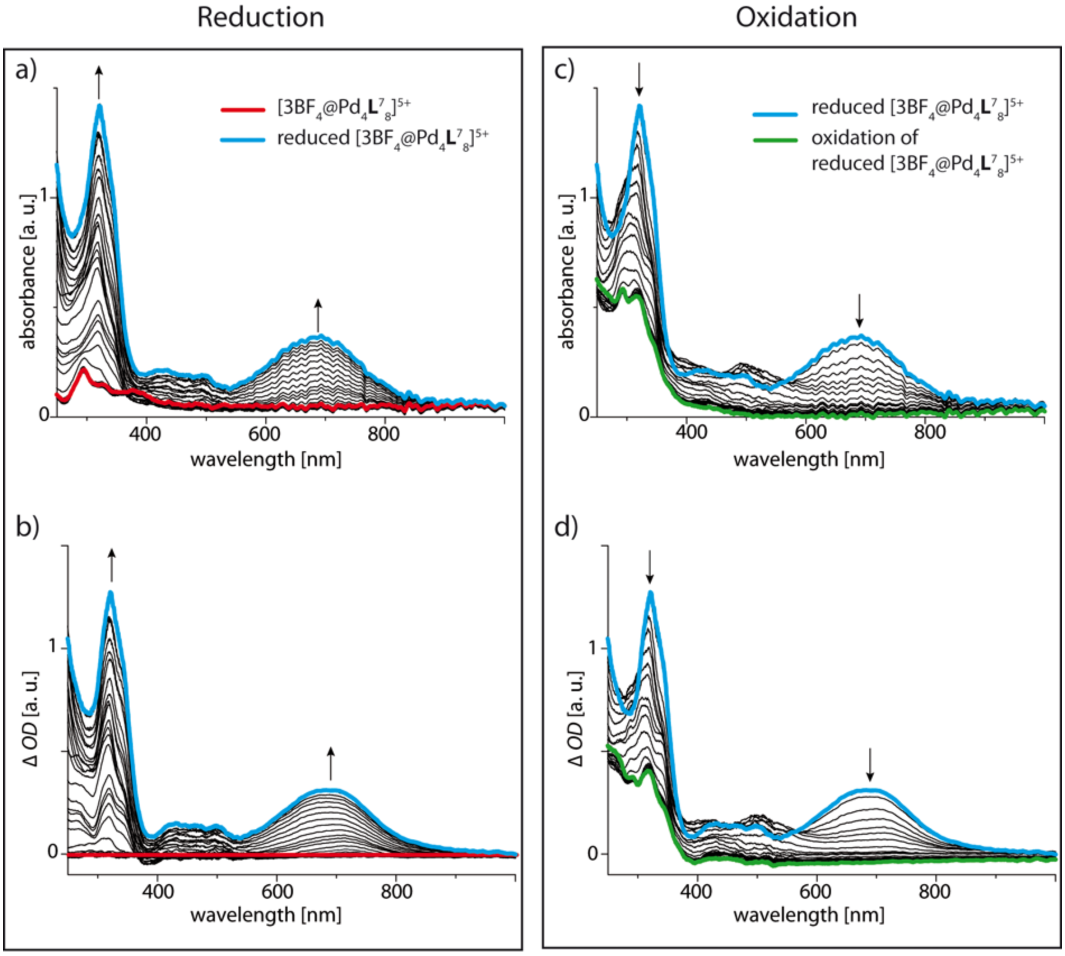

Figure AP-VI.25 UV/Vis spectra of double-cage [3BF$_4$@Pd$_4$**L**$^7{}_8$]$^{5+}$ (0.04 mM in CH$_3$CN, 0.1 M NBu$_4$BF$_4$) recorded during cyclic voltammetry with a scan rate of 0.01 V·s^{-1}, Pt gauze as working electrode and Ag/AgNO$_3$ as reference electrode. UV/Vis spectra of a) oxidation and c) reduction processes. Optical difference spectra (related to the spectrum of the non-oxidized double-cage [3BF$_4$@Pd$_4$**L**$^7{}_8$]$^{5+}$) are shown for b) oxidation and d) reduction processes.

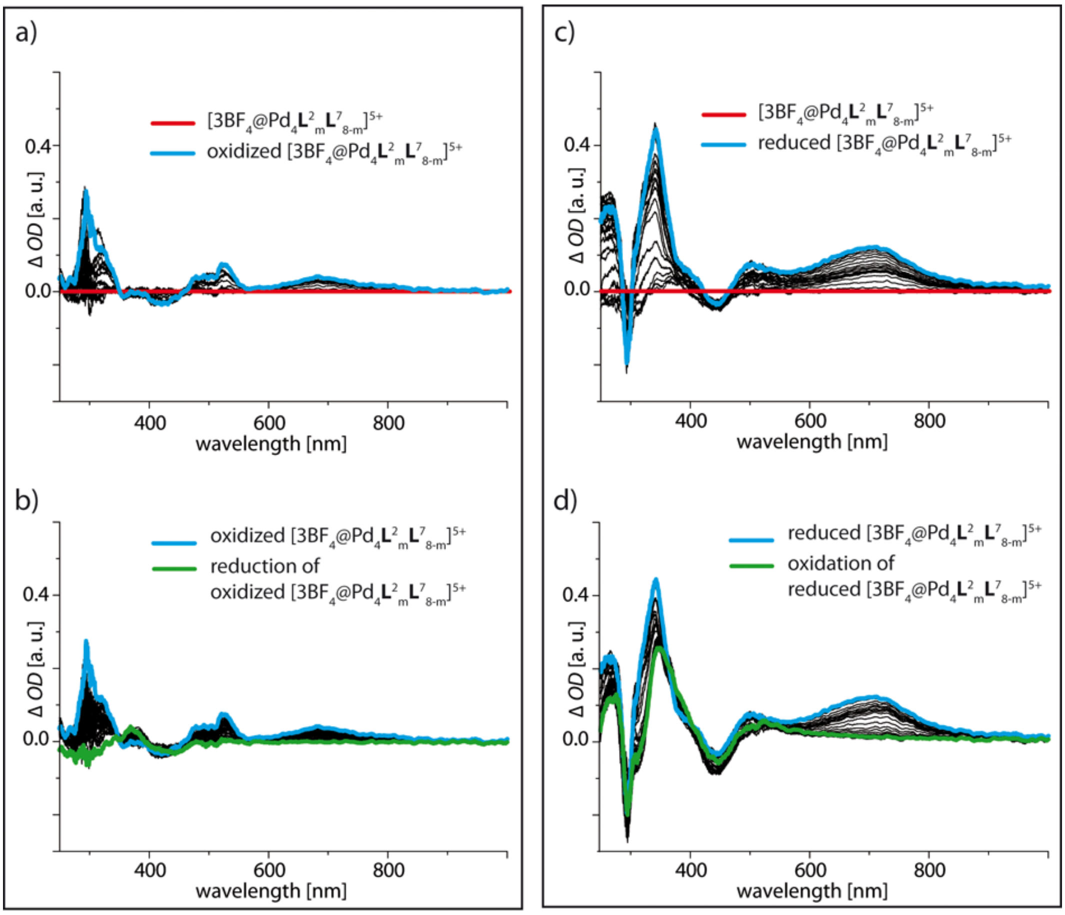

Figure AP-VI.26 UV/Vis spectra of the mixed cages $[3BF_4@Pd_4\mathbf{L}^2_m\mathbf{L}^7_{8-m}]^{5+}$ (0.04 mM in CH_3CN, 0.1 M NBu_4BF_4) recorded during cyclic voltammetry with a scan rate of 0.01 $V{\cdot}s^{-1}$, Pt gauze as working electrode and Ag/$AgNO_3$ as reference electrode. Optical difference spectra, compared to initial UV/Vis spectrum of the ligand, are shown for a) oxidation centered on $\mathbf{L}^2$, b) reduction centered on $\mathbf{L}^2$, c) reduction centered on $\mathbf{L}^7$ and d) oxidation centered on $\mathbf{L}^7$.

7. Transient pump-probe spectroscopy[177]

Experimental setup

Transient absorption spectra were measured with a laser system based on a 1 kHz Ti:sapphire regenerative amplifier system (Clark-MXR, CPA-1000) producing 150 fs laser pulses at 775 nm. Pump pulses at 387 nm were generated by second harmonic generation. For excitation in the range 400-440 nm a home-built optical parametric amplifier with subsequent fourth harmonic generation of the idler output was used. Pump pulse energies were attenuated to < 800 nJ and focused to a diameter of about 200 µm at the sample. With a small portion of the 775 nm laser light a white-light continuum was generated in a 4 mm CaF_2 crystal and split into a reference and a probe pulse. The latter was superimposed with the pump pulse at the sample. The relative plane of polarization between pump and probe was set to 54.7° to eliminate over-all molecular rotational effects to the signal. The reference and probe continua were each detected with a 256-element linear diode array attached to a spectrograph. The measured time-dependent transient spectra were corrected with respect to a wavelength dependent shift of the temporal overlap of pump and probe pulses due to group delay dispersion within the white-light-probe continuum. Experiments were performed in a flow cell of 2 mm optical path length equipped with CaF_2 windows. The flow rate was sufficiently high to exchange the sample in the pump focus between laser shots. For the experiment samples of palladium double-cages in acetonitrile were prepared at concentrations of 45 µM. The free acceptor and donor ligands and the corresponding homomeric double-cages $[3BF_4@Pd_4\mathbf{A}_8]^{5+}$ and $[3BF_4@Pd_4\mathbf{D}_8]^{5+}$ were studied in separate experiments.

---

[177] Transient pump-probe experiments were measured and analyzed by Jennifer Ahrens and Prof. Dirk Schwarzer from Max-Planck-Institute for Biophysical Chemistry, Am Fassberg 11, 37077 Göttingen (Germany).

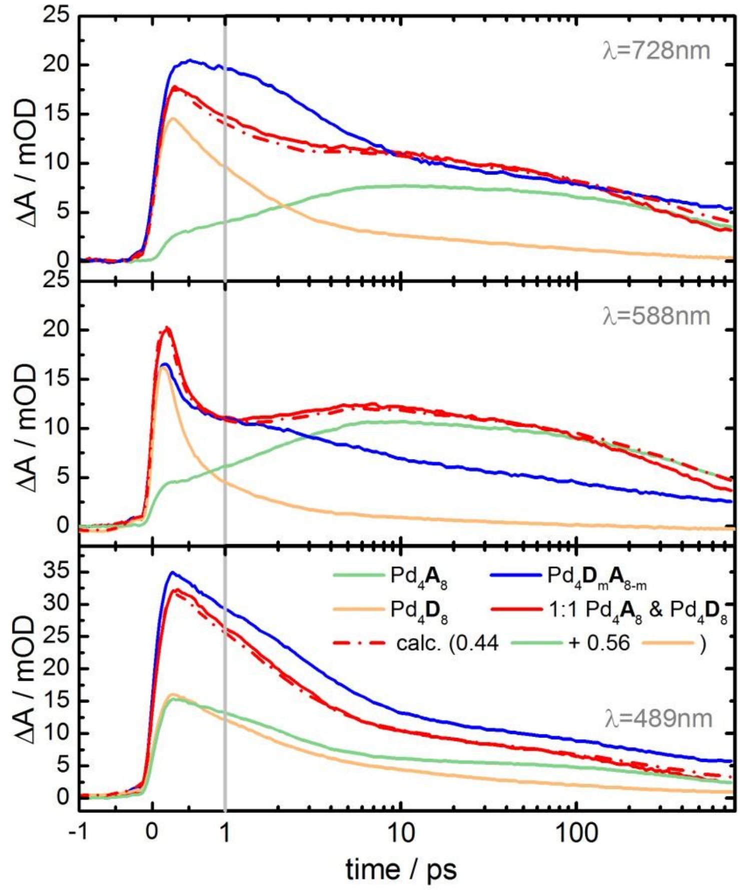

Figure AP-VI.27 Absorption time profiles for the mixed-ligand cage $[3BF_4@Pd_4\mathbf{D}_m\mathbf{A}_{8-m}]^{5+}$ (m = 8…0), the donor and acceptor cages $[3BF_4@Pd_4\mathbf{D}_8]^{5+}$ and $[3BF_4@Pd_4\mathbf{A}_8]^{5+}$, respectively, and a 1:1 mixture of the homo-octameric cages at three selected wavelengths. The signals of the 1:1 mixture (red, full line) can be represented by a weighted sum (red, dash dotted line) of the individual homomeric components (orange and green, respectively) which significantly differ from the mixed-ligand cage signal (blue). (Note: time axis up to 1 ps is linear; above 1 ps it is logarithmic).

The fluorescence of the free anthraquinone-based acceptor ligand is weak and shows a strong Stokes shift of ~6000 cm^{-1} indicating the charge-transfer character of the emitting state.[178] Figure AP-VI.28 summarizes the results obtained in the transient absorbance studies. The time dependence of the transient spectra of **A** shows the conversion of an excited state absorption. Initially the spectrum is dominated by the absorption with a

---

[178] J. H. Yang, A. Dass, A. M. M. Rawashdeh, C. Sotiriou-Leventis, M. J. Panzner, D. S. Tyson, J. D. Kinder, N. Leventis, *Chemistry of Materials* **2004**, *16*, 3457.

maximum at 480 nm which shifts within the duration of the excitation pulse into a broad feature with a maximum at 600 nm. Previous studies showed that an efficient intersystem crossing is the dominant relaxation channel of photo-excited anthraquinone and its derivatives.[179] According to this results, the time constant of $\tau_{S1} = (2.4\pm0.2)$ ps can be attributed to the transformation of the excited singlet into a long-lived triplet state. Thereby, the photophysics of the anthraquinone ligand is almost unchanged when the ligand is incorporated into the double-cage $[3BF_4@Pd_4\mathbf{A}^2_8]^{5+}$. The double-cage shows apart from small spectral shifts (the maximum of the singlet state absorption band now appears at 500 nm) almost identical time-dependent transients as the free ligand **A** (see Figure AP-VI.28(i)). For the excitation of $[3BF_4@Pd_4\mathbf{A}^2_8]^{5+}$ a long-lived triplet state within $\tau_{S1} = (2.2\pm0.2)$ ps was found.

---

[179] A. Lauer, A. L. Dobryakov, S. A. Kovalenko, H. Fidder, K. Heyne, *Phys. Chem. Chem. Phys.* **2011**, *13*, 8723.

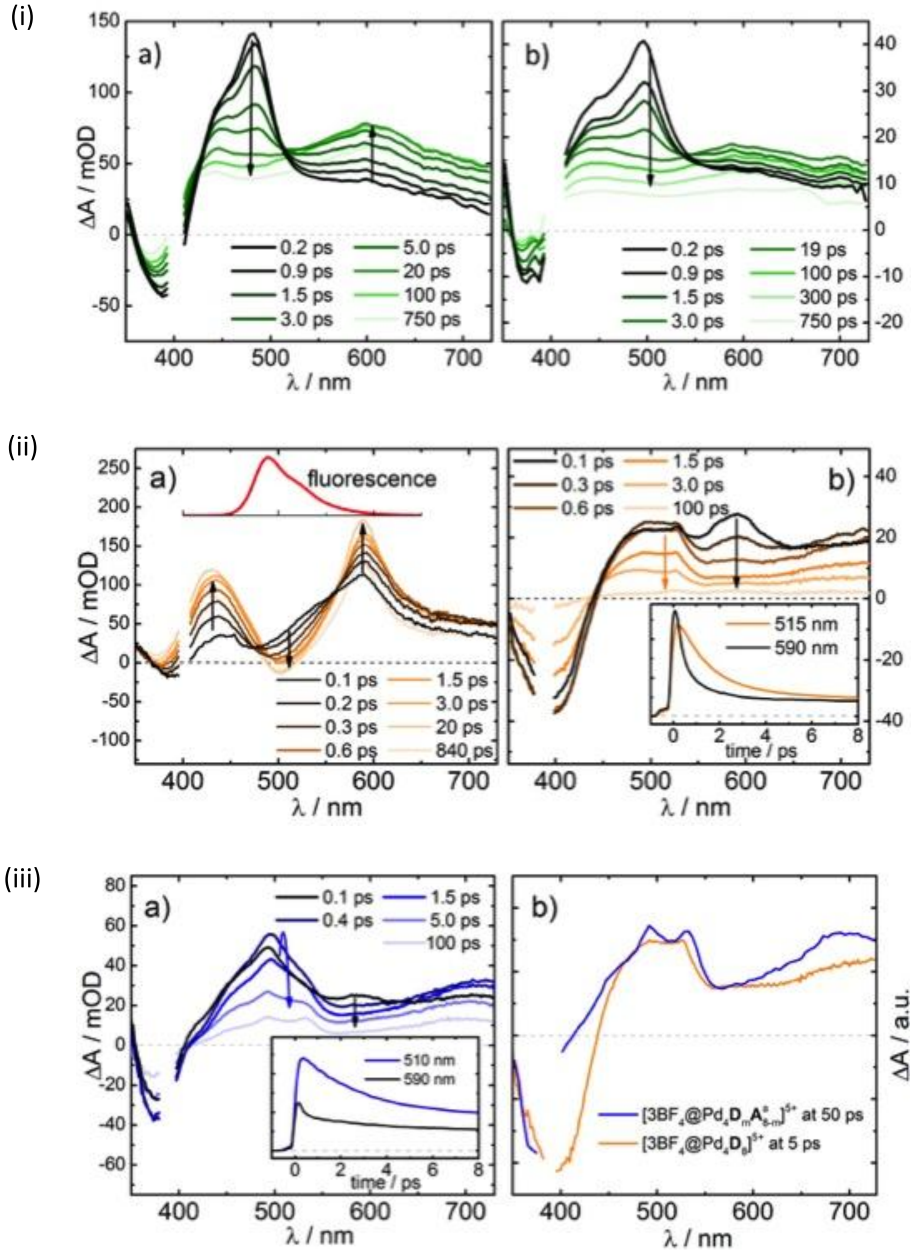

Figure AP-VI.28 (i) Transient difference spectra of (a) the free anthraquinone electron acceptor ligand **A** and (b) the homogeneous double-cage $[3BF_4@Pd_4\mathbf{A}_8]^{5+}$ at selected pump-probe delays (regions obscured by the pump wavelength at λ_{pump} = 400 nm were cut out). (ii) Transient absorption spectra of (a) the free phenothiazine electron donor ligand **D** (the stationary fluorescence spectrum of **D** is shown for comparison) and (b) the homogeneous double-cage $[3BF_4@Pd_4\mathbf{D}_8]^{5+}$ at selected pump-probe delays (the insert shows time-dependent traces at 515 and 590 nm). (ii) (a) Transient absorption spectra of the mixed-ligand cage $[3BF_4@Pd_4\mathbf{D}_m\mathbf{A}^2_{8\text{-}m}]^{5+}$ (m = 0…8) at selected pump-probe delays (the insert shows time traces at 510 and 590 nm). (b) Scaled transients of the mixed-ligand cage and the homogeneous donor cage $[3BF_4@Pd_4\mathbf{D}_8]^{5+}$ are compared. Reproduced with permission from reference [136]. Copyright © 2016 American Chemical Society.

Upon 400 nm excitation, the free phenothiazine donor ligand shows fluorescence with a maximum at 490 nm.[65] This fluorescence band shows up in the transient absorption spectrum as stimulated emission superimposed by strong excited state absorption causing a minimum at 500 nm and maxima at 430 and 590 nm and decays with a characteristic time of > 3 ns (see Figure AP-VI.28(ii)). Two time constants of 0.3 ± 0.05 ps and 7.6 ± 1.0 ps were derived from the time resolved experiments. Similar nanosecond singlet lifetimes were shown for other phenothiazine derivatives.[180] The situation changes completely when the donor ligand is bound in the double-cage $[3BF_4@Pd_4\mathbf{D}_8]^{5+}$. The steady-state fluorescence observed for free ligand **D** is completely quenched in the double-cage. The transient absorption spectrum of $[3BF_4@Pd_4\mathbf{D}_8]^{5+}$ directly after the pump pulse showed characteristics of the phenothiazine excited singlet state indicated by the peak at 590 nm. But this band vanished within 200 fs and absorption bands with maxima at 500 and 700 nm emerged. A comparison of the transient after 3.0 ps with spectra of the chemically or electrochemically oxidized double-cage (see Figure VI.17) shows similarities in the absorption pattern. Previous studies showed that excitation of phenothiazine in the presence of transition metal ions give rise to phenothiazine radical cations by efficient electron transfer.[181] Based on these results, the photo-induced dynamics of $[3BF_4@Pd_4\mathbf{D}_8]^{5+}$ can be attributed to a sub-picosecond ligand-to-metal electron transfer to the bound Pd(II) cations. In contrast to (electro-)chemical oxidation of the donor double-cage, which can yield the fully oxidized double-cage $[3BF_4@Pd_4\mathbf{D}_8{}^{(\bullet+)}]^{13++}$, the photo-excitation produces only a single exciton. This leads to a charge transfer resulting in the proposed compound $[3BF_4@Pd^{II}{}_3\mathbf{D}_7Pd^{I}\mathbf{D}^{(\bullet+)}]^{5+}$ with one phenothiazine radical cation, one palladium in oxidation state +1, and unchanged total charge. This difference can help to explain the small differences between the radical cation absorption spectra in Figures VI.17 and AP-VI.28. The insert in Figure AP-VI.28(ii)b shows the lifetime of the CT state, which was found to be very short. The decay of the phenothiazine radical cation absorption at 500 nm can be attributed to back electron transfer with a time constant of τ_{CT} = (1.3±0.1) ps.

Transient absorption spectra of mixed-ligand cages $[3BF_4@Pd_4\mathbf{D}_m\mathbf{A}^2{}_{8\text{-}m}]^{5+}$ (m = 0…8) were recorded after excitation at 385 nm. At this wavelength both donor and acceptor units are

---

[180] J. Shirdel, A. Penzkofer, R. Prochazka, Z. Shen, J. Daub, *Chem. Phys.* **2007**, *336*, 1.

[181] S. A. Alkaitis, G. Beck, M. Grätzel, *J. Am. Chem. Soc.* **1975**, *97*, 5723.

excited simultaneously with nearly equal probability (55% and 45%, respectively, see Figure AP-VI.28 (iii)). Shortly after excitation, these spectra show indication of the initially excited chromophore singlet states at 500 nm (anthraquinone) and 590 nm (phenothiazine) (compare to Figure AP-VI.28 (i) and (ii)). These bands vanish within a time period of 200 fs. For longer delay times characteristic signatures of the phenothiazine radical cation appear at 500 and 700 nm. Moreover, the transient spectra of the excited mixed-ligand double-cage show enhanced amplitude around the broad band absorption at 700 nm (see Figure AP-VI.28(iii)) which indicates the formation of the anthraquinone radical anion **A**$^{2\bullet-}$ as shown in Figure VI.17. Therefore, the observed dynamics in the photo-excited mixed-ligand double-cages can be assigned to an electron transfer reaction from the phenothiazine donor to the anthraquinone acceptor ligand (**DA**-CT) independent on the excitation sequence of the chromophores. Control experiments with a 1:1 mixture of the homomeric donor and acceptor double-cages in acetonitrile solution did not show any indication for a **DA**-CT process. In case of the mixture of homomeric double-cages, the transient absorption spectra (see Figure AP-VI.28) consist of a weighted sum of the individual spectra of homomeric double-cages which significantly differ from the absorption pattern of the mixed-ligand double-cage.

Appendix-Chapter VII

1. Experimental Raman and SERS Spectra[182]

The Raman and SERS spectra were collected with a standard system (Kaiser Optical System Inc., Ann Arbor, MI, USA); the 785 nm (line width 0.06 nm) GaAlAs diode laser (Invictus, Kaiser Optical Systems, Inc.) light was focused onto the sample. The incident power of the laser emission was ca. 50 mW at the probe head by a recording time of 10 and 5 s with 1 and 20 accumulations for SERS and Raman experiments, respectively. The diffracted light was recorded with a CCD camera (iDus, Andor Technology plc.) The spectral resolution was 5 cm^{-1}. The most important prerequisite when comparing Raman shifts is the reproducibility (or repeat- ability) of the experiment. Kaiser Optical Systems provide a Raman shift tolerance between ± 0.5 and ± 1.0 cm^{-1}. Individual system performance will not vary to this extent. Upon calibration, a system should yield Raman shift values repeatable to ± 0.1 cm^{-1}. For the normal Raman measurements the concentration was 2.80 mᴍ for the ligand and 0.35 mᴍ for the double-cage. The normal Raman spectra have been corrected by subtraction of the solvent bands. Two different solvents (acetonitrile and acetone) were employed to check for overlapping bands in various regions of the spectra. Due to subtraction artefacts only regions with no significant overlap with the solvent bands are depicted and discussed here. For the full spectra and the overlapping regions of the solvents and the analytes see Figure AP-VII.1. In the case of the SERS measurements 1 mL of the solutions were used to coat the Au substrate. The solvent was left to evaporate before the measurements.

Due to the background signal, the Raman and surface enhanced Raman spectra have to be corrected by a baseline correction. An algorithm for baseline correction was developed by connecting cubic splines.[183]

---

[182] The Raman and SERS measurements were performed by Sebastian Funke and Hainer Wackerbarth from Laser-Laboratorium Göttingen e.V., Hans-Adolf-Krebs-Weg 1, 37077 Göttingen, Germany

[183] H. Wackerbarth, C. Lenth, S. Funke, L. Gundrum, F. Rotter, F. Büttner, J. Hagemann, M. Wellhausen, U. Plachetka, C. Moormann, M. Strube, A. Walte, *Proc. SPIE*, **2013**, *8896*, 889609.

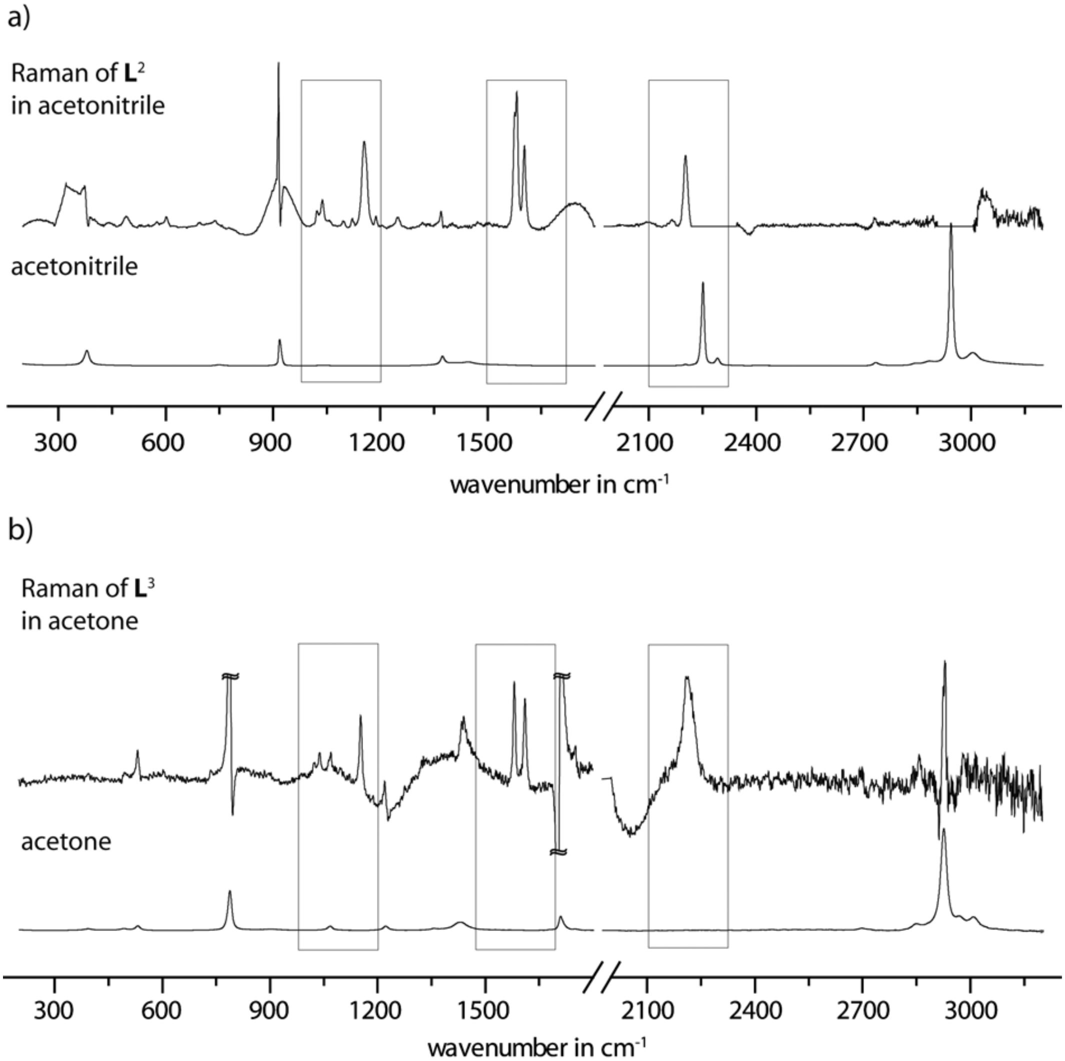

Figure AP-VII.1 a) Showcase overlay of a Raman spectrum for ligand a) **L**^{2} in acetonitrile and b) **L**^{3} in acetone and a spectrum of the correspondent solvent. The “derivative” like bands in the analyte spectrum have their origin in the subtraction of the solvent bands. For further investigation we have set our focus on the parts of the spectrum with a minimal superimposition (marked by grey boxes).

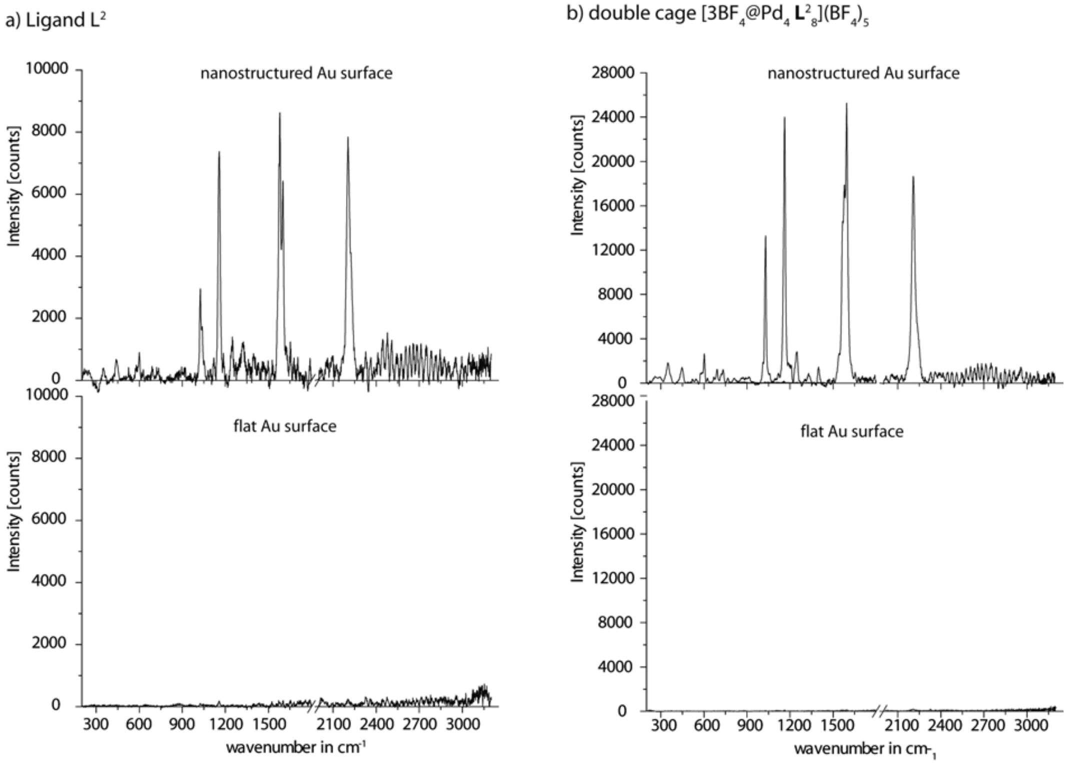

Figure AP-VII.2 SERS spectra of deposition of the substrate a) ligand L^2 and b) double-cage [$3BF_4@Pd_4L^2_8$](BF_4)$_5$ on a nanostructured and on an planar gold surface showing an enhancement of the signals when the nanostructured Au surface is used. Recording time was 10 s.

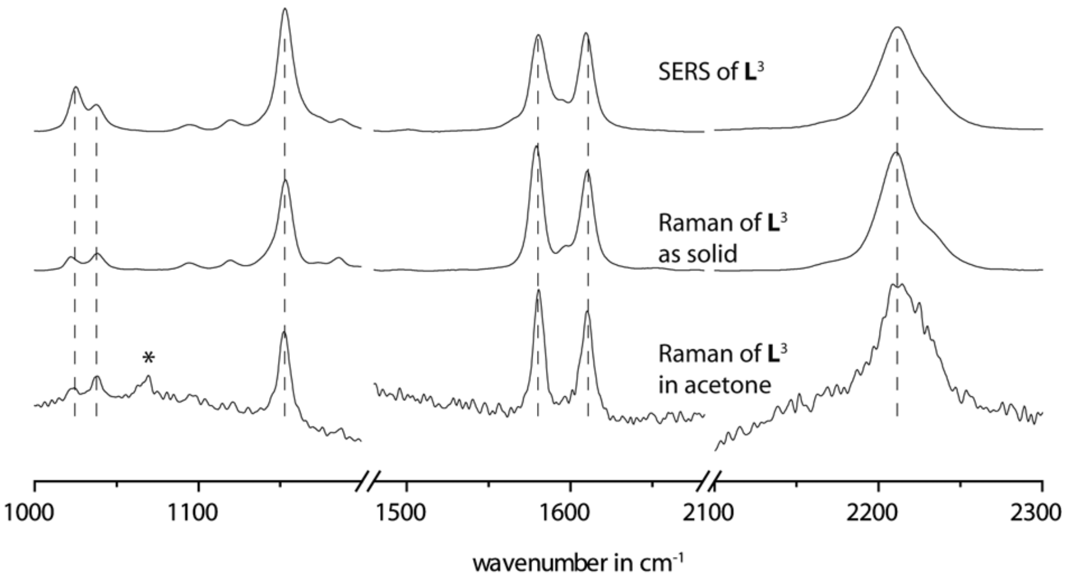

Figure AP-VII.3 Experimental Raman spectra in solution (acetone) and of a solid for the ligand $\mathbf{L}^3$ and SERS spectra on an Au coated surface in the ranges of 1000-1200 cm^{-1}, 1480-1680 cm^{-1} and 2100-2300 cm^{-1}. The auxiliary dashed lines are referenced to the middle spectrum. * denotes the residual signal arising from solvent subtraction.

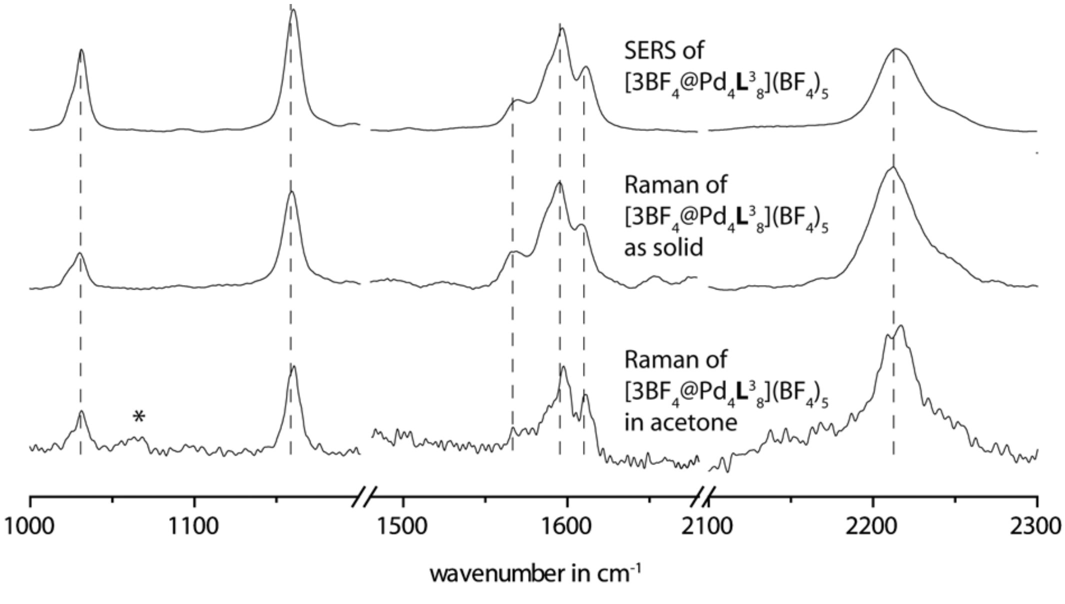

Figure AP-VII.4 Experimental Raman spectra in solution (acetone) and of a solid for the double-cage [$3BF_4@Pd_4\mathbf{L}^3{}_8$]($BF_4$)$_5$ and SERS spectra on an Au coated surface in the ranges of 1000-1200 cm^{-1}, 1480-1680 cm^{-1} and 2100-2300 cm^{-1}. The auxiliary dashed lines are referenced to the middle spectrum. * denotes the residual signal arising from solvent subtraction**.**

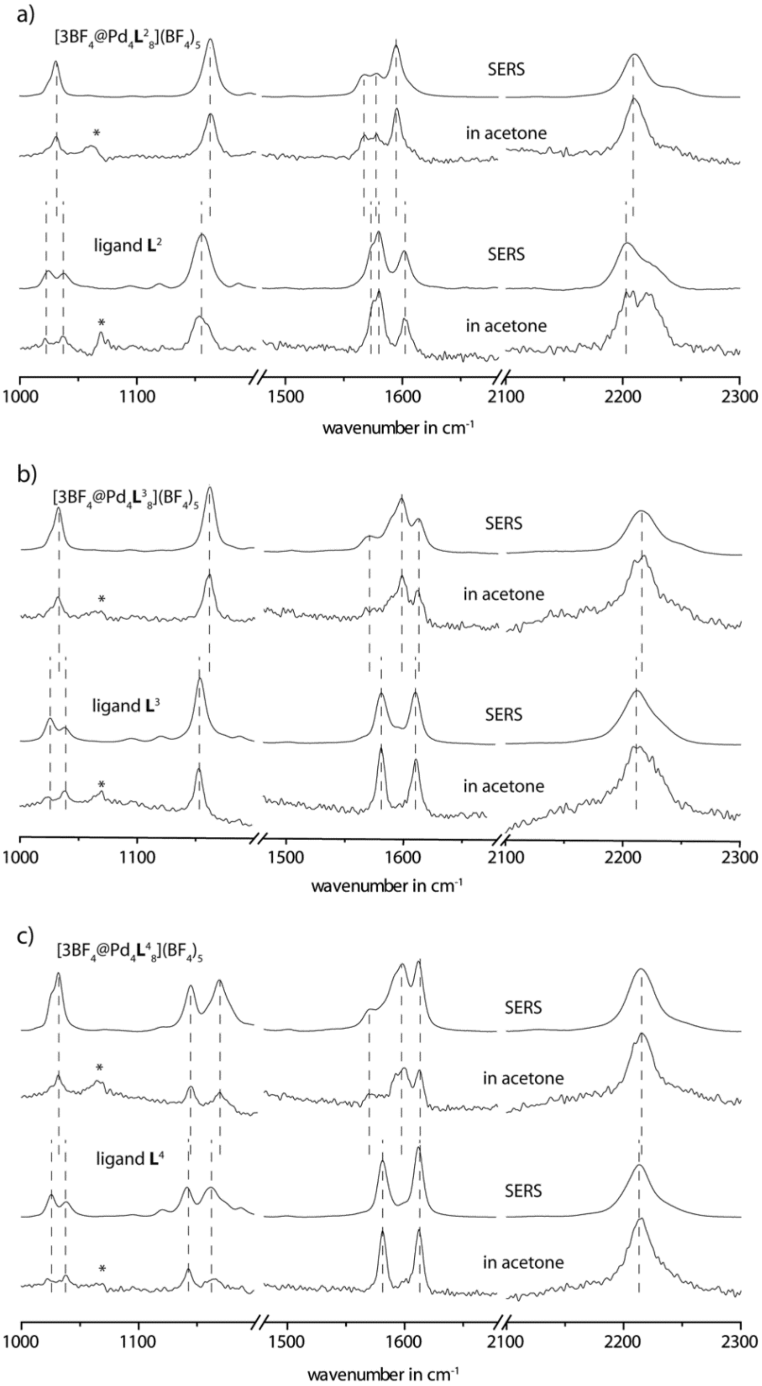

Figure AP-VII.5 Comparison between the experimental Raman spectra in solution (acetone) of the ligands **L**^{n} and their corresponding double-cages [3BF$_4$@Pd$_4$**L**$^n_8$](BF$_4$)$_5$ with a) n = 2, b) n= 3 and c) n=4 and SERS spectra on an Au coated surface in the ranges of 1000-1200 cm^{-1}, 1480-1680 cm^{-1} and 2100-2300 cm^{-1}. * denotes the residual signal arising from solvent subtraction.

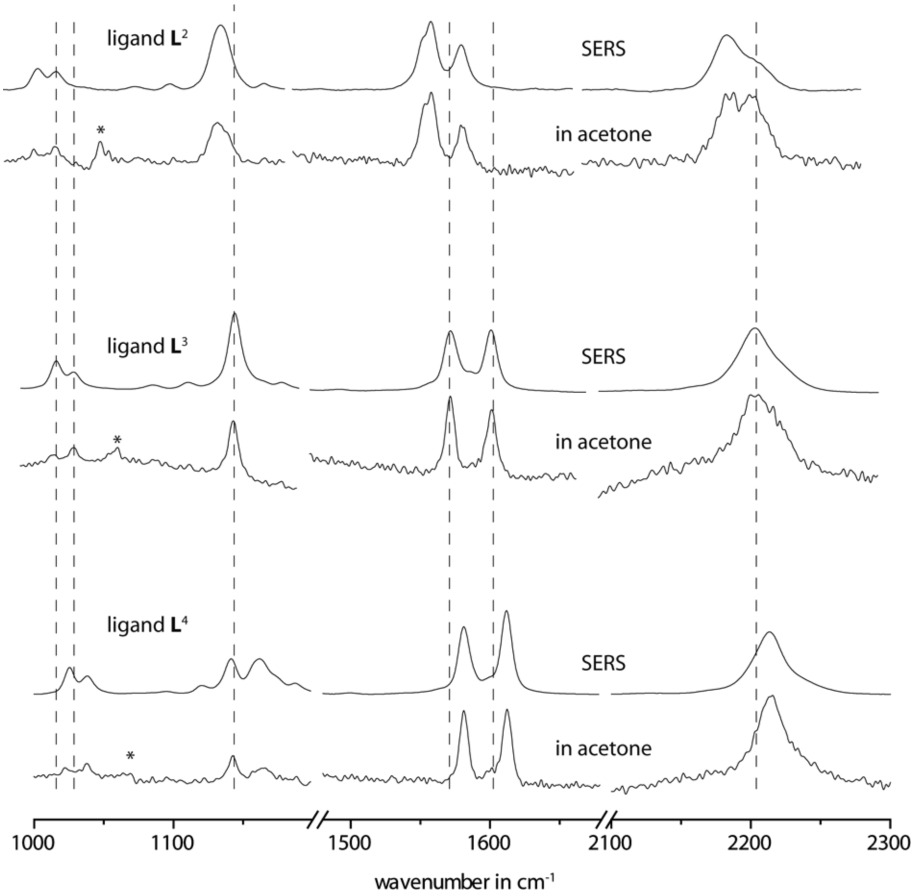

Figure AP-VII.6 Experimental Raman spectra in solution (acetone) of the ligands $\mathbf{L}^{2\text{-}4}$ and SERS spectra on an Au coated surface in the ranges of 1000-1200 cm^{-1}, 1480-1680 cm^{-1} and 2100-2300 cm^{-1}. The auxiliary dashed lines are referenced to the spectrum of ligand $\mathbf{L}^3$. * denotes the residual signal arising from solvent subtraction.

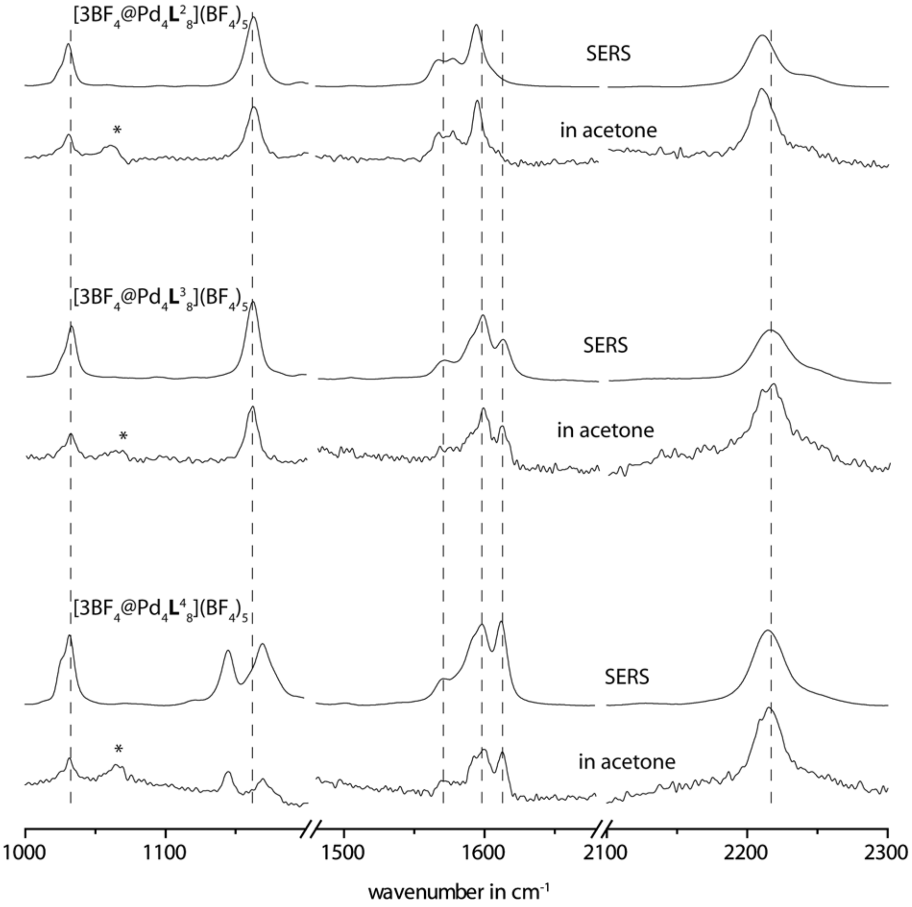

Figure AP-VII.7 Experimental Raman spectra in solution (acetone) of the self-assembled cages [3BF$_4$@Pd$_4$**L**^{n}$_8$](BF$_4$)$_5$ with n = 2-4 and SERS spectra on an Au coated surface in the ranges of 1000-1200 cm^{-1}, 1480-1680 cm^{-1} and 2100-2300 cm^{-1}. The auxiliary dashed lines are referenced to the spectrum of ligand [3BF$_4$@Pd$_4$**L**^{3}$_8$](BF$_4$)$_5$. * denotes the residual signal arising from solvent subtraction.

Table SI-VII.1 Vibrational experimental wavenumbers and intensities for the ligands **L**^{n} and the cages [3BF$_4$@Pd$_4$**L**$^n{}_8$](BF$_4$)$_5$ with n = 2-4.

Experimental frequencies[a] for the ligand **L**^{2} in cm^{-1}		Experimental frequencies[a] for the cage [3BF$_4$@Pd$_4$**L**$^2{}_8$](BF$_4$)$_5$ in		Experimental frequencies[a] for the ligand **L**^{3} in cm^{-1}		Experimental frequencies[a] for the cage [3BF$_4$@Pd$_4$**L**$^3{}_8$](BF$_4$)$_5$ in		Experimental frequencies[a] for the ligand **L**^{4} in cm^{-1}		Experimental frequencies[a] for the cage [3BF$_4$@Pd$_4$**L**$^4{}_8$](BF$_4$)$_5$ in cm^{-1}	
Raman	SERS	Raman	SERS	Raman	SERS	Raman	SERS	Raman	SERS	Raman	SERS
	347 w		348 w		445 w				609 w		610 m
	449 w		441 w		527 vw						668 vw
	602 w		600 w		600 w		599 w		692 vw		691 vw
1022 m	1025 m	1031 m	1031 s				668 w		732 w		733 w
1037 m	1038 m				690 vw		689 w	1022 w	1025 m		
1154 s	1156 vs	1163 s	1163 vs		733 w		733 w	1038 w	1038 m	1031 m	1031 vs
	1187 vw		1197 vw	1024 w	1025 m				1121 sh		1122 sh
	1248 w		1248 w	1038 m	1037 m	1031 m	1031 s	1142 m	1142 m	1145 m	1145 s
1576 sh	1575 vs	1568 m	1568 m		1094 vw			1166 w	1162 m	1169 m	1169 s
1580 vs	1580 vs	1578 m	1578 m		1120 w				1187 sh		1194 sh
1601 s	1602 s	1595 s	1595 vs	1152 s	1153 vs	1161 s	1160 vs		1276 vw		
2203 vs	2204 vs	2210 vs	2210 vs		1172 w				1298 w		1300 w
					1187 w		1197 vw		1330 w		1330 w
					1276 w		1276 vw			1593 sh	1571 sh
					1302 vw		1305 w	1581 vs	1581 vs	1599 s	1598 vs
					1326 vw		1332 w	1612 vs	1612 vs	1613 s	1612 vs
				1581 vs	1580 vs		1570 m	2216 vs	2213 vs	2215 vs	2215 vs
					1595 w	1598 s	1597 vs				
				1610 vs	1610 vs	1611 m	1611 s				
				2209 vs	2212 vs	2214 vs	2214 vs				

Experimental intensity description: vs = very strong; s = strong; m = medium; w = weak; vw = very weak; sh = shoulder.

[a] This work.

2. Calculated vibrational spectra for the ligands L^n with n =2-4

Density functional theory (DFT) calculations were performed using the Gaussian ’09[72] program with the Becke 3-Parameter Lee–Yang–Parr correlation functional (B3LYP) and the 6-31G* split-valence polarization basis set. No imaginary frequencies were observed for the optimized structures. The applied scaling equation for correcting the computed vibrational frequencies was found empirically. In order to save computation time the hexyl residues were truncated and replaced by ethyl groups.[184]

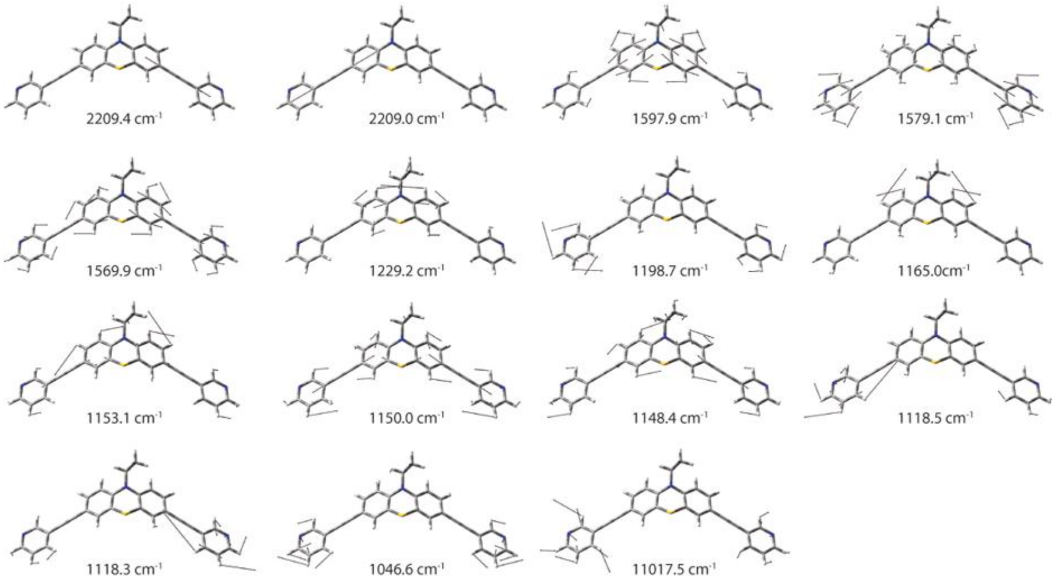

Figure AP-VII.8 Calculated vibrational modes with the highest intensity for the ligand $\mathbf{L}^2$.

---

[184] For different quantum mechanical continuum solvation models see: J. Tomasi, B. Mennucci, R. Cammi, *Chem. Rev.* **2005**, *105*, 2999.

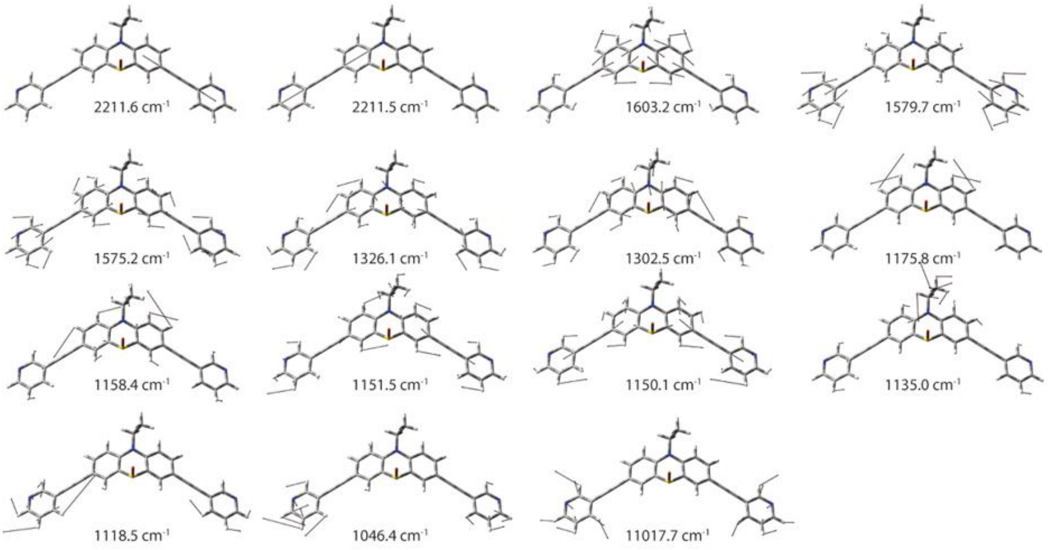

Figure AP-VII.9 Calculated vibrational modes with the highest intensity for the ligand **L**^{3} with the oxygen in axial position.

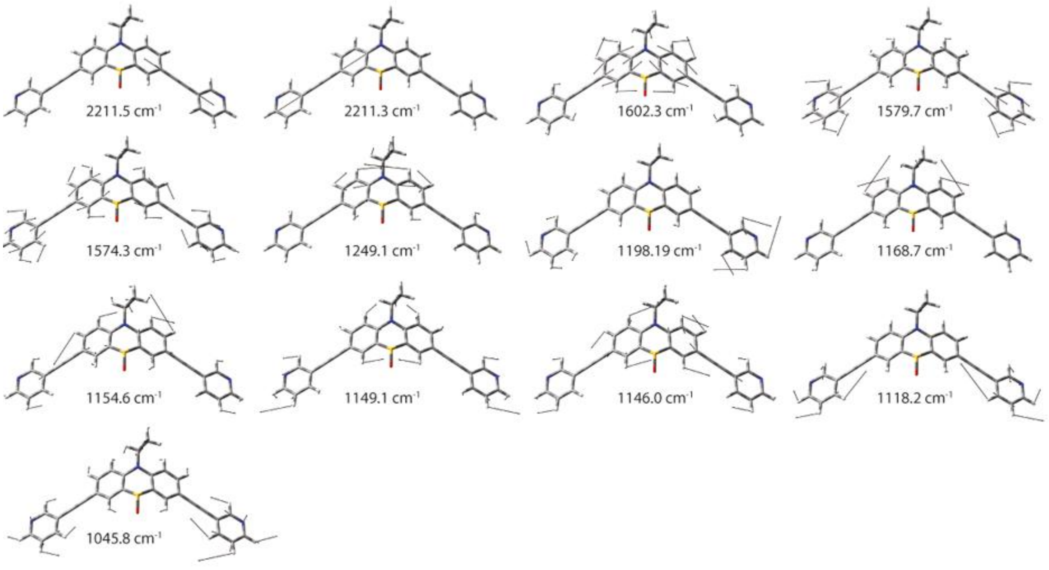

Figure AP-VII.10 Calculated vibrational modes with the highest intensity for the ligand **L**^{4}.

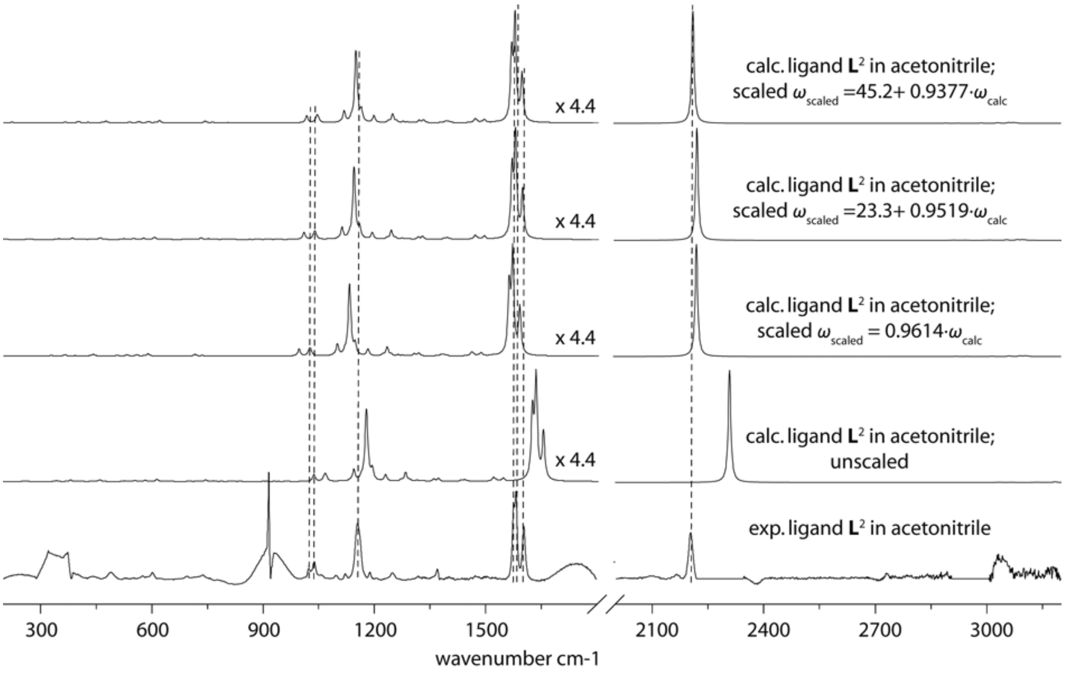

Figure AP-VII.11 Scaling methods for the calculated spectrum of the ligand **L**^{2}.

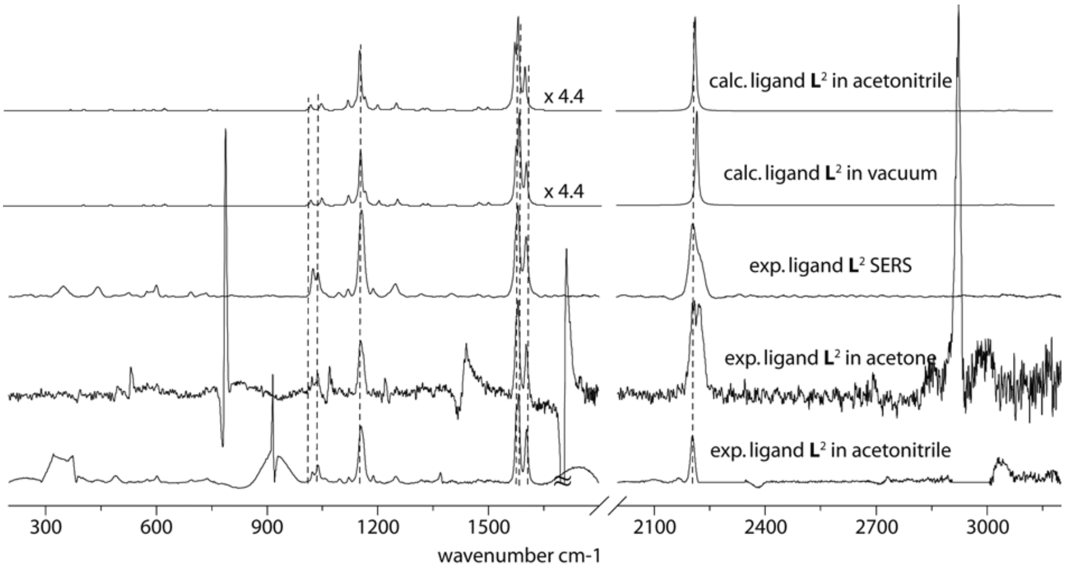

Figure AP-VII.12 Calculated vibrational spectra using a solvent (acetonitrile) and in vacuum for the ligand **L**^{2} vs. experimental spectra in solution (acetonitrile and acetone) and on Au surface (SERS). The range 200-1800 cm^{-1} of the calculated spectra was enlarged by a factor of 4.4.

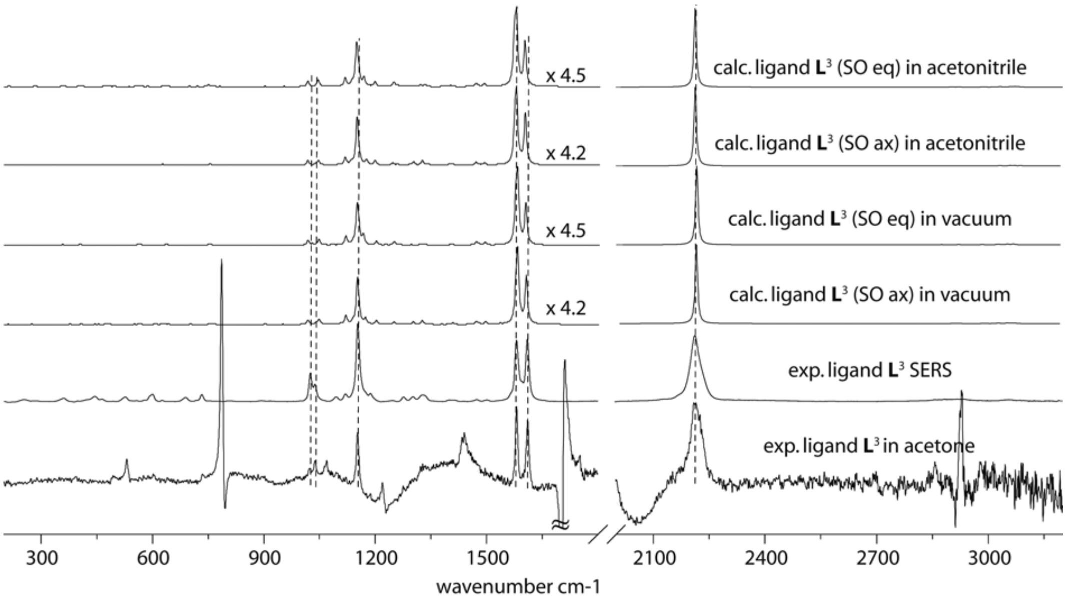

Figure SI-VII.13 Calculated vibrational spectra using a solvent (acetonitrile) and in vacuum for the ligand **L**^{3} with variation of the oxygen position vs. experimental spectra in solution (acetone) and on Au surface (SERS). The range 200-1800 cm^{-1} of the calculated spectra was enlarged by a factor of 4.2 for the oxygen in axial position and 4.5 for equatorial position.

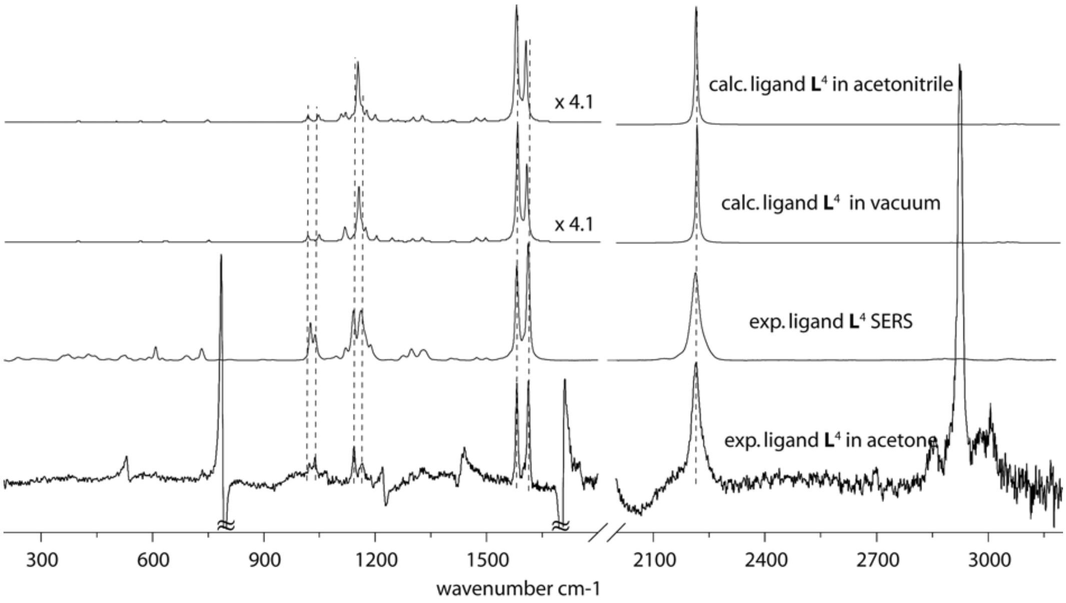

Figure SI-VII.14 Calculated vibrational spectra using a solvent (acetonitrile) and in vacuum for the ligand **L**^{4} vs. experimental spectra in solution (acetone) and on Au surface (SERS). The range 200-1800 cm^{-1} of the calculated spectra was enlarged by a factor of 4.1.

3. Vibrational spectra calculated for the double-cages $[3BF_4@Pd_4L^n{}_8](BF_4)_5$ with n =2-4

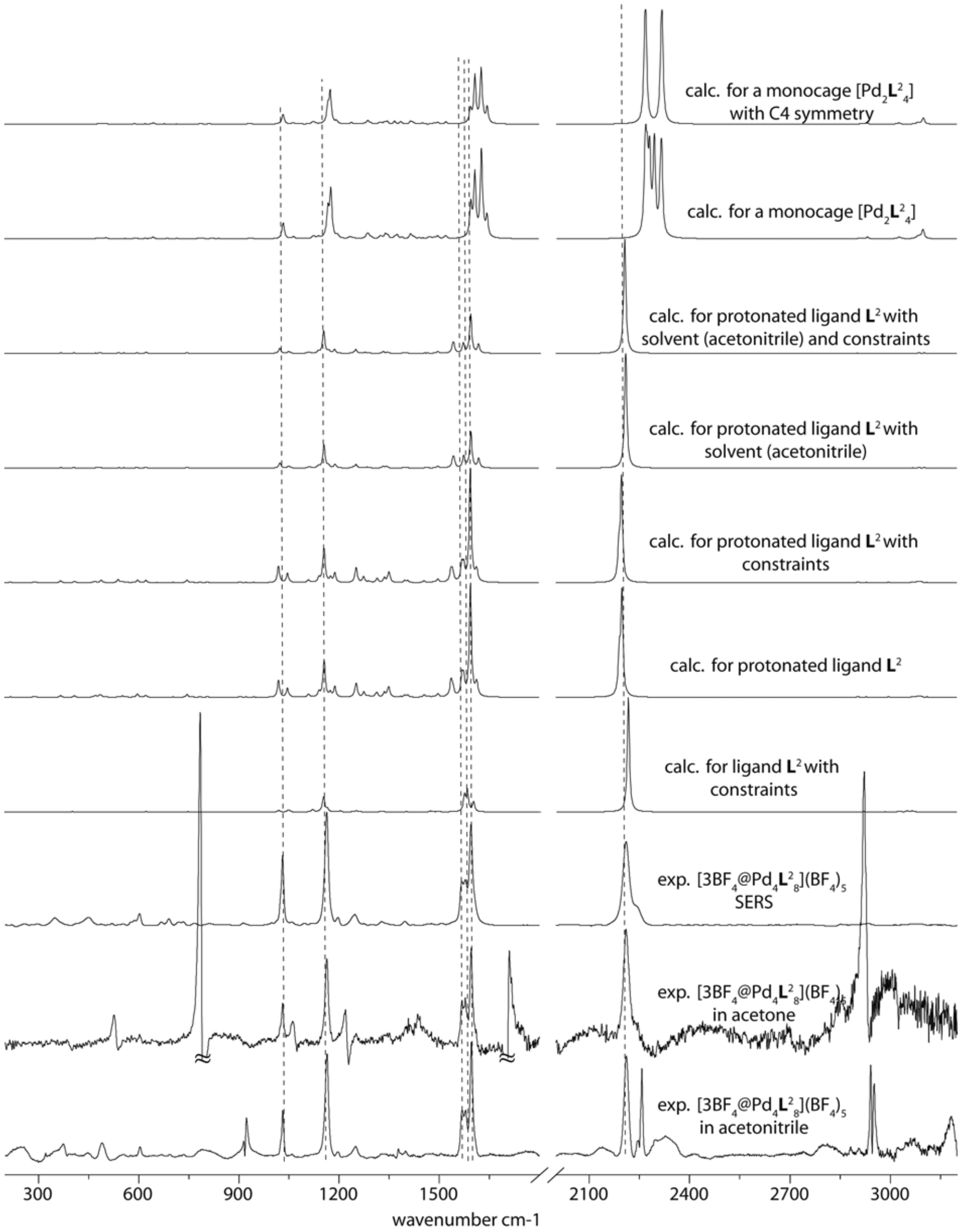

Figure AP-VII.15 Calculated vibrational spectra using different approaches such as i) defined distance between the pyridine atoms (abbr. constraints), ii) protonation of the ligand at the pyridine arms, iii) combination of defined distance and protonation, iv) protonation and solvation (acetonitrile), v) combination of defined distance, protonation and solvation, vi) a model of a monomeric cage $[Pd_2\mathbf{L}^2{}_4]^{4+}$ and vii) a model of a monomeric cage $[Pd_2\mathbf{L}^2{}_4]^{4+}$ with a C4 symmetry as a simplified model for the double-cage $[3BF_4@Pd_4\mathbf{L}^2{}_8](BF_4)_5$ vs. experimental spectra in solution (acetonitrile and acetone) and in solid state (SERS).

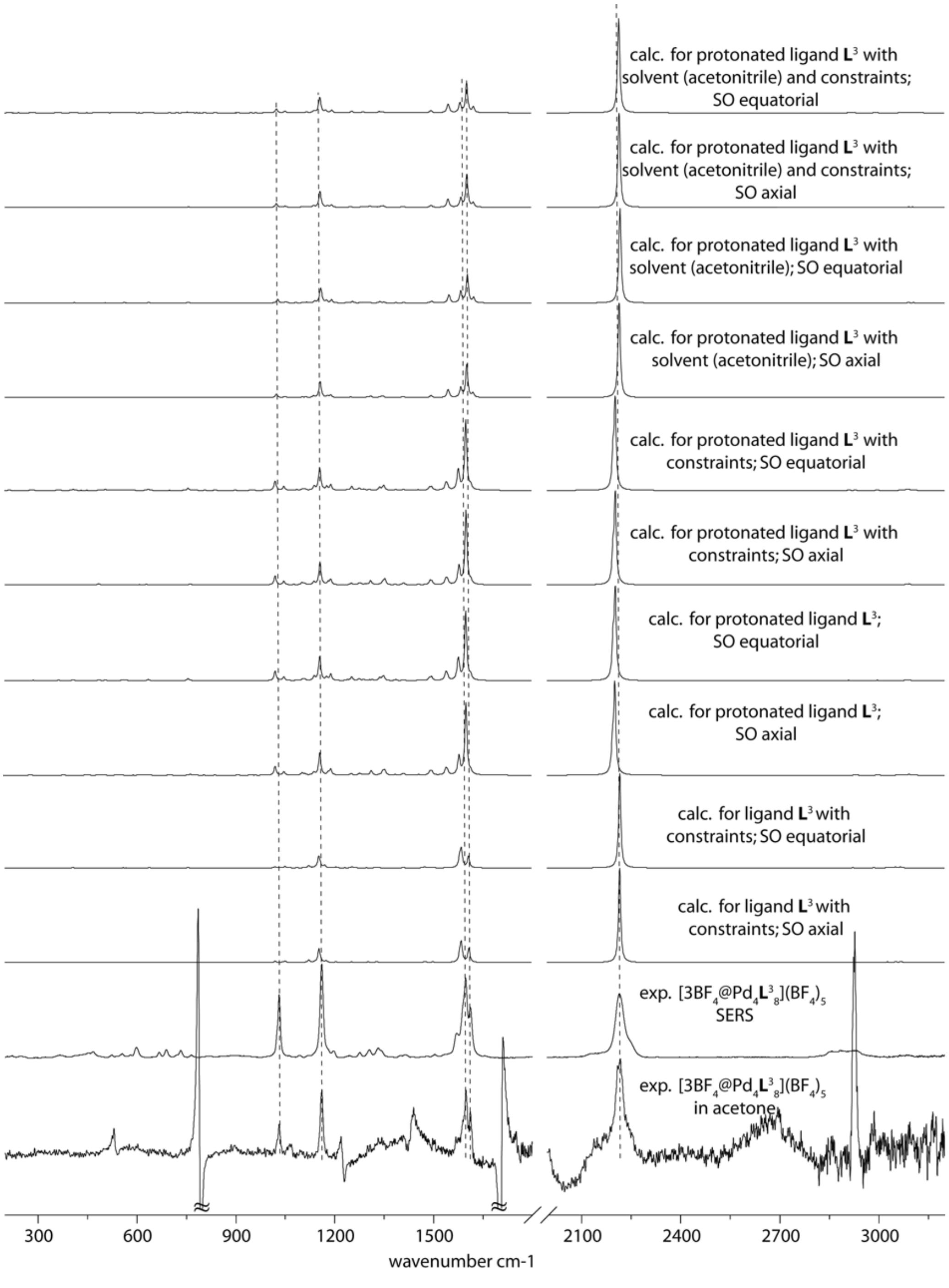

Figure AP-VII.16 Calculated vibrational spectra using different approaches such as i) defined distance between the pyridine atoms (abbr. constraints), ii) protonation of the ligand at the pyridine arms, iii) combination of defined distance and protonation, iv) protonation and solvation (acetonitrile), v) combination of defined distance, protonation and solvation as a simplified model for the double-cage $[3BF_4@Pd_4\mathbf{L}^3_8](BF_4)_5$ vs. experimental spectra in solution (acetone) and in solid state (SERS). The calculations were done for two possible positions of the oxygen atom (equatorial and axial orientation).

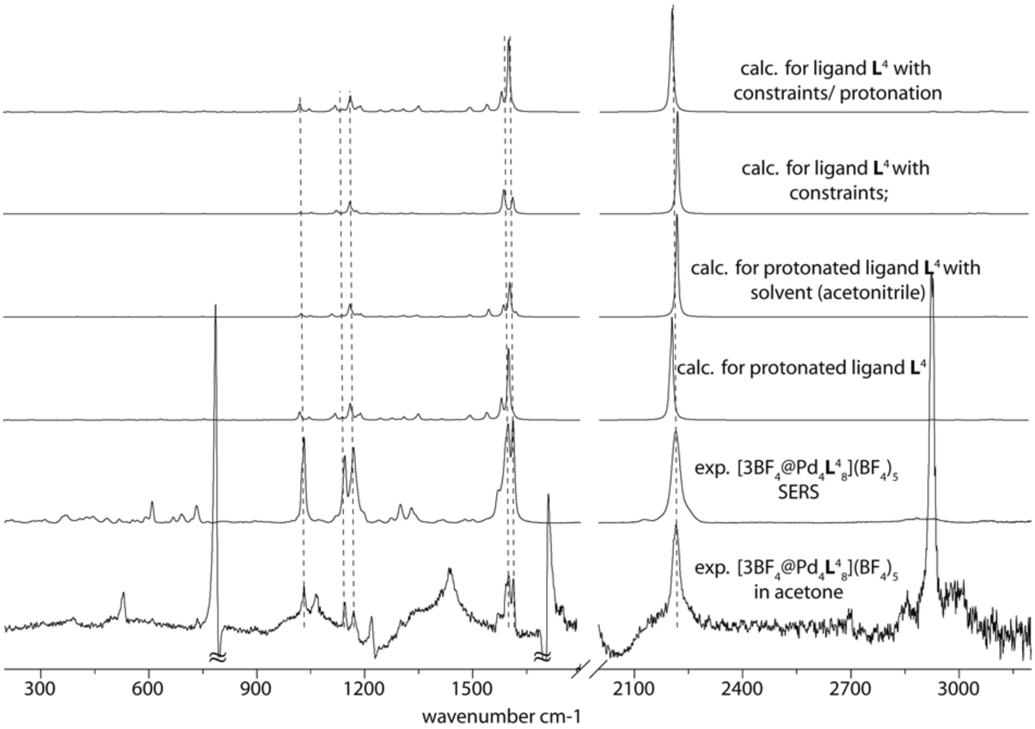

Figure AP-VII.17 Calculated vibrational spectra using different approaches such as i) protonation of the ligand at the pyridine arm, ii) combination of protonation and solvation (acetonitrile), iii) defined distance between the pyridine atoms (abbr. constraints) and iv) combination of defined distance and protonation as a simplified model for the double-cage $[3BF_4@Pd_4\mathbf{L}^4{}_8](BF_4)_5$ vs. experimental spectra in solution (acetone) and in solid state (SERS).

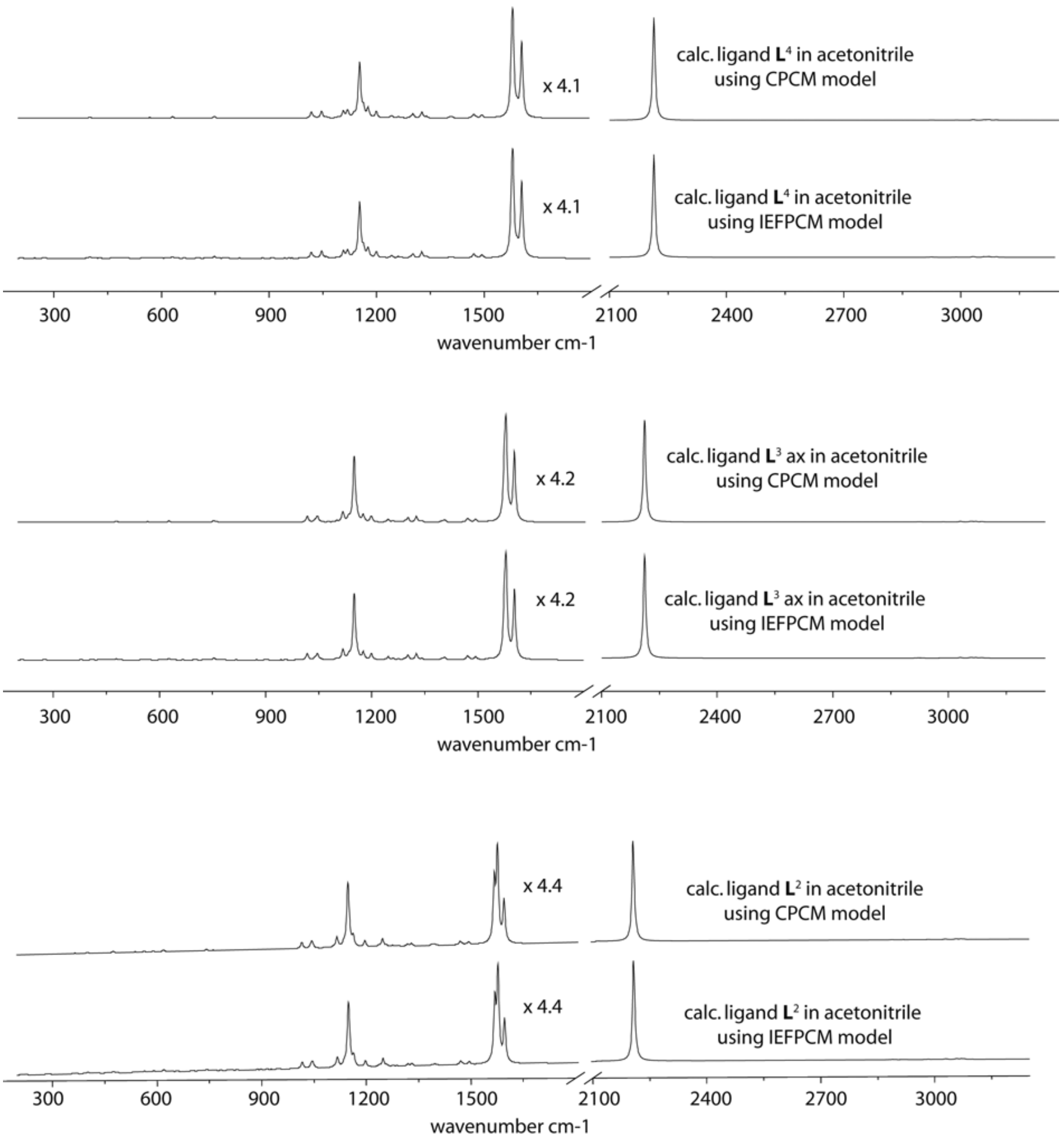

Figure AP-VII.18 Calculated vibrational spectra using different solvation models[**184**] for the ligands L^n with n = 2, 3 (O = axial) and 4. CPCM (polarizable conductor continuum model)[185,186] and the IEFPCM (integral equation formalism polarizable continuum model).[187]

---

[185] V. Barone and M. Cossi, *J. Phys. Chem. A*, **1998**, *102*, 1995.

[186] M. Cossi, N. Rega, G. Scalmani, and V. Barone, *J. Comp. Chem.*, **2003**, *24*, 669.

[187] G. Scalmani and M. J. Frisch,*.J. Chem. Phys.*, **2010**, *132*, 114110.